Metal-Organic Frameworks (MOFs) Derived Heteroatom-Doped Carbon for Energy and Environmental Applications

By

Vaishna Priya K

Registration No: 10CC17A39009

A thesis submitted to the

Academy of Scientific & Innovative Research

for the award of the degree of

DOCTOR OF PHILOSOPHY

in

SCIENCE

Under the supervision of

Dr. U. S. Hareesh

niist

सीएसआईआर का अंतर्विषयी आयाम

Interdisciplinary face of CSIR

CSIR-NATIONAL INSTITUTE FOR INTERDISCIPLINARY SCIENCE AND TECHNOLOGY (CSIR-NIIST) THIRUVANANTHAPURAM-695019, KERALA, INDIA

AcSIR

Academy of Scientific and Innovative Research

AcSIR Headquarters, CSIR-HRDC campus,

Sector 19, Kamla Nehru Nagar,

Ghaziabad, U.P. – 201 002, India

August 2023

Dedicated to my beloved family, friends and teachers….

CERTIFICATE

This is to certify that the work incorporated in this Ph.D. thesis entitled "*Metal-organic frameworks (MOFs) derived heteroatom-doped carbon for energy and environmental applications*" submitted by **Ms. Vaishna Priya K,** to the Academy of Scientific and Innovative Research (AcSIR), in partial fulfilment of the requirements for the award of the Degree of **Doctor of Philosophy in Science,** embodies original research work carried out by the student. We, further certify that this work has not been submitted to any other University or Institution in part or full for the award of any degree or diploma. Research materials obtained from other sources and used in this research work have been duly acknowledged in the thesis. Images, illustrations, figures, tables etc., used in the thesis from other sources, have also been duly cited and acknowledged.

Vaishna Priya K

(Student)

03.08.23

Dr. U. S. Hareesh

(Thesis Supervisor)

Thiruvananthapuram

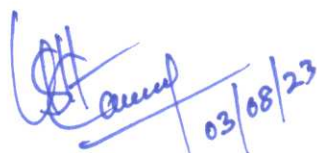August 2023

STATEMENTS OF ACADEMIC INTEGRITY

I, **Vaishna Priya K**, a Ph.D. student of the Academy of Scientific and Innovative Research (AcSIR) with Registration No. 10CC17A39009 hereby undertake that, the thesis entitled *"Metal-organic frameworks (MOFs) derived heteroatom-doped carbon for energy and environmental applications"* has been prepared by me and that the document reports original work carried out by me and is free of any plagiarism in compliance with the UGC Regulations on *"Promotion of Academic Integrity and Prevention of Plagiarism in Higher Educational Institutions (2018)" and* the CSIR Guidelines for *"Ethics in Research and in Governance (2020)".*

03/08/2023

Vaishna Priya K

August 2023

Thiruvananthapuram

It is hereby certified, that the work done by the student, under my supervision, is plagiarism free in accordance with the UGC Regulations on *"Promotion of Academic Integrity and Prevention of Plagiarism in Higher Educational Institutions (2018)"* and the CSIR Guidelines for *"Ethics in Research and in Governance (2020)".*

03/08/23

Dr. U.S. Hareesh

August 2023

Thiruvananthapuram

DECLARATION

I, Vaishna Priya K, bearing AcSIR Registration No. 10CC17A39009 declare that my thesis entitled, "***Metal-organic frameworks (MOFs) derived heteroatom-doped carbon for energy and environmental applications***" is plagiarism free in accordance with the UGC Regulations on *"Promotion of Academic Integrity and Prevention of Plagiarism in Higher Educational Institutions (2018)"* and the CSIR Guidelines for *"Ethics in Research and in Governance (2020)"*.

I would be solely held responsible if any plagiarised content in my thesis is detected, which is violative of the UGC regulations 2018.

03/08/2023

Vaishna Priya K

August 2023

Thiruvananthapuram

ACKNOWLEDGEMENTS

TABLE OF CONTENTS

LIST OF ABBREVIATIONS

MOF   Metal-organic framework

ZIF   Zeolitic imidazolate framework

MIL   Materials Institute Lavoisier framework

HKUST   Hong Kong University of Science and Technology

AFC   Alkaline Fuel Cell

ORR   Oxygen Reduction Reaction

RDE   Rotating disk electrode

RRDE   Rotating ring-disk electrode

eV   Electron Volts

LSV   Linear sweep voltammetry

K-L   Koutecky–Levich

CA   Chronoamperometry

CV   Cyclic Voltammetry

ADT   Accelerated Durability Test

AOP   Advanced oxidation processes

TENG   Triboelectric nanogenerator

N   Nitrogen

PXRD   Powder X-ray diffraction

FT-IR   Fourier Transform-Infrared spectroscopy

SEM   Scanning Electron Microscopy

EDS   Energy Dispersive Spectroscopy

BET   Brunauer-Emmett-Teller

BJH   Barrett-Joyner-Halenda

HRTEM   High Resolution Transmission Electron Microscope

TGA	Thermo Gravimetric Analysis
XPS	X-ray photoelectron spectroscopy
JCPDS	Joint Committee on Powder Diffraction Standards
Rh B	Rhodamine B
PS	Potassium peroxodisulfate
AC	Activated carbon
PAN	Polyacrylonitrile
WAXS	Wide-angle X-ray scattering

PREFACE

With the increasing rate of depletion of fossil fuels, the development of new renewable energy sources has become a major demand for sustainable development. Fuel cells and triboelectric nanogenerators are considered efficient energy conversion devices that can operate in an environment-friendly approach [6, 7]. Additionally, the rapid growth of industrialization and the associated discharge of untreated organic waste have also adversely affected the environment. Advanced Oxidation Process (AOP) employing persulfate activation is perceived as an effective approach for the removal of organic contaminants due to their non-selective degradation [8]. However, developing sustainable materials that can effectively address these problems is still a challenge. Porous carbon materials are considered as potential candidates for energy conversion devices and mitigation of pollutants from different sources due to their variable structures, economically viable preparation strategies, and higher stability. However, the chemical inertness and low electrical conductivity are some of the limitations of these traditional carbon materials that limit their applications. Heteroatom doping is considered as one of the efficient approaches for tuning the properties of carbon since it can alter the spin, and electronic states of the carbon leading to the generation of activated regions [9]. The preparation of heteroatom-doped carbon using Metal-organic frameworks (MOFs) precursors has attracted attention due to the easy synthesis strategy, tunable morphology and heteroatom doping. Hence in this regard, N-doped carbon and transition metal-incorporated carbon exploiting different MOFs are prepared and their efficiency is evaluated for energy conversion devices and organic pollutant degradation.

The thesis comprises of six chapters. **Chapter 1** gives an introduction to heteroatom-doped carbon, Metal-organic frameworks, Fuel cells, Advanced oxidation processes (AOPs), and triboelectric nanogenerators. A detailed review of the literature regarding the application of MOF derivatives for the mentioned applications is carried out for the definition of the problems mentioned.

Chapter 2 deals with the design of Heteroatom doped porous carbon electrocatalyst with enhanced oxygen reduction reaction (ORR) performance in an alkaline medium. High-temperature treatment of Ni-incorporated ZIF-8 frameworks of varying Ni/Zn molar ratio and its composite with g-C_3N_4 as a template led to the formation of porous carbon with

tuned morphology and porosity. The template-aided synthetic strategy using g-C$_3$N$_4$ helped in the controlled decomposition of composites leading to heterosporous sheet-like architectures with increased nitrogen content. The Ni/Zn ZIF-8 sample on heat treatment in the 800-1000 °C temperature range, led to the formation of Ni, N co-doped porous carbon (Ni-NPC) with Ni-C active sites. The defective sites induced by nickel carbide along with the distributed N atoms on the carbon surface enabled active O$_2$ adsorption sites. The high surface area, high degree of graphitization as well as the defects created by the well-dispersed N and Ni on the porous carbon matrices favored the charge separation leading to higher electrochemical ORR activity. The Ni, N co-doped carbon catalyst in an alkaline medium exhibited a limiting current density of 5.2 mAcm^{-2} with a half-wave potential of 0.76 V Vs RHE in 0.1 M KOH. The catalyst also showed improved methanol tolerance and better stability compared to the standard Pt/C catalyst.

Chapter 3 demonstrates the synthesis of a Co, N co-doped carbon by blending ZIF-67 derived Co-doped carbon with a high surface area microporous carbon prepared from a lotus seed shell. The combination of the two catalysts led to enhanced electrochemical ORR activity in an alkaline electrolyte medium. The optimized carbon catalyst ZL 600(3:1) exhibited a half-wave potential of 0.79 V vs. RHE and a current density of -4.38 mA/cm^2 in 0.1 M KOH solution. The catalyst also showed higher stability as well as methanol tolerance. The high micro-mesoporosity, pyridinic –pyrrolic nitrogen contents, as well as enriched Co active centers surrounded by carbon sheets, favorably contributed to the efficient ORR mechanism.

In **Chapter 4,** we utilized different MOF materials, such as ZIF-8, ZIF-67, MIL-100, and HKUST-1 to tune the triboelectric properties of polyacrylonitrile (PAN) fiber by incorporating them during the electrospinning process. Based on the concentration, particle size, central metal, and ligand, the triboelectric behavior of the PAN material changed, and even a reversal of the triboelectric polarity was achieved. A triboelectric device was fabricated with ZIF-8 and the carbonized C ZIF-8 incorporated PAN fibres as opposite triboelectric layers. The device generated an output of 80 V and 0.8 μA. This shows that adding MOF material is an efficient method to enhance and tune the triboelectric properties of polymer materials such as PAN. This can be utilized for self-powered tactile sensing or powering small electronic gadgets

Chapter 5 deals with the fabrication of Fe, Fe_3C encapsulated porous carbon by the high-temperature carbonization of the MIL-100 (Fe) metal-organic framework. The catalytic activity of the obtained carbon was tested towards the degradation of the targeted contaminant Rhodamine (B). 100 % degradation was realized within the initial 35 minutes with minimum catalyst loading of 100 mg/L in 30 mg/L contaminant solution. Also, the catalyst retained ~ 90 % of the removal rate even after 5 cycles of operation. The carbon exhibited high degradation activity towards various other organic compounds like Methylene blue, Benzoic acid, Nitro benzene, Phenol, 4-Chlorophenol, and antibiotics Tetracycline, Linezolid, Hydroxychloroquine, and Cefpodoxime Proxetil. The homogeneous dispersion of Fe^0, and Fe_3C species as well as the porous, morphology features obtained on carbonization of MOF has led to better adsorption of reactive species leading ultimately to efficient degradation.

The major findings of the research are summarized in the concluding chapter 6 of the thesis.

Introduction
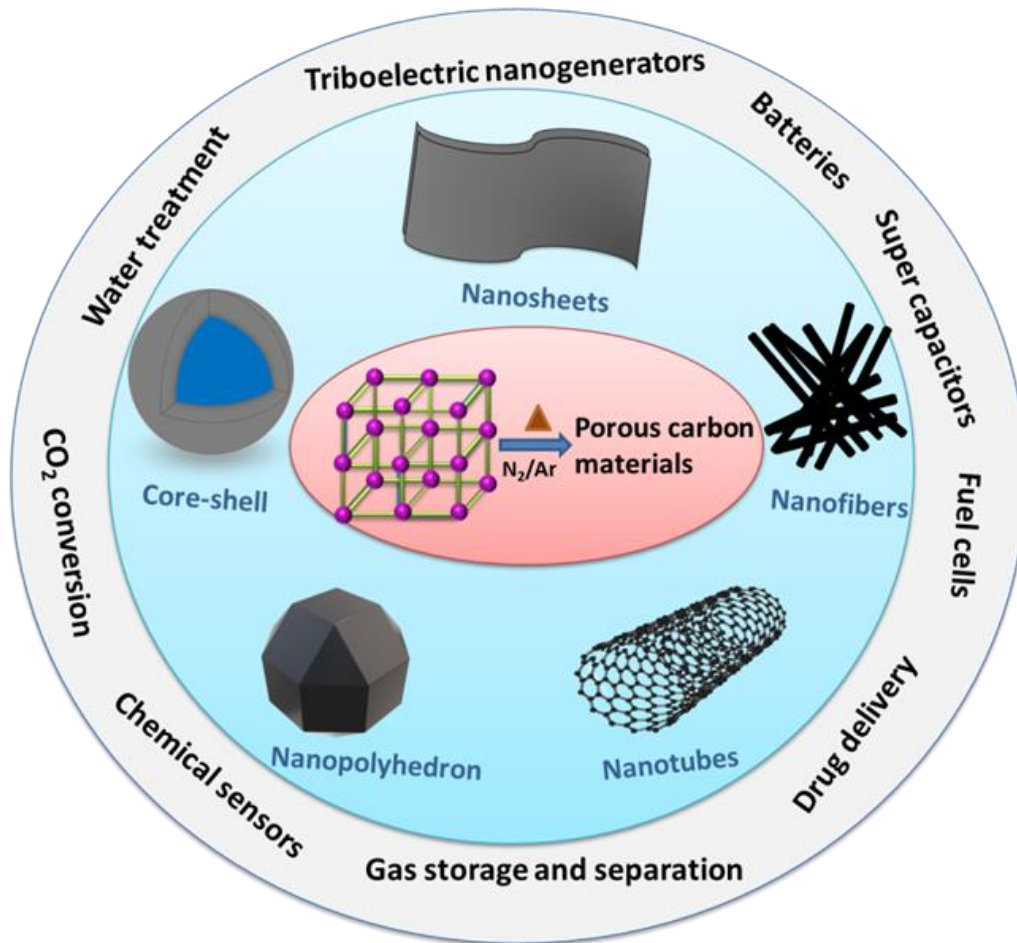
1.1. Porous carbon

The exploration of carbon materials has created a breakthrough in the global energy and environment sectors. Unique features such as low cost, high surface area, electrical conductivity, thermal and chemical stability, and flexibility for modification enable carbon to be a non-replaceable candidate in many areas. [1, 2] The adaptability of the carbon to form covalent bonds with other carbon atoms in varying hybridization states(catenation) has resulted in the existence of different allotropic forms in nature (**Figure 1.1**). The allotropic forms of carbon mainly include Graphene, Diamond, graphite, carbon nanotubes, fullerenes, etc. The physical and structural properties of carbon differ depending upon the allotropic forms and enable a multitude of applications in various fields, including electronics and catalysis.[3]
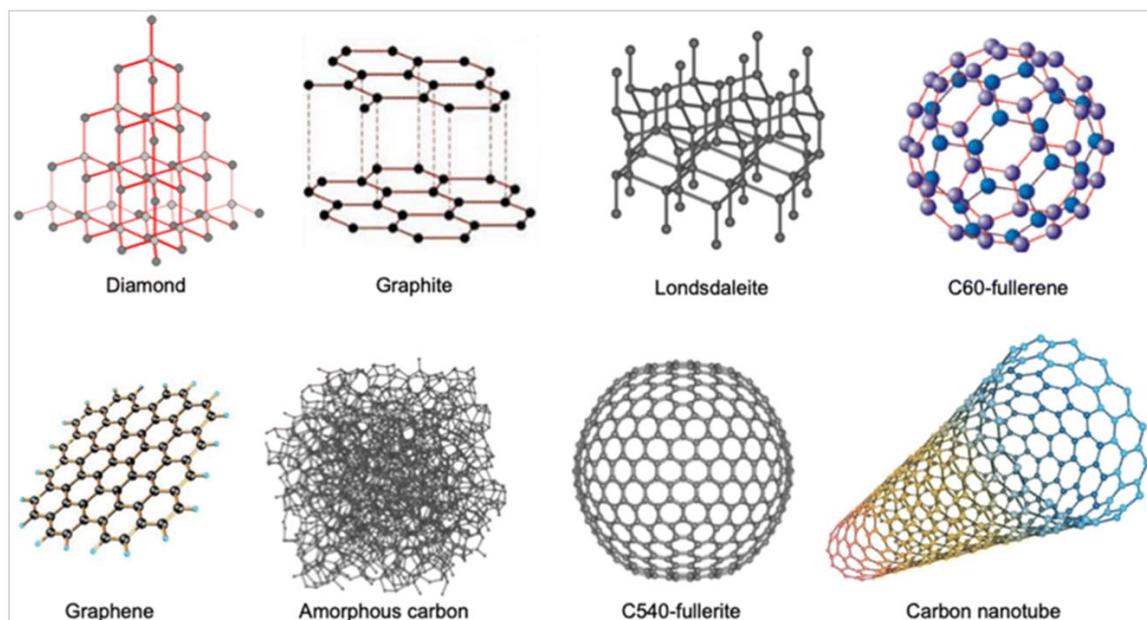
Figure 1.1. Different allotropic forms of carbon [4]

Among them, porous carbon materials with 1D to 3D networks are proven to be efficient candidates for energy storage devices, wastewater treatment, gas storage, and separation. As shown in **Figure 1.2,** porous carbon is usually characterized by connected channels extending throughout the carbon framework. Based on the types of pores present on this carbon, the carbon materials can be divided into; 1) microporous (pores < 2 nm), 2) mesoporous (2-50 nm), and 3) macroporous (pores > 50 nm) materials. Depending on the types of pores, the functional properties of the carbon materials are also varied. Microporous

materials possess a high surface area and are widely applied for adsorption applications. The mesoporous surfaces help promote mass transfer and diffusive transfer and are utilized for conversion reactions like CO_2 catalytic conversion, oxygen reduction reaction, pollutants degradation, etc. [5, 6] Newly designed porous carbon materials with controlled micro/meso porosity are demonstrated to perform exceptionally well in many fields, including heterogeneous catalysis and energy devices.[7]
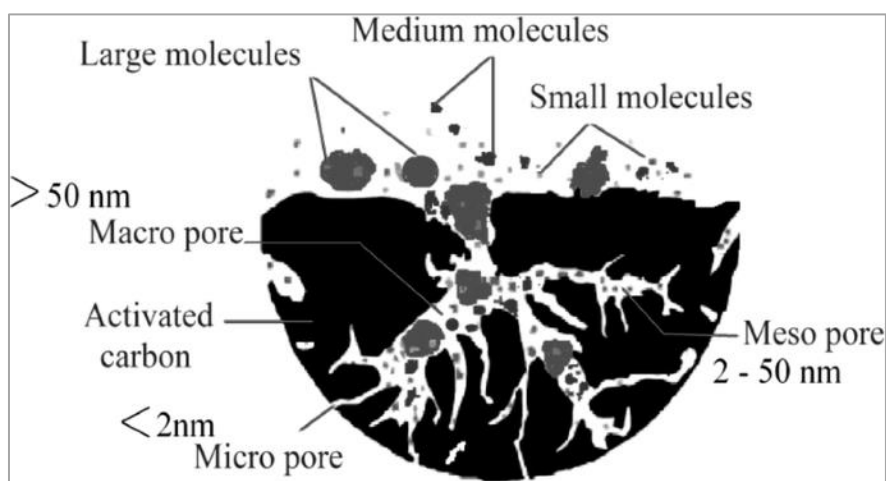
Figure 1.2. Adsorption on porous carbon channels [8]

1.2. **Heteroatom-doped carbon**

Traditional carbon materials face difficulty in their practical employment due to their chemical inertness and low electrical conductivity. In order to improve the properties, many attempts are made to modify the carbon structure. Heteroatom functionalization is considered one of the efficient approaches to impart better conductivity and for the creation of active centers on carbon. Doping of carbon with heteroatoms such as N, P, B, S, etc., is found to tune the physical as well as chemical properties of the carbon (**Figure 1.3.**). These heteroatoms usually possess differences in valence electrons and electronic states than carbon, and when doped in a carbon matrix, can hence modify the chemical and electronic states. Doping heteroatoms into the carbon can change their symmetry, ultimately changing their properties. It creates an activation region on the carbon that enhances the catalytic property of the carbon. Heteroatom-doped carbon is widely applied in energy storage devices and heterogeneous catalysis. [9, 10]
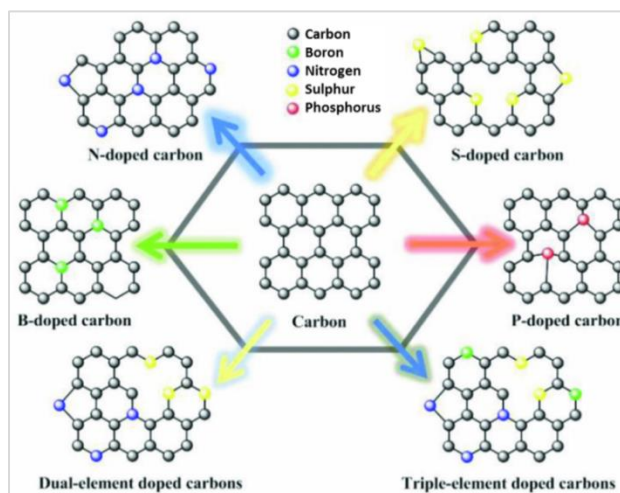
Figure 1.3. Representation of heteroatom-doped carbon [11]

1.2.1. N-doped carbon

  Among the heteroatom-doped carbon materials, N-doped carbon found attention due to the added advantage of carbon upon N-atom incorporation. Since N has almost a similar radius to carbon, it can be easily incorporated into carbon without any changes in the lattice, which may efficiently improve the surface energy, electrical conductivity, and reactivity of the carbon materials. The introduction of N into the sp^2 stated carbon lead to many types of bonding configuration, which are categorized into; 1) pyridinic, 2) pyrrolic, 3) Graphitic (Quarternary-N), and 4) Pyridinic N-O, shown in **Figure 1.4**. Pyridinic nitrogen is a type of nitrogen that form bonds with two carbon atoms in a hexagon ring. Pyrrolic nitrogen is bonded to two carbon in a pentagon. Graphitic nitrogen substitutes the carbon in a graphene layer by forming bonds with three sp2 carbon atoms. The presence of each N can affect the electronic states of the carbon differently. The N incorporation can create an n-type semiconductor effect on the carbon hence are, widely applied in electronic applications.[12, 13]
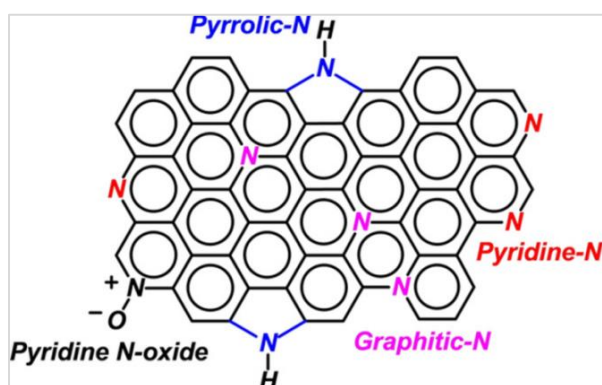
Figure 1.4. Different types of nitrogen doping on carbon [12]

1.2.2. Transition metal incorporated carbon

Transition metals, due to their partially occupied d orbitals, found applications in many areas, including catalysis in the form of their alloys, oxides, hydroxides, chalcogenides, etc. [14, 15] (**Figure 1.5**). However, these transition metal catalysts often possess low surface area, making it difficult to access the active sites. Also, the limited electrical conductivity and the tendency to form aggregates affect the stability and efficiency. It is found that when transition metals are incorporated into the carbon matrix, they enable an efficient electron transfer mechanism due to more exposed transition metal-based active sites that, in turn, enhance the catalytic properties of the carbon.   Also, these metal active sites are often protected by the surrounding carbon, improving the stability of the material. [16, 17] To date, different types of transition metal/carbon hybrid with varying morphology, like hollow spheres, nanotubes, core shells, yolk-shell structures, and nanosheets, are synthesized using diverse methods and are widely applied as heterogeneous catalysts with higher catalytic activity and stability. [18]
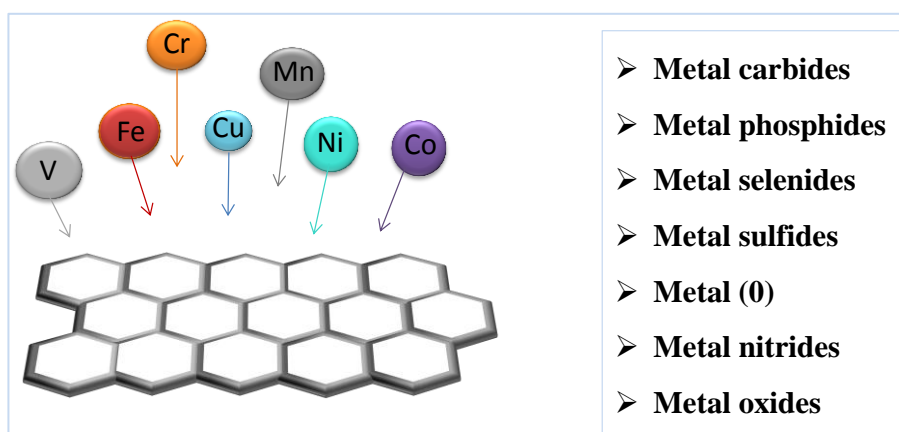
Figure 1.5. Different types of transition metal incorporation into the carbon

1.3.   Heteroatom doping strategies

Besides the surface area and morphology, heteroatom doping level is also a significant factor affecting the properties of the porous carbon. Different approaches are used to prepare heteroatom doped carbon, which can be mainly categorized into two methods; 1) In situ method and 2) Post-treatment method **(Table1).**

Table 1. Heteroatom doping strategies [19, 20]

	In situ methods	Post-synthesis methods
Synthesis	Direct carbonization of precursors or compounds containing carbon and heteroatoms	introduction of heteroatoms into the synthesized carbon materials using precursors
Synthesis methods	High-temperature carbonization, templated methods, and chemical vapour deposition.	Thermal treatment of carbon with heteroatom source, plasma treatment, arc discharge method etc.
Heteroatom doping	Heteroatom doping throughout the carbon matrix	Heteroatom doping on the surface only
Uniformity of heteroatom doping	Uniform heteroatom doping	Non-uniform heteroatom doping
Cost	Cost-effective and simple procedures	High production costs and complex experimental procedures
Precursors	Biomass, polymer, organic templates, MOFs	Organic, inorganic volatile compounds

1.4. Metal-Organic Frameworks

Metal-organic frameworks (MOFs) are a class of compounds formed by metal ions or clusters coordinated to organic ligands to form two or three-dimensional structures. MOFs have received remarkable attention due to their unusual properties, such as high surface area and good thermal and chemical stability. They are remarked as versatile materials in gas storage and separation, liquid separation and purification, electrochemical energy storage, and drug delivery applications.
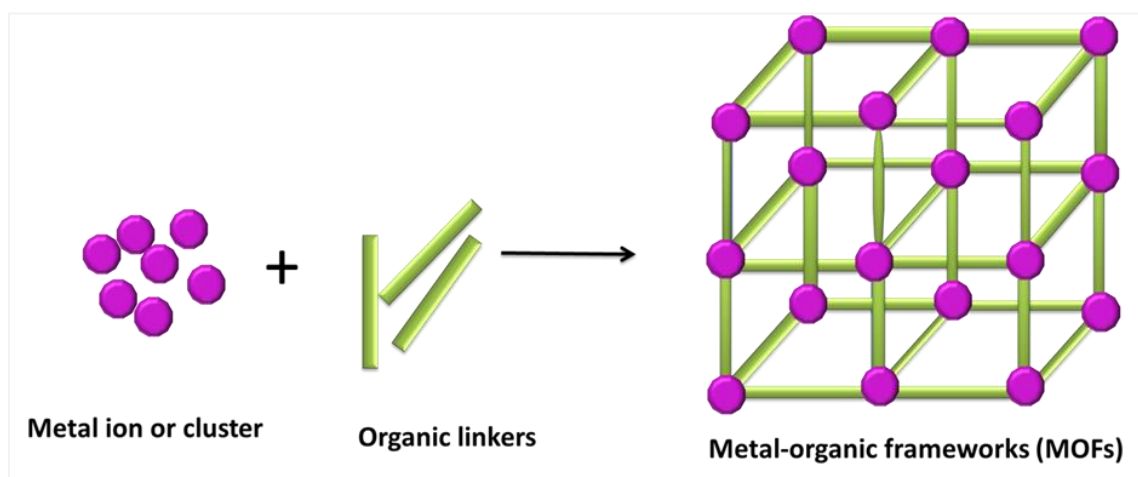
Figure 1.8. Schematic representation of the formation of Metal-organic framework

The MOFs consist of two components: A central metal ion or metal ion clusters and the organic molecules linked to it (**Figure 1.8.**). The organic ligands are usually mono, di, tri, or tetravalent molecules that act as a linker between the positively charged metal ions forming cage-like structures, thereby creating potential voids. Hence, MOFs usually possess very high internal surface area and stability. Due to the periodic arrangements of atoms, MOFs are usually found as crystalline structures. The stability of the MOFs will depend upon the strength of the metal-ligand bonds. The choice of metal ions and the linkers can adapt the linkage to a particular orientation and can exist in variable structural geometry, shape, and porosity. [21] MOFs can be categorized into subclasses depending on the coordinated metals and ligands. Zeolitic imidazolate frameworks (ZIFs) belong to a subclass of metal-organic frameworks formed by the tetrahedral coordination of metal ions with the imidazolate ligands. Materials Institute Lavoisier frameworks (MILs) are formed by coordinating trivalent metal ions (Fe, Al, and Cr) with carboxylic acid-based ligands. HKUST-1(Hong Kong University of Science and Technology) is another class of MOFs formed by coordinating copper with 1,3,5-benzene tricarboxylic acid struts between them. MOFs are usually formed by high valent metals, including 3d transition metals such as Cr, Mn, Fe, Co, etc., with highly Lewis base ligands. However, a few stable metal-organic frameworks with low valent metals nodes(e.g., Cu^I, Ag^I, Au^I, Ni^0, etc.) are also reported. [22, 23]

Prof. Omar M Yaghi pioneered the art of creating this new class of organic-inorganic MOFs in the late 1990s. In 1999, Prof.Mohamed Eddaoudi, O.M. Yaghi, and their group reported MOF-5, a metal-organic framework formed by the coordination of f 1,4-benzene dicarboxylate (BDC) with Zn^{2+} ions with high porosity and a Langmuir surface area of 2,900

$m^2 \ g^{-1}$ [24], followed by that, a chain of inventions have happened. Later, Twelve zeolitic imidazolate frameworks(ZIFs) formed by the coordination of either Zn(II) (ZIF-1 to -4, -6 to -8, and -10 to -11) or Co(II) (ZIF-9 and -12) with imidazolate-type links was reported, and some of their gas adsorption capacity was also measured. Since the coordination behavior and geometry of the metal and ligands are different, diverse varieties of MOFs are possible. To date, around 20,000 MOFs have been created, and their applications are studied in various fields. Some of the important MOFs and their applications are summarized in **Table 2.** So far, most of the reported MOFs are stable up to 300-400 °C enabling their applications in different fields. [25-27]

Table .2. Some important metal-organic frameworks and their applications [28, 29]

MOF	structure	Metal ion	Organic ligand	Year	applications
ZIF-7	Zn(PhIM)$_2$	Zn	benzimidazole	2006	gas adsorption and separation
ZIF-8	Zn(MeIM)$_2$	Zn	2-methylimidazolate	2006	Gas adsorption
ZIF-9	Co(PhIM)$_2$	Co	benzimidazole	2006	Adsorption Catalysts in Organic reactions
ZIF-11	Zn(PhIM)$_2$	Zn	benzimidazole	2006	Gas adsorption
ZIF-68	Zn(bIM)(nIM)	Zn	benzimidazole 2-nitroimidazole	2008	gas adsorption and separation
ZIF-69	Zn(cbIM)(nIM)	Zn	5chlorobenzimidazole 2-nitroimidazole	2008	gas adsorption and separation
ZIF-70	Zn(Im)$_{1.13}$(nIM)$_{0.87}$	Zn	imidazole 2-nitroimidazole	2008	gas adsorption and separation
ZIF-67	Co(mIM)$_2$	Co	2-methylimidazole	2008	Gas adsorption, separation, electrocatalysis and catalysis

ZIF-100	$Zn_{20}(cbIM)_{39}(OH)$	Zn	5chlorobenzimidazole	2008	Gas adsorption and storage
MIL-100	$Fe_3O(H_2O)_2OH(BTC)_2$	Fe	Benzene-1,3,5-tricarboxylate		Gas adsorption Drug delivery Catalysts for organic reactions
MIL-101	$Cr_3O(OH,F,H_2O)_3(1,4\text{-}bdc)_3$	Cr	1,4-benzenedicarboxylate	2006	Drug delivery
HKUST-1	$Cu_2(H_2O)_2(CO_2)_4$	Cu	Benzene-1,3,5-tricarboxylate	2006	Adsorption and storage Anti-bacterial
MOF-5	$Zn_4(1,4\text{-}bdc)_3$	Zn	1,4-benzenedicarboxylate	2002	Methane Storage
MOF-74	$Zn_2(C_8H_2O_6)$	Zn	2,5-dihydroxybenzene-1,4-dicarboxylic acid	2006	Adsorption and storage

1.4.1. Heteroatom doped carbon preparation from metal-organic frameworks

Metal-organic frameworks, formed by metal ions and the organic ligands rich in carbon and other heteroatoms such as nitrogen, oxygen, sulfur, etc., can leave behind heteroatom-doped porous carbon structures when treated in an inert atmosphere (under N_2 / Ar). The metal-ligand coordination can be rearranged on high-temperature carbonization to form heteroatom-doped carbon assisted by the volatilization of small volatile molecules. Due to the low boiling point of Zn ion, varieties of metal-organic frameworks containing zinc as central metal atoms are widely exploited to prepare metal-free heteroatom-doped carbon. It is reported that, unlike Zn, the other transition metals, such as Fe, Co, Ni, etc., cannot be vaporized during carbonization due to their high boiling point. Hence they serve as a metallic dopant in forming metal-doped carbon with porosity and tuned morphology. [30] Upon carbonization at a higher temperature, the metal elements in the MOFs frameworks may transform into metal, metal carbides, nitrides, oxides, sulfides, etc., dispersed or embedded on a carbon matrix derived from the surrounding ligands. [31] Compared to other conventional methods of preparation of heteroatom-doped carbon, MOF-derived heteroatom-doped carbon hybrid can inherit the porous features of the carbon, which will be beneficial for the exposure of active sites. It has been demonstrated that the structural and

9

morphological features of the heteroatom-doped carbon can be tuned by incorporating some changes in the precursor chemistry and reaction conditions. Due to these attractive features, MOF-derived carbon is widely applied in various sectors [32,33] (**Figure 1.9.**)
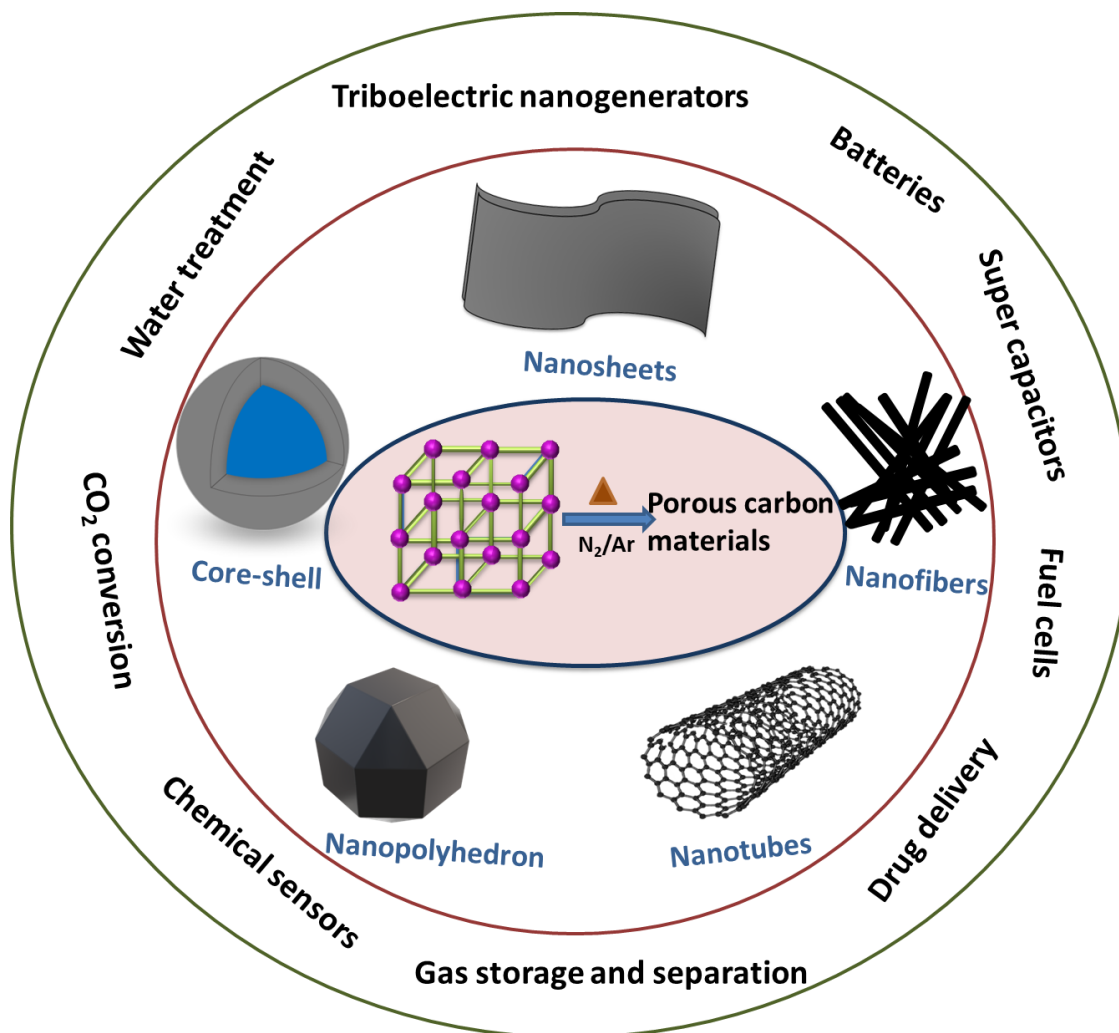
Figure 1.9. MOF-derived carbon structures and their applications

1.5. Fuel cell electrocatalysis

The worldwide concern on increasing energy consumption and depletion of fossil fuels has raised an urge for advanced energy storage and conversion devices based on renewable energy sources. However, the current renewable systems rooted in hydroelectricity, solar, and wind energy sources have been found to possess low efficacy due to their dependence on the climate. This necessitates alternate energy devices that can provide a continuous energy supply. Fuel cells are devices that provides a continuous supply of energy as long as the fuels are provided. The ability of the fuel cells to perform at higher efficiencies with lower emissions compared to current combustion-based systems highlights its advantages. Hence, these devices found a wide range of applications in transportation, stationary, portable, backup power applications, etc.[34, 35]
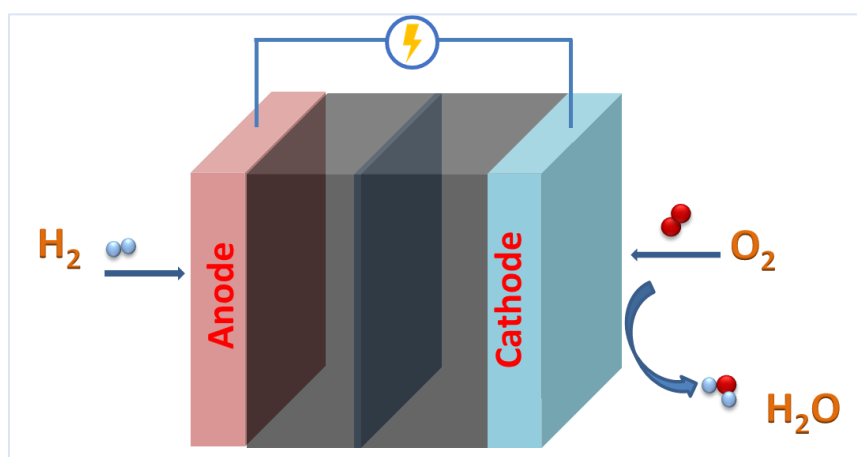
Figure 1.10. Schematic representation of a fuel cell

1.5.1. Classification of fuel cells

The fuel cell comprises an anode, a cathode, and an electrolyte, as represented in **Figure 1.10**. Depending upon the electrolyte and the fuels used, the fuel cells can be categorized into many types (**Table 3**). However, low-temperature fuel cells are preferred over high-temperature fuel cells due to their energy-efficient and environmentally benign operations.

Table 3. Classifications of fuel cells[36-38]

Fuel cell type	Electrolyte	Operating temperature (°C)	Charge carrier	Anode material	Cathode material	Efficiency (%)	Applications
Alkaline fuel cell (AFC)	Aq. KOH	60–90	OH^-	Nickel or precious metal	Platinum (Pt) Lithiated NiO	60	Military Space
Proton exchange membrane fuel cell (PEMFC)	Sulphonated organic polymer	70–100	H^+	Platinum	Platinum	40–45	Backup power Portable power Distributed generation Transportation Specialty vehicles
Solid oxide fuel cell (SOFC)	Yttria-stabilized zirconia (YSZ)	650–1000	O^{2-}	Nickel/Yttria-stabilized zirconia	Strontium doped lanthanum manganite	50–60	Auxiliary power Electric utility Distributed generation
Molten carbonate fuel cell (MCFC)	Molten lithium/sodium/ potassium carbonate	600–700	CO_3^{2-}	Nickel/Chromium Oxide	Nickel Oxide (NiO)	50–60	Electric utility Distributed generation
Phosphoric acid fuel cell (PAFC)	Phosphoric acid	150–220	H^+	Platinum	Platinum	40–45	Distributed generation

1.5.2. Alkaline fuel cells

The Alkaline fuel cells use an alkaline aqueous solution or polymer anion membrane as the electrolyte, which separates an anode and a cathode connected to the external circuit. The reaction drives the electrical energy upon providing H_2 gas at the anode and O_2 or air in the cathode, where water is obtained as the byproduct (**Figure 1.11**). The first alkaline fuel cell was invented by Francis Thomas Bacon in 1939. Due to its higher efficiency, AFCs were employed in American space vehicles. In the 1960s, NASA used AFC in space shuttle missions. They are demonstrated in space programs with 60 % efficiency. [39, 40]
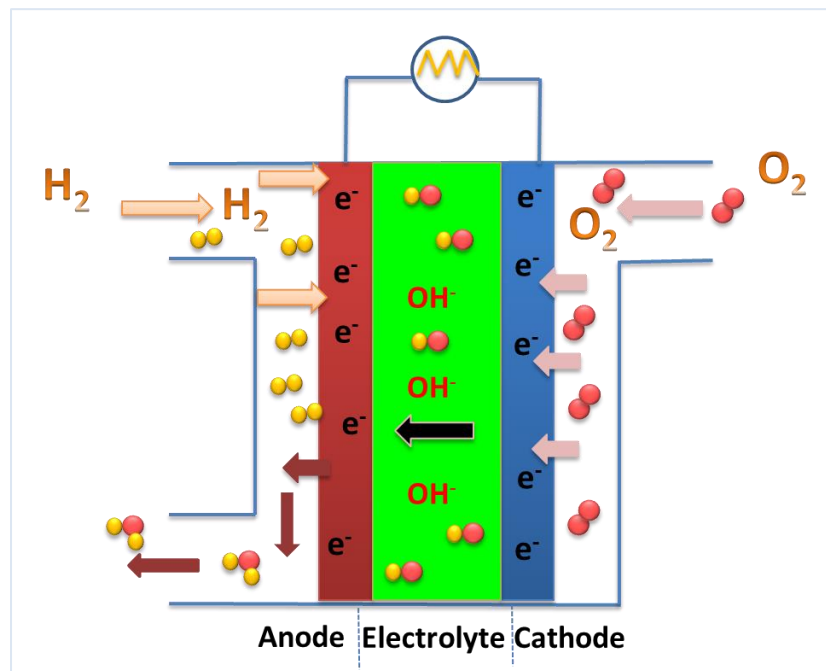
Figure 1.11. Schematic representation of an alkaline fuel cell

1.5.3. Fuel cell Mechanisms in alkaline fuel cells

Anode: $\qquad$ $2H_2 + 4OH^- \rightarrow 4H_2O + 4e^-$ $\qquad$ [1.1]

Cathode: $\qquad$ $O_2 + 2H_2O + 4e^- \rightarrow 4OH^-$ $\qquad$ [1.2]

Overall reaction $\quad$ $2H_2 + O_2 \rightarrow 2H_2O$ $\qquad$ [1.3]
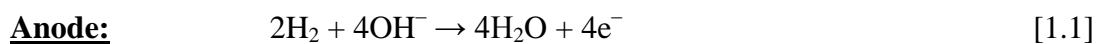
In alkaline fuel cells, due to the less corrosive electrolyte, various catalysts, including non-precious metal catalysts, can be used in the anode and cathode. The faster electron transfer kinetics in the alkaline medium often leads to higher efficiency. The use of an anion exchange membrane instead of an alkaline solution is a solution to mitigate the electrolyte

leakage problem of traditional alkaline fuel cells. Anion exchange membranes based on aliphatic or aromatic polymers with cationic groups, such as perfluorosulfonic acid (PFSA) membranes, are widely employed (Eg: Nafion)[41, 42]

1.5.4. Oxygen reduction reaction

The working of the fuel cell is based on the electrochemical reactions taking place at the electrode-electrolyte interphases that generate electricity, and water is formed as the byproduct. However, compared to the anodic hydrogen oxidation, the kinetics of the cathodic oxygen reduction reaction is slower, caused by the higher lattice enthalpy of the oxygen-oxygen pi bond. Hence it demands a catalyst to decline the activation energy barrier for the reduction reaction to reach the maximum efficiency of the fuel cells.[43, 44] Depending upon the electrolyte medium, the ORR kinetics can arise through different mechanisms that are represented in **Table 4**.

Table 4. Mechanism of different ORR pathways

ORR reaction condition	Direct 4 e⁻ pathway:	2 e⁻ pathway :
Acidic solutions	$O_2 + 4H^+ + 4\,e^- \rightarrow 2\,H_2O$ (E 0 = 1.23 V)	$O_2 + 2H^+ + 2\,e^- \rightarrow H_2O_2$ (E 0 = 0.695 V) $H_2O_2 + 2H^+ + 2\,e^- \rightarrow 2\,H_2O$ (E 0 = 1.776 V)
Alkaline solutions	$O_2 + 2\,H_2O + 4\,e^- \rightarrow 4\,OH^-$ (E 0 = 1.23 V)	$O_2 + H_2O + 2\,e^- \rightarrow H_2O^- + OH^-$ (E 0 = 0.695 V) $H_2O^- + H_2O + 2\,e^- \rightarrow OH^-$ (E 0 = 1.776 V)

1.5.5. Techniques for measuring ORR activity

The preliminary evaluation of the ORR activity of the catalyst is done by the rotating disk electrode (RDE) and rotating ring-disk electrode (RRDE) techniques. As shown in **Figure 1.12**, both setups consist of a three-electrode system comprising a reference electrode, a counter electrode, and a glassy carbon working electrode. Here the electrodes rotate at a constant rate to ensure the arrival of a constant flux of analyte to the electrode. The disk rotation is usually defined by the term angular velocity ω (Sec⁻¹). In RDE, a glassy carbon disk attached to a PTFE insulating material is used as the working electrode, and the changes

in the working electrode are recorded to analyze the electrochemical activity. The RRDE electrodes consist of a glassy carbon electrode surrounded by a Pt ring where the products generated at the glassy carbon get evaluated. [45, 46] The ORR activity is calculated in a typical cathodic half-cell reaction and compared with the state-of-the-art Pt catalysts. Using a linear sweep voltammetry (LSV) curve, the cathodic polarization is evaluated at a known RDE or RRDE rotation.
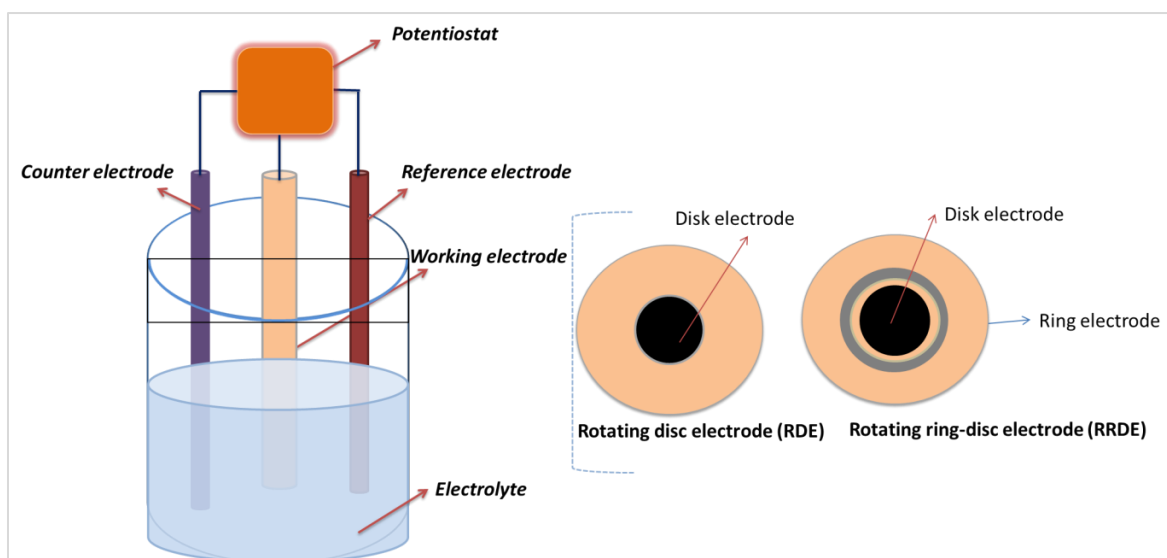
Figure 1.12. Schematic representation of the RDE and RRDE setup

A typical ORR polarization curve can be divided into three regions. The ORR kinetics occurs in different ways, as represented in **Figure 1.13**. In the kinetically controlled area, the ORR rate will be slow, and the current density will increase slowly as the potential decreases. The second region is called the mixed kinetic and diffusion-controlled zone, where the reaction progresses rapidly as the potential decreases, shown by a remarkable increase in the current density. In the third region, called the diffusion-controlled zone, the current density is determined by the rate of diffusion of the reactants reaching the electrode's surface at a particular rotation speed. The ORR activity is calculated from these three regions using the following terms;
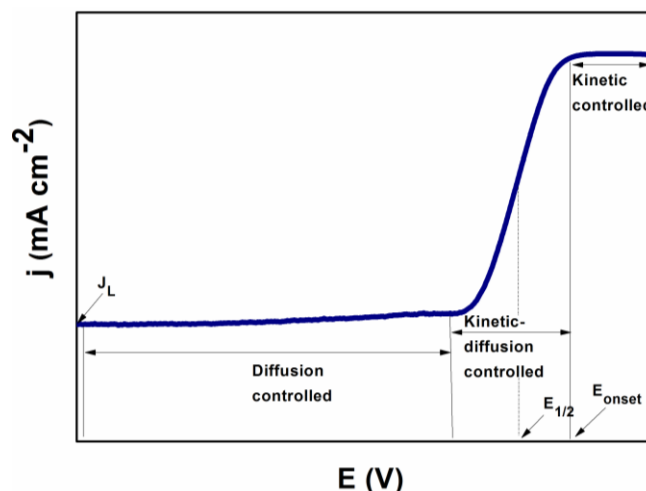
Figure 1.13. A typical ORR polarization curve

1.5.6. Onset (E_{onset}) and Half-wave ($E_{1/2}$) potential

E_{onset} is commonly defined as the potential corresponding to 5 % of the diffusion-limited current density. The half-wave potential is the potential at which the polarographic current attains half of the maximum current density (limiting current density, JL). The more positive the E_{onset} and $E_{1/2}$ values, the more active the catalyst is. For laboratory analysis, the values are compared with the state-of-the-art Pt catalyst.

1.5.7. Kinetic current density (J_k)

Kinetic current density defines the kinetics of the ORR mechanism. It can be calculated   via Koutecky–Levich (K-L) equation;

1/J= 1/J$_k$ + 1/J$_L$ [1.4]

Where **J** is the measured current density, **J$_K$** is the kinetic current density, and **J$_L$** is the limiting current density. The kinetic current density is usually measured at a higher potential. Usually, the contribution from the background current should be eliminated by subtracting the current density values obtained in the N_2 (blank) medium from the O_2 medium.

1.5.8. Electron transfer number (n)

The electron transfer number is calculated using the following equation;

$$\frac{1}{J} = \frac{1}{J_K} + \frac{1}{B\omega^{0.5}} \qquad \text{----------Eq.1}$$

16

Where **B**;

$$J_L = B\omega^{0.5} = 0.62nF(D_{O_2})^{\frac{2}{3}}v^{-\frac{1}{6}}C_{O_2}\omega^{0.5}$$ --------Eq.2

Where **n** is the number of electrons transferred during the reaction, **F** is the Faraday constant (96485 C/mol). C_{O_2} is the bulk concentration of O_2, D_{O_2} is the oxygen diffusion coefficient in the electrolyte, v is the kinetic viscosity of the electrolyte, and **ω** is the angular rotation rate. From the RRDE, **n** can be calculated using the equation;

$$4 I_d = n(I_d + I_r/N)$$ ------------ Eq. 3

Id and **Ir** are the disk current and ring current collected at the ring-disk electrode, and **N** is the current collection efficiency of the Pt ring. Here the disk current is used for ORR kinetics evaluation, and the ring current is used for H_2O_2 intermediate evaluation. The maximum efficiency is achieved through the 4-electron kinetics, where the conversion to H_2O occurs. The partial 2-electron mechanism may lead to the production of H_2O_2, which may reduce the fuel cell output.[47]

1.5.9. Catalysts for Oxygen reduction reaction

Platinum-based catalysts are widely accepted as potent catalysts for ORR applications due to their ability to support the four e- pathway. However, the higher cost of the Pt based catalyst can put the dream of economically viable fuel cells at bay.[48, 49] The inability of such catalysts to withstand CO_2 or methanol poisoning is also considered a major drawback. This prompts the demand for an alternate catalyst that can effectively compensate for the drawbacks of Pt-based catalysts.

Over the past few years, carbon-based materials have been widely studied as an alternative catalyst for Pt-based materials for electrocatalytic ORR in fuel cells. Enormous studies have emerged in designing carbon-based catalysts with desirable qualities to achieve maximum theoretical potential. Massive investigations are performed on different carbon materials, including metal-free heteroatom-doped carbon catalysts and metal/carbon hybrid catalysts (**Figure 1.14**). Studies have shown that incorporating transition metals and heteroatoms can effectively tune the spin states around the carbon, ultimately leading to defects-rich sites with activated regions on the carbon surface, which can stimulate higher electron conductivity and better kinetics favoring the ORR mechanism. [50, 51]
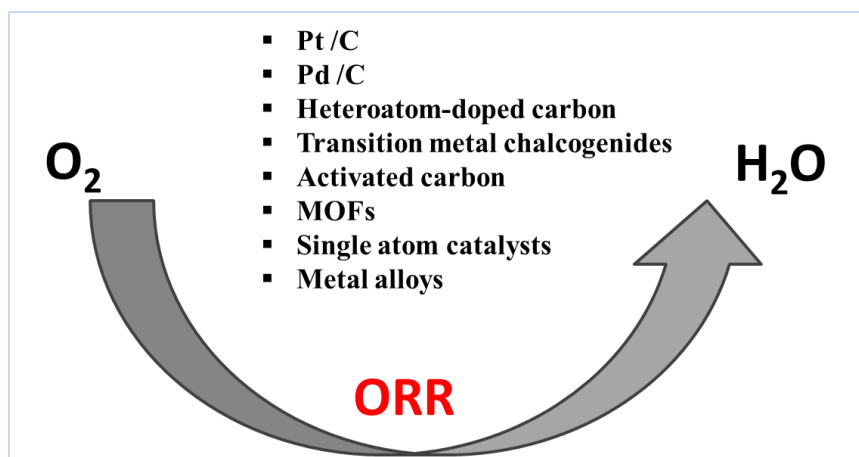
Figure 1.14. Different types of ORR electrocatalysts

Metal-organic frameworks (MOFs) are an ideal precursor for synthesizing well-tuned porous, heteroatom-doped carbon. The ability of MOFs to be used as a sacrificial template to synthesize heteroatom-doped carbon with highly tuned morphology and porosity makes it an attractive method to prepare the electrocatalyst with higher efficiency. These heteroatom-doped carbon materials have been widely investigated for oxygen reduction reactions and have exhibited excellent performance for fuel cell half-cell reactions. Studies have shown that the ORR activity depends upon the surface area, morphology, and heteroatom content of the catalysts. Over the past few years, many studies have emerged in enhancing the ORR catalytic activity of the MOF-derived carbon catalyst by tuning the porous features, heteroatom content, and morphology which can lead to highly active ORR catalysts comparable to commercial Pt/C catalysts. [52, 53]

1.5.10.   MOF-derived metal-free heteroatom doped carbon catalysts:

In the zinc-based metal-organic frameworks (MOFs), due to the highly volatile nature of zinc (boiling point $\approx$ 907 °C), the metal can be easily removed on high-temperature carbonization, leaving porous structures behind. Since the Zn metal is found to possess the least electrocatalytic activity, the absence of Zn upon carbonization does not affect the catalytic property of the carbon. Zeolitic imidazolate frameworks-8 (ZIF-8), formed by coordinating Zn2+ with imidazole, is widely exploited to prepare metal-free, heteroatom-doped carbon. Hence, many investigations have emerged using ZIF-8 as the template to prepare N-doped carbon. These N-doped carbons possessed higher electrocatalytic activity due to the catalytically active centres created by the synergy between the carbon and the nitrogen atoms.[54, 55]

Hong et al. reported the synthesis of N-doped porous carbon using ZIF-8 as the template. The obtained carbon retained the polyhedral morphology of ZIF-8 along with high nitrogen content, surface area, and hierarchical porosity. The samples NGPC-Tc-t was prepared by varying carbonization temperature Tc(Tc= 700, 800, 900, and 1000 °C) and carbonization time t (1, 5, and 10 h). The optimized sample NGPC-1000-10 was demonstrated to be an excellent catalyst for electrocatalytic ORR in an alkaline medium, as observed by its higher current density of 4.3 mA cm^{-2} at -0.6 V and a positively shifted onset potential of -0,2 V vs. Ag/AgCl. [56] It is reported that when external templates such as furfuryl alcohol, glucose, and melamine are incorporated into the ZIF-8, the carbonization leads to carbon with a large surface area and desired pore size distribution. [57] Apart from ZIF-8, other zinc-containing MOFs such as MOF-5, MOF-75, and bio-MOF-1 were also successfully demonstrated to be a template for synthesizing N-doped carbon for ORR.

It is found that doping carbon with multiple heteroatomic sites can enhance the electrocatalytic ORR activity arising from the change in the charge and spin density arising from the interaction of multiple heteroatomic sites with carbon contributing to better O2 adsorption, electron transfer, and better ORR.[58] Some of the important MOF-derived heteroatom doped carbon materials and their ORR activity are summarized in **Table 5**

1.5.11. **MOF-derived transition metal, heteroatom co-doped carbon catalysts**

Over the past decades, transition metal electrocatalysts have been widely investigated for electrochemical ORR applications in their different forms (oxides, sulfides, selenides, etc.). The electrocatalytic activity of the transition metals was found to be in the order Fe> Co>Mn>Cu>Ni.[59] However, the low surface area and less exposed catalytic sites hinder their ORR activity and stability. Recently, studies have proved that incorporating transition metal into the carbon can boost the electrocatalytic activity due to the combined synergistic effect of the metal and heteroatom with the carbon. Due to the high surface area of the incorporated carbon, more catalytically active sites will be exposed, thus boosting their electrocatalytic activity.[60, 61] Recently, MOFs containing transition metals either in the form of central metal or as incorporated host metal are widely exploited to prepare metal, heteroatom-doped carbon. On carbonization, the metal sites can be incorporated into the carbon matrix as metal carbides, oxides, nitrides, etc., which serve as active sites for the ORR mechanism.[29] ZIFs based systems are widely exploited as a precursor due to their high surface area and room temperature synthesis procedure. The cobalt-containing ZIF-67 frameworks have been widely used as a template for preparing Co-dispersed carbon catalysts. On high-temperature

carbonization, the ligand around the center metal cobalt decomposes into N-doped carbon enriched with dispersed cobalt sites. However, the higher amount of cobalt in the ZIF-67 may lead to the aggregation of cobalt, which may hinder the efficiency of the electrocatalytic activity.[62] Hence, different strategies are adopted to prevent the agglomeration of the metal particle and to get the finely dispersed metal particle on the carbon surface, including the change in the composition of the parent MOF and other template-incorporated approaches. Cobalt-doped ZIF-8 frameworks are usually adopted with tuned cobalt content that may lead to N-doped porous carbon with uniformly dispersed cobalt particles.[63]

One-dimensional (1D) carbon materials, such as carbon nanotubes (CNTs) and carbon fibers (CFs), are characterized by large surface areas, higher electrical conductivity, and stability, due to which they are highly desired for ORR catalysis. Transition metals such as Fe, Co, and Ni can catalyze the growth of carbon nanotubes.[64-66] Hence, incorporating these less volatile transition metals into the ZIFs can result in a tubular, transition metal, heteroatom co-doped carbon. Fe-N-C hybrid structure containing carbon nanotubes was synthesized from the Zn/Fe bimetallic structure. Here, the Fe could also act as a source for the growth of nanotubes. The catalyst FeNC-20-1000 with the molar ratio of Zn/Fe= 20 and carbonization temperature of 1000 °C exhibited higher ORR activity both in acidic and alkaline media.[67] A comparison of the electrocatalytic activity of some of the important MOF-derived transition metals, heteroatom-doped carbon, is listed in **Table 6**.

Table 5. ORR performance of MOF-derived metal-free carbon catalysts in 0.1 M KOH solution

Sample name	MOF source	External template	Electrocatalytic ORR activity			Ref
			Onset potential	Current density (mA cm^{-2})	Electron transfer number	
Carbon-L Carbon-S	ZIF-7	Glucose	0.86 V 0.84 V *vs. RHE*	-4.9 -4.43	3.6 3.6	[68]
GNPCSs-800 NPC	ZIF-8 ZIF-8	GO ------	0.957 V 0.914 V *vs. RHE*	-6 -3.12	3.98 3.7	[69]

Nitrogen-doped porous carbon (NPC)	Zn-MOF-74	----------	1.02 V *vs. RHE*	−5.85	3.89	[70]
PC-Al-1000	amino-MIL-53(Al)	----------------	- 0.13 V *vs Ag/AgCl*	- 0.1	≈ 4	[71]
NPS-C-MOF-5	MOF-5	dicyandiamide (DCDA) triarylphosphine (TPP) dimethyl sulfoxide (DMSO)	- 0.006 V *vs. Ag/AgCl*	-11.6	3.6	[72]
NPSpC	ZIF-8	sodium phytate solution dodecyl mercaptan	0.923 V *vs. RHE*	-4.89	3.9	[73]
NPC-1000-4	bio-MOF-1, $(Zn_8(Ad)_4(Bpdc)_6O \cdot 2 Me_2NH_2$)	--------------------	-0.012 V) *vs. Ag/AgCl*	-5.76	~4.00	[74]
CS-HPCN1000-5	Core-shell ZIF-8@ZIF-8	--------------------	-0.08 V *vs. RHE*	-3.75	~4.00	[75]

Table 6. ORR performance of different MOF-derived metal, heteroatom-doped carbon catalysts in 0.1 M KOH

Sample name	MOF source	External template	Electrocatalytic ORR activity			ref
			Onset potential	Current density (mA cm^{-2})	Electron transfer number	
HZPC	ZIF-67	Phenolic resin	0.98 V *vs. RHE*	~5	3.97	[76]
Cu/N-C	Cu ions adsorbed ZIF-8	-----------------	1.029 V *vs. RHE*	6.0	3.8	[77]
Co 9 S 8 @CNS *T*	MIL-101-NH$_2$,	[Co(TU)$_4$]Cl$_2$ compound	-0.05 V *vs.* Ag/AgCl	-5.6	3.9	[78]
NC@Co-NGC	ZIF-8@ZIF-67	---------------	0.92 V *vs. RHE*	-5.3	~4.00	[79]
Mn3O4/NCP	ZIF-8	--------------	0.92 V *vs. RHE*	-5.24	~4.00	[80]
Fe3C@NC-60-800	Zn-Fe-ZIF	---------------	0.987 V *vs. RHE*	-4.4	3.63	[81]
Fe–N–C	Zn/Fe-ZIF-7	--------------	1.04 V *vs. RHE*	-5.6	~4.00	[67]
Co/NBCNTs	Zn/Co-ZIF	g-C$_3$N$_4$	-0.9 V *vs. RHE*	-5.23	3.75	[82]
(ZCP-CFs	Zn, Co-ZIF	Co^{2+}/PAN fibres	-0.05 V *vs.* Ag/AgCl	-5.95	3.97	[83]
Co@N-CNTF	Co-Ade-MOF	---------------	0.91 V *vs. RHE*	~5.2	3.96	[84]
Fe-N-S CNN	Fe-ZIF-8	--------------	1.0 V vs. RHE	~5.8	~4	[85]
InFeCo@CNS900	InOF-24	---------------	0.865 V	5.15	3.61	[86]

Co–Fe/NC	MIL-101/ZIF-67	polystyrene	~1.0 eV	-6.5	3.8	87
CoFeNi/NC	ZIF-8/ZIF-67	PVP	0.914 V	2.593		88
Cu-Zn-N/C	Cu doped ZIF-8	----------------	0.90 V	5.8	~4.00	89
Co-Cu@CN	Cu-MOF@Co-MOF	----------------	0.936 V	6	~4.00	90

1.6. Treatment of organic pollutants in water

The global concern about the crisis caused by water pollution can be resolved only through viable methods of pollutant disposal. Polluted water contains different types of contaminants, including pharmaceuticals, pesticides, surfactants, etc. Many of these pollutants are organic compounds that adversely affect human health and the environment, even if their presence is in trace quantities (microgram per litre). The pollutants coming primarily from sources like domestic wastewater, hospital effluents, agricultural sectors, etc., contains non-biodegradable components, and some are partially degraded during the wastewater treatment process.[91-94]
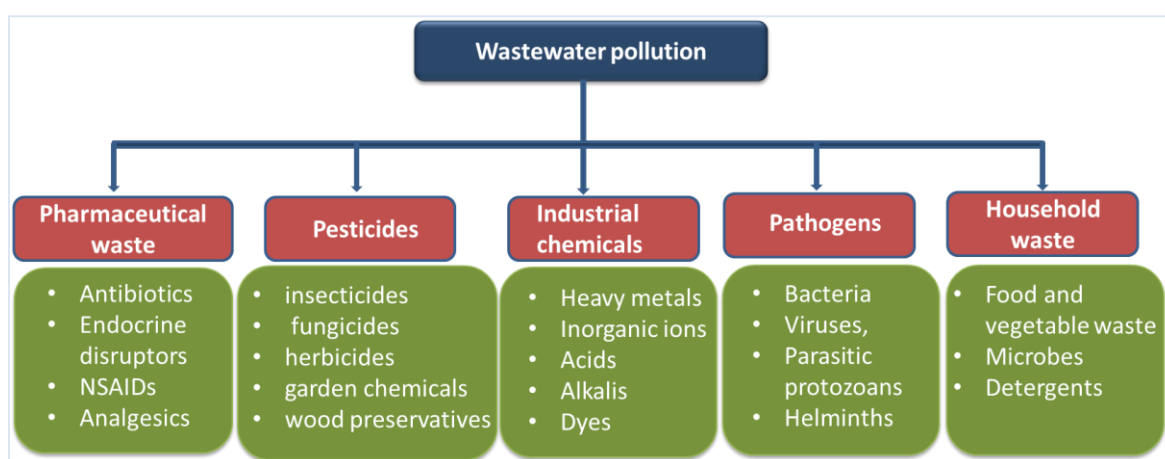
Figure 1.15. Different contaminants cause water pollution.

1.7. Wastewater treatment methods

Over the past few decades, various technologies have been invented to treat wastewater. Conventional wastewater treatment technology includes primary, secondary, and tertiary treatment processes. The various procedures adopted in each treatment process are represented in **Figure 1.16**. However, most of these wastewater treatment methods based on physical and biological conversion methods are unsuitable for removing toxic organic pollutants.[95, 96] It is, therefore, imperative to develop practically viable methods for advanced wastewater treatments that can convert toxic organic pollutants into less harmful byproducts.
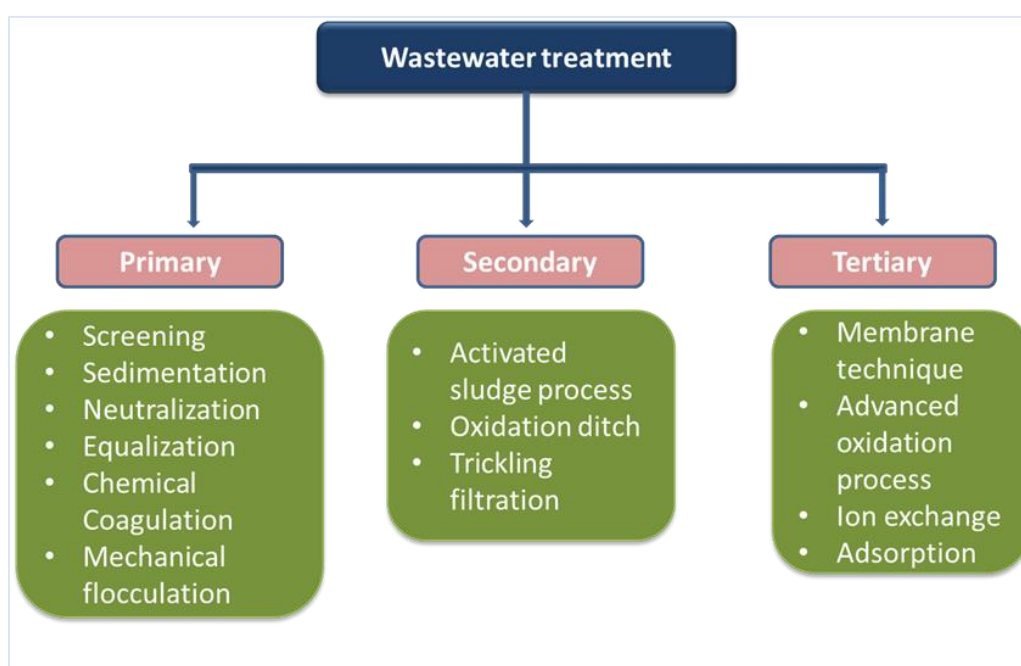
Figure 1.16. Different wastewater treatment methods

Among the existing wastewater treatment methods, advanced oxidation processes (AOP) are considered an advanced treatment method to remove organic pollutants present in water. AOPs, including photocatalytic degradation, ozonation, sonolysis, electrochemical oxidation, etc., are mainly rooted in the degradation of targeted organic contaminants by generating reactive species like sulfate radical, hydroxyl radical, superoxide radical, etc. Since AOPs are proven to be non-selective, they can destroy almost all organic pollutants to harmless, simple byproducts. Depending upon the reactive species formed, AOPs can be categorized as ozone-based, UV-based, electrochemical, physical, and catalytic AOPs [97, 98] (**Figure 1.17**).

1.7.1. Ozone-based AOPs:

Ozone is an oxidant that mainly attacks the organic functional groups such as double bonds and aromatic rings. Since the reaction of ozone with water produces reactive OH$^\bullet$, it can be used to treat the organic contaminants in water. However, the initiation reaction with water is relatively slow and is in the range of a second-order rate constant of 70 M^{-1}S^{-1}. Ozonation at higher pH and employing O$_3$/H$_2$O$_2$, O$_3$/UV, and O$_3$/catalysts are methods adopted to initiate the free radical formation reaction effectively.

1.7.2. UV based AOPs

It mainly focuses on using UV light with different reactive radical generating species. The most commonly used are the combination with H$_2$O$_2$, O$_3$, and persulfate sources. When used with H$_2$O$_2$ leads to the photolytic cleavage of H$_2$O$_2$ to OH$^\bullet$.In UV/O$_3$, UV irradiation results in the cleavage of O$_3$, followed by the reaction with water resulting in thermally excited H$_2$O$_2$ that further decomposes to OH$^\bullet$. UV irradiation with persulfate-generating species such as peroxodisulfate and peroxy mono sulfate generates sulfate radicals (SO$_4^{\bullet-}$). These free radicals then destroy organic contaminants present in wastewater.

1.7.3. Electrochemical AOPs

The electrochemical advanced oxidation process utilizes electrochemical methods to generate reactive free radicals. In this method, the reaction at the electrodes produces OH$^\bullet$ via O$_2$ evolution from water. The main electrodes used are metal oxides such as SnO$_2$, PbO$_2$, RuO$_2$, and Boron-doped diamond (BDD).

1.7.4. Catalytic advanced oxidation processes

Catalytic AOPs involve using homogeneous or heterogeneous catalysts to generate reactive free radicals in the medium. The catalyst produces reactive species via different methods. Based on the types of catalysts, the catalytic AOPs can be categorized into 1) Homogeneous catalytic oxidation and 2) Heterogeneous catalytic oxidation

i)   Homogeneous catalytic oxidation

Homogeneous catalytic oxidation involves the use of catalysts that are in the same phase as the reactants. Transition metals, including Fe^{2+}, Zn^{2+}, Mn^{2+}, Pb^{2+}, Co^{2+}, Ni^{2+}, Ti^{2+}, Cr^{3+}, Cd^{2+}, etc., are widely employed for homogeneous catalytic oxidation. Homogeneous

catalytic oxidation can be further divided into Fenton and Photo-Fenton-based processes. The Fenton process involves using Fe^{2+} catalysts to generate $OH^\bullet$. However, one of the limitations of this method is the formation of Fe^{3+} sludge which may slow down the reaction rate, and the reaction will not proceed once all the Fe^{2+} is consumed. The Photo-Fenton process involves the generation of $OH^\bullet$ from H_2O_2 using Fe^{2+} catalysts via photocatalytic reaction. Here, the formed Fe^{3+} may be further reduced to Fe^{2+} via photochemical regeneration, and the reaction can proceed further.[99]

ii)   Heterogeneous catalytic oxidation

  In heterogeneous catalytic oxidation, reactive species are usually generated from heterogeneous catalysts, mainly solid catalysts. Here the degradation efficiency will depend upon the choice of catalysts. The advantages of heterogeneous catalytic oxidation include easy preparation of catalysts, high stability, no sludge formation, etc. The catalysts such as TiO2, Fe2O3, activated carbon, etc., are widely studied for AOPs. The incorporation of transition metals on different matrixes, including polymers, zeolites, and activated carbon, is also found to exhibit good degradation performance. The degradation activity of the heterogeneous catalysts depends upon various factors like the pH, temperature, type of pollutants, and the presence of inorganic ions in water. The catalysts with high surface area and high dispersion of active sites are found to impart better degradation activity.
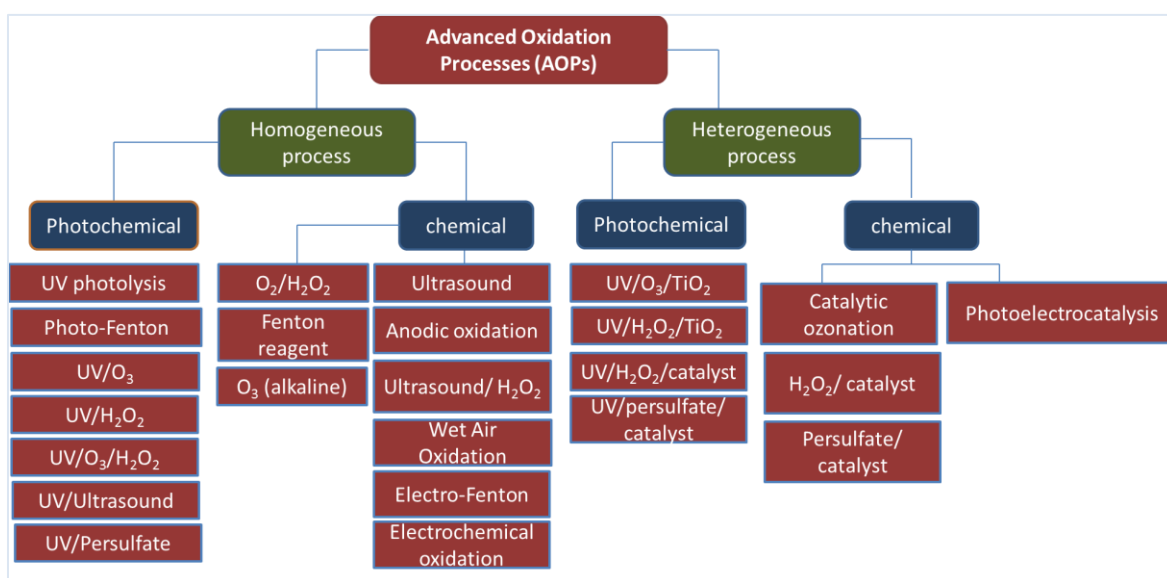
Figure 1.17. Various Advanced oxidation processes[100]

1.7.5. Sulfate species activated AOPs (SR-AOPs)

Recently, sulfate radical ($SO_4{}^{\bullet-}$) based AOPs using Persulfate (PS) and Peroxy Mono Sulphate (PMS) attracted much attention due to their cost-effective and environment-friendly operations. The features of $SO_4{}^{\bullet-}$ radical, such as its comparatively high redox potential (2.5-3.1 V), strong oxidizing ability, wide pH adaptive range (2-8), and long life span (30-40 µS), etc., make it a superior alternative to other methods. It can attack aromatic or organic unsaturated compounds and effectively be used for organic pollutant degradation. $SO_4{}^{\bullet-}$ radical can be generated in many ways, including heating, UV irradiation, ultrasonication, catalytic activation, etc.[101-103] Catalytic activation is considered as the most convenient method due to its simple and energy-efficient approach. There are numerous approaches for activating PS and PMS using different nanomaterial catalysts such as transition metals, metal oxides, metal-supported composites, activated carbon materials, etc. The sulfate radical in the medium can be covert to other intermediate reactive species like $^{\bullet}OH$ and $SO_3{}^{\bullet-}$ that can also effectively take part in the degradation process (**Figure 1.18**).
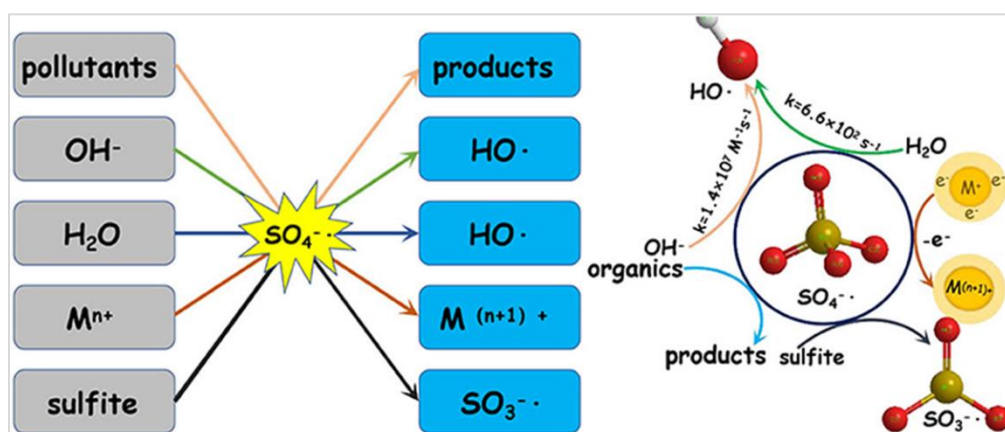
Figure 1.18. Mechanism and intermediate reactive species involved in the sulfate radical-mediated advanced oxidation processes.[104]

1.7.6. MOF derived metal-free heteroatom doped carbon for SR-AOPs

Recently, metal-organic frameworks derived heteroatom-doped carbon have found attention in the catalytic activation of sulfate radicals for advanced oxidation processes. A few studies have reported the use of conventional metal-organic frameworks as the precursor for heteroatom-doped carbon. Such carbon catalysts showed remarkable activity in

generating active sulfate radicals and degradation of various organic pollutants.[105] The kinetics and mechanism of the degradation activity will depend upon the types of active centers created and the surface and structural features.

Nitrogen-doped carbon found attention in activating persulfate towards organic contaminant degradation. Nitrogen can form stable bonds with carbon, and their synergy can lead to better stability and better degradation mechanism. The high-temperature carbonization of ZIF-8 can lead to N-doped porous carbon of high surface area and contain catalytically active centers for generating reactive species and degradation of pollutants. Miao et al. utilized Nitrogen-doped porous carbon (NPC) from ZIF-8 carbonized at 700 °C-900 °C. The catalyst NPC-800 was obtained with a higher nitrogen content of 15.20 %.The derived carbon was tested towards the PMS-activated degradation of Rhodamine B and Phenol and achieved a degradation efficiency of 85 % and 86.1 %, respectively. The radical quenching tests revealed the presence of $OH^\bullet$ and $SO4^{\bullet-}$. Here the presence of more graphitic nitrogen contributed to modulating the electronic structure of the carbon, hence acting as active catalytic centers for producing reactive free radicals.[106] T Mao et al. demonstrated the application of ZIF-8-derived carbon for the degradation of P-chloroaniline, 4-chlorophenol, and phenol degradation in a wide pH range of 3-10. The N-doped carbon exhibited a higher degradation rate by the mechanism involving radical and non-radical pathways.[107] When the formed N-doped carbon was modified with g-C_3N_4, the resultant composite exhibited broadened optical window for light harvesting, efficient interfacial charge separation, and created abundant active sites for PMS activation leading to excellent BPA degradation rate by the generated $SO4^{\bullet-}$.[108]

1.7.7. MOF derived Transition metal/ heteroatom incorporated carbon for SR-AOPs

Transition metals, such as Fe, Co, Ni, Mn, etc., are proven effective in the photochemical and photocatalytic activation of persulfate. Unlike zinc, the transition metals, by virtue of their high boiling points, even after carbonization at higher temperatures, will be preserved on the carbon leading to transition metal doped carbon. Therefore, transition metal-doped carbon is widely prepared from metal-organic frameworks such as ZIFs, MILs, HKUST, etc. Varieties of transition metal-incorporated carbon catalysts are prepared, and their activity towards the persulfate activation was tested for the degradation of various organic pollutants present in water (**Table 7**). Incorporating transition metals into the ZIF-8 framework is also considered one of the successfully adopted methods for preparing transition metal-doped carbon. Carbon with atomically dispersed FeNx sites was prepared from Fe-incorporated

ZIF-8. The catalyst showed higher activity towards organic pollutant degradation via the $^1O_2$ dominant mechanism by peroxymonosulfate activation. [109]

Different MIL frameworks are widely reported to be suitable catalysts for persulfate activation. MIL frameworks with Fe centres have recently been used as sacrificial templates to prepare Fe-doped carbon. Since Fe is reported to be a suitable catalyst for persulfate activation, MIL frameworks, including MIL-53, MIL-88 A, MIL-100, etc., are utilized to prepare Fe-containing carbon. Fe-based active centres in their different phases enable persulfate activation against different contaminants.[110-112]

Table 7. Summary of the MOF-derived carbon materials for organic pollutant degradation based on sulfate radical activated, advanced oxidation processes

Catalyst	MOF precursor	Reaction conditions	Pollutants	Time (min)	Degradation efficiency
NPC	ZIF-8	[RhB]=100 mg/L, [PMS/PS/] = 4.56 mmol/L, [NPC-800] = 0.20 g/L, temperature = 20 °C	RhB	60	85 % [104]
N-C-900	ZIF-8	[Catalyst]=100 mg/L [PDS]=5 mM, [phenol]=0.3 mM, [4-CP]= [PCA]=0.3 mM	PCA Phenol 4-CP	120	96.3 % [105] 93.5 % 100 %
Fe-N-C	Fe@ZIF-8	[Phenol]0 =20 mg/L, [PMS]=0.2 g/L, [catalyst]= 0.15 g/L, room T.	Phenol	30	100 % [109]
Co@N-PC	ZIF-67/ poplar sawdust	[MB] = 30 mg/L, [PMS] = 0.5 mM, [Co@N-PC] =10 mg, [T] = 25 ∘C, [initial	MB	30	100 % [113]

		pH] = 6.3			
3DG/Cu@C	HKUST-1/rGO	[3DG/Cu@C] = 25 mg/ L, [pH] = 3, [Applied current] = 30 mA, [RhB] = 40 mg/ L, [Na2SO4] = 0.05 M.	RhB	150	100 % [114]
ZIF-67-C Nanoporous carbons (NPCs)	Bimetallic ZIF-8/ZIF-67	20 ppm, [catalyst] = 0.1 g/L, [PMS] = 1 0.2 g/L, T = 25 °C	Phenol	10	100 % [115]
(PNC)	Zn–Co Prussian blue analogues	MB= 100 mg/L; Catalysts, 0.1 g/ L ; PMS, 1 g/L; T, 25 ^{0}C; pH, 6.3	MB	10	100 % [116]
(NCNTFs)	ZIF-67	[BPA] = 25 mg/L, [Catalyst]= 0.05 g/L, [Oxone] = 0.40 g/L, temperature =20 °C	BPA	30	97 % [117]
NPC (ZIF-8) NPC(IRMOF-3) (NH2MIL53) PC (MOF-5)	ZIF-8 IRMOF-3 NH2MIL-53 PC(MOF-5)	Phenol =20 mg/ L, Catalysts= 0.2 g/ L; PMS= 1.6 mM, T=25 ^{0}C	Phenol	50 60 60 60	100 % [118] 98 % 90 % 73 %
CBs@NCCs	Co-Fe PBAs	MB, 100 mg/L; catalyst, 0.06 g/L; Oxone, 1.00 g/L; T, 288 K	MB	60	100 % [119]
HCNFs	ZIF-8)/polyacrylonitrile (PAN)	[TC] = 50 mg/ L, initial pH = 3.2, [catalyst] = 0.2 g/ L, [PMS] = 0.5 g L−1, T = 25 °C	TC	20	80 % [120]
FeCo@NC	Fe-Co PBA	[BPA] = 20 mg/ L, [PMS] = 0.2 g L−1,	BPA	4	100 % [121]

		catalyst = 0.1 g/ L, T = 298 K			
MICN	MIL-88A	RhB = 10 mg/ L, oxidant = 300 mg/ L, MICN = 300 mg/ L, T = 25 °C	RhB	100	90 % [122]
FexMn6–xCo4–N@C	MnyFe1–y-Co PBA	[BPA] = 20 mg/ L, [PMS] = 0.2 g/ L, catalyst = 0.1 g/ L, T = 298 K	BPA	12	100 % [123]
CuNi@C	Cu-BTC	AO7 = 0.02 mM, PMS =0.675 mM, catalyst = 0.15g/ L	AO7	60	100 % [124]
MnxCo3-xS4	MnCo-ZIF	SMT = 55 mg/ L, PMS =0.3 g/ L, catalyst = 80 mg/L, pH = 6.5	(SMT)	8	97 % [125]

1.8. Nanogenerators

The dependency on natural resources to power energy devices is inadequate due to the lack of a continuous power supply. The miniaturization of the electronic system makes it thus possible to supply energy from the environment by different methods. The emerging area of smaller energy devices that operate with low power consumption, possibly by the energy harvested from the environment, is an advantage to society. It can ultimately reduce the environmental hazardousness caused by ample energy supplies such as batteries. Nanogenerators are self-powered devices mainly rooted in using nanomaterials to generate energy from the environment by different methods to power the micro/nanosystems. The attractive features of nano energy-based technology are easy availability, efficiency, and stability.

1.9. Triboelectric nanogenerators (TENGs)
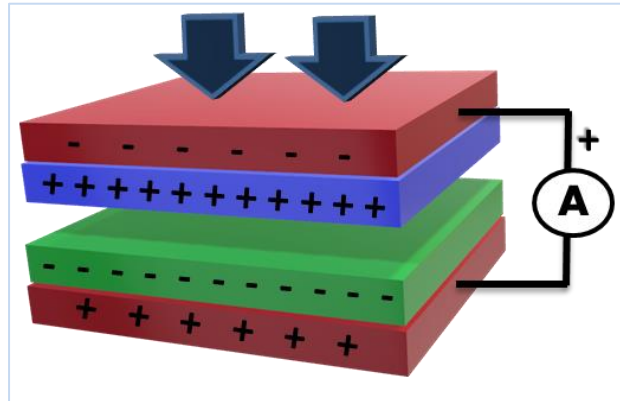
Figure 1.19. General schematic representation of a triboelectric nanogenerator

Triboelectric nanogenerators are devices that convert mechanical energy into electricity by the phenomenon called triboelectric effect or electrostatic induction. Here, the power is generated from the potential created due to charge transfer by the contact of any two materials of opposite tribo polarity. A schematic representation of the triboelectric nanogenerator is shown in **Figure 19**. When two surfaces of different materials come into contact, there will be movement of charges to make the potential equal. These charge transfers occur through electrons or ions, or molecules. When separated, these surfaces will be retained with charges, showing the tendency to move in the opposite direction. Insulators or less conducting materials usually show the triboelectric effect and vary with the effective contact area of the materials. The first triboelectric nanogenerator was demonstrated by Wang et al. in 2012. The triboelectric nanogenerators function by four different modes 1) Vertical contact-separation mode, 2) Lateral sliding mode, 3) Single electrode mode, and 4) Freestanding Triboelectric-layer mode (**Figure 20**). [126-128]

1.9.1. Vertical contact-separation mode

When two surfaces of dissimilar charges face each other, and potential is created as a result of contact, it is called vertical separation mode. Here the relative motion takes place perpendicular to the interfaces. Physical contact between the surfaces by external forces creates oppositely charged surfaces.

1.9.2. Linear sliding mode

In linear sliding mode, the potential is created due to the relative sliding of two materials parallel to the surfaces. Here, lateral polarization is observed, and the repeated sliding and closing generate power. The sliding can occur in planar motion, cylindrical, and disc rotation.

1.9.3. Single electrode mode

Here, the electrode on the bottom part will be grounded. Only the top layer will be connected to the electrode, while the bottom layer will serve as an electric potential reference. Some examples are humans walking on the ground and hand typing. The contact and separation of the top object from the bottom will create a local electronic charge distribution on the bottom surface generating a charge transfer. This can be employed by both contact separation mode and lateral sliding mode.

1.9.4. Freestanding triboelectric layer mode

In freestanding electrode mode, a pair of symmetric electrodes will be surrounded by free-moving objects instead of the reference electrode. An asymmetrical charge distribution is created when the free-moving objects come into contact and separate from an electrode. In order to balance the charge, electron flows between the two electrodes, and as a result, electrical energy is generated. In rotation mode, free rotation is possible without direct contact. Hence it can improve the durability of the TENG device.
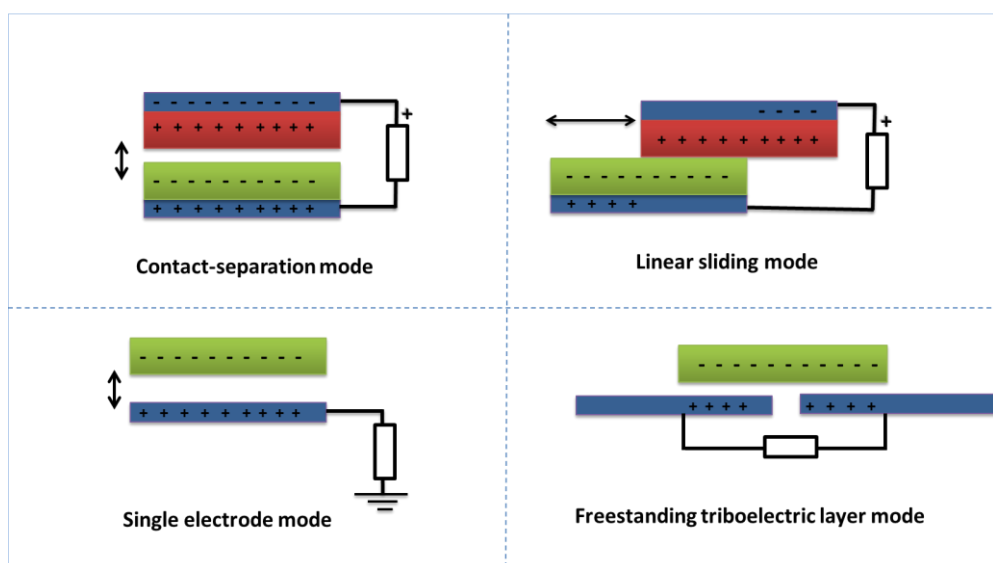
Figure 1.20. Different modes of operation of TENG

1.9.5. Metal-Organic frameworks based Tribo electric nanogenerators

Porous materials with a high surface area are reported to impart better tribo effect due to the better contact area and the ability of the pores to hold the charges for a long time. Metal-Organic Frameworks (MOFs), due to their heteroatom-rich surfaces and variable morphologies, are reported to exhibit appreciable triboelectric effects and are utilized in different powering devices. Since varieties of MOFs can be synthesized by varying the metal and ligand, various combinations of triboelectric series are possible with desirable output. Since MOFs are in powder form, different methods are studied to fabricate MOF based triboelectric later. The MOF-based triboelectric nanogenerator was fabricated for the first time by Kim et al., where ZIF-8 grown on indium-doped tin oxide (ITO)-polyethylene terephthalate (PET) and Kapton was used as the positive and negative triboelectric layers respectively. The MOF–TENG was used to power a temperature/humidity sensor using a capacitor and for wireless charging of a lithium (Li)-ion battery. The optimized triboelectric layer could achieve a power output of 164 V and 7 μA.[129] ZIF frameworks fabricated as tribo materials show high output owing to high surface area and porosity. TENG fabricated with ZIF -67 coated as a thin film on an Aluminium substrate, and PMMA could achieve a very high output voltage of 300 V, 47.5 μA, and a power density of 593 mW/m^2.[130] Metal-organic frameworks, besides ZIFs are also used as positive and negative elements for triboelectric applications. Weng et al. fabricated a high-output TENG under humidity by incorporating HKUST-1 into PDMS.[131] Fluorine-modified metal-organic frameworks KAUST-8 incorporated into PDMS was used as a pair with Al foil, which resulted in higher voltage power outputs.[132]

Recently, MOF-derived transition metal doped carbon was also tested for triboelectric applications. The ZIF-67-derived Co-NC carbon was incorporated into PVDF by electrospinning to obtain Co-NC/PVDF composite. The incorporation of Co-NC could improve the crystalline β-phase of PVDF, which improved the electronegativity of PVDF. Combining the Co-NC/PVDF composite as a negative triboelectric layer with electrospun Nylon-11 could achieve a higher output performance. The combination was fabricated as a biomechanical energy harvester and a self-powered pressure sensor for monitoring various human motions in a smart home control system. The summary of studies on various MOFs is shown in **Table 8**. There is still scope for exploring different MOFs for various self-powered systems.

Table 8. Summary of the use of MOF derivatives in triboelectric devices

Positive triboelectric layer	Negative triboelectric layer	Output performance			Applications	reference
		Voltage	Current	Power density ($mW\ m^{-2}$)		
ZIF-7 ZIF-9 ZIF-11 ZIF-12	Kapton	60 V 29 V 27 V 42 V	1.9 µA 0.36 µA 0.26 µA 0.62 µA	7.74 1.5 1.8 3.92	Capacitor	[133]
ZIF-8	Kapton	164 V	7 µA	392	UV counterfeit system Tetracycline sensor	[129]
ZIF-62	Teflon	62 V	1.4 µA	9.68	Fitness tracking Capacitor	[134]
ZIF-67	PMMA	300 V	47.5 µA	593	Self-powered electronics	[130]
MIL-88A	FEP	80 V	2.2 µA	16.2	Capacitor	[135]
Co/Zn BMOF / FCF	PTFE/Al	47 V	7 µA	1.1	Gas sensor	[136]
Al foil	KAUST-8/PDMS	530 V	3.2 µA	52 $\mu W\ cm^{-2}$	powering LCD and charging the capacitors	[132]
Nylon-11	Co-NC/PVDF	710 V	131 µA	19.24	self-powered pressure sensor	[137]

1.10. Definition of the present problem

The efficiency of the renewable energy devices such as fuel cells, triboelectric nanogenerators, are primarily rooted in developing highly effective materials with high stability, good textural features and abundance of active sites. Materials for advanced water treatment processes also necessitate desirable attributes such as high surface area, tuned morphology and high recyclability. Currently, most of these applications employ precious and non-precious metals and are often associated with the following difficulties

- Less surface area, which makes the accessibility to the active centres much more difficult
- High aggregation tendency, which reduces the efficiency of the materials
- Less stability and metal leaching from the surface causing secondary pollution.

Heteroatom-doped porous carbon materials with metal-free and transition metal-doped surfaces are demonstrated as effective materials for such applications. Incorporating heteroatoms like nitrogen, transition metals, etc., into the carbon matrix is one of the efficient approaches to break the chemical inertness of the carbon and improve its electrical conductivity. There are various methods adopted for the preparation of heteroatom-doped carbon. Among these, the in situ methods employing the carbonization of various precursors such as organic compounds, biomasses, and polymer materials are widely studied for the preparation of heteroatom-doped carbon. However, the following challenges are identified;

- Less control of the heteroatom content on the derived carbon. The high-temperature carbonization can often lead to the loss of heteroatom leading to non-uniformity in doped surfaces.
- Low activity on the microporous channels obtained
- Most of the precursors often require chemical activation methods for generating porosity.

Metal-organic frameworks (MOFs), formed by the coordination of transition metals and organic ligands containing heteroatoms, are demonstrated to be effective precursor templates for obtaining metal free as well as transition metal-containing heteroatom-doped carbon. The single-stage carbonization of MOFs can transform to uniform heteroatom-doped carbon as the MOF's crystalline networks are loaded with a regular arrangement of

heteroatoms. Moreover, the MOF-derived carbon has tunable pore characteristics, morphology, and heteroatom content that depend on the medium of synthesis, carbonization temperature, presence of metals in the frameworks, etc. This thesis explores the application of MOFs and MOFs derivatives for energy conversion devices and wastewater treatment. The main work elements of the present thesis are;

➢ Synthesis of high surface area metal-organic frameworks like ZIF-8, ZIF-67, MIL-100, HKUST-1, etc.

➢ Preparation of heteroatom-doped carbon from MOFs and their compositional, morphological, and porosity tuning via employing different approaches such as transition metal incorporation and external template-aided strategies.

➢ To estimate the role of different phases of heteroatoms through different characterization techniques, such as XPS, SEM, TEM, etc., in enhancing the activity of the materials for the mentioned applications.

➢ Application of MOFs and MOF derivatives to diverse areas such as fuel cell electrocatalysis, advanced oxidation processes based wastewater treatment, and triboelectric nanogenerators

1.11. References

1. Q. Chen, X. Tan, Y. Liu, S. Liu, M. Li, Y. Gu, P. Zhang, S. Ye, Z. Yang, Y. Yang, Biomass-derived porous graphitic carbon materials for energy and environmental applications, Journal of Materials Chemistry A 8(12) (2020) 5773-5811. https://doi.org/10.1039/C9TA11618D.

2. L.R. Radovic, Physicochemical Properties of Carbon Materials: A Brief Overview, Carbon Materials for Catalysis2008, pp. 1-44. doi.org/10.1002/9780470403709.ch1.

3. S.K. Tiwari, V. Kumar, A. Huczko, R. Oraon, A.D. Adhikari, G.C. Nayak, Magical Allotropes of Carbon: Prospects and Applications, Critical Reviews in Solid State and Materials Sciences 41(4) (2016) 257-317. https://doi.org/10.1080/10408436.2015.1127206.

4. V. Negri, J. Pacheco-Torres, D. Calle, P. López-Larrubia, Carbon Nanotubes in Biomedicine, Topics in Current Chemistry 378(1) (2020) 15. https://doi.org/10.1007/s41061-019-0278-8.

5. Y. Wang, J. Chen, H. Ihara, M. Guan, H. Qiu, Preparation of porous carbon nanomaterials and their application in sample preparation: A review, TrAC Trends in Analytical Chemistry 143 (2021) 116421. https://doi.org/https://doi.org/10.1016/j.trac.2021.116421.

6. R. Chakraborty, V. K, M. Pradhan, A.K. Nayak, Recent advancement of biomass-derived porous carbon based materials for energy and environmental remediation applications, Journal of Materials Chemistry A 10(13) (2022) 6965-7005. https://doi.org/10.1039/D1TA10269A.

7. S. Dutta, A. Bhaumik, K.C.W. Wu, Hierarchically porous carbon derived from polymers and biomass: effect of interconnected pores on energy applications, Energy & Environmental Science 7(11) (2014) 3574-3592. https://doi.org/10.1039/C4EE01075B.

8. M. Nouri, Potentials and challenges of date pits as alternative environmental clean-up ingredients, Biomass Conversion and Biorefinery 13(2) (2023) 1429-1456. https://doi.org/10.1007/s13399-020-01215-w.

9. J. Alom, M.S. Hasan, M. Asaduzaman, M.T. Alam, D. Belhaj, R. Selvaraj, M.A. Hossain, M. Zargar, M.B. Ahmed, Catalytical Performance of Heteroatom Doped and Undoped Carbon-Based Materials, 13(5) (2023) 823.

10. W. Tian, H. Zhang, X. Duan, H. Sun, G. Shao, S. Wang, Porous Carbons: Structure-Oriented Design and Versatile Applications, 30(17) (2020) 1909265. https://doi.org/https://doi.org/10.1002/adfm.201909265.

11. W. Chen, M. Wan, Q. Liu, X. Xiong, F. Yu, Y. Huang, Heteroatom-Doped Carbon Materials: Synthesis, Mechanism, and Application for Sodium-Ion Batteries, 3(4) (2019) 1800323. https://doi.org/https://doi.org/10.1002/smtd.201800323.

12. I.-Y. Jeon, H.-J. Noh, J.-B. Baek, Nitrogen-Doped Carbon Nanomaterials: Synthesis, Characteristics and Applications, 15(15) (2020) 2282-2293. https://doi.org/https://doi.org/10.1002/asia.201901318.

13. M. Inagaki, M. Toyoda, Y. Soneda, T. Morishita, Nitrogen-doped carbon materials, Carbon 132 (2018) 104-140. https://doi.org/https://doi.org/10.1016/j.carbon.2018.02.024.

14. H.J. Kim, H.Y. Kim, J. Joo, S.H. Joo, J.S. Lim, J. Lee, H. Huang, M.H. Shao, J. Hu, J.Y. Kim, B.J. Min, S.W. Lee, M.S. Kang, K. Lee, S. Choi, Y. Park, Y. Wang, J.J. Li, Z.C. Zhang, J.M. Ma, S.I. Choi, Recent advances in non-precious group metal-based catalysts for water electrolysis and beyond, JOURNAL OF MATERIALS CHEMISTRY A 10(1) (2021) 50-88. https://doi.org/10.1039/d1ta06548c.

15. R.J. Yang, Y.Y. Fan, Y.F. Zhang, L. Mei, R.S. Zhu, J.Q. Qin, J.G. Hu, Z.X. Chen, Y.H. Ng, D. Voiry, S. Li, Q.Y. Lu, Q. Wang, J.C. Yu, Z.Y. Zeng, 2D Transition Metal Dichalcogenides for Photocatalysis, Angewandte Chemie-International Edition (2023). https://doi.org/10.1002/anie.202218016.

16. G. Wu, A. Santandreu, W. Kellogg, S. Gupta, O. Ogoke, H.G. Zhang, H.L. Wang, L.M. Dai, Carbon nanocomposite catalysts for oxygen reduction and evolution reactions: From nitrogen doping to transition-metal addition, Nano Energy 29 (2016) 83-110. https://doi.org/10.1016/j.nanoen.2015.12.032.

17. A. Buthiyappan, A.R.A. Aziz, W. Daud, Recent advances and prospects of catalytic advanced oxidation process in treating textile effluents, Reviews in Chemical Engineering 32(1) (2016) 1-47. https://doi.org/10.1515/revce-2015-0034.

18. W. Li, C. Wang, X. Lu, Integrated transition metal and compounds with carbon nanomaterials for electrochemical water splitting, Journal of Materials Chemistry A 9(7) (2021) 3786-3827. https://doi.org/10.1039/D0TA09495A.

19. Y. Ji, J. Du, A. Chen, Review on Heteroatom Doping Carbonaceous Materials Toward Electrocatalytic Carbon Dioxide Reduction, Transactions of Tianjin University 28(4) (2022) 292-306. https://doi.org/10.1007/s12209-022-00332-z.

20. Y. Gao, Q. Wang, G. Ji, A. Li, J. Niu, Doping strategy, properties and application of heteroatom-doped ordered mesoporous carbon, RSC Advances 11(10) (2021) 5361-5383. https://doi.org/10.1039/D0RA08993A.

21. V.F. Yusuf, N.I. Malek, S.K. Kailasa, Review on Metal–Organic Framework Classification, Synthetic Approaches, and Influencing Factors: Applications in Energy, Drug Delivery, and Wastewater Treatment, ACS Omega 7(49) (2022) 44507-44531. https://doi.org/10.1021/acsomega.2c05310.

22. R.E. Sikma, S.M. Cohen, Metal-Organic Frameworks with Zero and Low-Valent Metal Nodes Connected by Tetratopic Phosphine Ligands, Angewandte Chemie (International ed. in English) 61(11) (2022) e202115454. https://doi.org/10.1002/anie.202115454.

23. J.-P. Zhang, X.-M. Chen, Metal–Organic Frameworks: From Design to Materials, in: B. Chen, G. Qian (Eds.), Metal-Organic Frameworks for Photonics Applications, Springer Berlin Heidelberg, Berlin, Heidelberg, 2014, pp. 1-26. https://doi.org/10.1007/430_2013_100.

24. H. Li, M. Eddaoudi, M. O'Keeffe, O.M. Yaghi, Design and synthesis of an exceptionally stable and highly porous metal-organic framework, Nature 402(6759) (1999) 276-279. https://doi.org/10.1038/46248.

25. S.L. Qiu, G.S. Zhu, Molecular engineering for synthesizing novel structures of metal-organic frameworks with multifunctional properties, Coordination Chemistry Reviews 253(23-24) (2009) 2891-2911. https://doi.org/10.1016/j.ccr.2009.07.020.

26. A.U. Czaja, N. Trukhan, U. Muller, Industrial applications of metal-organic frameworks, Chemical Society Reviews 38(5) (2009) 1284-1293. https://doi.org/10.1039/b804680h.

27. J. Panda, T. Sahoo, J. Swain, P.K. Panda, B.C. Tripathy, R. Samantaray, R. Sahu, The Journey from Porous Materials to Metal-organic Frameworks and their Catalytic Applications: A Review, Current Organic Synthesis 20(2) (2023) 220-237. doi.org/10.2174/1570179419666220223093955.

28. S. Eram, Z. Fahmina, Introductory Chapter: Metal Organic Frameworks (MOFs), in: Z. Fahmina, S. Eram (Eds.), Metal-Organic Frameworks, IntechOpen, Rijeka, 2016, p. Ch. 1. https://doi.org/10.5772/64797.

29. A. Phan, C.J. Doonan, F.J. Uribe-Romo, C.B. Knobler, M. O'Keeffe, O.M. Yaghi, Synthesis, Structure, and Carbon Dioxide Capture Properties of Zeolitic Imidazolate Frameworks, Accounts of Chemical Research 43(1) (2010) 58-67. https://doi.org/10.1021/ar900116g.

30. K. Shen, X. Chen, J. Chen, Y. Li, Development of MOF-Derived Carbon-Based Nanomaterials for Efficient Catalysis, ACS Catalysis 6(9) (2016) 5887-5903. https://doi.org/10.1021/acscatal.6b01222.

31. L. Yang, X. Zeng, W. Wang, D. Cao, Recent Progress in MOF-Derived, Heteroatom-Doped Porous Carbons as Highly Efficient Electrocatalysts for Oxygen Reduction Reaction in Fuel Cells, Advanced Functional Materials 28(7) (2018) 1704537. https://doi.org/https://doi.org/10.1002/adfm.201704537.

32. Y. Xue, Y. Guo, Q. Zhang, Z. Xie, J. Wei, Z. Zhou, MOF-Derived Co and Fe Species Loaded on N-Doped Carbon Networks as Efficient Oxygen Electrocatalysts for Zn-Air Batteries, Nano-Micro Letters 14(1) (2022) 162. https://doi.org/10.1007/s40820-022-00890-w.

33. S.S.A. Shah, T. Najam, M.K. Aslam, M. Ashfaq, M.M. Rahman, K. Wang, P. Tsiakaras, S. Song, Y. Wang, Recent advances on oxygen reduction electrocatalysis: Correlating the characteristic properties of metal organic frameworks and the derived nanomaterials, Applied Catalysis B: Environmental 268 (2020) 118570 doi.org/10.1016/j.apcatb.2019.118570.

34. R.K. Shah, Introduction to Fuel Cells, in: S. Basu (Ed.), Recent Trends in Fuel Cell Science and Technology, Springer New York, New York, NY, 2007, pp. 1-9. https://doi.org/10.1007/978-0-387-68815-2_1.

35. M.S. Whittingham, R.F. Savinell, T. Zawodzinski, Introduction: Batteries and Fuel Cells, Chemical Reviews 104(10) (2004) 4243-4244. https://doi.org/10.1021/cr020705e.

36. S.M.J.A.M. Haile, Fuel cell materials and components, 51 (2003) 5981-6000.

37. A.A. Gewirth, M.S. Thorum, Electroreduction of dioxygen for fuel-cell applications: materials and challenges, Inorg Chem 49(8) (2010) 3557-66. https://doi.org/10.1021/ic9022486.

38. M.K. Debe, Electrocatalyst approaches and challenges for automotive fuel cells, Nature 486(7401) (2012) 43-51. https://doi.org/10.1038/nature11115.

39. E. Gülzow, Alkaline Fuel Cells, Fuel Cells 4(4) (2004) 251-255. https://doi.org/https://doi.org/10.1002/fuce.200400042.

40. K. Kordesch, V. Hacker, J. Gsellmann, M. Cifrain, G. Faleschini, P. Enzinger, R. Fankhauser, M. Ortner, M. Muhr, R.R. Aronson, Alkaline fuel cells applications, Journal of Power Sources 86(1) (2000) 162-165. https://doi.org/https://doi.org/10.1016/S0378-7753(99)00429-2.

41. M. Hren, M. Božič, D. Fakin, K.S. Kleinschek, S. Gorgieva, Alkaline membrane fuel cells: anion exchange membranes and fuels, Sustainable Energy & Fuels 5(3) (2021) 604-637. https://doi.org/10.1039/D0SE01373K.

42. N. Ramaswamy, S. Mukerjee, Alkaline Anion-Exchange Membrane Fuel Cells: Challenges in Electrocatalysis and Interfacial Charge Transfer, Chemical Reviews 119(23) (2019) 11945-11979. https://doi.org/10.1021/acs.chemrev.9b00157.

43. C. Song, J. Zhang, Electrocatalytic Oxygen Reduction Reaction, in: J. Zhang (Ed.), PEM Fuel Cell Electrocatalysts and Catalyst Layers: Fundamentals and Applications, Springer London, London, 2008, pp. 89-134. https://doi.org/10.1007/978-1-84800-936-3_2.

44. S. Zaman, L. Huang, A.I. Douka, H. Yang, B. You, B.Y. Xia, Oxygen Reduction Electrocatalysts toward Practical Fuel Cells: Progress and Perspectives, Angewandte Chemie International Edition 60(33) (2021) 17832-17852. doi.org/10.1002/anie.202016977.

45. M.J. Whittingham, R.D. Crapnell, C.E. Banks, Additively Manufactured Rotating Disk Electrodes and Experimental Setup, Analytical Chemistry 94(39) (2022) 13540-13548. https://doi.org/10.1021/acs.analchem.2c02884.

46. W. Xia, A. Mahmood, Z. Liang, R. Zou, S. Guo, Earth-Abundant Nanomaterials for Oxygen Reduction, 55(8) (2016) 2650-2676. https://doi.org/https://doi.org/10.1002/anie.201504830.

47. P. Dange, N. Savla, S. Pandit, R. Bobba, S.-P. Jung, P.-K. Gupta, M. Sahni, R. Prasad, A Comprehensive Review on Oxygen Reduction Reaction in Microbial Fuel Cells, 10(3) (2022) 665--697.

48. C. Sealy, The problem with platinum, Materials Today 11(12) (2008) 65-68. https://doi.org/https://doi.org/10.1016/S1369-7021(08)70254-2.

49. R.J. Spiegel, Platinum and fuel cells, Transportation Research Part D: Transport and Environment 9(5) (2004) 357-371. https://doi.org/https://doi.org/10.1016/j.trd.2004.07.001.

50. F. Jaouen, E. Proietti, M. Lefèvre, R. Chenitz, J.-P. Dodelet, G. Wu, H.T. Chung, C.M. Johnston, P. Zelenay, Recent advances in non-precious metal catalysis for oxygen-reduction reaction in polymer electrolyte fuel cells, Energy & Environmental Science 4(1) (2011) 114-130. https://doi.org/10.1039/C0EE00011F.

51. V. Mazumder, Y. Lee, S. Sun, Recent Development of Active Nanoparticle Catalysts for Fuel Cell Reactions, Advanced Functional Materials 20(8) (2010) 1224-1231. https://doi.org/https://doi.org/10.1002/adfm.200902293.

52. M.H. Yap, K.L. Fow, G.Z. Chen, Synthesis and applications of MOF-derived porous nanostructures, Green Energy & Environment 2(3) (2017) 218-245. https://doi.org/https://doi.org/10.1016/j.gee.2017.05.003.

53. J. Ren, Y. Huang, H. Zhu, B. Zhang, H. Zhu, S. Shen, G. Tan, F. Wu, H. He, S. Lan, X. Xia, Q. Liu, Recent progress on MOF-derived carbon materials for energy storage, 2(2) (2020) 176-202. https://doi.org/https://doi.org/10.1002/cey2.44.

54. T. Palaniselvam, B.P. Biswal, R. Banerjee, S. Kurungot, Zeolitic Imidazolate Framework (ZIF)-Derived, Hollow-Core, Nitrogen-Doped Carbon Nanostructures for Oxygen-Reduction Reactions in PEFCs, Chemistry – A European Journal 19(28) (2013) 9335-9342. https://doi.org/https://doi.org/10.1002/chem.201300145.

55. S. Shen, Y. Sun, H. Sun, Y. Pang, S. Xia, T. Chen, S. Zheng, T. Yuan, Research Progress in ZIF-8 Derived Single Atomic Catalysts for Oxygen Reduction Reaction, 12(5) (2022) 525.

56. L. Zhang, Z. Su, F. Jiang, L. Yang, J. Qian, Y. Zhou, W. Li, M. Hong, Highly graphitized nitrogen-doped porous carbon nanopolyhedra derived from ZIF-8 nanocrystals as efficient electrocatalysts for oxygen reduction reactions, Nanoscale 6(12) (2014) 6590-6602. https://doi.org/10.1039/C4NR00348A.

57. Z. Song, N. Cheng, A. Lushington, X. Sun, Recent Progress on MOF-Derived Nanomaterials as Advanced Electrocatalysts in Fuel Cells, 6(8) (2016) 116.

58. D.-w. Kim, O.L. Li, N. Saito, Enhancement of ORR catalytic activity by multiple heteroatom-doped carbon materials, Physical Chemistry Chemical Physics 17(1) (2015) 407-413. https://doi.org/10.1039/C4CP03868A.

59. U. Martinez, E.F. Holby, S.K. Babu, K. Artyushkova, L. Lin, S. Choudhury, G.M. Purdy, P. Zelenay, Experimental and Theoretical Trends of PGM-Free Electrocatalysts for the Oxygen Reduction Reaction with Different Transition Metals, Journal of The Electrochemical Society 166(7) (2019) F3136. https://doi.org/10.1149/2.0201907jes.

60. X. Huang, T. Shen, T. Zhang, H. Qiu, X. Gu, Z. Ali, Y. Hou, Oxygen Reduction Reaction: Efficient Oxygen Reduction Catalysts of Porous Carbon Nanostructures Decorated with Transition Metal Species (Adv. Energy Mater. 11/2020), Advanced Energy Materials 10(11) (2020) 2070050. https://doi.org/https://doi.org/10.1002/aenm.202070050.

61. T.-F. Hung, S.-H. Chen, M.-H. Tu, Z.-H. Lu, C. Chen, R.-S. Liu, H. Greer, W. Zhou, M.-Y. Lo, D. Tai, Advances in Carbon-Incorporated Non-Noble Transition Metal Catalysts for Oxygen Reduction Reaction in Polymer Electrolyte Fuel Cells, Journal- Chinese Chemical Society Taipei 60 (2013) 0-0. https://doi.org/10.1002/jccs.201300286).

62. Y. Yu, S. You, J. Du, Z. Xing, Y. Dai, H. Chen, C. Zhuang, N.-Q. Ren, ZIF-67-derived CoO (tetrahedral Co2+)@nitrogen-doped porous carbon protected by oxygen vacancies-enriched SnO2 as highly active catalyst for oxygen reduction and Pt co-catalyst for methanol oxidation, Applied Catalysis B: Environmental 259 (2019) 118043. https://doi.org/10.1016/j.apcatb.2019.118043.

63. X. Wan, R. Wu, J. Deng, Y. Nie, S. Chen, W. Ding, X. Huang, Z. Wei, A metal–organic framework derived 3D hierarchical Co/N-doped carbon nanotube/nanoparticle composite as an active electrocatalyst for oxygen reduction in alkaline electrolyte, Journal of Materials Chemistry A 6(8) (2018) 3386-3390. https://doi.org/10.1039/C7TA10022A.

64. W. Zhang, X. Yao, S. Zhou, X. Li, L. Li, Z. Yu, L. Gu, Bifunctional Electrocatalysts: ZIF-8/ZIF-67-Derived Co-Nx-Embedded 1D Porous Carbon Nanofibers with Graphitic Carbon-Encased Co Nanoparticles as an Efficient Bifunctional Electrocatalyst (Small 24/2018), Small 14(24) (2018) 1870109. https://doi.org/https://doi.org/10.1002/smll.201870109.

65. M. Thomas, R. Illathvalappil, S. Kurungot, B.N. Nair, A.P. Mohamed, G.M. Anilkumar, T. Yamaguchi, U.S. Hareesh, Morphological Ensembles of N-Doped Porous Carbon Derived

from ZIF-8/Fe-Graphene Nanocomposites: Processing and Electrocatalytic Studies, 3(30) (2018) 8688-8697. https://doi.org/https://doi.org/10.1002/slct.201801419.

66. S.M. Unni, G.M. Anilkumar, M. Matsumoto, T. Tamaki, H. Imai, T. Yamaguchi, Direct synthesis of a carbon nanotube interpenetrated doped porous carbon alloy as a durable Pt-free electrocatalyst for the oxygen reduction reaction in an alkaline medium, Sustainable Energy & Fuels 1(7) (2017) 1524-1532. https://doi.org/10.1039/C7SE00249A.

67. T. Liu, P. Zhao, X. Hua, W. Luo, S. Chen, G. Cheng, An Fe–N–C hybrid electrocatalyst derived from a bimetal–organic framework for efficient oxygen reduction, Journal of Materials Chemistry A 4(29) (2016) 11357-11364. https://doi.org/10.1039/C6TA03265F.

68. P. Zhang, F. Sun, Z. Xiang, Z. Shen, J. Yun, D. Cao, ZIF-derived in situ nitrogen-doped porous carbons as efficient metal-free electrocatalysts for oxygen reduction reaction, Energy & Environmental Science 7(1) (2014) 442-450. https://doi.org/10.1039/C3EE42799D.

69. H.-x. Zhong, J. Wang, Y.-w. Zhang, W.-l. Xu, W. Xing, D. Xu, Y.-f. Zhang, X.-b. Zhang, ZIF-8 Derived Graphene-Based Nitrogen-Doped Porous Carbon Sheets as Highly Efficient and Durable Oxygen Reduction Electrocatalysts, Angewandte Chemie International Edition 53(51) (2014) 14235-14239. https://doi.org/https://doi.org/10.1002/anie.201408990.

70. L. Ye, G. Chai, Z. Wen, Zn-MOF-74 Derived N-Doped Mesoporous Carbon as pH-Universal Electrocatalyst for Oxygen Reduction Reaction, 27(14) (2017) 1606190. https://doi.org/https://doi.org/10.1002/adfm.201606190.

71. A. Radwan, H. Jin, D. He, S. Mu, Design Engineering, Synthesis Protocols, and Energy Applications of MOF-Derived Electrocatalysts, Nano-Micro Letters 13(1) (2021) 132. https://doi.org/10.1007/s40820-021-00656-w.

72. J.-S. Li, S.-L. Li, Y.-J. Tang, K. Li, L. Zhou, N. Kong, Y.-Q. Lan, J.-C. Bao, Z.-H. Dai, Heteroatoms ternary-doped porous carbons derived from MOFs as metal-free electrocatalysts for oxygen reduction reaction, Scientific Reports 4(1) (2014) 5130. https://doi.org/10.1038/srep05130.

73. H. Rong, T. Zhan, Y. Sun, Y. Wen, X. Liu, H. Teng, ZIF-8 derived nitrogen, phosphorus and sulfur tri-doped mesoporous carbon for boosting electrocatalysis to oxygen reduction in universal pH range, Electrochimica Acta 318 (2019) 783-793. https://doi.org/https://doi.org/10.1016/j.electacta.2019.06.122.

74. L. Yang, G. Xu, J. Ban, L. Zhang, G. Xu, Y. Lv, D. Jia, Metal-organic framework-derived metal-free highly graphitized nitrogen-doped porous carbon with a hierarchical porous structure as an efficient and stable electrocatalyst for oxygen reduction reaction, Journal of Colloid and Interface Science 535 (2018). https://doi.org/10.1016/j.jcis.2018.10.007.

75. P. Cao, Y. Liu, X. Quan, J. Zhao, S. Chen, H. Yu, Nitrogen-doped hierarchically porous carbon nanopolyhedras derived from core-shell ZIF-8@ZIF-8 single crystals for enhanced

oxygen reduction reaction, Catalysis Today 327 (2019) 366-373. https://doi.org/https://doi.org/10.1016/j.cattod.2018.03.020.

76. M. Zhang, C. Wang, R. Luo, W. Zhang, S. Chen, X. Yan, J. Qi, X. Sun, L. Wang, J. Li, A phenolic resin-assisted strategy for MOF-derived hierarchical Co/N-doped carbon rhombic dodecahedra for electrocatalysis, Journal of Materials Chemistry A 7(10) (2019) 5173-5178. https://doi.org/10.1039/C8TA10918D.

77. Y. Xie, C. Zhang, X. He, J.-W. Su, T. Parker, T. White, M. Griep, J. Lin, Copper-promoted Nitrogen-doped Carbon Derived from Zeolitic Imidazole Frameworks for Oxygen Reduction Reaction, Applied Surface Science 464 (2018). https://doi.org/10.1016/j.apsusc.2018.09.102.

78. Q.L. Zhu, W. Xia, T. Akita, R. Zou, Q. Xu, Metal-Organic Framework-Derived Honeycomb-Like Open Porous Nanostructures as Precious-Metal-Free Catalysts for Highly Efficient Oxygen Electroreduction, Advanced materials (Deerfield Beach, Fla.) 28(30) (2016) 6391-8. https://doi.org/10.1002/adma.201600979.

79. S. Liu, Z. Wang, S. Zhou, F. Yu, M. Yu, C.Y. Chiang, W. Zhou, J. Zhao, J. Qiu, Metal-Organic-Framework-Derived Hybrid Carbon Nanocages as a Bifunctional Electrocatalyst for Oxygen Reduction and Evolution, Advanced materials (Deerfield Beach, Fla.) 29(31) (2017). https://doi.org/10.1002/adma.201700874.

80. T. Najam, X. Cai, M. Aslam, M. Tufail, S.S.A. Shah, Nano-engineered directed growth of Mn3O4 quasi-nanocubes on N-doped polyhedrons: Efficient electrocatalyst for oxygen reduction reaction, International Journal of Hydrogen Energy 45 (2020). https://doi.org/10.1016/j.ijhydene.2020.02.205.

81. H. Peng, M. Zhang, K. Sun, X. Xie, H. Lei, G. Ma, Nitrogen-doped carbon nanoflowers with in situ generated Fe3C embedded carbon nanotubes for efficient oxygen reduction electrocatalysts, Applied Surface Science 529 (2020) 147174. https://doi.org/https://doi.org/10.1016/j.apsusc.2020.147174.

82. R. Wang, T. Yan, L. Han, G. Chen, H. Li, J. Zhang, L. Shi, D. Zhang, Tuning the dimensions and structures of nitrogen-doped carbon nanomaterials derived from sacrificial g-C3N4/metal–organic frameworks for enhanced electrocatalytic oxygen reduction, Journal of Materials Chemistry A 6(14) (2018) 5752-5761. https://doi.org/10.1039/C8TA00439K.

83. C. Liu, J. Wang, J. Li, J. Liu, C. Wang, X. Sun, J. Shen, W. Han, L. Wang, Electrospun ZIF-based hierarchical carbon fiber as an efficient electrocatalyst for the oxygen reduction reaction, Journal of Materials Chemistry A 5(3) (2017) 1211-1220.doi.org/10.1039/C6TA09193H.

84. H. Guo, Q. Feng, J. Zhu, J. Xu, Q. Li, S. Liu, K. Xu, C. Zhang, T. Liu, Cobalt nanoparticle-embedded nitrogen-doped carbon/carbon nanotube frameworks derived from a metal–organic framework for tri-functional ORR, OER and HER electrocatalysis, Journal of Materials Chemistry A 7(8) (2019) 3664-3672. https://doi.org/10.1039/C8TA11400E.

85. H. Jin, H. Zhou, D. He, Z. Wang, Q. Wu, Q. Liang, S. Liu, S. Mu, MOF-derived 3D Fe-N-S co-doped carbon matrix/nanotube nanocomposites with advanced oxygen reduction activity and stability in both acidic and alkaline media, Applied Catalysis B: Environmental 250 (2019) 143-149. https://doi.org/https://doi.org/10.1016/j.apcatb.2019.03.013.

86. Q. Huang, Y. Guo, X. Wang, L. Chai, J. Ding, L. Zhong, T.-T. Li, Y. Hu, J. Qian, S. Huang, In-MOF-derived ultrathin heteroatom-doped carbon nanosheets for improving oxygen reduction, Nanoscale 12(18) (2020) 10019-10025. https://doi.org/10.1039/D0NR02007A.

87. S.L. Zhang, B.Y. Guan, X.W. Lou, Co–Fe Alloy/N-Doped Carbon Hollow Spheres Derived from Dual Metal–Organic Frameworks for Enhanced Electrocatalytic Oxygen Reduction, Small 15(13) (2019) 1805324. https://doi.org/https://doi.org/10.1002/smll.201805324.

88. Y. Jing, Y. Cheng, L. Wang, Y. Liu, B. Yu, C. Yang, MOF-derived Co, Fe, and Ni co-doped N-enriched hollow carbon as efficient electrocatalyst for oxygen reduction reaction, Chemical Engineering Journal 397 (2020) 125539, doi.org/10.1016/j.cej.2020.125539.

89. L.-P. Yang, J.-L. Mi, H.-J. Wang, J.-H. Liang, X.-J. Yang, Y.-H. Feng, P. Zhang, L. Liu, Bimetallic Cu−Zn Co-Doped Porous N/C as Efficient Catalysts for Oxygen Reduction Reaction and Oxidation of 1,2-Propanediol, ChemCatChem 12(2) (2020) 584-592. https://doi.org/https://doi.org/10.1002/cctc.201900975.

90. Y. Zhou, B. Tang, S. Wang, J. Long, Cu-MOF@Co-MOF derived Co–Cu alloy nanoparticles and N atoms co-doped carbon matrix as efficient catalyst for enhanced oxygen reduction, International Journal of Hydrogen Energy 45(32) (2020) 15785-15795. https://doi.org/https://doi.org/10.1016/j.ijhydene.2020.04.049.

91. Ö. Arzu, A. Dilek, K. Muhsin, Pesticides, Environmental Pollution, and Health, in: L.L. Marcelo, S. Sonia (Eds.), Environmental Health Risk, IntechOpen, Rijeka, 2016, p. Ch. 1. https://doi.org/10.5772/63094.

92. R.M. Abu Shmeis, Chapter One - Water Chemistry and Microbiology, in: D.S. Chormey, S. Bakırdere, N.B. Turan, G.Ö. Engin (Eds.), Comprehensive Analytical Chemistry, Elsevier2018, pp. 1-56. https://doi.org/https://doi.org/10.1016/bs.coac.2018.02.001.

93. C. Chahal, B. van den Akker, F. Young, C. Franco, J. Blackbeard, P. Monis, Pathogen and Particle Associations in Wastewater: Significance and Implications for Treatment and Disinfection Processes, Advances in applied microbiology 97 (2016) 63-119. https://doi.org/10.1016/bs.aambs.2016.08.001.

94. S. Agarwal, S. Darbar, S. Saha, Chapter 25 - Challenges in management of domestic wastewater for sustainable development, in: A.L. Srivastav, S. Madhav, A.K. Bhardwaj, E. Valsami-Jones (Eds.), Current Directions in Water Scarcity Research, Elsevier2022, pp. 531-552. https://doi.org/https://doi.org/10.1016/B978-0-323-91838-1.00019-1.

95. P. Kokkinos, D. Mantzavinos, D. Venieri, Current Trends in the Application of Nanomaterials for the Removal of Emerging Micropollutants and Pathogens from Water, 25(9) (2020) 2016.

96. M. Nasiri, H. Ahmadzadeh, A. Amiri, Sample preparation and extraction methods for pesticides in aquatic environments: A review, TrAC Trends in Analytical Chemistry 123 (2020) 115772. https://doi.org/https://doi.org/10.1016/j.trac.2019.115772.

97. D.B. Miklos, C. Remy, M. Jekel, K.G. Linden, J.E. Drewes, U. Hübner, Evaluation of advanced oxidation processes for water and wastewater treatment – A critical review, Water Research 139 (2018) 118-131. https://doi.org/https://doi.org/10.1016/j.watres.2018.03.042.

98. D. Ma, H. Yi, C. Lai, X. Liu, X. Huo, Z. An, L. Li, Y. Fu, B. Li, M. Zhang, L. Qin, S. Liu, L. Yang, Critical review of advanced oxidation processes in organic wastewater treatment, Chemosphere 275 (2021) 130104.doi.org/10.1016/j.chemosphere.2021.130104.

99. A. Buthiyappan, A.R.A. Aziz, W.M.A.W. Daud, Recent advances and prospects of catalytic advanced oxidation process in treating textile effluents, 32(1) (2016) 1-47. https://doi.org/doi:10.1515/revce-2015-0034.

100. C. Amor, L. Marchão, M.S. Lucas, J.A. Peres, Application of Advanced Oxidation Processes for the Treatment of Recalcitrant Agro-Industrial Wastewater: A Review, 11(2) (2019) 205.

101. Hassani, J. Scaria, F. Ghanbari, P.V. Nidheesh, Sulfate radicals-based advanced oxidation processes for the degradation of pharmaceuticals and personal care products: A review on relevant activation mechanisms, performance, and perspectives, Environmental Research 217 (2023) 114789. https://doi.org/https://doi.org/10.1016/j.envres.2022.114789.

102. P. Neta, V. Madhavan, H. Zemel, R.W. Fessenden, Rate constants and mechanism of reaction of sulfate radical anion with aromatic compounds, Journal of the American Chemical Society 99(1) (1977) 163-164. https://doi.org/10.1021/ja00443a030.

103. T. Olmez-Hanci, I. Arslan-Alaton, Comparison of sulfate and hydroxyl radical based advanced oxidation of phenol, Chemical Engineering Journal 224 (2013) 10-16. https://doi.org/https://doi.org/10.1016/j.cej.2012.11.007.

104. X. Xia, F. Zhu, J. Li, H. Yang, L. Wei, Q. Li, J. Jiang, G. Zhang, Q. Zhao, A Review Study on Sulfate-Radical-Based Advanced Oxidation Processes for Domestic/Industrial Wastewater Treatment: Degradation, Efficiency, and Mechanism, 8 (2020). https://doi.org/10.3389/fchem.2020.592056.

105. Z. Xiong, Y. Jiang, Z. Wu, G. Yao, B. Lai, Synthesis strategies and emerging mechanisms of metal-organic frameworks for sulfate radical-based advanced oxidation process: A review, Chemical Engineering Journal 421 (2021) 127863. https://doi.org/https://doi.org/10.1016/j.cej.2020.127863.

106. W. Ma, Y. Du, N. Wang, P. Miao, ZIF-8 derived nitrogen-doped porous carbon as metal-free catalyst of peroxymonosulfate activation, Environmental science and pollution research international 24(19) (2017) 16276-16288. https://doi.org/10.1007/s11356-017-9191-2.

107. Y. Liu, W. Miao, X. Fang, Y. Tang, D. Wu, S. Mao, MOF-derived metal-free N-doped porous carbon mediated peroxydisulfate activation via radical and non-radical pathways: Role of

graphitic N and CO, Chemical Engineering Journal 380 (2020) 122584. https://doi.org/https://doi.org/10.1016/j.cej.2019.122584.

108. X. Chang, Y. Wang, X. Zhou, Y. Song, M. Zhang, ZIF-8-derived carbon-modified g-C3N4 heterostructure with enhanced photocatalytic activity for dye degradation and hydrogen production, Dalton Transactions 50(47) (2021) 17618-17624. https://doi.org/10.1039/D1DT03385A.

109. J. He, Y. Wan, W. Zhou, ZIF-8 derived Fe–N coordination moieties anchored carbon nanocubes for efficient peroxymonosulfate activation via non-radical pathways: Role of FeNx sites, Journal of Hazardous Materials 405 (2021) 124199. https://doi.org/https://doi.org/10.1016/j.jhazmat.2020.124199.

110. T. Zeng, M. Yu, H. Zhang, Z. He, J. Chen, S. Song, Fe/Fe3C@N-doped porous carbon hybrids derived from nano-scale MOFs: robust and enhanced heterogeneous catalyst for peroxymonosulfate activation, Catalysis Science & Technology 7(2) (2017) 396-404. https://doi.org/10.1039/C6CY02130A.

111. C. Liu, Y. Wang, Y. Zhang, R. Li, W. Meng, Z. Song, F. Qi, B. Xu, W. Chu, D. Yuan, B. Yu, Enhancement of Fe@porous carbon to be an efficient mediator for peroxymonosulfate activation for oxidation of organic contaminants: Incorporation NH2-group into structure of its MOF precursor, Chemical Engineering Journal 354 (2018) 835-848. https://doi.org/https://doi.org/10.1016/j.cej.2018.08.060.

112. X. Li, F. Liao, L. Ye, L. Yeh, Controlled pyrolysis of MIL-88A to prepare iron/carbon composites for synergistic persulfate oxidation of phenol: Catalytic performance and mechanism, Journal of Hazardous Materials 398 (2020) 122938. https://doi.org/https://doi.org/10.1016/j.jhazmat.2020.122938.

113. Z. Wang, X. Wang, L. Wang, Y. Wei, Z. Zhao, K. Du, D. Chen, X. Li, C. Zhou, G. Liu, Y. Luo, ZIF-67-derived Co@N-PC anchored on tracheid skeleton from sawdust with micro/nano composite structures for boosted methylene blue degradation, Separation and Purification Technology 278 (2021) 119489. https://doi.org/https://doi.org/10.1016/j.seppur.2021.119489.

114. Y. Yang, Y. Liu, X. Fang, W. Miao, X. Chen, J. Sun, B.-J. Ni, S. Mao, Heterogeneous Electro-Fenton catalysis with HKUST-1-derived Cu@C decorated in 3D graphene network, Chemosphere 243 (2020) 125423.doi.org/10.1016/j.chemosphere.2019.125423.

115. P. Liang, Q. Wang, J. Kang, W. Tian, H. Sun, S. Wang, Dual-metal zeolitic imidazolate frameworks and their derived nanoporous carbons for multiple environmental and electrochemical applications, Chemical Engineering Journal 351 (2018) 641-649. https://doi.org/https://doi.org/10.1016/j.cej.2018.06.140.

116. N. Wang, W. Ma, Z. Ren, Y. Du, P. Xu, X. Han, Prussian blue analogues derived porous nitrogen-doped carbon microspheres as high-performance metal-free peroxymonosulfate

activators for non-radical-dominated degradation of organic pollutants, Journal of Materials Chemistry A 6(3) (2018) 884-895. https://doi.org/10.1039/C7TA08472B.

117. W. Ma, N. Wang, Y. Fan, T. Tong, X. Han, Y. Du, Non-radical-dominated catalytic degradation of bisphenol A by ZIF-67 derived nitrogen-doped carbon nanotubes frameworks in the presence of peroxymonosulfate, Chemical Engineering Journal 336 (2018) 721-731. https://doi.org/https://doi.org/10.1016/j.cej.2017.11.164.

118. G. Wang, S. Chen, X. Quan, H. Yu, Y. Zhang, Enhanced activation of peroxymonosulfate by nitrogen doped porous carbon for effective removal of organic pollutants, Carbon 115 (2017) 730-739. doi.org/10.1016/j.carbon.2017.01.060.

119. N. Wang, W. Ma, Z. Ren, L. Zhang, R. Qiang, K.-Y.A. Lin, P. Xu, Y. Du, X. Han, Template synthesis of nitrogen-doped carbon nanocages–encapsulated carbon nanobubbles as catalyst for activation of peroxymonosulfate, Inorganic Chemistry Frontiers 5(8) (2018) 1849-1860. https://doi.org/10.1039/C8QI00256H.

120. C. Wang, J. Kim, M. Kim, H. Lim, M. Zhang, J. You, J.-H. Yun, Y. Bando, J. Li, Y. Yamauchi, Nanoarchitectured metal–organic framework-derived hollow carbon nanofiber filters for advanced oxidation processes, Journal of Materials Chemistry A 7(22) (2019) 13743-13750. https://doi.org/10.1039/C9TA03128F.

121. W. Zhang, M. Yang, H. Zhang, X. Yu, W. Zhang, A.T.S. Wee, X. Yan, J. Qi, J. Li, A confinement approach to fabricate hybrid PBAs-derived FeCo@NC yolk-shell nanoreactors for bisphenol A degradation, Chemical Engineering Journal 428 (2022) 131080. https://doi.org/https://doi.org/10.1016/j.cej.2021.131080.

122. K.-Y. Andrew Lin, F.-K. Hsu, Magnetic iron/carbon nanorods derived from a metal organic framework as an efficient heterogeneous catalyst for the chemical oxidation process in water, RSC Advances 5(63) (2015) 50790-50800. https://doi.org/10.1039/C5RA06043E.

123. X. Li, Z. Ao, J. Liu, H. Sun, A.I. Rykov, J. Wang, Topotactic Transformation of Metal–Organic Frameworks to Graphene-Encapsulated Transition-Metal Nitrides as Efficient Fenton-like Catalysts, ACS Nano 10(12) (2016) 11532-11540. https://doi.org/10.1021/acsnano.6b07522.

124. X. Huang, J. Zhang, X. Zhang, Q.-P. Wu, C.-H. Yan, Activation of Peroxymonosulfate by CuNi@C Derived from Metal–Organic Frameworks Precursor %J Australian Journal of Chemistry, 71(11) (2018) 874-881. doi.org/10.1071/CH18260.

125. H. Jiang, C. Zhu, Y. Yuan, C. Yue, C. Ling, F. Liu, A. Li, Enhanced activation of peroxymonosulfate with metal-substituted hollow MxCo3-xS4 polyhedrons for superfast degradation of sulfamethazine, Chemical Engineering Journal 384 (2020) 123302. https://doi.org/https://doi.org/10.1016/j.cej.2019.123302.

126. Z. Wang, L. Lin, S. Niu, Y. Zi, Triboelectric Nanogenerators, 2016. https://doi.org/10.1007/978-3-319-40039-6.

127. S. Wang, Y. Xie, S. Niu, L. Lin, Z.L. Wang, Freestanding Triboelectric-Layer-Based Nanogenerators for Harvesting Energy from a Moving Object or Human Motion in Contact and Non-contact Modes, 26(18) (2014) 2818-2824.doi.org/10.1002/adma.201305303.

128. W.-G. Kim, D.-W. Kim, I.-W. Tcho, J.-K. Kim, M.-S. Kim, Y.-K. Choi, Triboelectric Nanogenerator: Structure, Mechanism, and Applications, ACS Nano 15(1) (2021) 258-287. https://doi.org/10.1021/acsnano.0c09803.

129. G. Khandelwal, A. Chandrasekhar, N.P. Maria Joseph Raj, S.-J. Kim, Metal–Organic Framework: A Novel Material for Triboelectric Nanogenerator–Based Self-Powered Sensors and Systems, 9(14) (2019) 1803581.doi.org/10.1002/aenm.201803581.

130. S. Barsiwal, A. Babu, U.K. Khanapuram, S. Potu, N. Madathil, R.K. Rajaboina, S. Mishra, H. Divi, P. Kodali, R. Nagapuri, T. Chinthakuntla, ZIF-67-Metal–Organic-Framework-Based Triboelectric Nanogenerator for Self-Powered Devices, 2(4) (2022) 291-302.

131. R. Wen, J. Guo, A. Yu, J. Zhai, Z.l. Wang, Humidity-Resistive Triboelectric Nanogenerator Fabricated Using Metal Organic Framework Composite, 29(20) (2019) 1807655. https://doi.org/https://doi.org/10.1002/adfm.201807655.

132. Y. Guo, Y. Cao, Z. Chen, R. Li, W. Gong, W. Yang, Q. Zhang, H. Wang, Fluorinated metal-organic framework as bifunctional filler toward highly improving output performance of triboelectric nanogenerators, Nano Energy 70 (2020) 104517. https://doi.org/https://doi.org/10.1016/j.nanoen.2020.104517.

133. G. Khandelwal, N.P. Maria Joseph Raj, S.-J. Kim, Zeolitic Imidazole Framework: Metal–Organic Framework Subfamily Members for Triboelectric Nanogenerators, 30(12) (2020) 1910162. https://doi.org/https://doi.org/10.1002/adfm.201910162.

134. G. Khandelwal, N.P. Maria Joseph Raj, S.-J. Kim, ZIF-62: a mixed linker metal–organic framework for triboelectric nanogenerators, Journal of Materials Chemistry A 8(34) (2020) 17817-17825. https://doi.org/10.1039/D0TA05067A.

135. G. Khandelwal, N.P. Maria Joseph Raj, V. Vivekananthan, S.-J. Kim, Biodegradable metal-organic framework MIL-88A for triboelectric nanogenerator, iScience 24(2) (2021). https://doi.org/10.1016/j.isci.2021.102064.

136. N. Jayababu, D. Kim, Co/Zn bimetal organic framework elliptical nanosheets on flexible conductive fabric for energy harvesting and environmental monitoring via triboelectricity, Nano Energy 89 (2021) 106355. doi.org/10.1016/j.nanoen.2021.106355.

137. M.T. Rahman, S.M.S. Rana, M.A. Zahed, S. Lee, E.-S. Yoon, J.Y. Park, Metal-organic framework-derived nanoporous carbon incorporated nanofibers for high-performance triboelectric nanogenerators and self-powered sensors, Nano Energy 94 (2022) 106921. https://doi.org/https://doi.org/10.1016/j.nanoen.2022.106921.

Chapter 2

Template-assisted Synthesis of Ni, N co-doped Porous Carbon from Ni Incorporated ZIF-8 Frameworks for Electrocatalytic Oxygen Reduction Reaction
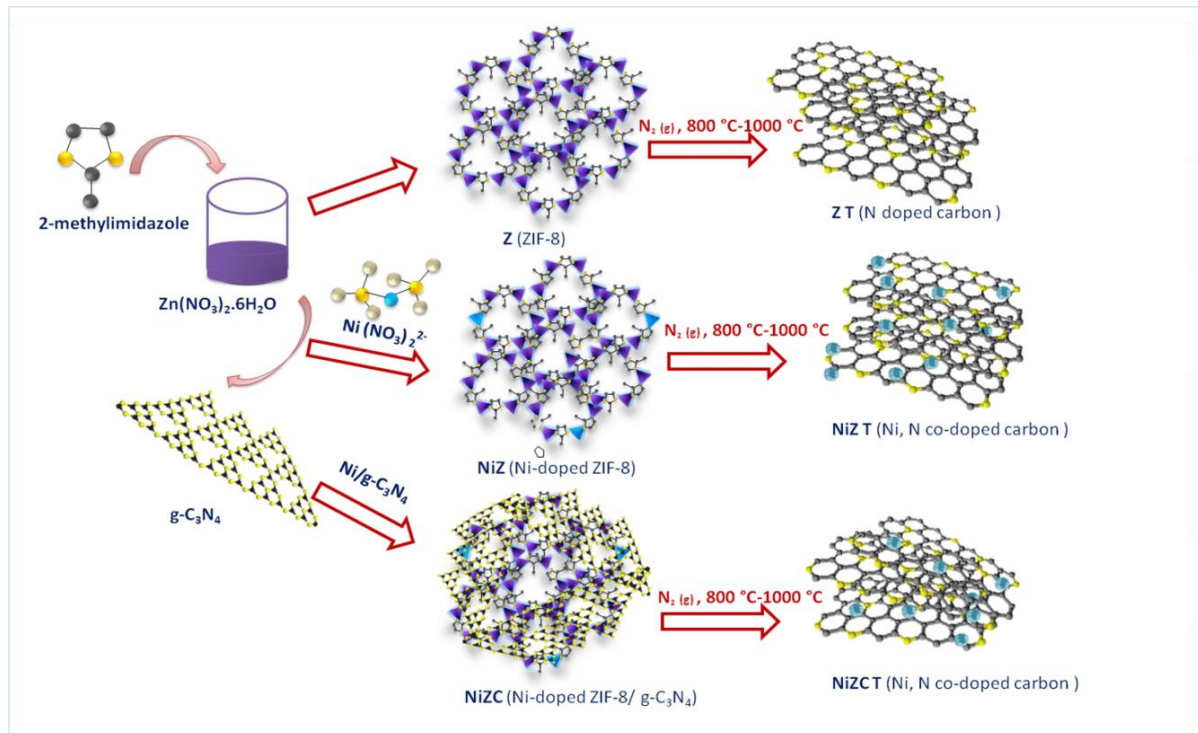
Abstract

Heteroatom-doped porous carbon electrocatalyst with enhanced oxygen reduction reaction (ORR) performance in an alkaline medium was obtained by the high-temperature treatment of Ni-incorporated ZIF-8 frameworks and its composite with g-C$_3$N$_4$ as a supporting matrix template. The morphology and porosity of this heteroatom-doped carbon were tuned by varying the Ni: Zn molar ratio in the Ni/Zn ZIF-8 and the Ni/Zn ZIF-8@g-C$_3$N$_4$ compositions. The template-aided synthetic strategy using g-C$_3$N$_4$ helped in the controlled decomposition of composites leading to heteroporous sheet-like architectures with increased nitrogen content. The Ni/Zn ZIF-8 sample on heat treatment in the 800-1000 °C temperature range led to the formation of Ni, N co-doped porous carbon (Ni-NPC) with Ni-C active sites. The defective sites induced by nickel carbide, along with the distributed N atoms on the carbon surface, enabled active O$_2$ adsorption sites. The high surface area, high degree of graphitization, and the defects created by the well-dispersed N and Ni on the porous carbon matrices favoured the charge separation leading to higher electrochemical ORR activity. The Ni, N co-doped carbon catalyst, NiZC(1:2) 1000 in an alkaline medium exhibited a limiting current density of 5.2 mAcm^{-2} with a half-wave potential of 0.76 V vs. RHE in 0.1 M KOH. The catalyst also showed improved methanol tolerance and better stability compared to the standard Pt/C catalyst.

2.1. Introduction

The undesirable climatic variations induced by global warming could be ascribed primarily to the uncontrolled emission of greenhouse gases as fossil fuel consumption is increased manifold. This prompted a genuine demand for greener energy storage /conversion technologies. A Fuel cell is perceived to be an electrochemical energy conversion device that promises reliability and environmentally benign operating conditions.[1-3] The efficiency of fuel cells is rooted in the electrochemical redox reaction kinetics occurring at the membrane electrode assembly (MEA). The sluggish kinetics of oxygen reduction reaction (ORR) occurring at the cathode of the electrochemical cell necessitates the use of a catalyst for the appreciable performance of fuel cells.[4-6] However, the use of platinum-based metal catalysts increases the fuel cell cost and hinders its widespread commercial applications.[7,8] Among low-temperature fuel cell technologies, alkaline fuel cells (AFC) are preferred over proton exchange membrane fuel cells (PEMFCs) owing to the advantages of relatively faster ORR kinetics in an alkaline medium and the less corrosive environment. AFCs thus offer higher efficiency and the possibility of employing non-noble metal catalysts.[9-11] This could lead to a viable strategy of making the fuel cell cost-effective by replacing the precious noble metal-based catalysts with high surface area porous carbon catalysts.[12-14] However, the application of porous carbon requires further improvements to combat the poor conductivity and catalytic properties. It is well accepted that doping heteroatom into the porous carbon is an effective method to impart better catalytic activity by altering the spin density and charge separation of the carbon matrix.[15,16] Consequently, carbon-based catalysts incorporating heteroatoms like B, N, S, P, and transition metals are currently being explored as ORR electrocatalysts.[17-23] Studies show that co-doping transition metal with N can boost the electrocatalytic performance of the carbon owing to the better conductivity and high active surface area imparted by synergistic effects.[24,25] Over the past few years, nickel being a metal occupying the same group as that of platinum, has got considerable attention due to its higher electrical conductivity, corrosion resistance properties, and larger abundance, enabling it to be a promising electrocatalyst for Oxygen Reduction Reaction (ORR), Oxygen Evolution Reaction (OER) and Hydrogen Evolution Reaction (HER).[26] Nickel

dispersed on carbon matrix has been recently investigated for electrochemical applications. B. Devi et al. have made a notable contribution by synthesizing N-doped graphitized carbon encapsulated with Ni nanoparticles from Ni(II)-dimeric complex with pyridine derivatives for trifunctional (ORR, OER, and HER) applications.[27] Tyagi et al. have reported ORR studies on atomically dispersed nickel (Ni)/nickel sulfide (NixSy) on heteroatom doped hierarchical porous carbonaceous sheets from nickel nitrate and guanidine thiocyanate.[28]

Metal-Organic Frameworks (MOFs), by virtue of their high surface area and designed morphology, are widely used as precursor materials to synthesize heteroatom-doped porous carbons. Moreover, the precursor chemistry could easily be tuned to incorporate the dopant elements of choice, and its direct conversion by pyrolysis could yield heteroatom-doped carbons with high surface area and favourable pore characteristics.[29-31] Among MOFs, Zeolitic Imidazolate Frameworks (ZIFs) are considered as promising materials with a multitude of applications due to their exceptional chemical and temperature stability. ZIFs are transition metal coordinated imidazolate frameworks with the 3-D sodalite topology. The structural resemblances to zeolites enable them to be promising materials for adsorption and separation applications.[32-35] One of the featured applications of ZIFs is to utilize them as precursors for synthesizing high surface area porous carbon. These materials have potential electrochemical applications as electrode materials for fuel cell systems and other energy storage devices.[36-38]

An efficient method to synthesize transition metal, N co-doped carbon with tuned morphology, is by incorporating less volatile transition metals into the parent ZIF frameworks. The incorporated metal centres of cobalt, iron, and nickel could contribute as catalytically active centres for the growth of various morphologies of carbon.[39-43] Based on these, notable contributions have emerged in the development of highly graphitized porous carbon surfaces doped with nickel from bimetallic Ni/Zn ZIF-8 frameworks, prepared by chemical vapour deposition (CVD) and hydrothermal techniques [44,45] The resultant porous carbons displayed improved electrocatalytic activity for HER, OER, and ORR in alkaline medium. Nevertheless, the ZIF-derived carbon has limitations in its application due to the less efficient adsorption-diffusion pathways around the microporous sites during

electrocatalysis. Template-assisted carbonization was thus employed as an efficient method to modulate the pore characteristics and to improve the catalytic activity. Consequently, studies are reported that the incorporation of templates like rGO,[46,47] melamine sponge,[48] carbohydrates[49,] etc., can effectively improve the porosity distribution and perform as self-sacrificing templates. Recently, Wang et al. obtained highly efficient ORR catalysts of Co, N co-doped porous carbon with bamboo-like carbon nanotubes by using g-C_3N_4 as the sacrificial template with bimetallic Co/Zn ZIF frameworks. The g-C_3N_4 served as a medium for the growth of ZIF particles by attracting the metal precursors of ZIF to its electron-rich sites, and the catalyst exhibited remarkable ORR activity and stability.[50]

Herein, we have made an attempt to synthesize Ni, N co-doped porous carbon with nickel carbide active centres by the high-temperature treatment of g-C_3N_4 incorporated Ni-containing ZIF-8 frameworks. The added g-C_3N_4 aided easy decomposition of the ZIF frameworks that led to sheet-like hetero-porous carbon and compensated for the severe nitrogen loss upon high-temperature carbonization. Since the self-sacrificing g-C_3N_4 template was finally converted to the N-doped porous carbon upon carbonization, no complex etching procedure was required for the removal of an external template on the final catalyst, highlighting the advantage of g-C_3N_4 as the template in N doped carbon systems. As the rate of coordination of Ni^{2+} is slower than Zn^{2+}, attempts were made to study the effect of nickel concentration and carbonization temperature on the formed frameworks. The surface area, porosity, morphological features, and the electrochemical oxygen reduction activity of the resulting carbon catalysts were influenced by the Ni/Zn molar ratio of the precursor of ZIF and the carbonization temperature. The catalyst exhibited good ORR activity, stability, and methanol tolerance in an alkaline medium by virtue of its high surface area and nitrogen content.

2.2. Experimental

2.2.1. Materials

Analytical grade Zinc nitrate hexahydrate ($Zn(NO_3)_2.6H_2O$, Merck, India), Nickel nitrate hexahydrate ($Ni(NO_3)_2.6H_2O$, Merck, India), 2-methylimidazole (2-MeIm, $C_4H_6N_2$,98%, Sigma Aldrich), Methanol (CH_3OH, ≥99.8%, Merck, India) and

Urea (NH$_2$CONH$_2$, Merck, India) . All the reagents were used 'as received' without any further purification.

2.2.2. Preparation of ZIF-8 (Z)

The preparation of ZIF-8 in methanol was analogous to a previously reported procedure. [36] In a typical synthesis, 1.466 g of Zn(NO$_3$)$_2$.6H$_2$O dissolved in 200 mL methanol was added to a solution containing 3.325 g of 2-MeIm in 200 mL methanol (the molar ratio of Zn:2-MeIm: Methanol was 1:8:700). The precursor solution was then kept under stirring for 15 h at room temperature. The white precipitate formed was collected after washing with methanol by centrifugation. The sample was further dried overnight at 60 °C in an air oven.

2.2.3. Preparation of Ni /Zn ZIF-8 (NiZ):

The synthesis of NiZ was similar to the synthesis of ZIF-8 with some modifications. Initially, a mixture of Ni(NO$_3$)$_2$.6H$_2$O and Zn(NO$_3$)$_2$.6H$_2$O with specific molar ratio of Ni^{2+}/Zn^{2+} was prepared in methanol as follows:

The desired concentration of Ni^{2+}/Zn^{2+} was prepared by adding Ni(NO$_3$)$_2$.6H$_2$O salt into a solution of 1.466 g of Zn(NO$_3$)$_2$.6H$_2$O in 200 mL methanol. This mixture was then added to a solution containing 3.325 g of 2-MeIm in 200 mL methanol and stirred for 15 h. The procedure was repeated by changing the concentration of Ni(NO$_3$)$_2$.6H$_2$O to get the molar concentration of Ni^{2+}:Zn^{2+} as 1:2 and 1:1 while keeping the molar ratio of Zn:2-MeIm: Methanol constant (1:8:700). The pale blue precipitate formed was collected by centrifugation after washing with methanol and then dried at 60 °C. The obtained samples were named NiZ(X: Y), where X and Y stand for the molar ratios of Ni and Zn, respectively.

2.2.4. Preparation of Ni /Zn ZIF-8-C$_3$N$_4$ composite (NiZC):

g-C$_3$N$_4$ was prepared by the heat treatment of urea at 550 °C for 4 h in a muffle furnace.[51] A dilute suspension of g-C$_3$N$_4$ was made by dispersing 1 g of g-C$_3$N$_4$ in 150 mL methanol by ultrasonication for 1 h. Similar to the synthesis of NiZ, a mixture of Zn(NO$_3$)$_2$.6H$_2$O and Ni(NO$_3$)$_2$.6H$_2$O with specific Ni^{2+}/Zn^{2+} molar ratios (molar ratio of Ni^{2+}:Zn^{2+} as 1:2 and 1:1) was prepared in 50 mL methanol. The above solution was added to g-C$_3$N$_4$ dispersion and ultrasonicated for 2 h. This mixture was added to 3.325 g of 2-MeIm in 200 mL methanol, followed by stirring for 15 h. The formed precipitate was collected by centrifugation after washing with

excess methanol and dried at 60 °C. The amount of g-C_3N_4 added to the reaction mixture was constant for all the samples. The samples prepared with varying Ni^{2+}/Zn^{2+} molar ratios were named NiZC(X: Y), where the additional letter C indicates the presence of g-C_3N_4.

2.2.5. Preparation of N-doped carbon from ZIF-8 (Z T)

The ZIF-8 powder was carbonized in the temperature range of 800-1000 °C for 2 h under a nitrogen atmosphere at a heating rate of 3 °C/min in a quartz tube and cooled to obtain the N- doped porous carbon. The resulting carbon was then acid leached by overnight soaking in 3 M H_2SO_4 at room temperature, followed by washing multiple times with deionized water to remove unreactive species from the surface of the porous carbon, which may otherwise decrease the activity of the catalyst by clogging the pores.[52] The samples were named "Z T," where Z represents ZIF-8 and T denotes the temperature at which the samples were carbonized (Z 800, Z 900 & Z 1000).

2.2.6. Preparation of Ni, N co-doped porous carbon from NiZ and NiZC (NiZ T& NiZC T)

The prepared NiZ and NiZC samples were subjected to high-temperature carbonization in the temperature range of 800-1000 °C, followed by acid washing as described above. The resulting samples were denoted as NiZ(X:Y) T and NiZC(X:Y) T, where X:Y represents the $Ni^{2+}:Zn^{2+}$ ratio of the precursor and T, the carbonization temperature.

2.2.7. Material characterization

The phase purity and crystalline phase of the samples were analyzed by powder X-ray diffraction (PXRD) analysis (PW1710 Philips, The Netherlands) using Cu Kα radiation. The infrared spectrum of the samples was analyzed using Fourier Transform-Infrared spectroscopy (Perkin Elmer, FT-IR, Spectrum Two). The morphological features of the samples were observed through a Scanning Electron Microscopy (JEOL, JSM-35) operating at 15 kV and by a high-resolution Transmission Electron Microscope (HRTEM, TecnaiG2, FEI, The Netherlands) operating at 300 KV. The elemental mapping and quantification of the samples were carried out by Energy Dispersive Spectroscopy (EDS). Raman spectra were recorded utilizing an alpha 300 R confocal Raman microscope (WI Tec, Germany)

using a laser beam of excitation wavelength 633 nm. The surface chemistry & elemental composition of the samples were analyzed using X-ray Photoelectron Spectroscopy (ULVAC-PHI Inc., USA) equipped with a monochromatic Al-Kα X-Ray source (hν= 1486.6 eV) having micro-focused beam (200 μm, 15 KV). Survey scans were recorded using an X-ray source power of 50 W and pass energy of 187.85 eV. A pass energy of 46.95 eV was used to record the high-resolution spectra of the elements. The surface area and porous characteristics of the samples were analyzed using N_2 adsorption-desorption measurement technique (Tristar II, Micrometrics, USA). The total pore volume and micropore volume were calculated from the isotherm at a P/P_0 value of 0.990 and 0.035, respectively, for easier comparison of the values and the porous structures. However, micropore volume values may have been influenced by monolayer adsorption in some cases. Thermo Gravimetric Analysis (TGA) was conducted (Perkin Elmer STA6000 TGA) at a heating rate of 3 °C min^{-1} in N_2 atmosphere.

2.2.8. Electrochemical characterization

All the electrochemical measurements were performed in a Bio-Logic electrochemical workstation. A three-electrode rotating disk setup was used to analyze the activity of the catalyst for the electrochemical oxygen reduction reaction in which Hg/HgO was used as the reference electrode, and a graphitic rod was used as the counter electrode. The working electrode was prepared according to the following procedure: Catalyst slurry was prepared by adding a mixture of 1 mL of isopropyl alcohol-water (1:3) and 40 μL of Nafion solution into 5 mg of the catalyst, followed by sonication for 1 h. The electrode was prepared by coating 10 μL of the prepared catalyst slurry on a glassy carbon electrode (surface area 0.196 cm^2), followed by drying at room temperature. All the ORR measurements were conducted in 0.1 M KOH solution, and the analysis was carried out by saturating with N_2 and O_2 gases. For comparison of the electrocatalytic activity of the samples, the state-of-the-art electrocatalyst with 40 wt.% Pt/C (Johnson Matthey) was used under the same procedure. The rotating ring disk electrode (RRDE) experiments were performed under the same conditions with the catalyst coated on a glassy carbon (surface area 0.2826 cm^2) electrode having a platinum ring around the surface as the working electrode. The stability of the catalyst was analyzed by accelerated durability test (ADT) and by performing linear sweep voltammetry

(LSV) before and after 5000 cycles of CV performed in the potential range of 0.57 V to 0.97 V at a scan rate of 100 mV s^{-1} in 0.1 M KOH.

2.3.   Results and Discussion
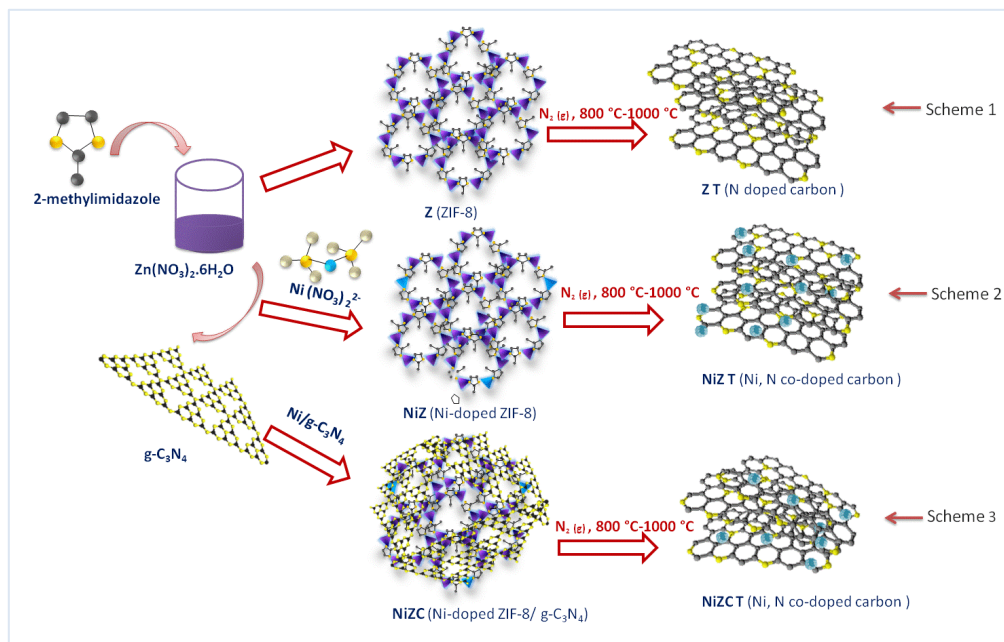
Figure 1. Scheme showing the formation of N-doped carbon and Ni, N co-doped carbon.

Figure 1 depicts the schematic diagram of the synthesis of ZIF-8, NiZ, and NiZC samples in methanol medium by chemical precipitation method at room temperature. The ZIF-8 was synthesized according to the reported procedure in methanol medium, and the high-temperature carbonization resulted in N-doped carbon (**Scheme 1**). In the second stage, ZIF-8 was modified by incorporating Ni in the matrix with varying Ni^{2+}/Zn^{2+} in the precursor medium (**Scheme 2**). As a subsequent stage, the influence of the supporting template on the formation of porous carbon was studied by preparing Ni-incorporated ZIF-8 (NiZ) samples on the surfaces of g-C$_3$N$_4$ sheets by introducing a dispersion of g-C$_3$N$_4$ in methanol in the reaction medium containing Zn^{2+}, Ni^{2+} and 2-MeIm (**Scheme 3**). The carbonization of NiZ(X: Y) and NiZC(X: Y) samples in the N$_2$ atmosphere in the temperature range of 800-1000°C resulted in Ni, N co-doped porous carbon matrices.

2.3.1. Phase analysis

The powder X-ray diffraction (PXRD) patterns recorded for all the samples indicated the formation of pure ZIF-8 (JCPDS 00-062-1030),[53], with sodalite topology. XRD pattern of the NiZ sample confirmed the absence of any other phase than ZIF-8. The XRD pattern of g-C₃N₄ contained the characteristic peaks at around 13.1° of (100) plane and at 27.4° of (002) plane (JCPDS 87-1526) corresponding to the packing of the in-plane structural motif of the graphite-like structure and hexagonal tri-s-triazine units of graphitic carbon nitride respectively. [54] The XRD patterns of composites exhibited all the peaks of ZIF-8 and g-C₃N₄, indicating the growth of ZIF-8 phase on the g-C₃N₄ matrices. The peaks corresponding to nickel phases were not observed, probably due to the very small amount incorporated. However, a modification in the (011) plane of the ZIF phase was observed in the nickel-incorporated samples as evidenced by the shift of 2θ value from 7.3° to 7.2° in NiZ(1:2) & NiZC(1:2) samples and 7.1° in NiZ(1:1) & NiZC(1:1) samples. The shift was more visible with increasing nickel content and could indicate nickel species present in the frameworks (**Figure 2a & 2b**).
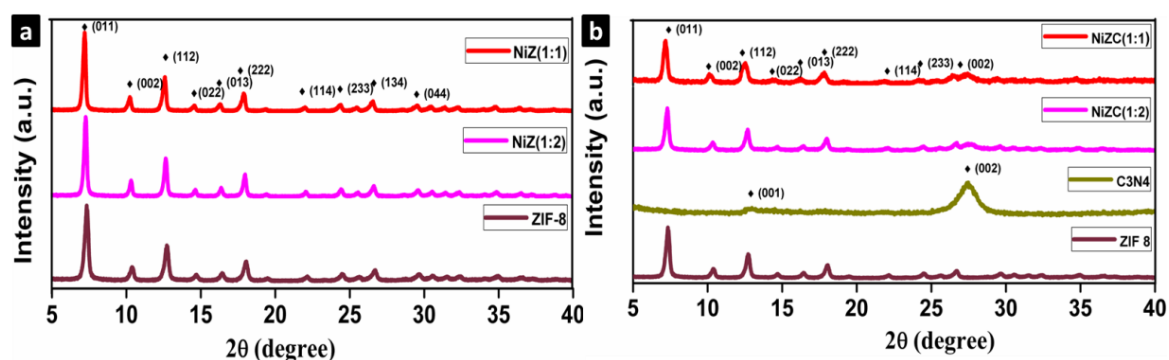
Figure 2. PXRD patterns of a) ZIF-8 and NiZ samples and b) g-C₃N₄ and NiZC composites

The XRD patterns of the reaction product obtained after the reaction of Ni salt (with no Zn addition) with 2-MeIm were also recorded, and the results indicated the absence of any zeolitic imidazolate type of framework (**Figure 3**). The XRD peaks of the reaction product between Ni and 2-MeIm could be attributed to the square planar or distorted octahedral Ni complexes with imidazolate in the reaction medium, which is the preferred geometry of Ni complexes or Ni-MOFs.[55] It is clear that Ni imidazolate frameworks,

analogous to ZIF-8, were not formed in the absence of Zn^{2+} in the medium. It can be thus inferred that while employing the Ni/Zn mixture, some of the Ni^{2+} ions present in the medium are presumably incorporated into the 3D ZIF framework mimicking the tetrahedral geometrical alignment of Zn^{2+} with imidazolate ions.
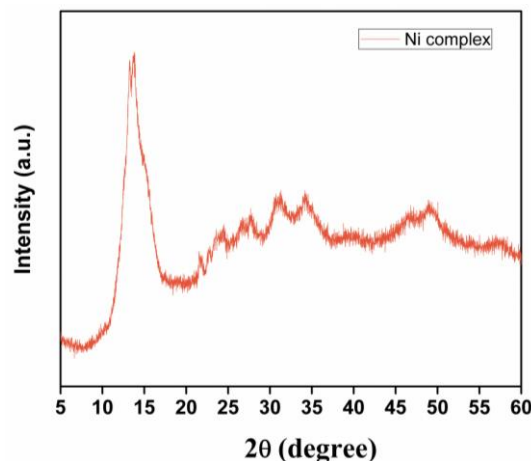
Figure 3. PXRD pattern of Ni-methylimidazolate complex

In the high-temperature carbonization process, the Zn ion in the coordination sphere volatilized, due to which network structure collapsed around the metal atom, forming N-doped porous carbon matrices. The peaks at the 2θ values of 26° and 44°, corresponding respectively to the (002) plane and (100) plane, were due to the diffraction from the polyarene planes and confirmed the formation of graphitized N-doped carbon (**Figure 4b & 4b**).[56]
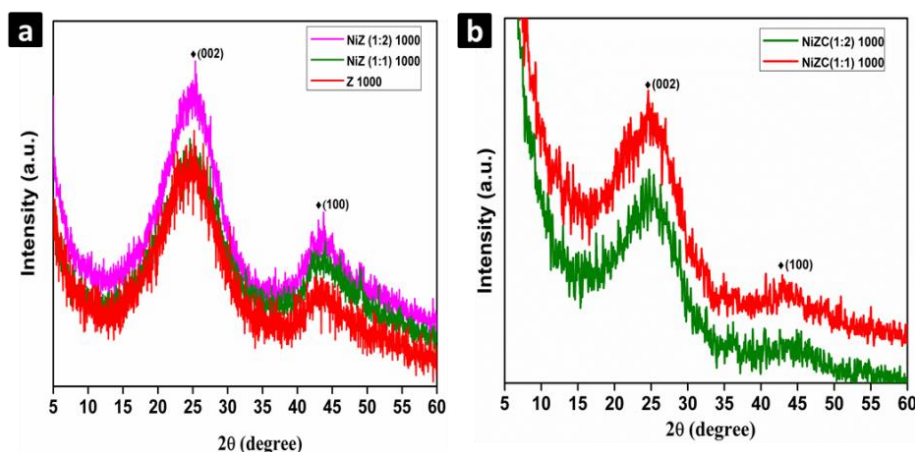
Figure 4. PXRD patterns of carbon samples derived at 1000 °C

2.3.2. Fourier transform infrared (FT-IR) analysis

The FT-IR analysis evidenced C-N, C=C, and metal-C bonds in "as-synthesized" metal-organic frameworks and in the carbonized samples (**Figure 5a & 5b**). The IR pattern of the NiZ sample was similar to ZIF-8, confirming the similarity in the bonding type of NiZ with ZIF-8 and its variation from Ni-MOF. For carbonized samples, the IR pattern showed characteristic peaks of unsaturated hetero atomic bonding of the C-N bonded carbon and M-C functional group, indicating the creation of heteroatomic bonding into the carbon matrix. Compared to Z 1000, the NiZ 1000 and NiZC 1000 samples exhibited a shift in the transmittance peak of C-N stretching frequency to lower wave number, probably due to the weakening of C-N bond strength upon the electron donation by the incorporated nickel atom.[36]
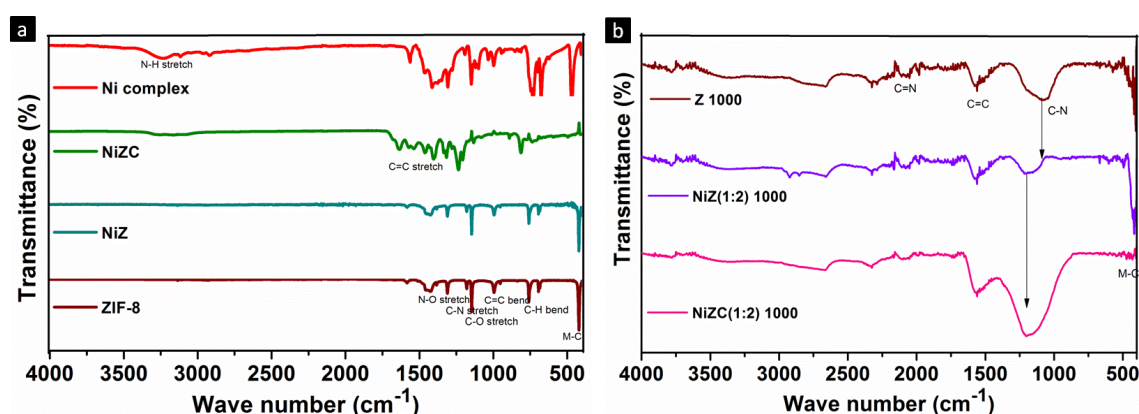
Figure 5. FT-IR spectra of a) ZIF-8, NiZ, NiZC and Ni-Imidazolate complex and b) Carbonized ZIF-8, NiZ and NiZC at 1000 °C

2.3.3. Thermo gravimetric analysis (TGA)

To elucidate the carbonization pathways of the samples, thermo gravimetric analysis (TGA) of the composite sample was performed in a flowing N_2 atmosphere. As can be interpreted from the TG curves (**Figure 6**), the presence of less volatile nickel reduced the weight loss in the Ni/Zn ZIF-8 framework during carbonization. While Zn^{2+} ions get easily volatilized during the high-temperature carbonization, the nickel persisted in the matrix due to its high boiling temperature of ~2732 °C. In addition, the g-C_3N_4 containing NiZC(1:2) sample exhibited higher weight loss than pure ZIF-8. The decomposition profiles of the composites

were shifted to lower temperature because of the presence of an easily decomposing g-C_3N_4 template.[57]
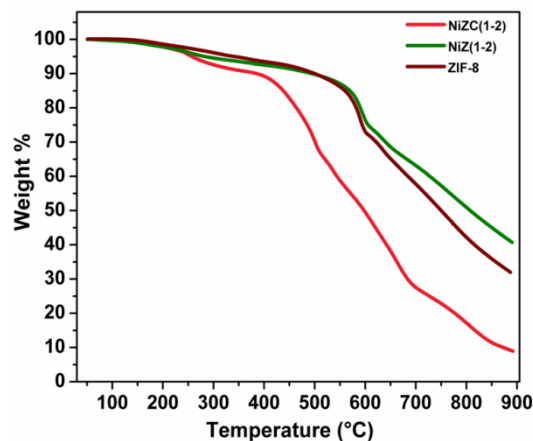
Figure 6. TGA curves of ZIF-8, NiZ(1:2) and NiZC(1:2)

2.3.4. Surface area analysis

The specific surface area and pore characteristics of the samples were evaluated using the N_2 adsorption-desorption analysis. The ZIF-8 and NiZ samples showed Type I adsorption isotherm indicative of the microporous nature of the framework material (**Figure 7a**). At the same time, the rise in adsorption at large P/P_0 values > 0.9 indicated condensation of adsorbates in the interparticle voids of the samples constituted by secondary pores from the aggregation of the particles.[58,59] The surface area values were 1246, 1260, and 1275 m^2/g for ZIF-8, NiZ(1:2), and NiZ(1:1), respectively. The g-C_3N_4 supported NiZC samples exhibited a predominantly microporous nature though some larger pores were also observed, presumably originating from folded g-C_3N_4 sheets (**Figure 7b**). The surface area values of the g-C_3N_4 supported samples were 663 and 692 m^2/g for NiZC(1:2) and NiZC(1:1), respectively, much lower compared to pure ZIF-8, g-C_3N_4 has relatively less surface area (108 m^2/g) and its incorporation inherently reduced the surface area of the composite samples (**Table 1**). The formation of a porous structure was also aided by the vaporization of Zn metal from the coordination spheres. The decomposition of framework structures on high-temperature carbonization led to a decrease in surface area.
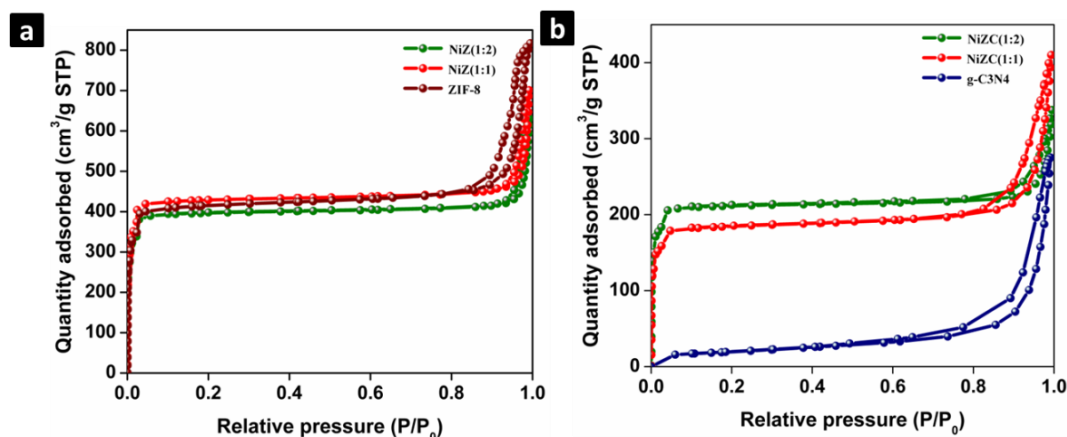
Figure 7. N_2 adsorption-desorption isotherms of a) ZIF-8 and NiZ samples, b) g-C_3N_4 and NiZC samples.

Table 1. Surface areas and pore volumes of the samples before carbonization.

Sample	Before carbonization		
	S_{BET} (m²/g)	V_{total} (cm³/g)	V_{micro} (cm³/g)
g-C_3N_4	108	0.42	0.01
Z (ZIF-8)	1246	1.26	0.61
NiZ(1:2)	1260	0.98	0.59
NiZ(1:1)	1275	1.09	0.63
NiZC(1:2)	663	0.51	0.30
NiZC(1:1)	692	0.63	0.26

After carbonization, the ZIF-8 and NiZ samples derived carbon retained their Type I adsorption behaviour, but the surface area varied with varying Ni/Zn ratio and the carbonization temperature (**Figure 8 & 9**). The high-temperature carbonization resulted in porous carbon with surface area values in the range of 349-1050 m²/g.The surface area of the carbon derived from ZIF-8 was found to increase with increasing temperature above 800 °C and the sample after carbonization at 1000 °C exhibited the highest surface area of 1050 m²/g, owing to the formation of fully extended porous textures upon the evaporation of zinc (**Table 2**). ZIF and NiZ samples showed decreased micro-porosity and surface area on heat treatment at 800 °C, obviously due to incomplete carbonization at this temperature. NiZ(1:2)

and ZIF-8 samples showed a systematic increase in micro-porosity and surface area on heat treatment from 800 to 1000 °C, although the evolution of micro-porosity was slightly delayed in NiZ(1:2) sample (lower micro-porosity at 800 but similar at 900 and 1000 °C). This delay should be due to the increased thermal stability of the materials owing to the presence of Ni and Zn. The lower volatility of Ni should be the reason; the more Ni-containing sample NiZ(1:1), in fact, has shown an even further delay in the evolution of microporous carbon structure (very low micro-porosity at 800 and 900 but high at 1000 °C). Hence, the metal content seems to have a significant influence on pore structure formation. In the case of NiZC samples, an increase in heat treatment from 800 °C to 1000 °C only slightly increased their surface area, and the micro-porosity remained more or less the same. It could be expected that the carbonization was more or less complete by 800 °C in these samples due to the easier decomposition of g-C_3N_4 present. While the porous carbon derived from ZIF frameworks retained its microporous structure, the template-assisted synthesis of porous carbon using g-C_3N_4 facilitated the formation of the hetero-porous architecture of the derived carbon, as clearly indicated by the Type IV isotherms with H3 hysteresis. At higher temperatures, the pore volume of NiZC(X: Y) T samples was found to be higher, aided by the hybrid structure formed by the micro-mesoporous architectures of the NiZ-C_3N_4 combination. This extended micro-meso porosity of the catalysts, upon using g-C_3N_4 as the supporting matrix, might be beneficial for the easier diffusion of the O_2 molecules toward the catalytic sites. All the samples had macro porosity due to the presence of secondary aggregates.
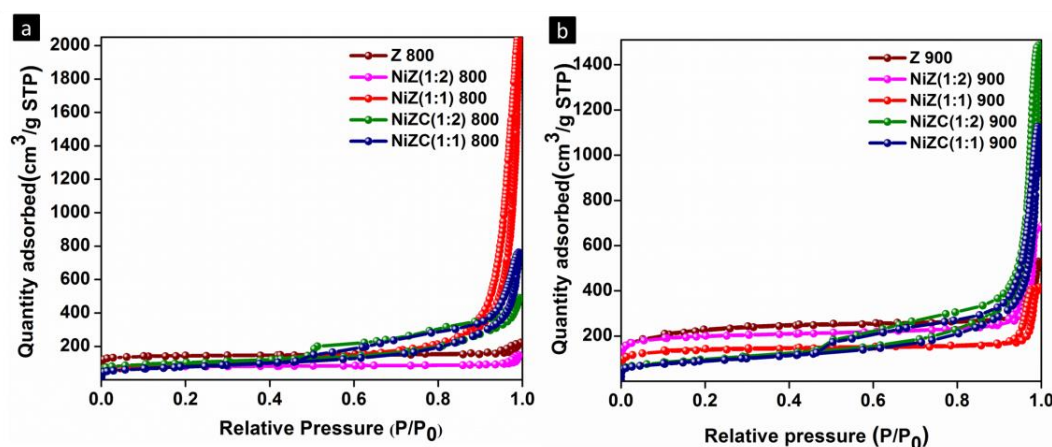
Figure 8. N_2 adsorption-desorption isotherms of carbon samples obtained at a) 800 °C and b) 900 °C
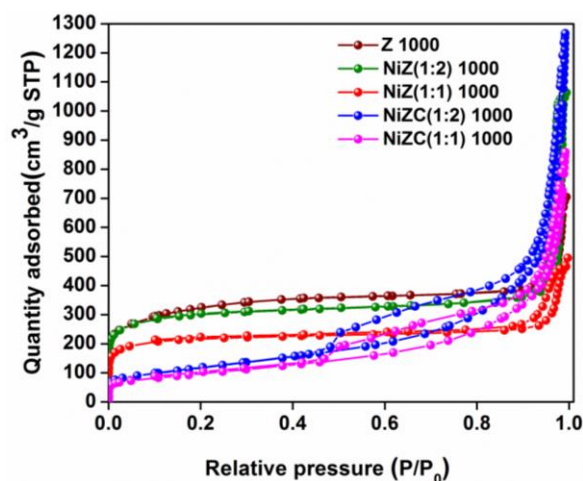
Figure 9. N_2 adsorption-desorption isotherms of carbon samples obtained at 1000 °C

Table 2. Surface areas and pore volumes of samples carbonized at 800 °C, 900 °C and 1000 °C

Sample	After carbonization								
	800 °C			**900 °C**			**1000 °C**		
	S_{BET} (m^2/g)	V_{total} (cm^3/g)	V_{micro} (cm^3/g)	S_{BET} (m^2/g)	V_{total} (cm^3/g)	V_{micro} (cm^3/g)	S_{BET} (m^2/g)	V_{total} (cm^3/g)	V_{micro} (cm^3/g)
Z (ZIF-8)	453	0.35	0.20	751	0.82	0.27	1050	1.08	0.39
NiZ(1:2)	252	0.23	0.11	644	1.06	0.26	933	1.63	0.39
NiZ(1:1)	339	3.2	0.1	449	0.45	0.09	672	0.73	0.28
NiZC(1:2)	338	0.75	0.12	337	2.29	0.1	426	1.93	0.13
NiZC(1:1)	271	1.18	0.08	314	1.74	0.1	349	1.31	0.10

The NLDFT curves were drawn for the carbons derived from ZIF-8, NiZ(1:2), and NiZC(1:2) samples at 1000 °C to understand the pore size distribution. The cavity created by the tetrahedral coordination of Zn^{2+} ions to 2-MeIm led to 3-D frameworks with many channels and open pores in the microporous size range of < 2 nm. As can be seen from the NLDFT curves, the NiZ-derived carbon at 1000 °C exhibited the same amount of microporosity compared to the ZIF-8 derived ones. However, the carbon derived from NiZC samples exhibited a well-defined micro-mesoporous architecture evidencing the ability of the g-C_3N_4 to tune the pore characteristics of the matrix (**Figure 10**). Thus, the templating strategy with g-C_3N_4 resulted in hetero-porous architecture for the carbonized catalyst, which can

facilitate better transport of O_2 molecules across the porous channels in the catalytically active surface, thus enhancing ORR efficiency.
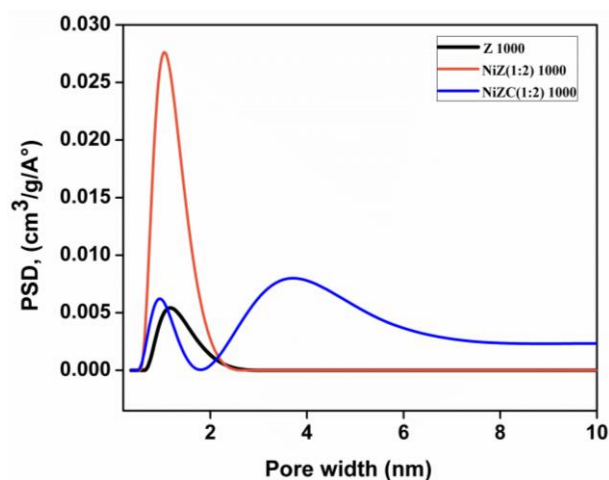
Figure 10. NLDFT pore size distribution curves of the samples carbonized at 1000 °C.

2.3.5. Electrochemical Analysis

The electrocatalytic ORR activity of the samples was investigated by analyzing the cathodic cyclic voltammetry (CV) profiles obtained in N_2/O_2 saturated 0.1 M KOH solution. The CV profiles were initially analyzed in N_2 saturated solution followed by O_2 saturated solution. The CV curves showed a characteristic shift in current at a potential of around 0.80 V compared to that in the N_2 saturated solution indicating the reductive nature of the catalysts in the presence of O_2 (**Figure 11**).
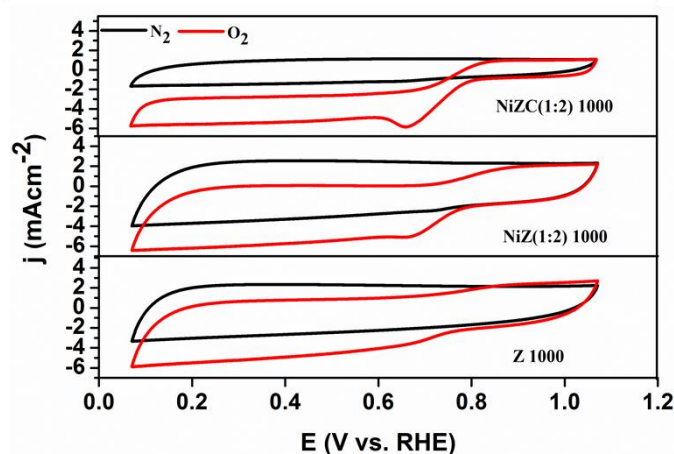
Figure 11. Cyclic voltammograms recorded in N_2 and O_2 saturated 0.1M KOH solution of Z 1000, NiZ(1:2) 1000, and NiZC(1:2) 1000 samples

The ORR activity of the carbon samples was further confirmed by evaluating the linear sweep voltammetry (LSV) curves in 0.1 M KOH solution saturated with O_2 gas at 1600 rpm. To study the influence of the carbonization temperature on the electrocatalytic activity, a comparison of the LSV curves was made for the ZIF-8 derived Z 800, Z 900, and Z 1000 samples. The activity was found to increase from 800 to 1000 °C, and the carbon derived at 1000 °C exhibited the maximum catalytic activity (**Figure 12a**). The activity was then evaluated further on all the samples prepared at the optimized temperature of 1000 °C, and a variation in the order ZT < NiZ(X: Y) T < NiZC(X: Y) T was observed (**Figure 12b**). The sample NiZC(1:2) 1000 exhibited maximum ORR activity, with a limiting current density of 5.2 mA/cm^2 and a half-wave potential of ~0.76 V vs RHE. The current density exceeded over 40% Pt/C catalysts and is higher than other reported nickel-containing carbon materials in the literature (**Table 7**). The sample NiZC(1:2) 1000 exhibited better ORR performance compared to NiZC(1:1) 1000. The high metal content in NiZC(1:1) 1000 may have created the aggregation of particles on the surface, leading to the reduction in the surface area and, thereby, active catalytic surface, as evident from the BET isotherm curves. This subsequently led to a reduction in the electrocatalytic ORR activity.
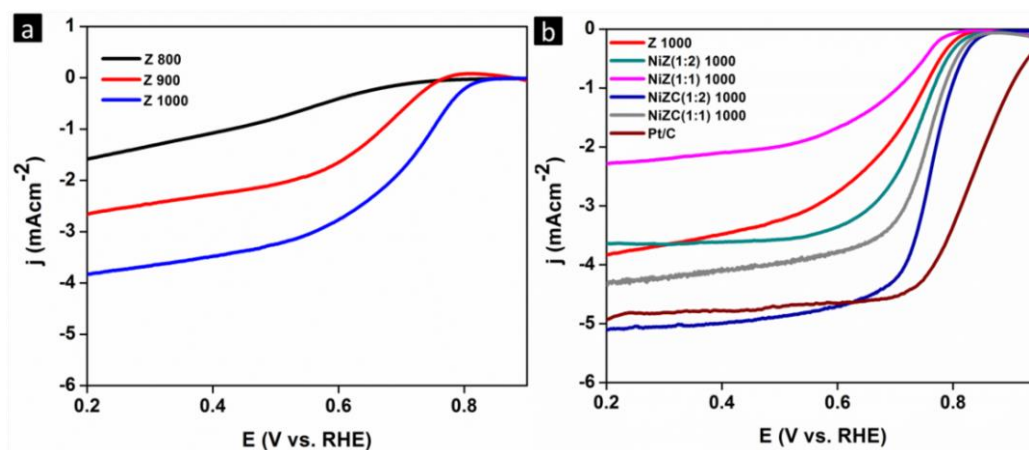
Figure 12. a) LSV curves of ZIF-8 derived carbon samples obtained after carbonization at different temperatures b) Compared LSV curves of carbon samples obtained at 1000 °C with Pt/C in O_2 saturated 0.1 M KOH solution under 1600 rpm.

2.3.6. Morphology and Microstructure Analysis

In order to get further insights into the correlation between the electrocatalytic activity of the samples with their microstructural features, the morphological analysis of the samples

was carried out. The microstructure evaluations of the ZIF-8, NiZ(1:2), and NiZC(1:2) samples were carried out by TEM analysis. **Figure 13a** shows ZIF-8 as dodecahedral particles with an average diameter of around 80 nm. **Figure 13b** shows the NiZ(1:2) particles with similar morphology as that of ZIF-8. Even though the addition of Ni has no influence on particle shape, the size of the particles was found to be reduced ($\approx$ 50 nm) compared to pure ZIF-8 particles. This may be primarily due to the higher number of cationic sites due to the presence of extra Ni^{2+} ions together with the Zn^{2+} ions in the synthesis medium. After the addition of g-C_3N_4, the composites appeared with mixed morphology, as shown in **Figure 13c**, where the dodecahedral particles of Ni incorporated ZIF-8 of 50 nm size were found grown on the sheet-like structures of g-C_3N_4. On high-temperature treatment, the 3-D frameworks composed of the C-N, C-C, and Zn-N linkage were ruptured, leading to Ni, N co-doped porous carbon. As discussed previously, the microporosity mainly arose from the volatilization of Zn from the framework. As can be interpreted from the TEM pictures, the substitution of nickel in the Zn-imidazolate frameworks and the presence of g-C_3N_4 helped in tuning the morphology of the resulting carbon. The samples Z 1000 and NiZ(1:2) 1000 exhibited distorted hexagonal morphology of parent ZIF structures. The decomposition aided by g-C_3N_4 helped in the formation of sheet-like morphology in NiZC(1:2) 1000, as shown in **Figure 13(d-f)**.
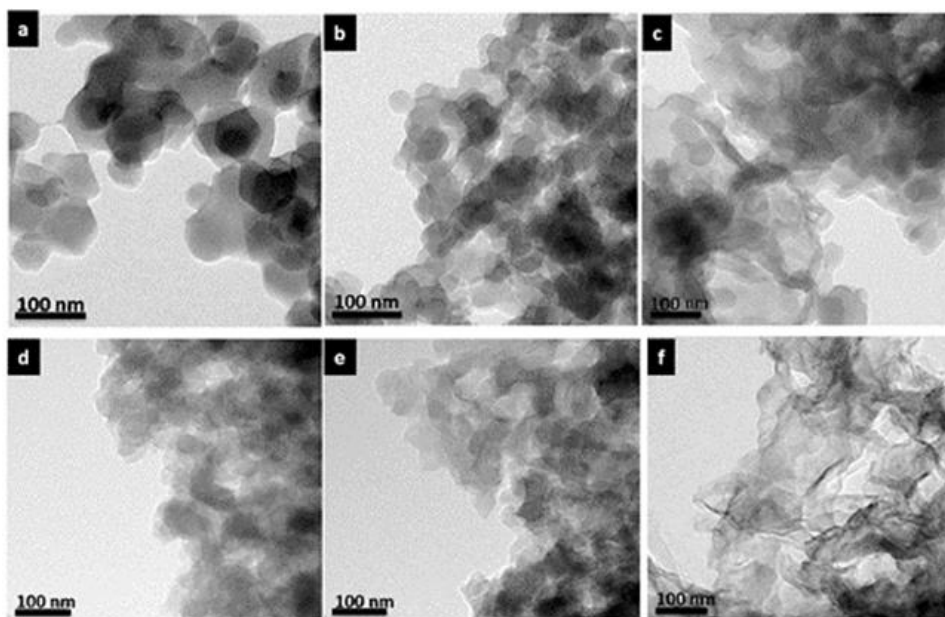
Figure 13. TEM images of a) ZIF-8, b) NiZ(1:2), c) NiZC(1:2), and (d-f) corresponding carbon samples obtained after carbonization at 1000 °C.
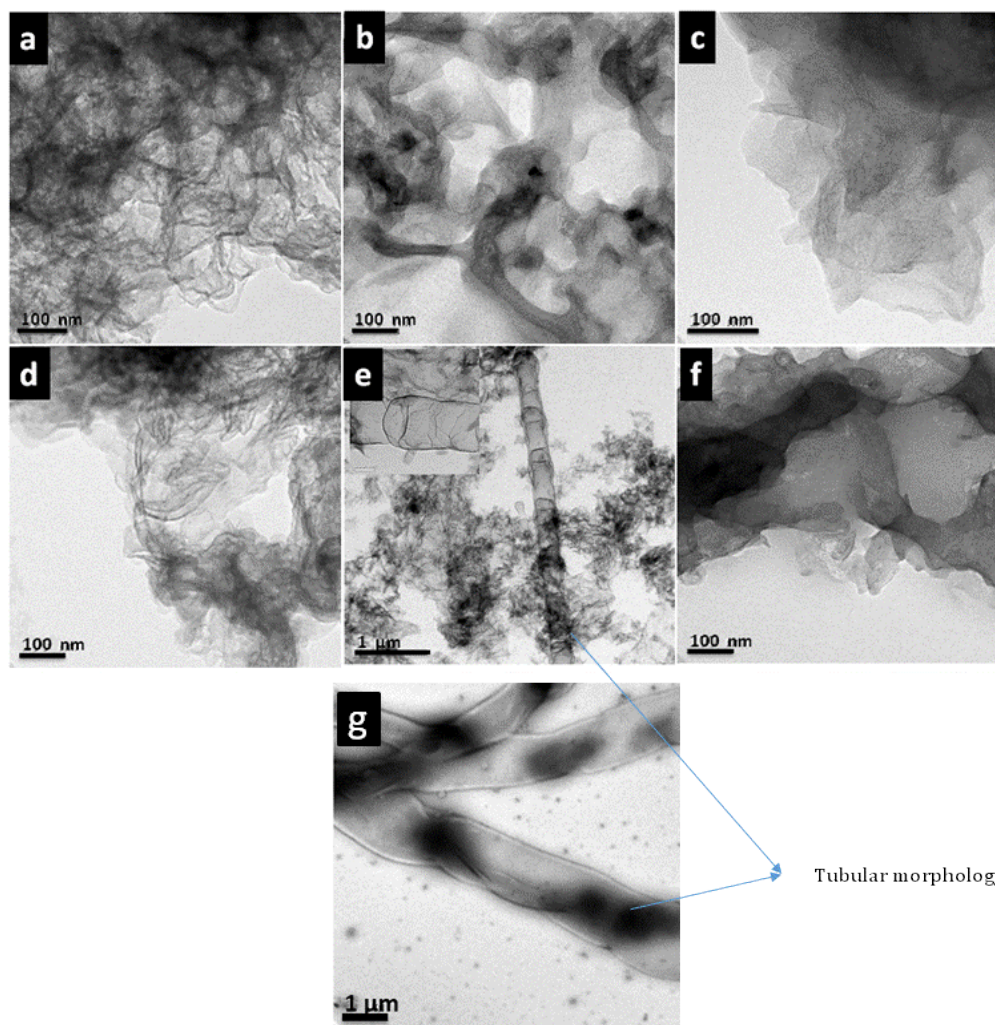
Figure 14. TEM images of ; a) NiZC(1:2) 800, b) NiZC(1:2) 900, c) NiZC(1:2) 1000, d) NiZC(1:1) 800, e) NiZC(1:1) 900 f) NiZC(1:1) 1000 and g) NiZ(1:1) 800 with various morphologies .

Distorted hexagonal structures, tubes, and sheets were formed, influenced by the carbonization temperature, the supporting template, and the molar ratio of nickel ions (**Figure 14**). The incorporation of nickel helped in catalyzing the growth of tube-like morphology, while g-C_3N_4 as a template influenced the formation of sheet-like structures in the derived carbon.

The SEM image of the NiZC(1:2) composite again confirmed the growth of spherical NiZ particles on the sheet-like g-C_3N_4 template (**Figure 15a & 15b**).
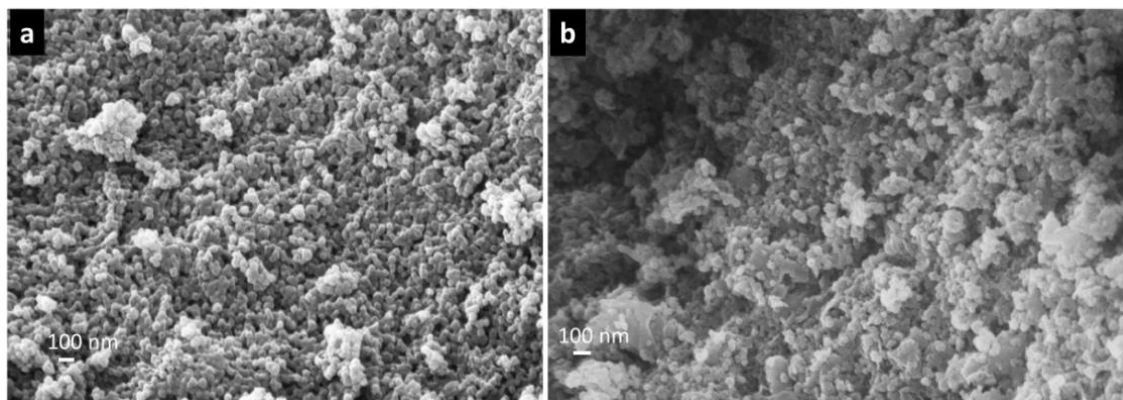
Figure 15. a) SEM images of NiZ(1:2) and b) NiZC(1:2)

The SEM-EDS analysis of the samples detected the presence of C, N, and Ni elements. The distribution ratio of the various elements is summarized in **Table 3**. The presence of nickel, identified in trace amounts (0.01 - 0.3 at. %), indicated that the incorporation of nickel was only minimal. It is to be noted that the competing effect of the Ni^{2+} to form a zeolitic type framework during the room temperature synthesis condition is very limited as Ni^{2+} favours the yellowish brown square planar complexes (**Figure 16**). Since the reaction rate of Zn^{2+} ions with imidazolate ligand is higher, the ZIF-8 structure is formed with only a few metal centres occupied by Ni^{2+} ions. The remaining unreacted Ni^{2+} ion, along with Zn, gets leached away during the washing of the precipitate with excess methanol and water. The surface atomic percentage of the nitrogen content was identified as 32.85% for the NiZ(1:2) and 58.11% for the NiZC(1:2) composites. The excess nitrogen is contributed by the g-C_3N_4 in the composite. The g-C_3N_4 is a polymer formed by tri-s-triazine units of carbon and nitrogen and contains a remarkably higher amount of nitrogen. As a result, the composite of ZIF frameworks with g-C_3N_4 improved the total nitrogen content because of the contribution from both the ZIF and g-C_3N_4 components.

Table 3. Distribution of various elements in samples obtained from SEM-EDS data

Sample name	Elemental distribution (Atomic %)			
	C	**N**	**Ni**	**Zn**
NiZ(1:2)	62.02	32.85	0.04	5.09
NiZC(1:2)	40.63	58.11	0.01	1.25
Z 1000	79.01	20.26	-------	-------
NiZ(1:2) 1000	80.07	19.71	0.22	-------
NiZC(1:2) 1000	71.89	27.90	0.21	-------

Figure 16. Photographs of a) ZIF-8, b) NiZ, c) NiZC, and d) Ni-methyl imidazolate complex powder samples

The SEM-EDS analysis of the carbonized samples shows that the atomic percentage of nitrogen reduced from 20.26 % to 19.71 % for the Z 1000 and NiZ(1:2) 1000 samples. The loss of nitrogen was more evident for NiZ samples, probably due to distortion in the size and topology of ZIF-8 upon incorporation of Ni atoms. The existence of double metallic centres with different atomic radii and the associated electronic characteristics might have caused some distortion in the ZIF frameworks, facilitating easy volatilization of the nitrogen atoms at high temperatures. The atomic percentage of nitrogen was found to increase to 27.9 % in NIZC(1:2) 1000 due to the presence of g-C_3N_4 **(Figure 17)**. As we increased the carbonization temperature from 800 to 1000 °C, the presence of nitrogen was reduced from 48.24% to 27.9% (**Table 4**), indicating severe loss of nitrogen at higher temperatures as volatile N_2 gas.
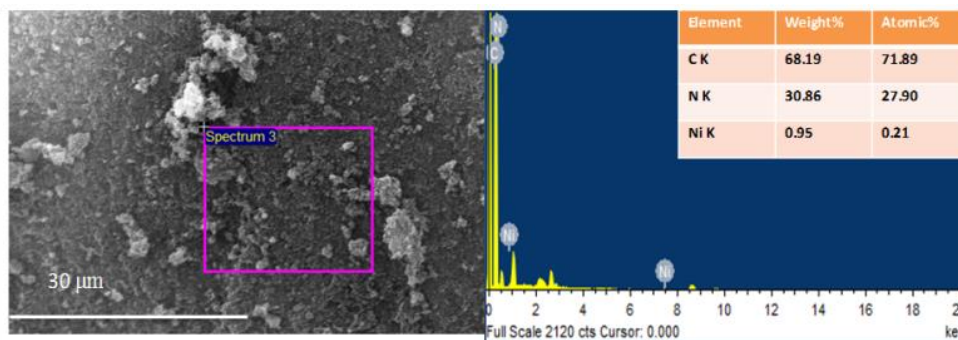
Figure 17. SEM-EDS analysis of NiZC(1:2) 1000 along with elemental composition.

Table 4. Distribution of various elements in NiZC(1:2) T samples obtained from SEM-EDS data

Sample name	Elemental distribution (Atomic %)		
	C	**N**	**Ni**
NiZC(1:2) 800	51.50	48.24	0.26
NiZC(1:2) 900	67.77	31.85	0.38
NiZC(1:2) 1000	71.89	27.90	0.21

The elemental mapping of the sample NiZC(1:2) 1000 further revealed the distribution pattern of C, N, and Ni elements on the porous carbon surfaces (**Figure 18**). The well-dispersed dopants might create active regions for the O_2 adsorption and subsequent reduction reaction.
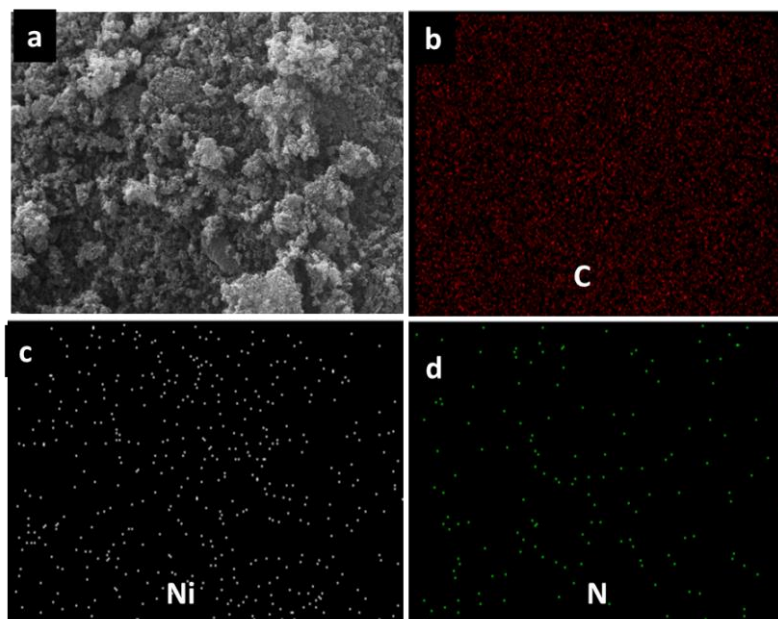
Figure 18. SEM image of NiZC (1:2) 1000 and the corresponding elemental distribution

2.3.7. X-ray photoelectron spectroscopy (XPS) analysis

The presence of elements in the carbonized samples was further confirmed and quantified by XPS analysis. The XPS survey spectrum showed the presence of carbon, nitrogen, and oxygen in Z 1000, NiZ(1:2) 1000, and NiZC(1:2) 1000 samples (**Figure 19**). Due to the insignificant quantity in the carbon matrix, the binding energy peaks corresponding to the nickel species were absent in the survey spectrum. The atomic percentage of C, N, O, and Ni in samples Z 1000, NiZ(1:2) 1000, and NiZC(1:2) 1000 are presented in **Table 5**. Nitrogen content in ZIF-8 derived carbon (Z 1000) was 8 at. % and upon Ni incorporation, the atomic percentage of nitrogen was decreased to 5.9 % in NiZ(1:2) 1000 sample. This nitrogen loss was primarily due to the decomposition of the frameworks induced by the defect formation upon nickel incorporation in the ZIF-8 frameworks.[60] The template-mediated synthesis of porous carbon with g-C_3N_4 resulted in an overall increase of total N content (9.2 at. %), highlighting the contribution of g-C_3N_4 in the composites. At high temperatures, the g-C_3N_4 transformed completely into N-doped carbon along with the ZIF-8 frameworks and compensated for the N loss by providing its own N atoms to the carbon matrix.[61]
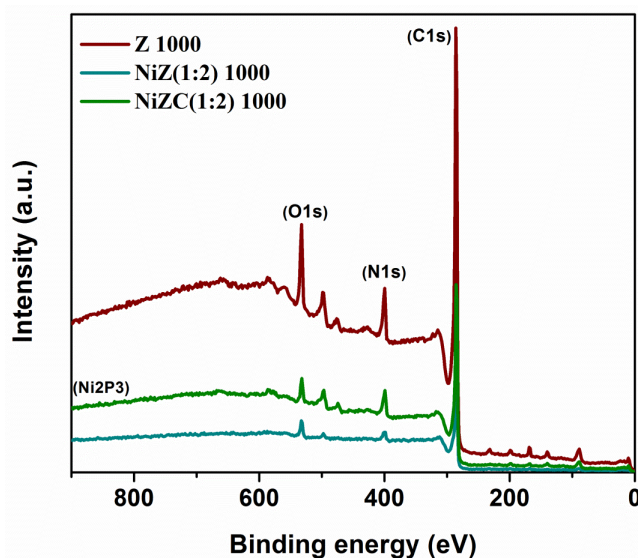
Figure 19. XPS Survey spectra of the samples derived at 1000 °C

Table 5. Distribution of various elements on the carbon samples in atomic % obtained from XPS.

Sample name	Elemental distribution (Atomic %)			
	C	N	O	Ni
Z 1000	85	8	7	------
NiZ(1:2) 1000	87.3	5.9	6.1	0.7
NiZC(1:2) 1000	85.8	9.2	4.7	0.3

The deconvoluted C1s spectrum was particularly resolved into five types of carbon binding. It included a high intense sp^2 graphitic C-C bond of carbon (284.6 eV), C-N (285.2 eV), C-O ($\approx$286.0 eV), and O-C=O (288 eV) bonds (**Figure 20 (a-c)**). A satellite peak corresponding to the π-π* transition in the aromatic carbon rings contributed by the graphitic type of carbon (291.0 eV) indicated the conducting nature of carbon surfaces. In addition to these, the resolved spectra of NiZ(1:2) 1000 and NiZC(1:2) 1000 contained an additional peak at around 283.6 eV arising from the C-Ni bonding and confirmed the incorporation of nickel as nickel carbide in the carbon matrix [62-65] (**Figure 20 b&c**). The modification of the density of states (DOS) of the valence band of the parent nickel atom, caused by the electronic interaction between the nickel and the carbon atom in the nickel carbide [66], can provide suitable binding energy for the O_2 molecule in the medium. Moreover, the higher synergistic effect of transition metal carbide and the sufficient amount of nitrogen distributed in the porous carbon surface could have led to higher affinity for oxygen adsorption, conduction, and reduction in alkaline solution.
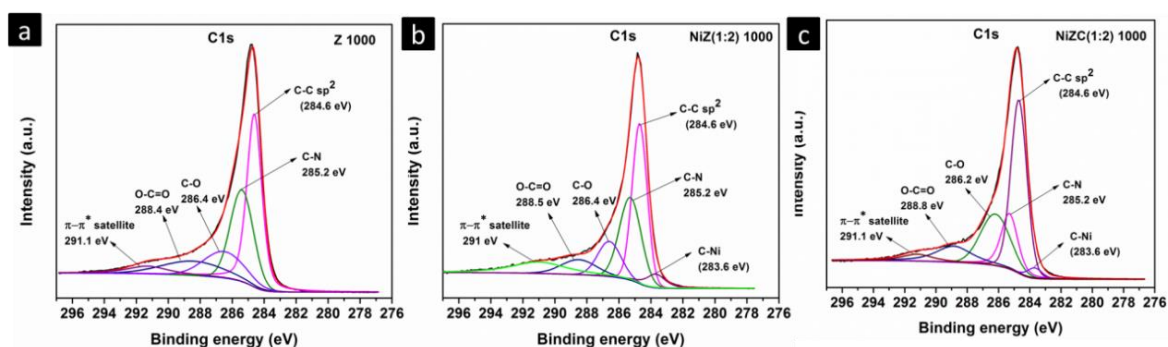
Figure 20. XPS deconvoluted C 1s spectra of a) Z 1000, b) NiZ(1:2) 1000 , and c) NiZC(1:2) 1000

The resolved Ni2p spectra of NiZ (1:2) 1000 and NiZC(1:2) 1000 could be divided into mainly two regions (**Figure 21**). The peaks at the low binding energy region (852-860 eV) indicated the $2p_{3/2}$ states of Ni^{2+}, and the region corresponding to high binding energy (860-875 eV) indicated the $2p_{1/2}$ states of Ni^{2+} confirming the Ni-C binding states. [67] Even though the XPS analysis detected the Ni-C bonded phase in the carbonized materials, the corresponding XRD peaks were absent for the carbonized samples. This is possibly due to the overlapping of high intense (113) peak of Ni_3C, which is present in low amounts with the broad (100) plane of graphitic carbon.
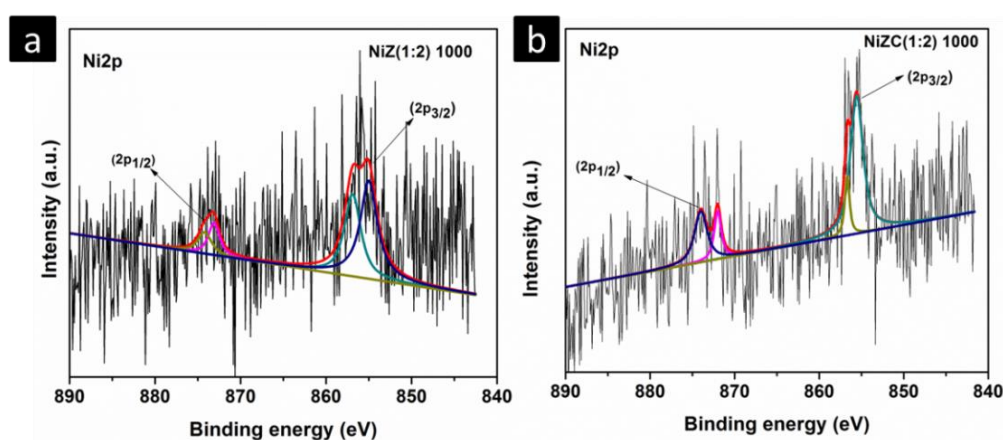
Figure 21. XPS deconvoluted Ni 2p spectra of a) NiZ (1:2) 1000, and b) NiZC(1:2) 1000

The high-resolution spectrum of N1s detected the presence of pyridinic (398.7 eV), pyrrolic (399.9 eV), graphitic (401.2 eV), and surface pyridinic N-O species (402.4 eV) in NiZ(1:2) 1000 and NiZC(1:2) 1000 (**Figure 22**). The presence of pyridinic and graphitic nitrogen can generate an accumulated polarity on the carbon surface and can easily attract other electronegative elements like oxygen, contributing towards a better catalytic effect during the oxygen reduction reaction. The atomic percentage of the different types of N present in the samples is compared (**Figure 23 & Table 6**). The atomic percentages of pyridinic and pyridinic N-O were 4.74 % and 1.45 % for NiZC(1:2) 1000. These pyridinic active sites presumably offer a better ORR kinetic pathway during electrocatalysis.[68]
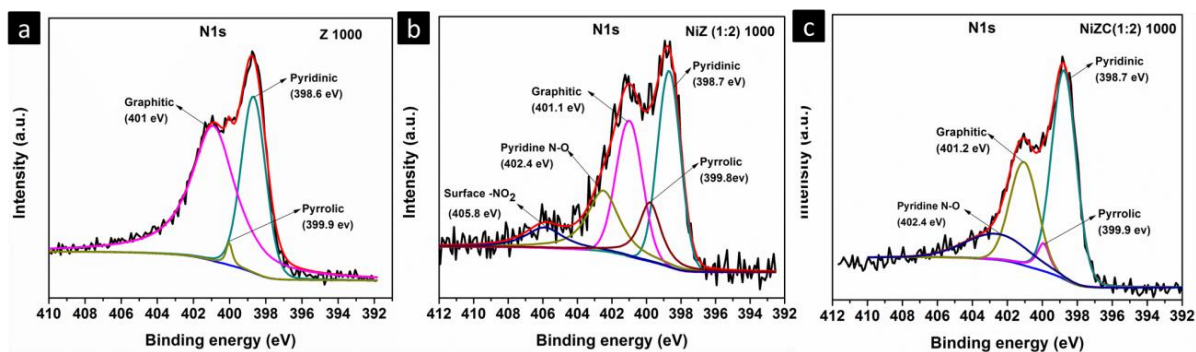
Figure 22. XPS deconvoluted N 1s spectra of a) Z 1000, b) NiZ(1:2) 1000 and c) NiZC(1:2) 1000
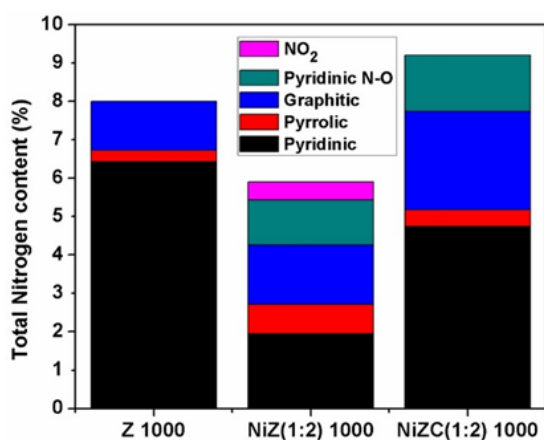
Figure 23. Distribution of various types of nitrogen in the Z 1000, NiZ(1:2) 1000, and NiZC(1:2) 1000 samples.

Table 6. Distribution of various types of nitrogen in Z 1000, NiZ(1:2) 1000 and NiZC(1:2) 1000 samples obtained from XPS deconvoluted spectrum

Sample name	N content (At %)				
	Pyridinic	Pyrrolic	Graphitic	Pyridinic N-O	-NO$_2$
Z 1000	6.431	0.286	1.281	-------	-------
NiZ(1:2) 1000	1.946	0.771	1.546	1.161	0.473
NiZC(1:2) 1000	4.743	0.43	2.571	1.454	------

2.3.8. Raman spectroscopy analysis

In order to get an idea of the extent of graphitization, as well as the defect formation on the electrocatalytic activity, Raman analysis was performed. The two distinct peaks observed around 1350 cm^{-1} and 1580 cm^{-1} corresponded to the defective or diamond-like band (D band) and graphitic band (G band), respectively (**Figure 24**). The D band was generated from the sp^3 bonded states on the graphitic carbon lattice caused by imperfections or defects. The G band at the higher frequency region was due to the vibrations of the sp^2 bonded states of the perfect graphitic plane.[69,70] The calculated I_D/I_G ratios were 1.08, 1.43, and 0.51 for the samples Z 1000, NiZ(1:2) 1000, and NiZC(1:2) 1000, respectively. It is inferred that the carbonization of Ni-incorporated ZIF-8 presumably created more defects due to the incorporation of nickel atoms along with nitrogen in the carbon matrix. While in the case of NiZC(1:2) 1000, the extent of graphitization was increased along with the concurrent defective nature of the heteroatom-doped surfaces. The extra carbon and nitrogen atoms contributed by the g-C$_3$N$_4$ sheets might have helped the formation of the hybridized surface of the graphitic structure with a certain amount of defects. While the defects created adsorption sites for O$_2$, the graphitic structure helped to create an efficient conductive pathway for the electrons during the electrochemical oxygen reduction reaction.
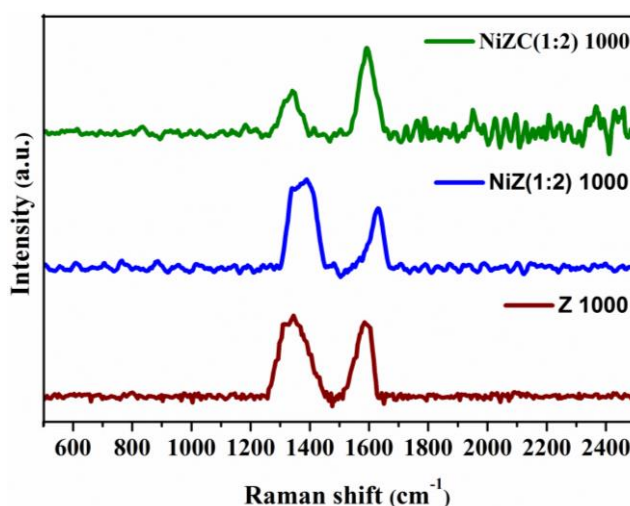
Figure 24. Raman spectra of the samples carbonized at 1000 °C.

2.3.9. Analysis of ORR kinetics

To further look into the electron transfer mechanism during ORR, RDE experiments at different rotation rates were conducted (**Figure 25 (a-c)**). As evident from the figures, with the increase in rotation rate, the number of electrons transferred also increased, contributing to the increase in high current density. The kinetic parameters were investigated by calculations according to the Koutecky-Levich plot (K-L plot) from equations **[1] & [2]**:

$$\frac{1}{J} = \frac{1}{J_K} + \frac{1}{B\omega^{0.5}} ----[1]$$

Where, J is the obtained current density, J_K is the kinetic current density, and ω is the angular rotation rate. The constant B can be calculated from the equation:

$$B = 0.62nF\left(D_{O_2}\right)^{\frac{2}{3}}v^{-\frac{1}{6}}C_{O_2} ---- [2]$$

Where n is the number of transferred electrons during oxygen reduction reaction, F is the Faraday's constant indicating the charge associated with the electron transfer, D_{O_2} is the diffusion coefficient of O_2 gas molecules in 0.1 M KOH solution (1.9×10^{-5} $cm^2 s^{-1}$), v is the kinematic viscosity of the used electrolyte (0.01 $cm^2 s^{-1}$) and C_{O_2} is the concentration of O_2 (1.2×10^{-3} mol L^{-1}).

The K-L plots obtained by plotting 1/J against $\omega^{-1/2}$ drawn for Z 1000, NiZ(1:2) 1000, and NiZC(1:2) 1000 at 0.6 V (**Figure 25d**), showed an increase in electron transfer number in the order NiZC(1:2) 1000> NiZ(1:2) 1000> Z 1000.
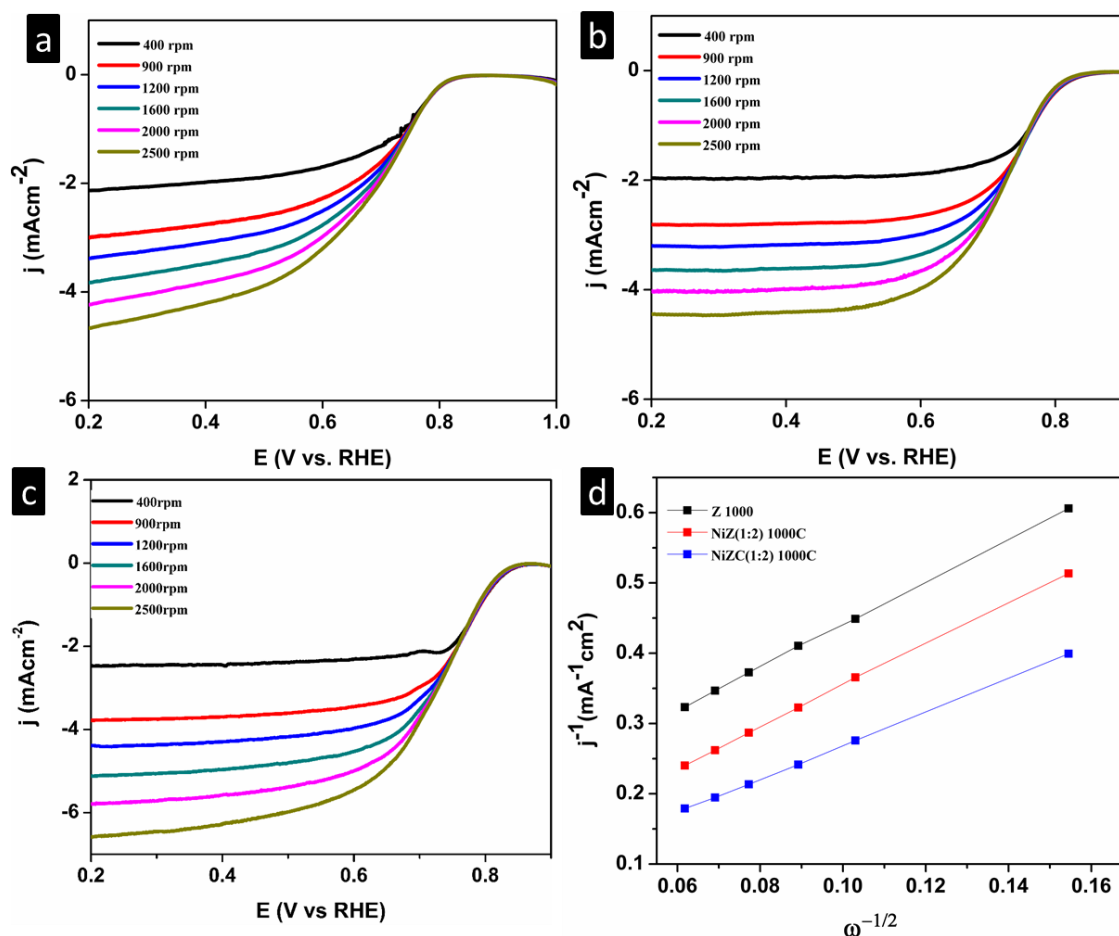
Figure 25. a) LSV curves of a) Z 1000, b) NiZ(1:2) 1000, and c) NiZC(1:2) 1000 under different rotation rates, and d) K-L plots of samples at 0.6 V in O_2 saturated 0.1 M KOH solution

The RRDE experiments were conducted to analyze the intermediate product H_2O_2 produced due to the partial 2 e⁻ mechanism. The average amount of H_2O_2 produced during the electrochemical oxygen reduction was around 26%, 16%, and 13% for the Z 1000, NiZ(1:2) 1000, and NiZC(1:2) 1000 samples, respectively (**Figure 26 a**). The corresponding number of electron transfer was found to be around 3.5-3.6 for Z 1000, 3.6-3.7 for NiZ(1:2) 1000, and increased to 3.8 for NiZC(1:2) 1000 (**Figure 26 b**), which confirmed that the incorporation of nickel ion as well as g-C_3N_4 into the supporting matrix have favourably contributed for the easy transport of the O_2 molecule as well as the efficient electron transport mechanism on the porous carbons derived at high temperature, thereby increasing the overall ORR activity.
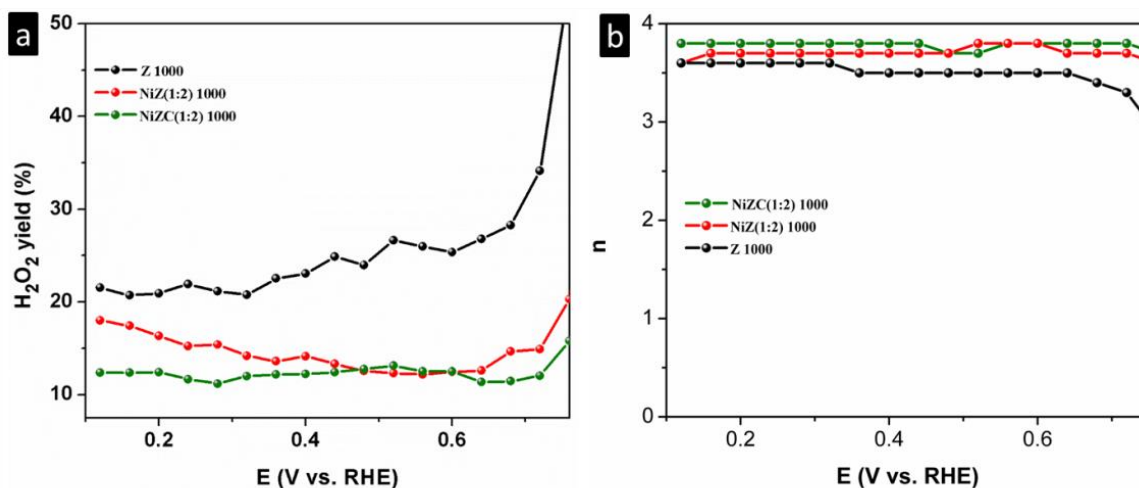
Figure 26. % H_2O_2 yield and d) number of f electron transferred for Z 1000, NiZ(1:2), and NiZC(1:2) 1000 from the RRDE experiment in 0.1 M KOH.

In addition to the high ORR activity, the stability and methanol tolerance of the catalysts are also important parameters that decide the applicability of the catalysts. In order to understand the sensitivity of the electrocatalyst in the presence of methanol, the chronoamperometry test was carried out for the best-performing electrocatalyst and was compared to the commercial Pt/C catalyst. The chronoamperometry test was carried out in O_2 saturated 0.1 M KOH solution under a rotation rate of 1600 rpm for 1800 s under an applied potential of 0.60 V. 3 M MeOH solution was added into the above O_2 saturated KOH solution at the time period of 300 s, and the variation in current was measured. As can be observed in **Figure 27**, the NiZC(1:2) 1000 sample was almost insensitive to the addition of methanol. On the other hand, the current density of the Pt/C has shown a sharp decline as a response to methanol addition revealing its sensitivity to methanol. This ensures better stability of the prepared catalyst material in an alkaline medium towards methanol tolerance.
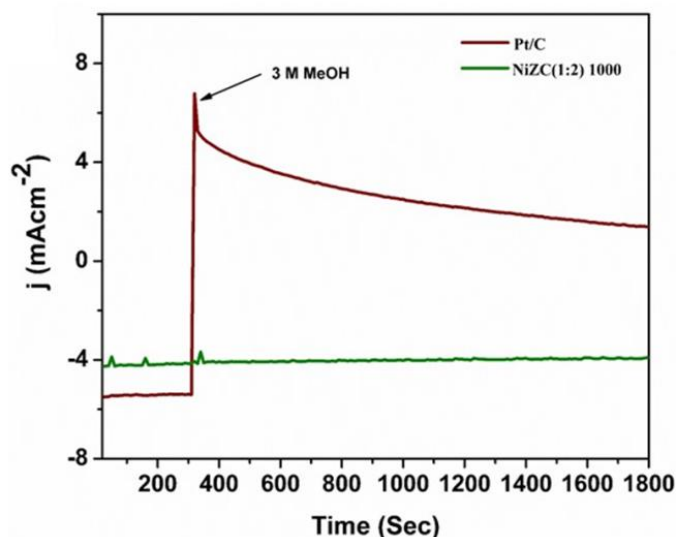
Figure 27. Methanol tolerance curves of NiZC(1:2) and Pt/C

The stability of the best catalyst was investigated further by accelerated durability test (ADT) in 0.1 M KOH electrolyte solution by performing CV at a scan rate of 100 mV s^{-1}. The measurement was done under a rotation rate of 1600 rpm, and the recorded LSV was compared before and after 5000 cycles of the ADT test. After 5000 cycles, the catalyst exhibited 96% retention in limiting current. The half-wave potential of the NiZC(1:2) 1000 samples underwent a negative shift of 14 mV while that of Pt/C was found to be 30 mV, further confirming the better stability of the prepared catalyst materials relative to that of Pt/C (**Figure 28**).
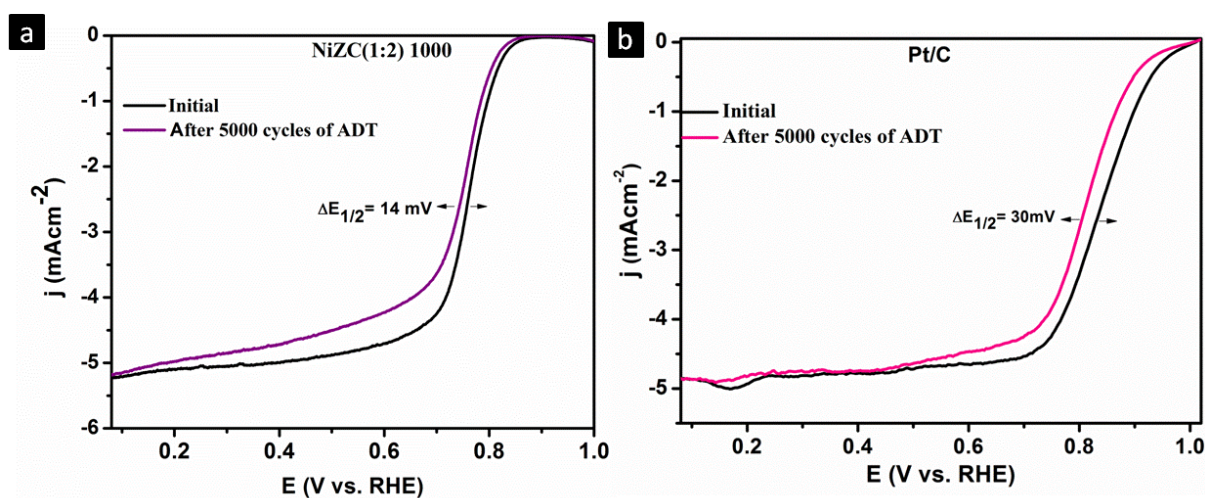
Figure 28. Durability curves of a) NiZC(1:2) and b) commercial Pt/C.

Table 7. Comparison of ORR performance of Ni incorporated catalysts in 0.1 M KOH with recent literature

Sample name	Onset	Half wave	Current density (mA cm^{-2})	Electron transfer number	reference
Ni@N-CNCs	0.04 V (vs. Ag/AgCl)	-0.19 V(Vs Ag/AgCl)	-4.8	4.0	[71]
Ni$_3$(HITP)$_2$ framework	0.82 V (vs. RHE)	---------	−2.5	--------	[72]
NCNTs/E-NNPs	0.96 V (vs. RHE)	0.86 V (vs. RHE)	-3.8	3.7	[73]
Ni-NC700	0.86 V (vs. RHE	0.75 V (vs. RHE)	-2.2	------	[27]
Ni/ rGO	0.80 V (vs. RHE)	O.60 V (vs. RHE)	-4.6	≈2.8	[74]
Ni-GT-750-A	0.89 V (vs. RHE)	------	-3.90	---------	[28]
NiZC(1:2) 1000	0.86 V (vs. RHE)	0.76 V (vs. RHE)	-5.2	3.8	[Present work]

Thus, it has been observed that the template-assisted synthesis of heteroatom-doped porous carbon from Ni-incorporated ZIF-8 frameworks has resulted in Ni, N co-doped hetero-porous carbon with Ni-C active centers with appreciable ORR performance in an alkaline medium. The defective sites created by the incorporated heteroatoms were beneficial for creating adsorption sites for the O$_2$ molecule, thus initiating the ORR mechanism. The modulation in the surface electronic properties facilitated by the combined synergistic effect of Ni-C along with the N atom on the porous carbon surface could have contributed to the high ORR activity. The catalysts exhibited maximum ORR at the optimum nickel concentration of the sample NiZC(1:2) at the higher carbonization temperature of 1000 °C. Furthermore, the template-assisted synthetic strategy using g-C$_3$N$_4$ aided in the

easy decomposition of the ZIF-8 framework and the formation of hetero-porous sheet-like architectures with well-dispersed nitrogen content. The fugitive template also helped to compensate for the severe nitrogen loss upon high-temperature carbonization of ZIF-8 by completely transforming into N-doped carbon together with the parent ZIF framework. The chemical, morphological and structural changes induced in the newly designed catalyst derived at 1000 °C enabled easier diffusion and conduction of O_2 molecules through the catalyst surfaces, thus providing excellent ORR performance with higher current density.

2.4. Conclusions

In summary, we have successfully synthesized Ni, N co-doped porous carbon by the high-temperature decomposition of g-C_3N_4 templated Ni-doped ZIF-8 precursors. By varying the Ni/Zn molar ratio and the carbonization temperature, we were able to get heteroatom-doped porous carbon with various architectures and pore characteristics. The nickel ion contributed towards the creation of defective sites through the formation of nickel carbide, and the presence of g-C_3N_4 in the composite enabled the formation of micro-mesoporous architectures with high nitrogen content and surface area. Incorporating the guest metal atom Ni and the sacrificial template of g-C_3N_4 has contributed to the evolution of carbon surfaces of varying morphology with an increase in electrocatalytic activity for ORR in alkaline medium. The sample NiZC(1:2) 1000 exhibited higher electrocatalytic activity than other samples with a limiting current density of 5.2 mAcm^{-2} and a half-wave potential of 0.76 V Vs RHE. The sample also exhibited higher durability and methanol tolerance in the alkaline medium compared to commercial Pt/C electrocatalyst. The hetero-porous carbon electrocatalysts thus developed can contribute towards the development of economically viable fuel cells.

2.5.   References

1. P.P. Edwards, V.L. Kuznetsov, W.I.F. David, N.P. Brandon, Hydrogen and fuel cells: Towards a sustainable energy future, Energy Policy 36(12) (2008) 4356-4362. https://doi.org/https://doi.org/10.1016/j.enpol.2008.09.036.

2. M. Momirlan, T.N. Veziroglu, The properties of hydrogen as fuel tomorrow in sustainable energy system for a cleaner planet, International Journal of Hydrogen Energy 30(7) (2005) 795-802. https://doi.org/https://doi.org/10.1016/j.ijhydene.2004.10.011.

3. M.S. Dresselhaus, I.L. Thomas, Alternative energy technologies, Nature 414(6861) (2001) 332-337. https://doi.org/10.1038/35104599.

4. S.M.J.A.M. Haile, Fuel cell materials and components, 51 (2003) 5981-6000.

5. A.A. Gewirth, M.S. Thorum, Electroreduction of Dioxygen for Fuel-Cell Applications: Materials and Challenges, Inorganic Chemistry 49(8) (2010) 3557-3566. https://doi.org/10.1021/ic9022486.

6. M.K. Debe, Electrocatalyst approaches and challenges for automotive fuel cells, Nature 486(7401) (2012) 43-51. https://doi.org/10.1038/nature11115.

7. Y. Sun, M. Delucchi, J. Ogden, The impact of widespread deployment of fuel cell vehicles on platinum demand and price, International Journal of Hydrogen Energy 36(17) (2011) 11116-11127. https://doi.org/https://doi.org/10.1016/j.ijhydene.2011.05.157.

8. C. Sealy, The problem with platinum, Materials Today 11(12) (2008) 65-68. https://doi.org/https://doi.org/10.1016/S1369-7021(08)70254-2.

9. P. Gouérec, L. Poletto, J. Denizot, E. Sanchez-Cortezon, J.H. Miners, The evolution of the performance of alkaline fuel cells with circulating electrolyte, Journal of Power Sources 129(2) (2004) 193-204. https://doi.org/10.1016/j.jpowsour.2003.11.032.

10. J.R. Varcoe, R.C.T. Slade, Prospects for Alkaline Anion-Exchange Membranes in Low Temperature Fuel Cells, 5(2) (2005) 187-200. doi.org/10.1002/fuce.200400045.

11. S. Mekhilef, R. Saidur, A. Safari, Comparative study of different fuel cell technologies, Renewable and Sustainable Energy Reviews 16(1) (2012) 981-989. https://doi.org/https://doi.org/10.1016/j.rser.2011.09.020.

12. M. Zhang, L. Dai, Carbon nanomaterials as metal-free catalysts in next generation fuel cells, Nano Energy 1(4) (2012) 514-517. doi.org/10.1016/j.nanoen.2012.02.008.

13. H.-W. Liang, W. Wei, Z.-S. Wu, X. Feng, K. Müllen, Mesoporous Metal–Nitrogen-Doped Carbon Electrocatalysts for Highly Efficient Oxygen Reduction Reaction, Journal of the American Chemical Society 135(43) (2013) 16002-16005. https://doi.org/10.1021/ja407552k.

14. A. Morozan, B. Jousselme, S. Palacin, Low-platinum and platinum-free catalysts for the oxygen reduction reaction at fuel cell cathodes, Energy & Environmental Science 4(4) (2011) 1238-1254. https://doi.org/10.1039/C0EE00601G.

15. J. Alom, M.S. Hasan, M. Asaduzaman, M.T. Alam, D. Belhaj, R. Selvaraj, M.A. Hossain, M. Zargar, M.B. Ahmed, Catalytical Performance of Heteroatom Doped and Undoped Carbon-Based Materials, 13(5) (2023) 823. doi.org/10.3390/catal13050823

16. R. Paul, Q. Zhai, A.K. Roy, L. Dai, Charge transfer of carbon nanomaterials for efficient metal-free electrocatalysis, 1(1) (2022) 28-50. doi.org/10.1002/idm2.12010.

17. R. Gutru, Z. Turtayeva, F. Xu, G. Maranzana, R. Thimmappa, M. Mamlouk, A. Desforges, B. Vigolo, Recent progress in heteroatom doped carbon based electrocatalysts for oxygen reduction reaction in anion exchange membrane fuel cells, International Journal of Hydrogen Energy 48(9) (2023) 3593-3631. https://doi.org/https://doi.org/10.1016/j.ijhydene.2022.10.177.

18. X. Feng, Y. Bai, M. Liu, Y. Li, H. Yang, X. Wang, C. Wu, Untangling the respective effects of heteroatom-doped carbon materials in batteries, supercapacitors and the ORR to design high performance materials, Energy & Environmental Science 14(4) (2021) 2036-2089. https://doi.org/10.1039/D1EE00166C.

19. A. Parkash, N. Solangi, T.H. Seehar, G. Zhang, M. Akram, S. Ali, Review—Heteroatom-Doped High Porous Carbon Metal Free Nanomaterials for Energy

Storage and Conversion, ECS Journal of Solid State Science and Technology 11(9) (2022) 091006. https://doi.org/10.1149/2162-8777/ac8dbe.

20. J. Ma, H. Liu, Z. Tao, J. Liu, B. Yuan, W. Pan, Z. Shi, The activity of Fe/Co/Ni multi-metal doped electrocatalysts for oxygen reduction reaction, Journal of Materials Research 38(9) (2023) 2359-2368. doi.org/10.1557/s43578-023-00944-8.

21. J. Quílez-Bermejo, E. Morallón, D. Cazorla-Amorós, Metal-free heteroatom-doped carbon-based catalysts for ORR: A critical assessment about the role of heteroatoms, Carbon 165 (2020) 434-454.doi.org/10.1016/j.carbon.2020.04.068.

22. V. Duraisamy, S.M. Senthil Kumar, N and P dual heteroatom doped mesoporous hollow carbon as an efficient oxygen reduction reaction catalyst in alkaline electrolyte, International Journal of Hydrogen Energy 47(41) (2022) 17992-18006. https://doi.org/https://doi.org/10.1016/j.ijhydene.2022.03.284.

23. H.C. Pandhurnekar, C.P. Pandhurnekar, N. Sharma, Recent advances in the energy harvesting device technology using hetero-atom doped carbon nanotubes, Materials Today: Proceedings 73 (2023) 41-49. doi.org/10.1016/j.matpr.2022.09.081.

24. B. Li, L. Zhang, J. Zhang, Y. Su, Recent Insight in Transition Metal Anchored on Nitrogen-Doped Carbon Catalysts: Preparation and Catalysis Application, 3(3) (2022) 520-537.

25. F. Dong, M. Wu, Z. Chen, X. Liu, G. Zhang, J. Qiao, S. Sun, Atomically Dispersed Transition Metal-Nitrogen-Carbon Bifunctional Oxygen Electrocatalysts for Zinc-Air Batteries: Recent Advances and Future Perspectives, Nano-Micro Letters 14(1) (2021) 36. https://doi.org/10.1007/s40820-021-00768-3.

26. V. Vij, S. Sultan, A.M. Harzandi, A. Meena, J.N. Tiwari, W.-G. Lee, T. Yoon, K.S. Kim, Nickel-Based Electrocatalysts for Energy-Related Applications: Oxygen Reduction, Oxygen Evolution, and Hydrogen Evolution Reactions, ACS Catalysis 7(10) (2017) 7196-7225. https://doi.org/10.1021/acscatal.7b01800.

27. B. Devi, R.R. Koner, A. Halder, Ni(II)-Dimeric Complex-Derived Nitrogen-Doped Graphitized Carbon-Encapsulated Nickel Nanoparticles: Efficient Trifunctional Electrocatalyst for Oxygen Reduction Reaction, Oxygen Evolution Reaction, and

Hydrogen Evolution Reaction, ACS Sustainable Chemistry & Engineering 7(2) (2019) 2187-2199. https://doi.org/10.1021/acssuschemeng.8b04883.

28. A. Tyagi, K.K. Kar, H. Yokoi, Atomically dispersed Ni/NixSy anchored on doped mesoporous networked carbon framework: Boosting the ORR performance in alkaline and acidic media, Journal of Colloid and Interface Science 571 (2020) 285-296. https://doi.org/https://doi.org/10.1016/j.jcis.2020.03.043.

29. C. Yang, X. Ma, J. Zhou, Y. Zhao, X. Xiang, H. Shang, B. Zhang, Recent advances in metal-organic frameworks-derived carbon-based electrocatalysts for the oxygen reduction reaction, International Journal of Hydrogen Energy 47(51) (2022) 21634-21661. https://doi.org/https://doi.org/10.1016/j.ijhydene.2022.05.025.

30. F. Zhan, S. Liu, Q. He, X. Zhao, H. Wang, M. Han, Y. Yamauchi, L. Chen, Metal–organic framework-derived heteroatom-doped nanoarchitectures for electrochemical energy storage: Recent advances and future perspectives, Energy Storage Materials 52 (2022) 685-735. https://doi.org/10.1016/j.ensm.2022.08.035.

31. K. Dhanabalan, M. Perumalsamy, G. Sriram, N. Murugan, Shalu, T. Sadhasivam, T.H. Oh, Metal–Organic Framework (MOF)-Derived Catalyst for Oxygen Reduction Reaction (ORR) Applications in Fuel Cell Systems: A Review of Current Advancements and Perspectives, 16(13) (2023) 4950. doi.org/10.3390/en16134950

32. H. Hayashi, A.P. Côté, H. Furukawa, M. O'Keeffe, O.M. Yaghi, Zeolite A imidazolate frameworks, Nature Materials 6(7) (2007) 501-506. https://doi.org/10.1038/nmat1927.

33. R. Banerjee, A. Phan, B. Wang, C. Knobler, H. Furukawa, M. O'Keeffe, O.M. Yaghi, High-throughput synthesis of zeolitic imidazolate frameworks and application to CO2 capture, Science (New York, N.Y.) 319(5865) (2008) 939-43. https://doi.org/10.1126/science.1152516.

34. K. Li, D.H. Olson, J. Seidel, T.J. Emge, H. Gong, H. Zeng, J. Li, Zeolitic Imidazolate Frameworks for Kinetic Separation of Propane and Propene, Journal of the American Chemical Society 131(30) (2009) 10368-10369. doi.org/10.1021/ja9039983.

35. X.C. Huang, Y.Y. Lin, J.P. Zhang, X.M. Chen, Ligand-directed strategy for zeolite-type metal-organic frameworks: zinc(II) imidazolates with unusual zeolitic topologies, Angewandte Chemie (International ed. in English) 45(10) (2006) 1557-9. https://doi.org/10.1002/anie.200503778.

36. C. Gao, S. Mu, R. Yan, F. Chen, T. Ma, S. Cao, S. Li, L. Ma, Y. Wang, C. Cheng, Recent Advances in ZIF-Derived Atomic Metal–N–C Electrocatalysts for Oxygen Reduction Reaction: Synthetic Strategies, Active Centers, and Stabilities, 18(14) (2022) 2105409. https://doi.org/https://doi.org/10.1002/smll.202105409.

37. Y. Song, C. Yu, D. Ma, K. Liu, Recent progress on ZIF-8 based MOF derivatives for electrocatalysis, Coordination Chemistry Reviews 499 (2024) 215492. https://doi.org/https://doi.org/10.1016/j.ccr.2023.215492.

38. X. Li, H. Liang, X. Liu, Y. Zhang, Z. Liu, H. Fan, Zeolite Imidazolate Frameworks (ZIFs) Derived Nanomaterials and their Hybrids for Advanced Secondary Batteries and Electrocatalysis, 22(10) (2022) e202200105. https://doi.org/https://doi.org/10.1002/tcr.202200105.

39. C. Fan, Q. Yin, Y. Yuan, J. Yu, Q. Sun, Y. Chen, L. Yu, L. Dong, ZnCo-ZIF-based nanoarchitectonics of honeycomblike N-doped carbon for oxygen reduction reaction and supercapacitor, Diamond and Related Materials 136 (2023) 109997. https://doi.org/https://doi.org/10.1016/j.diamond.2023.109997.

40. J. Zhang, Z. Deng, S. Bai, C. Liu, M. Zhang, C. Peng, X. Xu, J. Jia, T. Luan, Fe, N, S co-doped carbon network derived from acetate-modified Fe-ZIF-8 for oxygen reduction reaction, Journal of Colloid and Interface Science 658 (2024) 373-382. https://doi.org/https://doi.org/10.1016/j.jcis.2023.12.047.

41. J. Zhou, C. Yang, R. Cui, D. Wang, Y. Zhao, X. Xiang, X. Pang, B. Zhang, H. Shang, Molten salt synthesis of ZIF derived CoFe alloy embedded in 2D ultrathin N-doped porous carbon nanosheets for efficient alkaline media oxygen electrocatalysis, Journal of Alloys and Compounds 939 (2023) 168792. doi.org/10.1016/j.jallcom.2023.168792.

42. K. Li, Y. Zhang, P. Wang, X. Long, L. Zheng, G. Liu, X. He, J. Qiu, Core-Shell ZIF-67@ZIF-8-derived multi-dimensional cobalt-nitrogen doped hierarchical carbon

nanomaterial for efficient oxygen reduction reaction, Journal of Alloys and Compounds 903 (2022) 163701. https://doi.org/10.1016/j.jallcom.2022.163701.

43. L. Wang, J. Liu, C. Tian, W. Zhao, P. Li, W. Liu, L. Song, Y. Liu, C.-A. Wang, Z. Xie, MOF-Derived CoNi Nanoalloy Particles Encapsulated in Nitrogen-Doped Carbon as Superdurable Bifunctional Oxygen Electrocatalyst, 13(4) (2023) 715.

44. S. Gadipelli, Z. Li, T. Zhao, Y. Yang, T. Yildirim, Z. Guo, Graphitic nanostructures in a porous carbon framework significantly enhance electrocatalytic oxygen evolution, Journal of Materials Chemistry A 5(47) (2017) 24686-24694. https://doi.org/10.1039/C7TA03027D.

45. H.-x. Zhong, J. Wang, Y.-w. Zhang, W.-l. Xu, W. Xing, D. Xu, Y.-f. Zhang, X.-b. Zhang, ZIF-8 Derived Graphene-Based Nitrogen-Doped Porous Carbon Sheets as Highly Efficient and Durable Oxygen Reduction Electrocatalysts, 53(51) (2014) 14235-14239. https://doi.org/https://doi.org/10.1002/anie.201408990.

46. J. Mao, P. Liu, J. Li, D. Liang, J. Yan, W. Song, Proliferating Oxygen Reduction Reaction by High Volume of Mesopores in Regular Nickel–Nitrogen Codoped Carbon Nanocubes, 6(20) (2019) 1901186. https://doi.org/10.1002/admi.201901186.

47. M. Thomas, R. Illathvalappil, S. Kurungot, B.N. Nair, A.A. Mohamed, G.M. Anilkumar, T. Yamaguchi, U.S. Hareesh, Graphene Oxide Sheathed ZIF-8 Microcrystals: Engineered Precursors of Nitrogen-Doped Porous Carbon for Efficient Oxygen Reduction Reaction (ORR) Electrocatalysis, ACS Appl Mater Interfaces 8(43) (2016) 29373-29382. https://doi.org/10.1021/acsami.6b06979.

48. G. Jia, W. Zhang, G. Fan, Z. Li, D. Fu, W. Hao, C. Yuan, Z. Zou, Three-Dimensional Hierarchical Architectures Derived from Surface-Mounted Metal–Organic Framework Membranes for Enhanced Electrocatalysis, 56(44) (2017) 13781-13785. https://doi.org/https://doi.org/10.1002/anie.201708385.

49. P. Zhang, F. Sun, Z. Xiang, Z. Shen, J. Yun, D. Cao, ZIF-derived in situ nitrogen-doped porous carbons as efficient metal-free electrocatalysts for oxygen reduction reaction, Energy & Environmental Science 7(1) (2014) 442-450. doi.org/10.1039/C3EE42799D.

50. R. Wang, T. Yan, L. Han, G. Chen, H. Li, J. Zhang, L. Shi, D. Zhang, Tuning the dimensions and structures of nitrogen-doped carbon nanomaterials derived from sacrificial g-C3N4/metal–organic frameworks for enhanced electrocatalytic oxygen reduction, Journal of Materials Chemistry A 6(14) (2018) 5752-5761. https://doi.org/10.1039/C8TA00439K.

51. J. Liu, T. Zhang, Z. Wang, G. Dawson, W. Chen, Simple pyrolysis of urea into graphitic carbon nitride with recyclable adsorption and photocatalytic activity, Journal of Materials Chemistry 21(38) (2011) 14398-14401. https://doi.org/10.1039/C1JM12620B.

52. X.X. Wang, D.A. Cullen, Y.-T. Pan, S. Hwang, M. Wang, Z. Feng, J. Wang, M.H. Engelhard, H. Zhang, Y. He, Y. Shao, D. Su, K.L. More, J.S. Spendelow, G. Wu, G. Wu, Nitrogen-Coordinated Single Cobalt Atom Catalysts for Oxygen Reduction in Proton Exchange Membrane Fuel Cells, Advanced materials (Deerfield Beach, Fla.) 30(11) (2018). https://doi.org/10.1002/adma.201706758.

53. A.F. Gross, E. Sherman, J.J. Vajo, Aqueous room temperature synthesis of cobalt and zinc sodalite zeolitic imidizolate frameworks, Dalton Transactions 41(18) (2012) 5458-5460. https://doi.org/10.1039/C2DT30174A.

54. W.J. Eilbeck, F. Holmes, C.E. Taylor, A.E. Underhill, Cobalt(II), nickel(II), and copper(II) complexes of 2-methylimidazole, Journal of the Chemical Society A: Inorganic, Physical, Theoretical (0) (1968) 128-132. doi.org/10.1039/J19680000128.

55. C. Hu, Y.-C. Chu, Y.-R. Lin, H.-C. Yang, K.-H. Wang, Photocatalytic Dye and Cr(VI) Degradation Using a Metal-Free Polymeric g-C3N4 Synthesized from Solvent-Treated Urea, 11(1) (2019) 182.

56. A. Chakrabarti, J. Lu, J.C. Skrabutenas, T. Xu, Z. Xiao, J.A. Maguire, N.S. Hosmane, Conversion of carbon dioxide to few-layer graphene, Journal of Materials Chemistry 21(26) (2011) 9491-9493. https://doi.org/10.1039/C1JM11227A.

57. N. Bao, X. Hu, Q. Zhang, X. Miao, X. Jie, S. Zhou, Synthesis of porous carbon-doped g-C3N4 nanosheets with enhanced visible-light photocatalytic activity, Applied Surface Science 403 (2017) 682-690. https://doi.org/10.1016/j.apsusc.2017.01.256.

58. J.L.C. Rowsell, E.C. Spencer, J. Eckert, J.A.K. Howard, O.M. Yaghi, Gas Adsorption Sites in a Large-Pore Metal-Organic Framework, 309(5739) (2005) 1350-1354. https://doi.org/doi:10.1126/science.1113247.

59. S.K. Nune, P.K. Thallapally, A. Dohnalkova, C. Wang, J. Liu, G.J. Exarhos, Synthesis and properties of nano zeolitic imidazolate frameworks, Chemical Communications 46(27) (2010) 4878-4880. https://doi.org/10.1039/C002088E.

60. S. Gadipelli, W. Travis, W. Zhou, Z. Guo, A thermally derived and optimized structure from ZIF-8 with giant enhancement in CO2 uptake, Energy & Environmental Science 7(7) (2014) 2232-2238. https://doi.org/10.1039/C4EE01009D.

61. J. Liu, Y. Zhang, L. Zhang, F. Xie, A. Vasileff, S.-Z. Qiao, Graphitic Carbon Nitride (g-C3N4)-Derived N-Rich Graphene with Tuneable Interlayer Distance as a High-Rate Anode for Sodium-Ion Batteries, 31(24) (2019) 1901261. https://doi.org/https://doi.org/10.1002/adma.201901261.

62. L. Qin, D. Huang, P. Xu, G. Zeng, C. Lai, Y. Fu, H. Yi, B. Li, C. Zhang, M. Cheng, C. Zhou, X. Wen, In-situ deposition of gold nanoparticles onto polydopamine-decorated g-C(3)N(4) for highly efficient reduction of nitroaromatics in environmental water purification, J Colloid Interface Sci 534 (2019) 357-369. https://doi.org/10.1016/j.jcis.2018.09.051.

63. Y. Fu, P. Xu, D. Huang, G. Zeng, C. Lai, L. Qin, B. Li, J. He, H. Yi, M. Cheng, C. Zhang, Au nanoparticles decorated on activated coke via a facile preparation for efficient catalytic reduction of nitrophenols and azo dyes, Applied Surface Science 473 (2019) 578-588. https://doi.org/https://doi.org/10.1016/j.apsusc.2018.12.207.

64. Y.-C. Chiang, W.-H. Lin, Y.-C. Chang, The influence of treatment duration on multi-walled carbon nanotubes functionalized by H2SO4/HNO3 oxidation, Applied Surface Science 257(6) (2011) 2401-2410. https://doi.org/10.1016/j.apsusc.2010.09.110.

65. F.A. Permatasari, A.H. Aimon, F. Iskandar, T. Ogi, K. Okuyama, Role of C-N Configurations in the Photoluminescence of Graphene Quantum Dots Synthesized by a Hydrothermal Route, Scientific reports, 2016, p. 21042.

66. Y. Liu, T.G. Kelly, J.G. Chen, W.E. Mustain, Metal Carbides as Alternative Electrocatalyst Supports, ACS Catalysis 3(6) (2013) 1184-1194. https://doi.org/10.1021/cs4001249.

67. H. Wang, C.M.B. Holt, Z. Li, X. Tan, B.S. Amirkhiz, Z. Xu, B.C. Olsen, T. Stephenson, D. Mitlin, Graphene-nickel cobaltite nanocomposite asymmetrical supercapacitor with commercial level mass loading, Nano Research 5(9) (2012) 605-617. https://doi.org/10.1007/s12274-012-0246-x.

68. D. Guo, R. Shibuya, C. Akiba, S. Saji, T. Kondo, J. Nakamura, Active sites of nitrogen-doped carbon materials for oxygen reduction reaction clarified using model catalysts, Science (New York, N.Y.) 351(6271) (2016) 361-5. doi.org/10.1126/science.aad0832.

69. T. Jawhari, A. Roid, J. Casado, Raman spectroscopic characterization of some commercially available carbon black materials, Carbon 33(11) (1995) 1561-1565. https://doi.org/https://doi.org/10.1016/0008-6223(95)00117-V.

70. A.C. Ferrari, J. Robertson, Interpretation of Raman spectra of disordered and amorphous carbon, Physical Review B 61(20) (2000) 14095-14107. https://doi.org/10.1103/PhysRevB.61.14095.

71. B. Li, H. Nam, J. Zhao, J. Chang, N. Lingappan, F. Yao, T.H. Lee, Y.H. Lee, Nanoreactor of Nickel-Containing Carbon–Shells as Oxygen Reduction Catalyst, 29(7) (2017) 1605083. https://doi.org/https://doi.org/10.1002/adma.201605083.

72. E.M. Miner, T. Fukushima, D. Sheberla, L. Sun, Y. Surendranath, M. Dincă, Electrochemical oxygen reduction catalysed by Ni3(hexaiminotriphenylene)2, Nature communications 7 (2016) 10942. https://doi.org/10.1038/ncomms10942.

73. J. Huai, K. Ma, Y. Lu, T. Chen, Z. Zhao, In-situ One-Step Preparation of Nickel-Tipped N-doped Carbon Nanotubes for Oxygen Reduction, 11(19) (2019) 4818-4821. https://doi.org/https://doi.org/10.1002/cctc.201901239.

74. G. Fu, X. Yan, Y. Chen, L. Xu, D. Sun, J.-M. Lee, Y. Tang, Boosting Bifunctional Oxygen Electrocatalysis with 3D Graphene Aerogel-Supported Ni/MnO Particles, 30(5) (2018) 1704609.https://doi.org/10.1002/adma.201704609.

ZIF-67 derived Co, N decorated carbon catalyst modified with biomass-derived high surface area porous carbon for enhanced oxygen reduction reaction
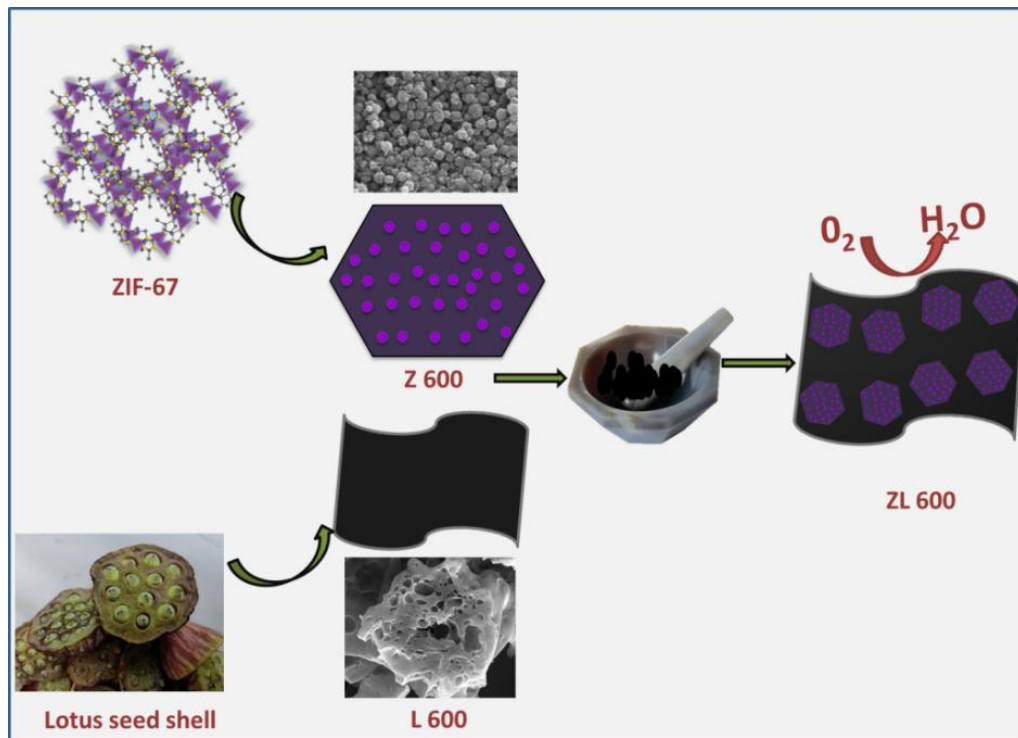
Abstract

Non-precious transition metal-based catalysts are perceived to be viable alternatives for high cost Pt/C catalysts for Oxygen reduction reaction (ORR) in fuel cells. Metal-organic frameworks are considered ideal precursors for the synthesis of transition metal, heteroatom doped catalysts. However, MOF-derived carbon with agglomerated metal sites upon carbonization may hinder the activity due to the lack of proper channels for molecular transport. Herein, we demonstrate the synthesis of a Co, N co-doped carbon by blending ZIF-67 derived Co-doped carbon with a high surface area porous carbon prepared from lotus seed shell. The combination of the two catalysts led to enhanced electrochemical ORR activity in an alkaline electrolyte medium. The optimized carbon catalyst ZL 600(3:1) exhibited a half-wave potential of 0.79 V vs. RHE and a current density of -4.38 mA cm^{-2} in 0.1 M KOH solution. The catalyst also showed higher stability as well as methanol tolerance. The high micro-mesoporosity, pyridinic –pyrrolic nitrogen contents, as well as enriched Co active centres surrounded by carbon sheets favourably contributed to the efficient ORR mechanism.

3.1. Introduction

The incessant urge for environment-friendly energy storage and conversion devices caused by the increasing population and the associated urbanization has led to the emergence of renewable devices such as fuel cells. Fuel cells are considered greener energy devices where the energy is generated in the form of electricity via the conversion of fuels into harmless byproducts.[1-3] However, the efficiency of the fuel cells is based on the ability of the catalyst to forward the kinetics of the rate-limiting oxygen reduction reaction at the cathode. Developing efficient catalysts for the trouble-free operation of fuel cells is thus an essential requirement for commercial needs. [4, 5]

Pt-based catalysts are demonstrated to be ideal candidates for fuel cell ORR applications. However, the low surface area and dispersity of Pt catalysts necessitate a support material to perform to its full potential. Currently, carbon black is considered the ideal support for Pt catalysts due to its high surface area and mesoporosity that enable homogeneous dispersion of the Pt particles and provide surface supports that act as promising electrocatalysts with minimum Pt loading. [6-9] However, such activated carbon supports are derived from hydrocarbons such as petroleum products and are again dependent on non-renewable sources. This demands focused efforts on developing alternative low-cost catalysts that can impart comparable electrocatalytic activity with that of Pt/C in fuel cells. Over the past years, diverse preparation strategies have been employed to prepare activated carbon with desirable features like high surface area, porosity, etc., by employing different sources. Biomasses, including agricultural waste, are considered a cheap source for the preparation of activated carbon for application in various fields, such as adsorption and conversion reactions. [10-12] However, they were found to exhibit significantly less activity due to the lack of proper active centres and agglomeration leading to poor ORR performance. Functionalization of the surface of the carbon is an effective strategy to improve the activities of the activated carbon.[13] Doping the activated carbon with heteroatoms such as nitrogen and transition metals is proven to be an ideal method to impart better catalytic activity to activated carbon. [14-17]

Transition metals such as Co, Ni, Cu, Fe, etc., have been widely exploited for replacing Pt catalysts with high ORR performance as they act as efficient catalytic centres due to their partially filled d orbitals. [18-21] Metal-organic frameworks (MOFs) are widely exploited as a sacrificial template for preparing transition metal-doped carbon catalysts. MOFs

containing central metal nodes and organic ligands containing carbon and other heteroatoms such as nitrogen, oxygen, etc., can lead to the transition metal, heteroatom-doped carbon upon carbonization under an inert atmosphere. This heteroatom content is also found to be beneficial as they can perform as active centres due to the synergy between the carbon and the heteroatoms. Also, compared to other preparation methods, MOFs as a precursor can provide better control on heteroatom doping due to the periodicity in the arrangement of atoms in the MOFs.[22-24] However, pure MOF-derived carbon possesses limited activity due to the agglomeration of excess adjacent metal particles and the associated reduction in effective active centres available to initiate electrocatalytic activity. [25-27] Recent studies reported that using biomass-derived activated carbon as support for the metal-organic frameworks and their derived transition metal-doped carbon can impart enhanced ORR activity due to the effective dispersion of active sites. The catalysts found better electrocatalytic activity in alkaline electrolytes. ZIF-67 incorporated into Pomelo peel-derived N-doped carbon has enhanced ORR activity compared to ZIF-67 and N-doped carbon prepared from Pomelo peel. The abundant Co-N_4 sites in ZIF-67@NPC favourably contributed to enhanced ORR activity with a higher half-wave potential of 0.82 V vs. RHE and a kinetic current density of -4.97 mA cm^{-2} at 0.80 V. [28] Qi et al. were able to prepare Co/Co_3O4@N doped carbon catalyst from ZIF-67/poplar flowers composite that intern exhibited better ORR performance compared to ZIF-67 derived Co@NC and poplar flower derived PL-bio-C.[29]

Herein, we demonstrate a facile approach for synthesizing Co, N decorated micro-meso porous carbon from ZIF-67 and lotus seed shell. ZIF-67-derived carbon was incorporated into high surface area microporous carbon prepared from lotus seed shells with different weight ratios via physical mixing. Compared to ZIF-67 derived Z 600 and lotus seed shell derived L 600, the composite carbon samples exhibited enhanced electrocatalytic activity towards oxygen reduction reaction in an alkaline medium. The sample ZL 600 (3:1) exhibited a half-wave potential of 0.79 V and a current density of -4.38 mA cm^{-2}. The sample also showed a lower Tafel slope of 68 mV dec^{-1}, good stability, and methanol tolerance in the alkaline medium.

3.2. Experimental

3.2.1. Materials and methods

Lotus seed shells were collected from the local farm nearby. Analytical grade Co $(NO_3)_2.6H_2O$ (≥98 %, Sigma Aldrich), 2- Methylimidazole (2-MeIm, $C_4H_6N_2$, 98 %, Sigma Aldrich), Methanol (CH_3OH, ≥99.8 %, Merck, India), KOH and HCL were used as received.

3.2.2. Preparation of porous carbon from lotus seed shell (L 600)

L 600 was prepared according to a previously reported procedure. [30] Lotus seed shells were collected, cut into small pieces, and treated with 0.5 M NaOH solution for 15 h, followed by washing with distilled water to remove impurities. The alkaline washing aids in removing any soluble impurities present and loosens the lignocellulose structure since the components like ester, acetyl groups are sensitive to NaOH. [31, 32] Then, the cleaned lotus shells were dried in an oven at 120 °C and ground to a fine powder in a mixer jar. The powder was pre-treated at 450 °C in an inert furnace in a flowing nitrogen atmosphere at a flow rate of 5 cm^3/min to obtain porous properties and stable carbon product.[33] The resulting pre-treated biomass was then mixed with KOH, where the material: KOH ratio was 1:3, followed by carbonization at 600 °C for 1h. The obtained powder was soaked in 1 M HCl overnight to remove the unreactive species, if any were present, and thoroughly washed with distilled water till the supernatant attained pH 7. The obtained carbon residue was dried in a vacuum oven at 150 °C.

3.2.3. Preparation of Co, N decorated carbon from ZIF-67 (Z 600)

Z 600 was prepared according to the previously described procedure. Initially, ZIF-67 was prepared in the aqueous medium according to a previous report where the Co^{2+}:2-methylimidazole: water ratio was 1:60:2228. [34, 35] Dried ZIF-67 powder was transferred into a crucible and carbonized at 600 °C for 1 h under a flowing nitrogen stream to obtain Co, N co-doped carbon. The obtained powder was soaked in 1 M HCl overnight and thoroughly washed with distilled water till the supernatant attained pH 7. The obtained carbon residue was dried in a vacuum oven at 150 °C.

3.2.4. Preparation of ZL 600 (X: Y)

The prepared ZIF-67 derived Z 600 was ground with lotus seed shell-derived carbon L 600 in a 1:3, 1:1, and 3:1 ratio to form ZL 600 carbon catalysts. The resulting carbon was

labelled as ZL 600 (X; Y), where X represents the weight of Z 600, and Y is the weight of L 600 carbon. The obtained powder was used for analyzing electrocatalytic ORR activity.

3.2.5. Material Characterization

The formation of carbon was analyzed using powder X-ray diffraction technique (PXRD, Malvern PANalytical B.V, EMPYREAN 3). The decomposition pattern of samples in the N_2 atmosphere was analyzed using Thermogravimetric analysis (TGA, Perkin Elmer, STA-6000). The surface area and porosity of the material were analyzed by N_2 adsorption-desorption analysis from BET (Tristar II, Micrometric, USA). The surface morphology and elemental distribution were recorded by scanning electron microscopy and SEM-EDS (JEOL, JSM-35). A deep understanding of the morphology was obtained from a High-resolution transmission electron microscope (HR-TEM, JEOL JEM- F200). The surface electronic binding states of the carbon sample were analyzed from XPS spectra (ULVAC-PHI Inc., USA). Confocal Raman microscopy (WI Tec, Germany) operated at 633 nm was used to analyze the structural features of carbon.

All the electrochemical analysis was conducted on a Bio-Logic (model SP-300) rotating disk electrode workstation. A three-electrode system was used where Hg/HgO was used as the reference electrode, and graphite rod was used as the counter electrode. The catalyst slurry for the working electrode was prepared according to the previously done procedure; initially, 5 mg of the catalyst was mixed with 1 mL isopropanol: water in a 1:3 ratio and 40 μL of Nafion solution, followed by sonication of the slurry for 1h. The working electrode was made by coating 10 μL of this slurry on a glassy carbon electrode of a surface area of 0.196 cm^2 and dried under an IR lamp. All the electrochemical analyses were performed in 0.1 M KOH solution. Initially, the electrolyte solution was saturated with N_2 gas, followed by saturating with O_2. The electrochemical activity of the catalyst was compared with the state-of-the-art catalyst 40 % Pt/C. The Rotating ring-disk electrode (RRDE) measurements were also conducted under the same conditions with ring-disk glassy carbon as a working electrode with a surface area of 0.2826 cm^2 having a Pt ring surrounding the glassy carbon surface.

3.3. Results and Discussion

3.3.1. Phase analysis
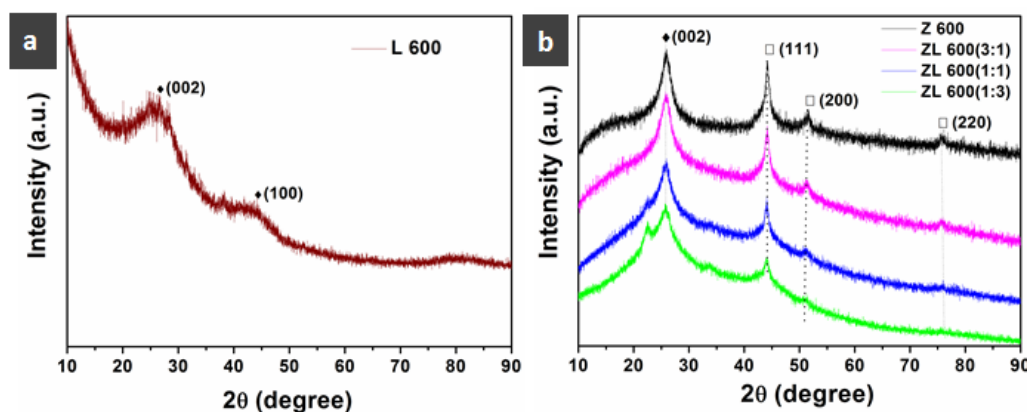
Figure 1. PXRD patterns of; a) L 600 and b) Z 600 and composite carbon samples

The powder X-ray diffraction pattern of the L 600 sample exhibited peaks of carbon located at 26 ° corresponding to the (002) plane of graphitic carbon. In addition to that, Z 600 exhibited characteristic peaks of Co phase at 44.2 °, 51.6 °, and 75.8 ° corresponding to the (111), (200), and (220) planes, respectively(JCPDS file no. 00-015-0806& 00-008-0415), indicating that the carbonization of the ZIF-67 resulted in the successful formation of Co phase as reported in the literature.[36, 37] The composite carbon ZL 600 (1:3), ZL 600 (1:1), and ZL 600 (3:1) also exhibited all the peaks of Co and carbon with the intensity of Co followed an increasing order from ZL 600 (1:3) to ZL 600 (3:1), that correlate with the increase in the percentage of Z 600 content (**Figure 1a&1b**).

3.3.2. Thermogravimetric Analysis (TGA)

The decomposition profile of Lotus seed shell and ZIF-67 was followed by Thermogravimetric analysis (TGA) conducted in an N_2 atmosphere up to 700 °C at a heating rate of 5 °C/min. The TGA curve of the Lotus seed shell shows a gradual weight loss starting from 50 °C. The initial weight loss below 200 °C at the pre-pyrolysis stage might be due to the volatilization of moisture and other volatile gaseous impurities from the surface. The second stage of weight loss between 200 °C- 400 °C is presumably due to the decomposition of cellulose and hemicellulose in the biomass. The sample showed a low weight loss between 600 °C -700 °C, attributed probably to the decomposition of lignin present in the shell, and reached up to 42 % yield at 700 °C.[38, 39] The activation of the Lotus shell was thus carried out at 600 °C since the material tends to show stability

after 600 °C. The TGA profile of ZIF-67 showed two stages of weight loss. The initial weight loss below 200 °C could be attributed to the removal of coordinated water molecules from the framework. The second stage weight loss after 400 °C is due to the decomposition of the framework and the associated rearrangements within the frameworks leading to Co, N- doped carbon with a yield of 20.5 % (**Figure 2**). [40]
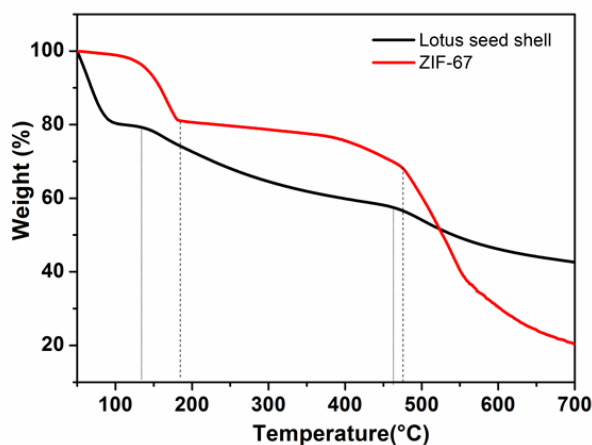
Figure 2. TGA profile of lotus seed shell and ZIF-67

3.3.3. Surface area analysis

The N_2 adsorption-desorption analysis was done to understand the surface area and porous features of the carbon samples. The L 600 carbon exhibited Type-1 adsorption isotherm with an exceptionally high surface area of 2694 m^2/g with a predominant microporosity feature. However, the ZIF-67 derived Z 600 carbon showed micro-mesoporous characteristics as the isotherm resembled type-II b type with H4 hysteresis and a surface area value of 414 m^2/g. [41] Upon forming the composites, the resulting carbon exhibited characteristics of both L 600 and Z 600, as evidenced by the surface area and porous features (**Figure 3a & 3b**). The samples showed gradual variation in the micro and mesoporosity according to the percentage of Z 600 and L 600. The sample ZL 600 (1:3) with the higher percentage composition of L 600 showed higher microporosity with a surface area of 995 m^2/g and a total pore volume of 0.66 cm^3/g. As can be observed from **Table 1**, with an increase in Z 600 content, the surface area showed a decreasing tendency, probably due to the incorporation of Z 600 into the pores of L 600, and the isotherm curve also resembled more toward Z 600. The micropore volume of carbon samples calculated at a P/P_0 value of 0.03 also showed a decreasing tendency with

the increase in Z 600 percentage. The Pore size distribution further showed the same tendency as can be observed from the NLDFT curve (**Figure 3c&3d**).
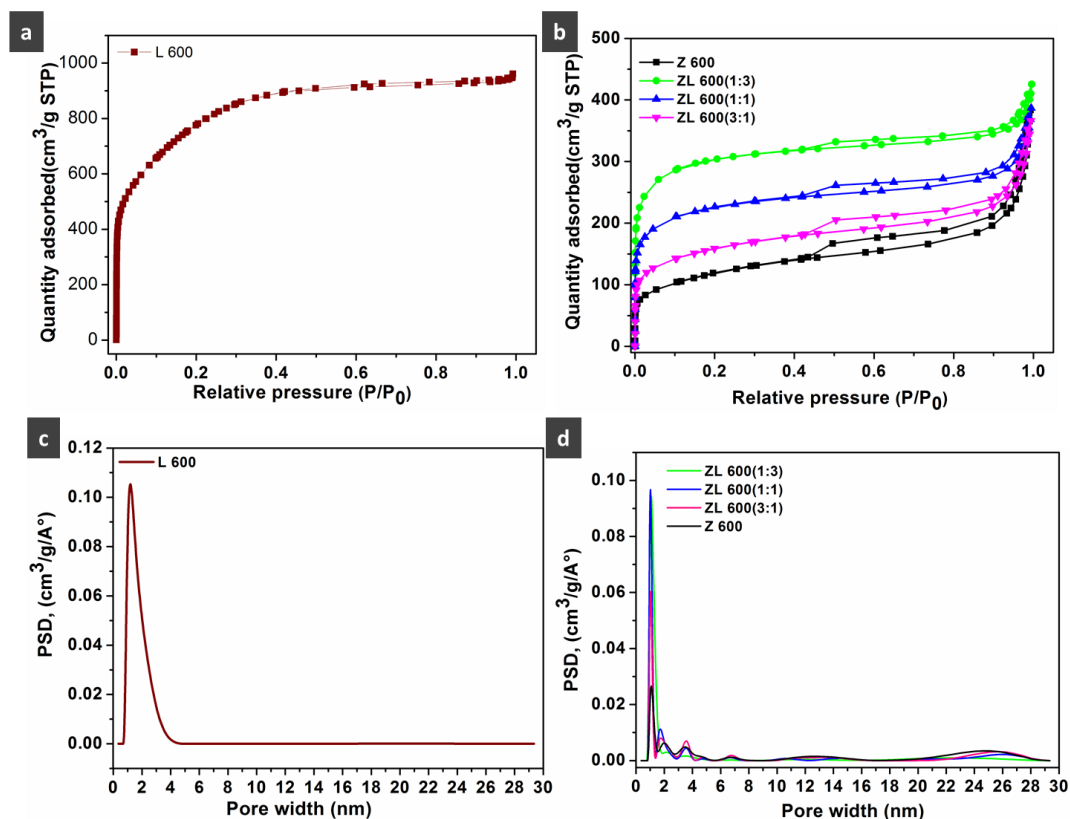
Figure 3. a,b) N_2 adsorption-desorption isotherms of L 600, Z 600, and ZL 600 composites c,d) Pore size distribution curves of carbon samples

Table 1. Surface area and pore volume of the carbon samples calculated from the BET isotherms

Sample	Surface area (m^2/g)	Total Pore volume (cm^3/g)	Micropore volume (cm^3/g)
L 600	2,694	1.51	0.84
Z 600	414	0.60	0.13
ZL 600(1:3)	995	0.66	0.39
ZL 600(1:1)	718	0.60	0.28
ZL 600(3:1)	527	0.57	0.19

3.3.4. Electrochemical analysis

The electrochemical ORR activity of the samples was initially analyzed by performing cyclic voltammetry (CV) profiles in N_2 and O_2 atmospheres, respectively, at a scan rate of 50 mV S^{-1} in 0.1 M KOH solution. All the samples showed a shift in current density in the O_2 medium, showing the oxygen reduction activity of the samples. Compared to L 600 and Z 600 samples, all the ZL 600 composite samples exhibited a more positive shift in potential and increased current density indicating the enhanced ORR activity upon composite formation **(Figure 4 (a-c))**.
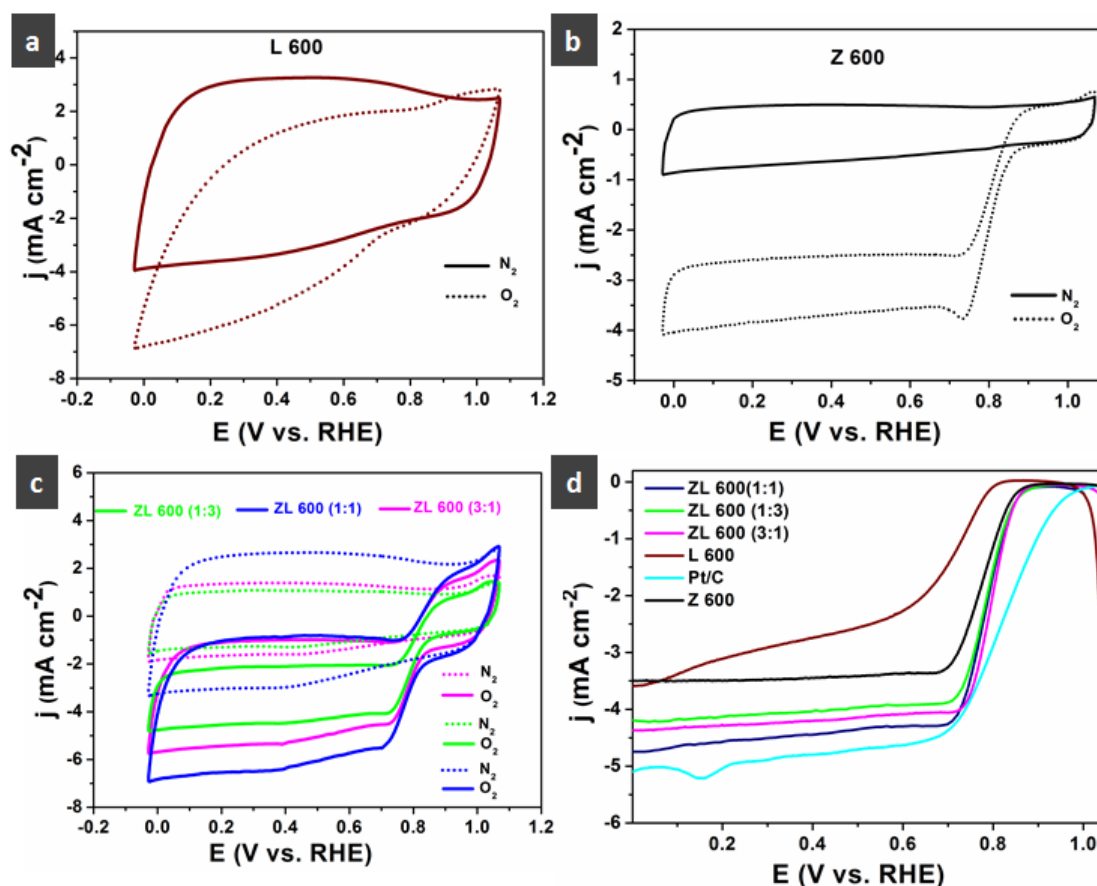
Figure 4. (a-c) Cyclic voltammograms of L 600, Z 600, and ZL 600 samples recorded respectively in N_2 and O_2 saturated 0.1 M KOH electrolyte and, d) LSV curves of carbon catalysts recorded in O_2 saturated 0.1 M KOH solution

The electrochemical ORR performance of the prepared L 600, Z 600, and ZL 600 samples were further analyzed using linear sweep voltammetry (LSV) curve recorded at 1600 rpm (**Figure 4d**). The carbon samples L 600 and Z 600 exhibited an onset potential of 0.80 V and 0.88V and a limiting current density of -3.6 mA cm^{-2} and -3.48 mA cm^{-2},

respectively. The sample Z 600 exhibited higher ORR activity even though the surface area was higher for L 600. This indicates the positive impact of the presence of Co centres along with mesoporosity in Z 600 samples to contribute to enhanced ORR performance. The sample L 600 exhibited a limiting current density of -3.6 mA cm^{-2} owing to the higher surface area and microporosity. However, the ORR activity was not in linear proportion to the surface area in L 600. It can be attributed to the difficulty in the accessibility of O_2 molecules to reach the active centres inside the micropores. [42, 43] Compared to pure L 600 and Z 600, the ZL 600 carbon samples exhibited enhanced ORR activity regarding both onset potential and current density. The catalysts exhibited a more positive shift in terms of onset and half-wave potential in the increasing order of ZL 600(3:1) > ZL 600(1:1)> ZL 600(1:3)> Z 600> L 600 (**Table 2**). This indicates the role of both micropores and mesopores on the carbon surface to facilitate the ORR pathway. [44]

Table 2: Summary of ORR activity of the carbon samples obtained from the LSV curve

Sample	E_{Onset} (V vs. RHE)	J (mA cm^{-2})	$E_{1/2}$ (V vs. RHE)
L 600	0.82	-3.6	0.66
Z 600	0.88	-3.48	0.77
ZL 600 (1:3)	0.90	-4.21	0.78
ZL 600 (1:1)	0.90	-4.74	0.78
ZL 600 (3:1)	0.91	-4.38	0.79
Pt/C	0.98	-5.02	0.81

3.3.5. Structural and Morphological studies

The morphological features of the optimized catalysts for ORR were analyzed by Scanning Electron Microscopy (SEM). Porous channels extending to micrometer dimensions were observed on the surface of sheets in L 600 sample. In the case of Z 600 carbon, deformed hexagonal-shaped particles of dimension ≈ 200 nm were observed. However, the carbon ZL 600 (3:1) exhibited mixed morphology containing both

hexagonal and sheets (**Figure 5**). Since the pores on the L 600 range in micrometer dimensions, Z 600 particles might be easily incorporated into the pores of the L 600 sheets, due to which a decrease in the surface area of L 600 upon Z 600 addition was observed. The SEM-elemental mapping of ZL 600 (3:1) shows the uniform distribution pattern of C, Co, and N, which can form active centres on the carbon for efficient oxygen reduction reaction (**Figure 6 (a-d)**).
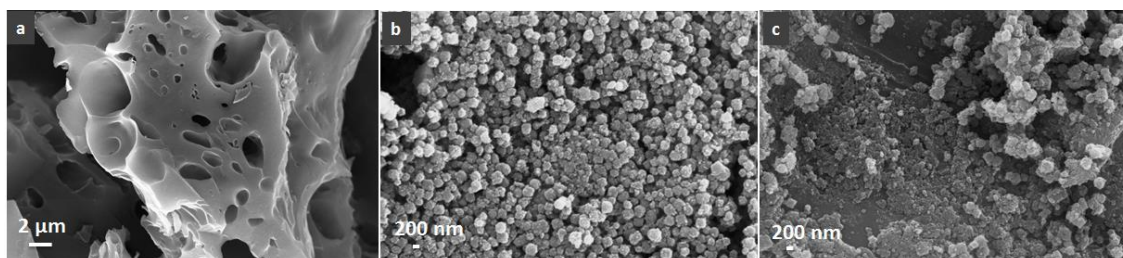
Figure 5. SEM images of a) L 600, B) Z 600, and C) ZL 600(3:1)
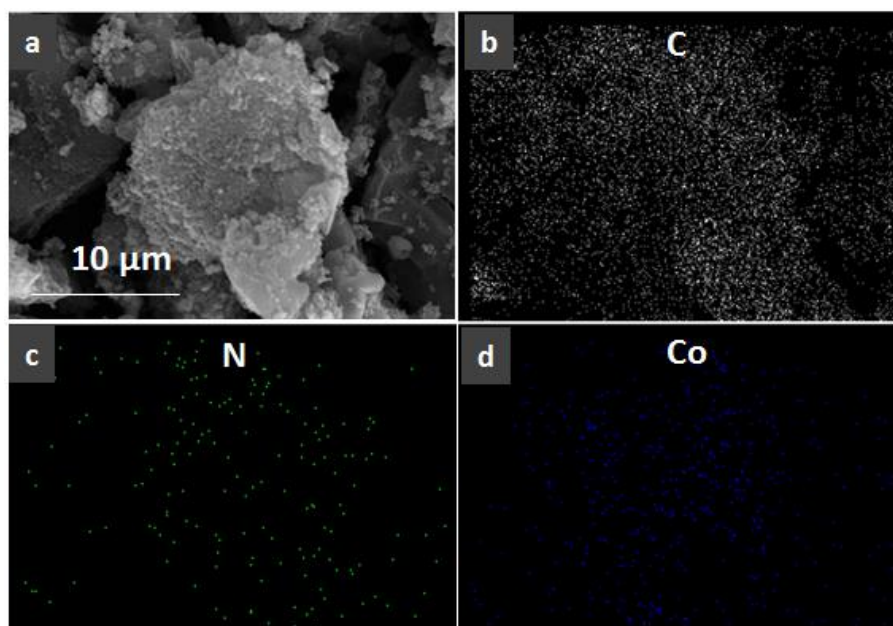
Figure 6. SEM image and corresponding elemental mapping of ZL 600 (3:1)

 The TEM image of the L 600 carbon sample exhibited sheet-like morphology after the decomposition of all the cellulosic and lignin components in the lotus seed shell (**Figure 7a**). In Z 600, cobalt particles of size ≈20 nm decorated on carbon shells were observed. However, the carbonized Z 600 retained the morphology of parent ZIF-67 as separate deformed hexagonal particles. A tubular morphology was also tending to emerge from the

carbon shell, evidencing the role of Co to catalyze the nanotube formation (**Figure 7b**). Recent studies reported the ability of nanotubes to enhance the overall ORR activity due to better electronic conductivity. [45, 46] Here, the central cobalt metal was reduced to Co^0 upon carbonization, whereas the imidazole linkage served as a carbon matrix for dispersing the cobalt atoms uniformly. The morphology of Z 600 was retained in ZL 600 (3:1) also (**Figure 7c**). The HRTEM image shows a d-spacing value of 0.2002 nm and is assigned to the (111) plane of the Co phase, further proving the doping of cobalt on carbon (**Figure 7d**). Here, instead of individual particles, a connected sheet-like morphology was observed dispersed with Co metal centres that may benefit the ORR mechanism since the porous channel has the added advantage of forming diffusion channels for O_2 during the ORR mechanism. [47]
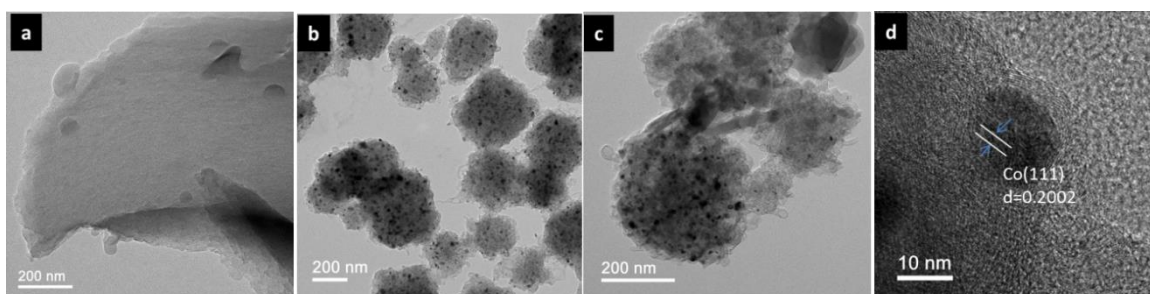
Figure 7. (a-c) TEM images of L 600, Z 600, and ZL 600(3:1) samples, respectively, d) HRTEM image of ZL 600 (3:1).

The surface binding state of the carbon sample was evaluated using X-ray photoelectron spectroscopy (XPS). The XPS survey spectrum of L 600 showed the presence of C, N, and O. Whereas Z 600 and the composite samples evidenced the presence of cobalt along with C, N, and O emerging from the parent MOF (**Figure 8a**). The low surface percentage of Co in the samples might be attributed to the surrounding carbon shells that may hinder the detection of cobalt (**Table 3**). [48] The deconvoluted C1s spectrum exhibited peaks at 284.6 eV, 285.2 eV, 286 eV, 286.8 eV, and 289.1 eV, corresponding to C=C sp^2, C-C sp^3, C-N, C-O, and C=O respectively. [49, 50] The C 1s spectrum exhibited a predominant peak of C-C sp^3 hybridization, evidencing the creation of defects (**Figure 8b**). The high-resolution Co 2p spectrum drawn for ZL 600 (3:1) exhibited 2 peaks at 778.3 eV and 793.8, corresponding to $2p_{3/2}$ and $2p_{1/2}$ bands of the Co^0 phase (**Figure 8c**). [51, 52]
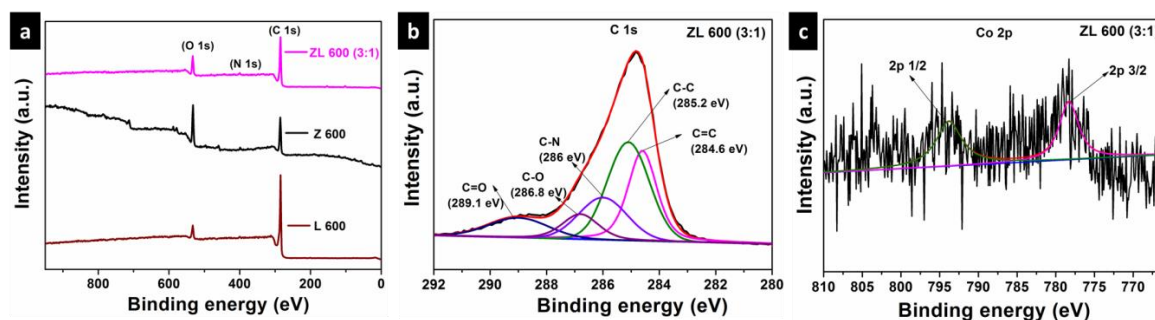
Figure 8. XPS a) survey spectra, b,c) High-resolution C1sand Co 2p spectra of ZL 600(3:1)

Table 3. Elemental distribution of carbon samples obtained from XPS

Sample name	Elemental distribution (Atomic %)			
	C	0	N	Co
L 600	91.2	7.5	1.3	-------
Z 600	68.7	27.8	2.8	0.7
ZL 600 (3:1)	85.2	12.7	1.4	0.6

The deconvoluted N 1s spectrum of L 600 exhibited only one peak at 400.1 eV corresponding to Pyrrolic nitrogen. The deconvoluted N 1s spectrum of Z 600 was resolved into 2 peaks at 398 eV and 400.5 eV, corresponding to the pyridinic and pyrrolic nitrogen, respectively. [53] In ZL 600 (3:1) also, both pyridinic and pyrrolic nitrogen were observed (**Figure 9**). The distribution of different types of nitrogen is shown in **Figure 10**. It is reported that pyridinic and pyrrolic nitrogen could boost oxygen reduction activity in an alkaline medium. Hence the presence of both nitrogen species in the carbon samples contributed to an increase in the half-wave potential and limiting the current density. [54, 55]
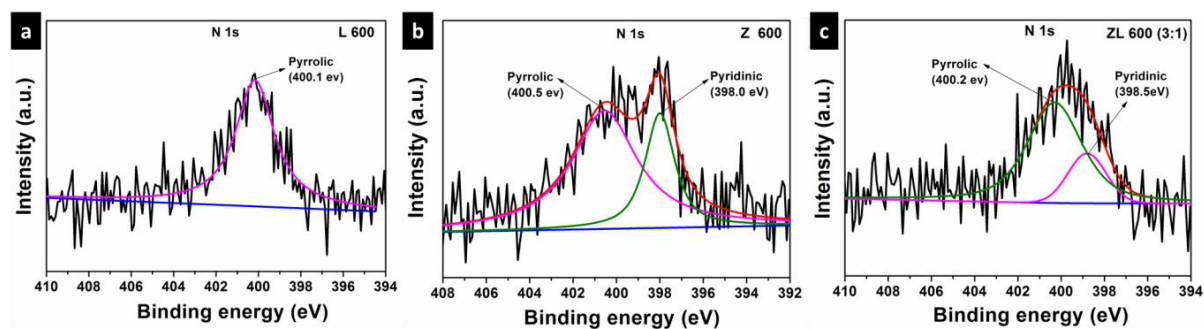
Figure 9. High-resolution XPS N 1s spectra of L 600, Z 600 and ZL 600 (3:1), respectively
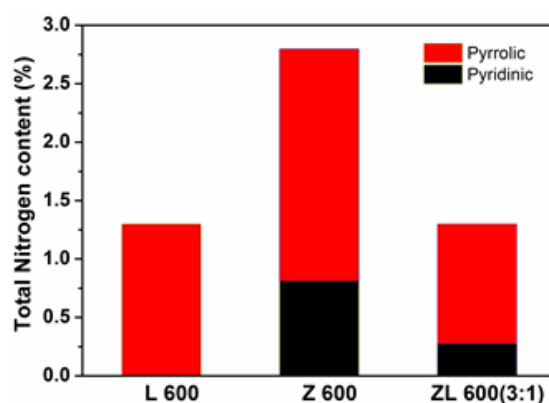
Figure 10. Distribution ratios of pyridinic and pyrrolic nitrogen in the carbonized samples

Raman spectroscopy was used to understand the surface structure of the carbon samples. The spectrum showed the presence of two bands, the D band (1350 cm^{-1}) and the G band (1580 cm^{-1}), attributed to defects and graphitization on the carbon surface, respectively.[56] The I_D/I_G ratio was calculated to understand the extent of defect formation and graphitization. The I_D/I_G values of L 600, Z 600, and ZL 600(3:1) samples were 1.37, 1.47, and 1.60, respectively (**Figure 11**). Compared to pure L 600 and Z 600 carbon samples, the composite ZL 600(3:1) exhibited a higher I_D/I_G ratio due to the higher amount of defect formation upon mixing. These defects on carbon sheets can contribute to the higher surface area and form better channels for O_2 diffusion, contributing to better ORR activity. [47]
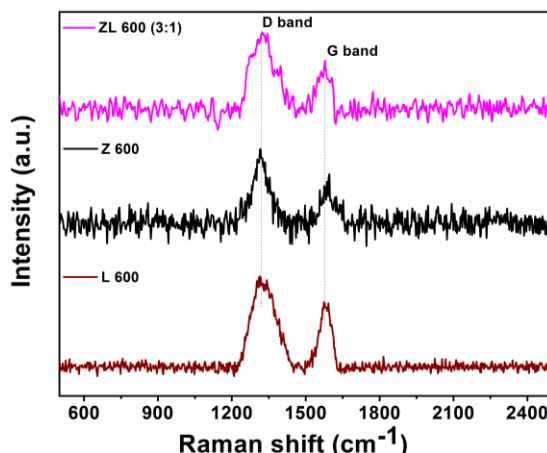
Figure 11. Raman spectra of carbon samples

3.3.6. Analysis of electrochemical kinetics

To understand the kinetics of the ORR, LSV curves of the ZL 600 (3:1) sample were compared at different rotations. Here the current density increased with an increase in rotation rate due to an improvement in ORR kinetics (**Figure 12a**). The electron transferred during the ORR was calculated from the K-L plot. The K-L plots obtained by plotting 1/J against $\omega^{-1/2}$ are shown in **Figure 12b**. From K-L plots, the electron transfer number of ≈4 was obtained, indicating a 4-electron reaction mechanism for the reduction of O_2 with H_2O as the byproduct.
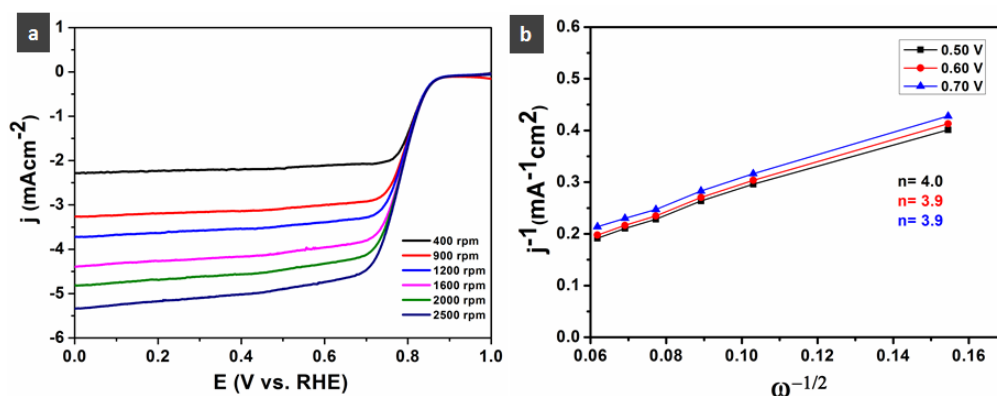
Figure 12. a) LSV curves of ZL 600(3:1) at different rotation rates, and b) K-L plots of ZL 600(3:1) at various potential ranges

The electron transfer mechanism and the amount of H_2O_2 produced by the partial 2 electron mechanisms were calculated further by conducting RRDE experiments. The ZL 600(3:1) sample was found to show an electron transfer number of ≈ 3.7, and the amount

of H_2O_2 produced was estimated to be $\approx$ 15.87, indicating that the 4 electron transfer mechanism was dominating during the oxygen reduction reaction (**Figure 13**).
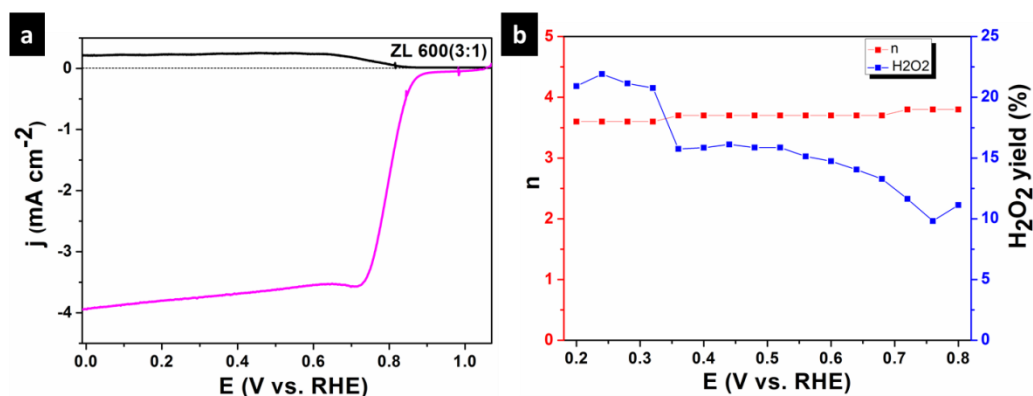
Figure 13. a) RRDE voltammogram of ZL 600(3:1) and b) electron transfer number and H_2O_2 yield of ZL 600(3:1) calculated from RRDE

The oxygen reduction reaction kinetics was further evaluated from the Tafel plot. Tafel plot was obtained by plotting the logarithm of kinetic current density against the corresponding potential in the onset region of the LSV curve taken at 1600 rpm **(Figure 14)**. The Tafel slope value calculated for the sample ZL 600 (3:1) was the least (68 mv/decade) compared to Z 600 (71 mv/decade) and L 600 (73 mv/decade) which was close to Pt/C (66 mv/decade) indicating that the optimized carbon catalyst exhibited better electron transfer kinetics.
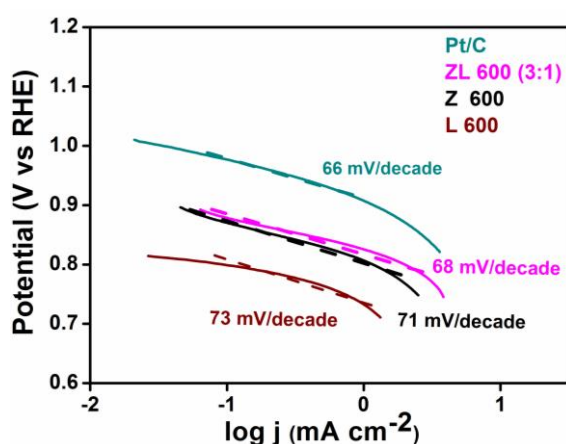
Figure 14.) Tafel plot drawn from LSV curves at 1600 rpm of the samples

The applicability of the catalyst in the methanol-based fuel cells was tested by conducting a methanol tolerance test. The methanol crossover effect of the sample was analyzed by performing a chronoamperometry test carried out in 0.1 M KOH solution for 600s

(**Figure 15**). 3 M MeOH solution was introduced into the electrolyte at a time interval of 300 s, and the response was measured. Notably, the sample showed appreciable resistance to methanol, as there was no deviation in the current upon adding MeOH. The commercial Pt/C showed a response to methanol with a deviation in the current density as it was decreased by 1.4 mA cm^{-2}, evidencing the limitation of conventional Pt-based ORR catalysts in fuel cells.
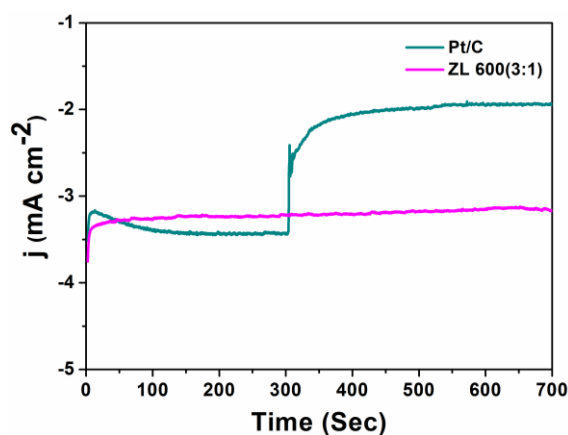
Figure 15.) methanol crossover study conducted by chronoamperometry analysis for ZL 600(3:1) and Pt/C samples.

 The stability of the catalyst for further application was tested by running an ADT experiment. LSV was recorded before and after performing 5000 cycles of CV in alkaline 0.1 M KOH. The catalyst ZL 600 (3:1) exhibited a shift in the half-wave potential value by ≈ 22 mV, where the current remained at 99 % of the initial quantity proving the stability of the catalyst (**Figure 16**).
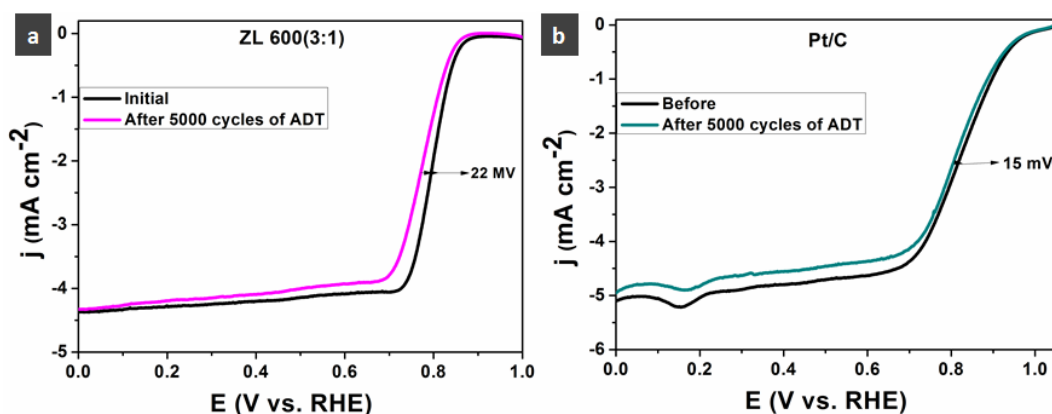
Figure 16.) LSV curves of ZL 600(3:1) and Pt/C before and after 5000 cycles

Thus, the prepared ZL 600(3:1) carbon decorated with Co, N heteroatoms exhibited considerable ORR activity proving the scope of non-precious transition metal doped carbon for fuel cell catalysis. Here the prepared carbon with micro-meso porosity, well-connected Co decorated sheet morphology, and defect creation could efficiently facilitate the electron transfer mechanism.

3.4. Conclusions

We have demonstrated the synthesis of a sustainable Co, N decorated micro-meso porous carbon from the ZIF-67 framework and lotus seed shell. The high surface area porous carbon derived from the lotus seed shell was used as a support matrix for the Co, N decorated carbon derived from ZIF-67. The simple addition via physical mixing of the two carbons in different weight ratios could tune the surface area and micro-meso porosity. The prepared carbon samples were tested as electrocatalysts in alkaline 0.1 M KOH. Compared to ZIF-67 derived Z 600 carbon and lotus seed shell derived L 600 carbon, the composite carbon catalysts ZL 600 exhibited enhanced electrocatalytic activity towards oxygen reduction reaction. The optimized sample ZL 600 (3:1) exhibited a half-wave potential of 0.79 V and a current density of -4.38 mA cm^{-2}. The low Tafel value of 68 mv dec^{-1} indicates the improved electron transfer kinetics upon composite formation. The sample also showed higher stability and tolerance towards methanol in the alkaline electrolyte medium. Here the synergistic effects of Co^0 active centres, Pyridinic/Pyrrolic nitrogen species, micro/meso porosity, and higher surface area have favourably contributed to enhanced oxygen reduction activity.

3.5. References

[1] OZ. Sharaf, M.F. Orhan, An overview of fuel cell technology: Fundamentals and applications, Renewable and Sustainable Energy Reviews 32 (2014) 810-853. https://doi.org/https://doi.org/10.1016/j.rser.2014.01.012.

[2] A.G. Olabi, T. Wilberforce, M.A. Abdelkareem, Fuel cell application in the automotive industry and future perspective, Energy 214. doi.org/10.1016/j.energy.2020.118955.

[3] R.-A. Felseghi, E. Carcadea, M.S. Raboaca, C.N. TRUFIN, C. Filote, Hydrogen Fuel Cell Technology for the Sustainable Future of Stationary Applications, 12(23) (2019) 4593.

[4] J.Wang,H.Wang, Y. Fan, Techno-Economic Challenges of Fuel Cell Commercialization, Engineering 4(3) (2018) 352-360. doi.org/10.1016/j.eng.2018.05.007.

[5] C. Song, J. Zhang, Electrocatalytic Oxygen Reduction Reaction, in: J. Zhang (Ed.), PEM Fuel Cell Electrocatalysts and Catalyst Layers: Fundamentals and Applications, Springer London, London, 2008, pp. 89-134. https://doi.org/10.1007/978-1-84800-936-3_2.

[6] K. Kodama, T. Nagai, A. Kuwaki, R. Jinnouchi, Y. Morimoto, Challenges in applying highly active Pt-based nanostructured catalysts for oxygen reduction reactions to fuel cell vehicles, Nature Nanotechnology 16(2) (2021) 140-147. https://doi.org/10.1038/s41565-020-00824-w.

[7] X. Ren, Q. Lv, L. Liu, B. Liu, Y. Wang, A. Liu, G. Wu, Current progress of Pt and Pt-based electrocatalysts used for fuel cells, Sustainable Energy & Fuels 4(1) (2020) 15-30. https://doi.org/10.1039/C9SE00460B.

[8] M. Tang, S. Zhang, S. Chen, Pt utilization in proton exchange membrane fuel cells: structure impacting factors and mechanistic insights, Chemical Society Reviews 51(4) (2022) 1529-1546. https://doi.org/10.1039/D1CS00981H.

[9] M. Watanabe, D.A. Tryk, The Role of Carbon Blacks as Catalyst Supports and Structural Elements in Polymer Electrolyte Fuel Cells, in: N. Nakashima (Ed.),

Nanocarbons for Energy Conversion: Supramolecular Approaches, Springer International Publishing, Cham, 2019, pp. 81-118. https://doi.org/10.1007/978-3-319-92917-0_4.

[10] J. Deng, M. Li, Y. Wang, Biomass-derived carbon: synthesis and applications in energy storage and conversion, Green Chemistry 18(18) (2016) 4824-4854. https://doi.org/10.1039/C6GC01172A.

[11] H. He, R. Zhang, P. Zhang, P. Wang, N. Chen, B. Qian, L. Zhang, J. Yu, B. Dai, Functional Carbon from Nature: Biomass-Derived Carbon Materials and the Recent Progress of Their Applications, n/a(n/a) 2205557. https://doi.org/https://doi.org/10.1002/advs.202205557.

[12] Z. Gao, Y. Zhang, N. Song, X. Li, Biomass-derived renewable carbon materials for electrochemical energy storage, Materials Research Letters 5(2) (2017) 69-88. https://doi.org/10.1080/21663831.2016.1250834.

[13] J. Lee, K.-H. Kim, E.E. Kwon, Biochar as a Catalyst, Renewable and Sustainable Energy Reviews 77 (2017) 70-79.https://doi.org/10.1016/j.rser.2017.04.002.

[14] S. De, A.M. Balu, JC van der Waal, R. Luque, Biomass-Derived Porous Carbon Materials: Synthesis and Catalytic Applications, 7(11) (2015) 1608-1629. https://doi.org/https://doi.org/10.1002/cctc.201500081.

[15] J. Wang, P. Nie, B. Ding, S. Dong, X. Hao, H. Dou, X. Zhang, Biomass derived carbon for energy storage devices, Journal of Materials Chemistry A 5(6) (2017) 2411-2428. https://doi.org/10.1039/C6TA08742F.

[16] V. Charles, X. Zhang, M. Yuan, K. Zhang, K. Cui, J. Zhang, T. Zhao, Y. Li, Z. Liu, B. Li, G. Zhang, CoNi nano-alloy anchored on biomass-derived N-doped carbon frameworks for enhanced oxygen reduction and evolution reactions, Electrochimica Acta 402 (2022) 139555. https://doi.org/https://doi.org/10.1016/j.electacta.2021.139555.

[17] M. Iwanow, T. Gärtner, V. Sieber, B. König, Activated carbon as catalyst support: precursors, preparation, modification and characterization, Beilstein Journal of Organic Chemistry 16 (2020) 1188-1202. https://doi.org/10.3762/bjoc.16.104.

[18] W. Gu, L. Hu, J. Li, E. Wang, Recent Advancements in Transition Metal-Nitrogen-Carbon Catalysts for Oxygen Reduction Reaction, 30(7) (2018) 1217-1228. https://doi.org/https://doi.org/10.1002/elan.201700780.

[19] H. Chen, Q. Wu, Y. Wang, Q. Zhao, X. Ai, Y. Shen, X. Zou, d–sp orbital hybridization: a strategy for activity improvement of transition metal catalysts, Chemical Communications 58(56) (2022) 7730-7740. https://doi.org/10.1039/D2CC02299K.

[20] B.Li,L.Zhang, J.Zhang,Y.Su,Recent Insight in Transition Metal Anchored on Nitrogen-Doped Carbon Catalysts: Preparation and Catalysis Application,3(3) (2022) 520-537.

[21] P. Jiao, D. Ye, C. Zhu, S. Wu, C. Qin, C. An, N. Hu, Q. Deng, Non-precious transition metal single-atom catalysts for the oxygen reduction reaction: progress and prospects, Nanoscale 14(39) (2022) 14322-14340. https://doi.org/10.1039/D2NR03687H.

[22] K. Shen, X. Chen, J. Chen, Y. Li, Development of MOF-Derived Carbon-Based Nanomaterials for Efficient Catalysis, ACS Catalysis 6(9) (2016) 5887-5903. https://doi.org/10.1021/acscatal.6b01222.

[23] C. Yang, X. Ma, J. Zhou, Y. Zhao, X. Xiang, H. Shang, B. Zhang, Recent advances in metal-organic frameworks-derived carbon-based electrocatalysts for the oxygen reduction reaction, International Journal of Hydrogen Energy 47(51) (2022) 21634-21661. https://doi.org/https://doi.org/10.1016/j.ijhydene.2022.05.025.

[24] W. Yang, X. Li, Y. Li, R. Zhu, H. Pang, Applications of Metal–Organic-Framework-Derived Carbon Materials, 31(6) (2019) 1804740. https://doi.org/https://doi.org/10.1002/adma.201804740.

[25] Y.V. Kaneti, S. Dutta, M.S.A. Hossain, M.J.A. Shiddiky, K.-L. Tung, F.-K. Shieh, C.-K. Tsung, K.C.-W. Wu, Y. Yamauchi, Strategies for Improving the Functionality of Zeolitic Imidazolate Frameworks: Tailoring Nanoarchitectures for Functional Applications, 29(38) (2017) 1700213. https://doi.org/10.1002/adma.201700213.

[26] J. Guo, S. Gadipelli, Y. Yang, Z. Li, Y. Lu, D.J.L. Brett, Z. Guo, An efficient carbon-based ORR catalyst from low-temperature etching of ZIF-67 with ultra-small cobalt nanoparticles and high yield, Journal of Materials Chemistry A 7(8) (2019) 3544-3551. https://doi.org/10.1039/C8TA10925G.

[27] S. Sohrabi, M. Ghalkhani, Metal–Organic Frameworks as Electrocatalysts for Oxygen Reduction Reaction in Electrochemical Technologies, Journal of Electronic Materials 48(7) (2019) 4127-4137. https://doi.org/10.1007/s11664-019-07187-6.

[28] H. Wang, F.-X. Yin, B.-H. Chen, X.-B. He, P.-L. Lv, C.-Y. Ye, D.-J. Liu, ZIF-67 incorporated with carbon derived from pomelo peels: A highly efficient bifunctional catalyst for oxygen reduction/evolution reactions, Applied Catalysis B: Environmental 205 (2017) 55-67. https://doi.org/https://doi.org/10.1016/j.apcatb.2016.12.016.

[29] Y. Wu, Y. Wang, Z. Xiao, M. Li, Y. Ding, M.-l. Qi, Electrocatalytic oxygen reduction by a Co/Co3O4@N-doped carbon composite material derived from the pyrolysis of ZIF-67/poplar flowers, RSC Advances 11(5) (2021) 2693-2700. https://doi.org/10.1039/D0RA09615F.

[30] L. Wu, Y. Cai, S. Wang, Z. Li, Doping of nitrogen into biomass-derived porous carbon with large surface area using N2 non-thermal plasma technique for high-performance supercapacitor, International Journal of Hydrogen Energy 46(2) (2021) 2432-2444. https://doi.org/https://doi.org/10.1016/j.ijhydene.2020.10.037.

[31] A. Kumar, H.M. Jena, Preparation and characterization of high surface area activated carbon from Fox nut (Euryale ferox) shell by chemical activation with H3PO4, Results in Physics 6 (2016) 651-658. https://doi.org/https://doi.org/10.1016/j.rinp.2016.09.012.

[32] W. Wang, X. Wang, Y. Zhang, Q. Yu, X. Tan, X. Zhuang, Z. Yuan, Effect of sodium hydroxide pretreatment on physicochemical changes and enzymatic hydrolysis of herbaceous and woody lignocelluloses, Industrial Crops and Products 145 (2020) 112145. https://doi.org/10.1016/j.indcrop.2020.112145.

[33] C.H. Yun, Y.H. Park, C.R. Park, Effects of pre-carbonization on porosity development of activated carbons from rice straw, Carbon 39(4) (2001) 559-567. https://doi.org/https://doi.org/10.1016/S0008-6223(00)00163-9.

[34] K. Kida, M. Okita, K. Fujita, S. Tanaka, Y. Miyake, Formation of high crystalline ZIF-8 in an aqueous solution, CrystEngComm 15(9) (2013) 1794-1801. https://doi.org/10.1039/C2CE26847G.

[35] J. Zhang, T. Zhang, D. Yu, K. Xiao, Y. Hong, Transition from ZIF-L-Co to ZIF-67: a new insight into the structural evolution of zeolitic imidazolate frameworks (ZIFs) in

aqueous systems, CrystEngComm 17(43) (2015) 8212-8215. https://doi.org/10.1039/C5CE01531F.

[36] Y. Su, Y. Zhu, H. Jiang, J. Shen, X. Yang, W. Zou, J. Chen, C. Li, Cobalt nanoparticles embedded in N-doped carbon as an efficient bifunctional electrocatalyst for oxygen reduction and evolution reactions, Nanoscale 6(24) (2014) 15080-15089. https://doi.org/10.1039/C4NR04357J.

[37] Y. Gao, Z. Han, S. Hong, T. Wu, X. Li, J. Qiu, Z. Sun, ZIF-67-Derived Cobalt/Nitrogen-Doped Carbon Composites for Efficient Electrocatalytic N2 Reduction, ACS Applied Energy Materials 2(8) (2019) 6071-6077. https://doi.org/10.1021/acsaem.9b01135.

[38] N. Manić, B. Janković, D. Stojiljković, V. Jovanović, MJTS Radojević, TGA-DSC-MS analysis of pyrolysis process of various agricultural residues, (2019).

[39] X. Wang, X. Zeng, D. Cao, Biomass-derived nitrogen-doped porous carbons (NPC) and NPC/ polyaniline composites as high performance supercapacitor materials, 2018.

[40] T. Truong, T.M. Hoang, C.K. Nguyen, Q.T.N. Huynh, N.T.S. Phan, Expanding applications of zeolite imidazolate frameworks in catalysis: synthesis of quinazolines using ZIF-67 as an efficient heterogeneous catalyst, RSC Advances 5(31) (2015) 24769-24776. https://doi.org/10.1039/C4RA16168H.

[41] M. Thommes, K. Kaneko, A.V. Neimark, J.P. Olivier, F. Rodriguez-Reinoso, J. Rouquerol, K.S.W. Sing, Physisorption of gases, with special reference to the evaluation of surface area and pore size distribution (IUPAC Technical Report), 87(9-10) (2015) 1051-1069. https://doi.org/doi:10.1515/pac-2014-1117.

[42] T.J. Bandosz, Revealing the impact of small pores on oxygen reduction on carbon electrocatalysts: A journey through recent findings, Carbon 188 (2022) 289-304. https://doi.org/https://doi.org/10.1016/j.carbon.2021.11.071.

[43] A. Gabe, R. Ruiz-Rosas, C. González-Gaitán, E. Morallón, D. Cazorla-Amorós, Modeling of oxygen reduction reaction in porous carbon materials in alkaline medium. Effect of microporosity, Journal of Power Sources 412 (2019) 451-464. https://doi.org/https://doi.org/10.1016/j.jpowsour.2018.11.075.

[44] L. Du, G. Zhang, X. Liu, A. Hassanpour, M. Dubois, A.C. Tavares, S. Sun, Biomass-derived non-precious metal catalysts for oxygen reduction reaction: The demand-oriented engineering of active sites and structures, 2(4) (2020) 561-581. https://doi.org/https://doi.org/10.1002/cey2.73.

[45] M.M. Mohideen, Y. Liu, S. Ramakrishna, Recent progress of carbon dots and carbon nanotubes applied in oxygen reduction reaction of fuel cell for transportation, Applied Energy 257 (2020) 114027. https://doi.org/10.1016/j.apenergy.2019.114027.

[46] X.-M. Qu, S.-H. Yin, Y.-N. Yan, J. Yang, Y.-R. Li, X.-Y. Cheng, F. Lu, C.-T. Wang, Y.-X. Jiang, S.-G. Sun, In-situ growth of carbon nanotubes for improving the performance of Co-N/C catalysts in proton exchange membrane fuel cell, Chemical Engineering Journal 461 (2023) 142054. https://doi.org/10.1016/j.cej.2023.142054.

[47] W. Yuan, F. Zhang, Y. Wu, X. Chen, C. Fang, C. Li, Point-Defect-Rich Carbon Sheets as the High-Activity Catalyst Toward Oxygen Reduction and Hydrogen Evolution, 9(4) (2019) 386.

[48] M. Melchionna, P. Fornasiero, M. Prato, Into the carbon: A matter of core and shell in advanced electrocatalysis, APL Materials 8(2) (2020). https://doi.org/10.1063/1.5134466.

[49] D. Kourtidou, D. Karfaridis, T. Kehagias, G. Vourlias, D.N. Bikiaris, K. Chrissafis, Incorporating Graphene Nanoplatelets and Carbon Nanotubes in Biobased Poly(ethylene 2,5-furandicarboxylate): Fillers’ Effect on the Matrix’s Structure and Lifetime, 15(2) (2023) 401.

[50] Y.C. Chiang, W.H. Lin, Y.C. Chang, The influence of treatment duration on multi-walled carbon nanotubes functionalized by H_2SO_4/HNO_3 oxidation,Applied Surface Science 257(6) (2011) 2401-2410. https://doi.org/10.1016/j.apsusc.2010.09.110.

[51] Ö. Metin, S. Özkar, Hydrogen Generation from the Hydrolysis of Ammonia-borane and Sodium Borohydride Using Water-soluble Polymer-stabilized Cobalt(0) Nanoclusters Catalyst, Energy & Fuels 23(7) (2009) 3517-3526. https://doi.org/10.1021/ef900171t.

[52] M. Chen, R. Xiong, X. Cui, Q. Wang, X. Liu, SiO2-Encompassed Co@N-Doped Porous Carbon Assemblies as Recyclable Catalysts for Efficient Hydrolysis of Ammonia Borane, Langmuir 35(3) (2019) 671-677. https://doi.org/10.1021/acs.langmuir.8b03921.

[53] M. Ayiania, M. Smith, A.J.R. Hensley, L. Scudiero, J.-S. McEwen, M. Garcia-Perez, Deconvoluting the XPS spectra for nitrogen-doped chars: An analysis from first principles, Carbon 162 (2020) 528-544. https://doi.org/10.1016/j.carbon.2020.02.065.

[54] S. Kabir, K. Artyushkova, A. Serov, P. Atanassov, Role of Nitrogen Moieties in N-Doped 3D-Graphene Nanosheets for Oxygen Electroreduction in Acidic and Alkaline Media, ACS Applied Materials & Interfaces 10(14) (2018) 11623-11632. https://doi.org/10.1021/acsami.7b18651.

[55] M. Skorupska, A. Ilnicka, J.P. Lukaszewicz, The effect of nitrogen species on the catalytic properties of N-doped graphene, Scientific Reports 11(1) (2021) 23970. https://doi.org/10.1038/s41598-021-03403-8.

[56] M.A. Pimenta, G. Dresselhaus, MS Dresselhaus, L.G. Cançado, A. Jorio, R. Saito, Studying disorder in graphite-based systems by Raman spectroscopy, Physical Chemistry Chemical Physics 9(11) (2007) 1276-1290. https://doi.org/10.1039/B613962K.

Chapter-4

Metal-organic Frameworks Enabled Tailoring of Contact Electrification in a Triboelectric Nanogenerator for Harnessing Mechanical Energy
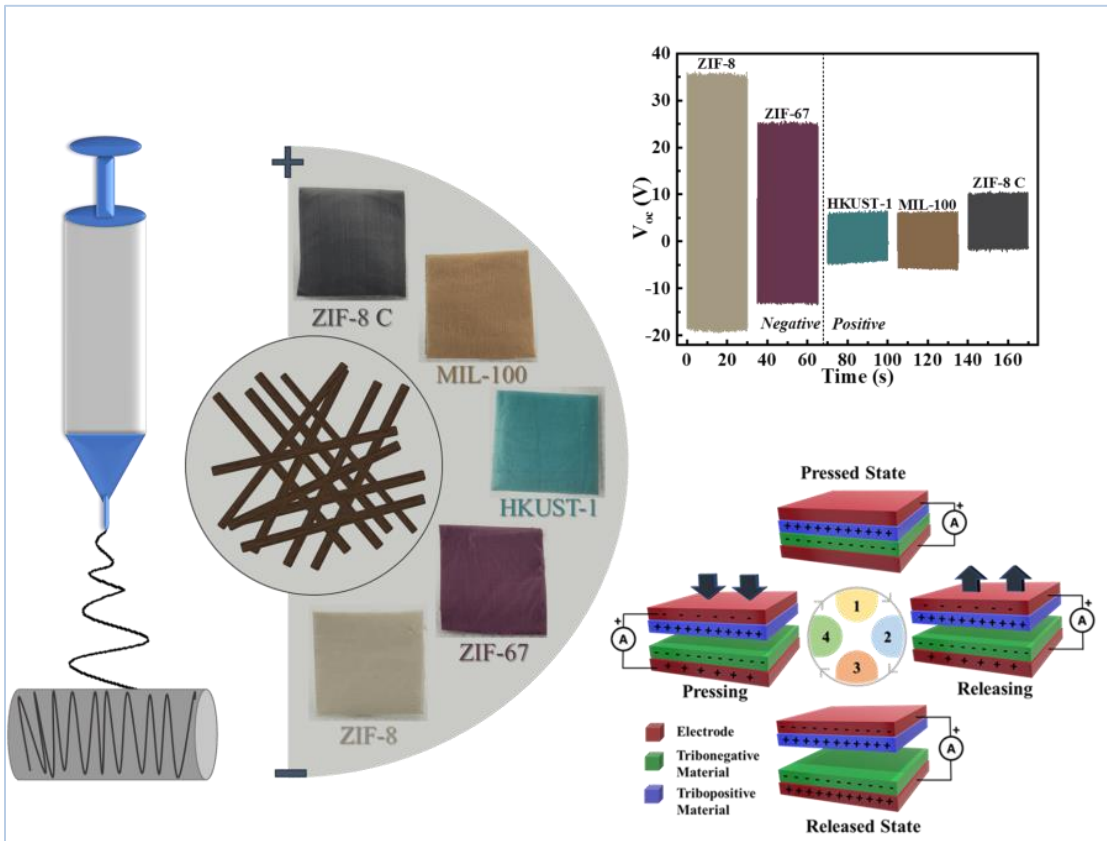
Abstract

Polymer materials are widely employed in triboelectric applications due to their flexibility and easy fabrication methods. However, their low output is still a challenge that limits their applications in triboelectric devices. Porous metal-organic frameworks attracted significant attention as a contact material for triboelectric devices due to their surface charges and higher output by virtue of their capability to hold charges in porous surfaces. Herein, for the first time, we have utilized different MOF materials, such as ZIF-8, ZIF-67, MIL-100, and HKUST-1, to tune the triboelectric properties of PAN fibre by incorporating them during the electrospinning process. Based on the nature of the ligand, the amount of the MOF loading, and the particle size, the triboelectric behaviour of the PAN material changes, and even a reversal of the triboelectric polarity is achieved. The ZIF-8 and MIL-100 showed opposite trends, and the pair generated an open-circuit output voltage of 100 V, short-circuit current of 1.35 μA, and a power density of 18.4 mW/m^2, respectively. It can be utilized for powering small electronic gadgets as well as self-powered tactile sensing applications. The effect of carbonization on MOF is also evaluated, where it was found that the carbonization of ZIF-8 reversed the triboelectric polarity of PAN nano fibres by incorporating the same as compared to the pristine ZIF-8. Incorporation of MOF into the triboelectric contact layer thus demonstrated to be an efficient method to enhance and tune the triboelectric properties of polymer materials such as PAN.

4.1. Introduction

The rapid revolution in portable and wearable devices has made a breakthrough in energy-related sectors. Triboelectric nanogenerators (TENGs), devices that convert mechanical energy into electricity by virtue of charge transfer by the contact of any two materials of opposite tribo polarity, are considered the next generation's energy conversion devices due to their simple design-operation mode and cost-effective implementation. Over the past few years, TENG devices have been widely explored in developing biosensors, self-powered electronics, sensors, etc. Moreover, the adaptability of the TENG to perform with a broad range of combinations of materials led to a rise in research interests in fabricating different types of materials for TENG applications.[1-3]

Polymer-based materials are utilized as triboelectric materials due to their flexibility, lightweight and easy fabrication methods.[4-7] However, their thermal and mechanical stability and low output are still challenging aspects that limit their application. The methods commonly employed to optimize the output of the polymer-based materials, include tuning the morphology, functionalizing the polymer chains, doping, and adding inorganic fillers.[8, 9] The addition of inorganic fillers such as 2-D materials and metallic oxides was found to improve the output of the TENGs as well as enhance the triboelectric performance of the parent polymer. [10-12] The fabrication methods of the polymer layer are another aspect that affects the triboelectric behavior of a particular polymer. Electrospun polymer fibres have shown prominence due to their enhanced surface area and surface roughness, which can impart better contact and lead to better triboelectric performance. It has been reported that polymers in the form of fibres can impart better strength and stability compared to other morphologies.[11, 13, 14] Polyacrylonitrile (PAN) is a dielectric polymer with low conductivity that is widely used in the electrospinning process in the form of composite fibres and carbon fibres.[15, 16] The properties of electrospun fibres, such as thickness and morphology, can be modulated by the applied voltage and solution parameters. [17-20]

Recently, porous materials have also found attention in triboelectric devices due to the capability of such materials to hold charges for a long time, which in turn can improve triboelectric performance. Metal-organic frameworks (MOFs) are demonstrated as contact materials for TENG applications in self-powered electronics and sensing applications. [21-23] Metal-organic frameworks, which are the frameworks formed by the

coordination of metal ions surrounded by organic linkers, possess high thermal and mechanical stability and are highly porous by virtue of the 3-D linkage between the metal and the organic moieties. Due to the presence of metal and other elements in the framework, MOFs can create free charges on the surface and act as triboelectric materials.[24-26] The high surface area and porous features of MOFs can facilitate an enhanced contact surface between the tribo-layers. Due to their structure tunability and porous features, MOF-based materials can be exploited in many ways, like functionalization, doping, and bimetallic MOFs are also prepared to modulate the triboelectric behaviour. However, it demands systematic investigation on fabricating such powder materials to achieve its maximum efficiency. MOFs are fabricated as triboelectric layers by dip coating method, film formation, etc. Even though electrospun MOF-polymer fibre materials have been widely used, it is not explored that much in triboelectric devices. [10, 27-32] The features of electrospun MOF-polymer fibre will depend upon the choice of the polymers. Hence, a systematic study is needed to understand the change in polymer material behaviour upon MOFs incorporation. However, developing sustainable MOFs is also essential for effectively utilizing such materials in wide scale applications.

In the present work, we have successfully demonstrated the tuning of triboelectric properties of electrospun Polyacrylonitrile fibres using different metal-organic frameworks and MOF-derived carbon. Herein, four metal-organic frameworks were prepared by facile solvothermal, hydrothermal, and precipitation methods and incorporated into PAN fibres during electrospinning. The changes in the triboelectric properties of MOFs were recorded and are positioned in the triboelectric series. The triboelectric nature of the electrospun PAN fibre varied with the incorporation of different MOFs and was found to depend upon the features of the incorporated MOFs, such as particle size, morphology as well as the coordinated ligand, as they can directly influence the charge transfer efficiency upon contact. The triboelectric output also was enhanced upon the % of MOF incorporation, elucidating the inevitable role of MOFs in tuning the triboelectric nature of PAN polymer.

4.2. Experimental

4.2.1. Materials

Zn(NO$_3$)$_2$.6 H$_2$O($\geq$ 98%, Sigma-Aldrich), Co (NO$_3$)$_2$. 6 H$_2$O($\geq$ 98%, Sigma-Aldrich), 2-Methylimidazole (2-MeIm, C$_4$H$_6$N$_2$, 98%, Sigma-Aldrich), Fe(NO$_3$)$_3$.9 H$_2$O ($\geq$ 98%, Sigma-Aldrich), Cu(NO$_3$)$_2$ · 3 H$_2$O, Trimesic acid (H$_3$BTC, 95 %, Sigma-Aldrich), Polyacrylonitrile (Sigma-Aldrich, Mw: 150000), N, N-Dimethyl Formamide (DMF, 99 %, HPLC. PVT.LTD) were used as received.

4.2.2. Preparation of ZIF-8 & ZIF-67:

ZIF-8 and ZIF-67 are frameworks formed by coordinating Zn^{2+} and Co^{2+} with the 2-methylimidazole ligands, respectively. ZIF-8 & ZIF-67 nanoparticles were synthesized according to a room temperature synthesis method reported.[33, 34] Initially, Zn (NO$_3$)$_2$. 6 H$_2$O or Co(NO$_3$)$_2$. 6 H$_2$O and 2-MeIm were dissolved separately in water, where the molar ratio of Zn $^{2+}$: 2-MeIm: H2O was 1:60:2228. The solutions were then mixed and allowed to stir for 3 hrs. The white/purple coloured precipitate formed was collected by centrifugation after repeated washing with distilled water followed by methanol. The ZIF-8 powder was collected after drying under vacuum conditions at 60 ℃.

4.2.3. Synthesis of MIL-100 (Fe)

MIL-100 (Fe) was synthesized according to a reported hydrothermal method. Fe(NO$_3$)$_3$.9 H$_2$O and Trimesic acid were taken in 1.5:1 ratio and ground in an agate mortar until the mixture was uniform. Then the mixture was transferred to a hydrothermal vessel and kept at 160 °C for 4 h. The obtained orange powder was collected after washing with distilled water and ethanol.[35]

4.2.4. Synthesis of HKUST-1

HKUST-1 was prepared according to a reported solvothermal method. Initially, 1.087 g Cu(NO$_3$)$_{2.3}$ H$_2$O and 0.525 g Trimesic acid were dissolved in 15 mL water and 15 mL ethanol, respectively. Then the two solutions were mixed by stirring for 30 minutes. It was then placed in a hydrothermal chamber and heated at 120 °C for 12 h. The formed precipitate was washed thoroughly with ethanol, dried under vacuum at 60 °C, and collected. [36]

4.2.5. Synthesis of C ZIF-8

The prepared ZIF-8 powder was carbonized in the temperature range of 900 °C for 2 h under a nitrogen atmosphere at a heating rate of 5 °C/min and cooled to obtain the N- doped porous carbon. The resulting carbon was then soaked in 1 M HCl at room temperature overnight, followed by washing multiple times with deionized water to remove unreactive species from the surface of the carbon.[37]

4.2.6. Preparation of MOF /PAN fibre composite

Initially, 2 g of Polyacrylonitrile was dissolved in 24 ml DMF at 40 °C. Then, 0.5 g of synthesized MOF was added to the solution and mixed well in a magnetic stirrer for 12 h. The prepared mixture was placed in a syringe in an electrospinning chamber. The nanofibres were produced at 15 kV while maintaining a flow rate of 0.5 ml/h, and the distance between the syringe and the collector was 10 cm. The formed fibres were collected as a fibre mat on an aluminum foil.[38]

4.2.7. Fabrication of Triboelectric Nanogenerator

The nanofibre mats were taken in the required dimensions of 2 cm^2 for the positioning in the triboelectric series and 4 cm^2 for device applications. For initial characterization, pure PAN nanofibre was paired with all the other MOF/PAN composites. Different MOF/PAN composites were taken as pairs for further testing. Following that, copper leads are attached to the double-sided conducting copper tape that has been adhered to one of the surfaces of these two layers to serve as the electrode material. Then these were attached to a mylar supporting structure to form each TENG device.

4.2.8. Characterization Tools

The formation of the MOF fibre was confirmed using wide-angle X-ray diffraction (WAXD) measurements on a XEUSS SAXS/WAXS system (Xenocs) operated at 50 kV and 0.60 mA in the transmission mode using Cu Kα radiation of wavelength 1.54 Å. The functional groups of the composites were identified using Fourier transform- Infrared spectroscopy ((Perkin Elmer, FT-IR, Spectrum Two). The morphology of the samples was characterized using scanning electron microscopy (JEOL, JSM-35) operated at 15 kV and transmission electron microscopy ((HR-TEM, JEOL JEM F-200). The surface area and porous features of the samples were analyzed using a BET surface area analyzer

(Micrometrics, Tristar II, and USA). The elemental compositions of the samples were carried out using SEM-EDS and X-ray photoelectron spectroscopy (ULVAC-PHI Inc., USA). The triboelectric performance was evaluated with the help of a custom-made force imparting system, a source measurement unit (Keithley 2450 SMU, Tektronix), and a low-noise current preamplifier (SR570, Stanford Research).

4.3. Results and Discussion

4.3.1. Wide-Angle X-ray Scattering (WAXS)

Initially, the MOFs, ZIF-8 and ZIF-67 were synthesized by room temperature precipitation methods in the aqueous phase, and MIL-100 and HKUST-1 were synthesized by hydrothermal and solvothermal methods, respectively. These MOFs can be categorized into two sets according to the common ligands. The ZIF-8 and ZIF-67 frameworks, the Zeolitic imidazolate frameworks with sodalite topology, are formed by the coordination of zinc and cobalt ions with 2-methylimidazole, respectively. MIL-100 (Fe) and HKUST-1 are different classes of MOFs formed by the coordination of trimesic acid with the metal ions Fe and Cu, respectively. These MOFs were electrospun with PAN into fibre mats and tested in triboelectric devices. The 2D-Wide-angle X-ray scattering is recorded to confirm the formation of MOFs and fibres. The XRD peaks of electrospun PAN fibre showed distinguishable diffraction peaks at 17 ° and 29 ° corresponding to the (100) and (110) crystal planes, respectively (**Figure 1**).[39]
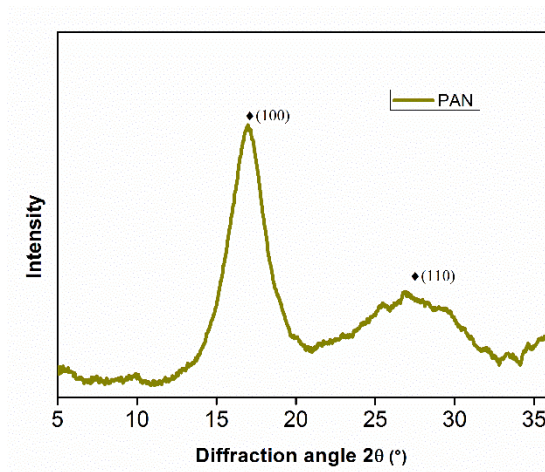
Figure 1. Wide-Angle X-ray Scattering pattern of electrospun PAN fibre

The XRD patterns of ZIF-8 and ZIF-67 resembled each other and were aligned with the sodalite topology of the ZIFs, as reported.[40] The XRD pattern of MIL-100 (Fe) and

HKUST-1 also resembled the pure phases of MOFs.[40-42] All the MOF-incorporated PAN fibres exhibited the XRD peaks of pristine MOF, suggesting that the phase of MOFs is not changed upon fibre formation (**Figure 2**). The XRD peaks of PAN were not visible in the composite fibres except in MIL-100 PAN fibres, possibly attributed to the highly crystalline nature of all other MOFs, which shielded the diffraction from the planes of PAN. However, the (100) plane of PAN fibre was visible at 17 ° in the MIL-100 PAN fibres due to the absence of crystalline peaks of MIL-100 in that particular 2θ range. The detailed positioning of the XRD peaks of MOFs is marked in **Table 1**.
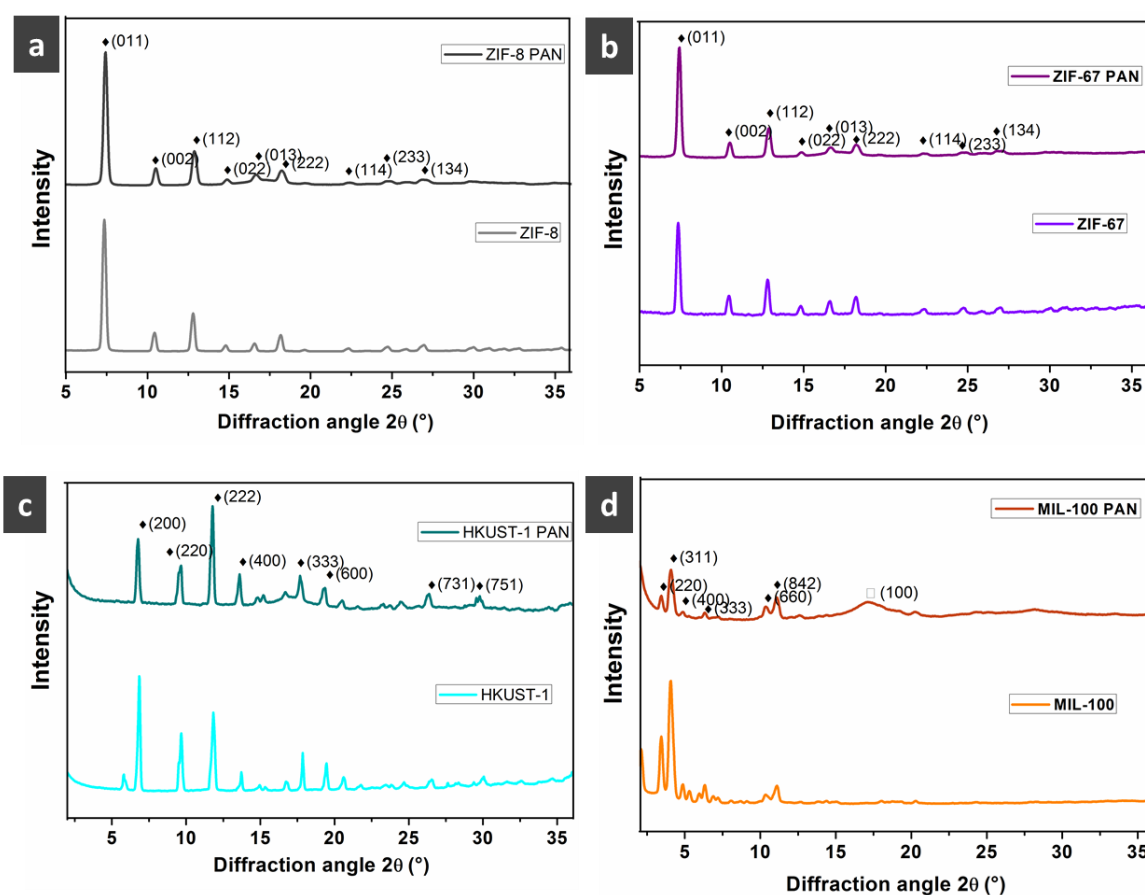
Figure 2. Wide-Angle X-ray Scattering pattern of electrospun MOFs and the corresponding MOF incorporated PAN fibres; a) ZIF-8, b) ZIF-67, c) HKUST-1, and d) MIL-100

Table 1. XRD peak positions of synthesized metal-organic frameworks

ZIF-8		ZIF-67		MIL-100		HKUST-1	
2θ (°)	hkl	2θ (°)	hkl	2θ (°)	hkl	2θ (°)	hkl
7.3	(011)	7.3	(011)	3.4	(220)	6.7	(200)
10.4	(002)	10.4	(002)	4.1	(311)	9.5	(220)
12.8	(112)	12.8	(112)	4.8	(400)	11.7	(222)
14.8	(022)	14.8	(022)	6.3	(333)	13.5	(400)
16.5	(013)	16.6	(013)	10.3	(440)	17.6	(333)
18.1	(222)	18.2	(222)	11.1	(422)	19.2	(600)
22.2	(114)	22.3	(114)	---------	---------	26.2	(731)
24.6	(233)	24.6	(233)	---------	---------	29.5	751)
26.8	(134)	26.8	(134)	---------	-------	---------	-------

4.3.2. FT-IR analysis

In order to understand the structural properties of the formed fibres, the FT-IR spectra of the MOFs, PAN fibre, and MOF fibre composites were recorded (**Figure 3**). The composite of ZIF-8 and ZIF-67 exhibited peaks of functional groups corresponding to the metal-imidazolate coordination. A slight shift in the peak position was observed, probably due to the replacement of Zn with cobalt which differs in size. The band at 420 cm^{-1} corresponds to the Zn-N stretching vibration of ZIF-8. The bands at 690-1145 cm^{-1} correspond to the bending of the HmIm ring and aromatic sp^2 C-H bending, respectively. The peak at 1310 cm^{-1} corresponds to the entire ring stretch, and the peak at 1450 cm^{-1} is due to the C-H bending of the methylene group. The band at 1580 cm^{-1} corresponds to the C=N stretching vibrations. The peaks of ZIF-8 PAN and PAN fibres at 2240 cm^{-1} are due to the C≡N stretching of PAN fibre chains. The bands at 2930 cm^{-1} and 3130 cm^{-1} correspond to aliphatic and aromatic C-H bond stretching, respectively. [43-45]
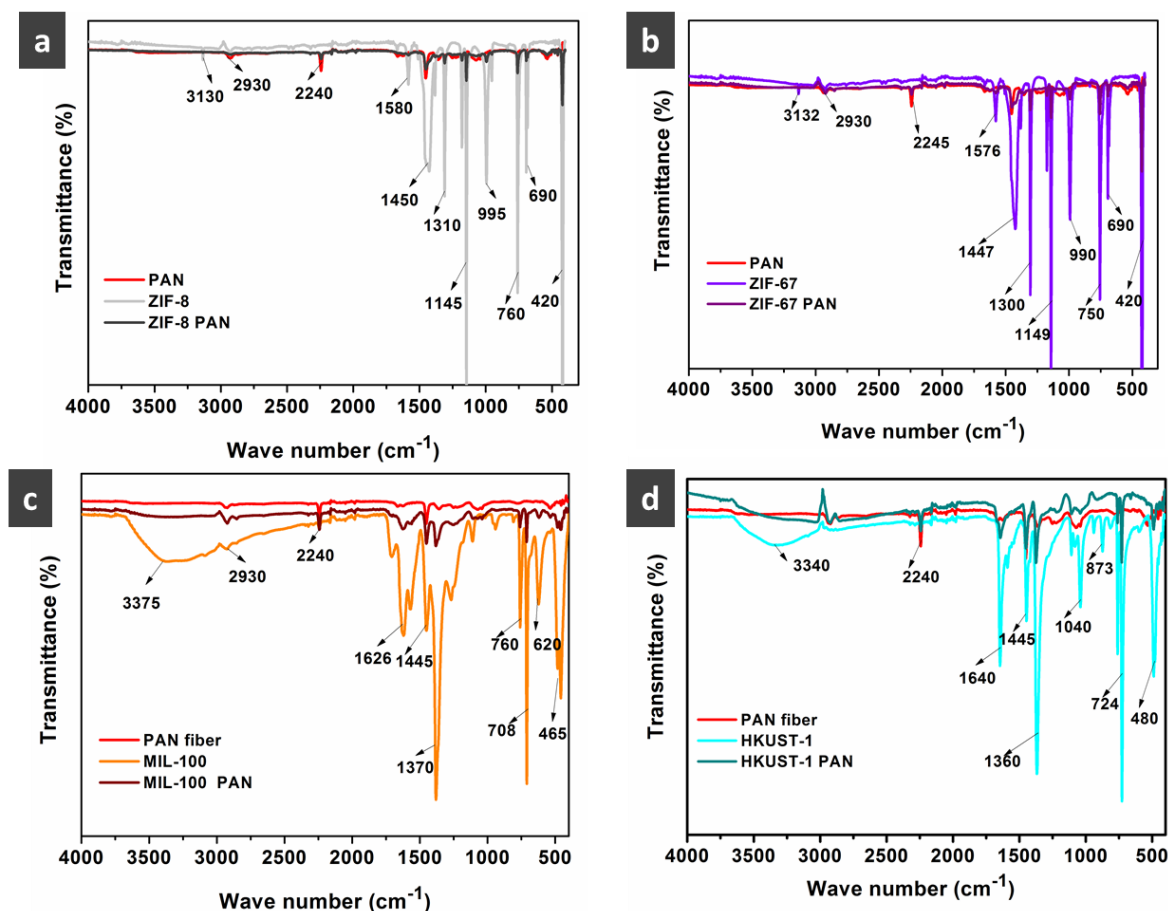
Figure 3. FT-IR patterns of electrospun MOFs and the corresponding MOF incorporated PAN fibres ; a) ZIF-8, b) ZIF-67, c) MIL-100, and d) HKUST-1

The other MOFs, HKUST-1, MIL-100, and their fibre form exhibited all the characteristic peaks of the metal-trimesic acid frameworks. The MIL–100 PAN fibre composites exhibited bands at 465 cm^{-1}, 620 cm^{-1}, 708 cm^{-1}, 760 cm^{-1}, 1370 cm^{-1}, 1445 cm^{-1}, 1626 cm^{-1}, 2240 cm^{-1}, 2930 cm^{-1} and 3375 cm^{-1}. The peak at 465 cm^{-1} corresponded to the Fe-O stretching vibrations. The peaks at 1370 cm^{-1}, 1445 cm^{-1}, and 1626 cm^{-1} corresponded to the symmetric and asymmetric vibrations of the O-C-O bonds and the C=O stretching vibration of the carboxylate groups, respectively. [46] HKUST-1 PAN fibre exhibited peaks at 480 cm^{-1}, 724 cm^{-1}, 873 cm^{-1}, 1040 cm^{-1}, 1360 cm^{-1}, 1445 cm^{-1}, 1630 cm^{-1}, 2240 cm^{-1} and 3340 cm^{-1}. The peak at 724 cm^{-1} corresponded to the Cu-O stretching along with the C-O and C=O vibrations at 1360 cm^{-1}, 1445 cm^{-1}, and 1630 cm^{-1}. [47]

4.3.3. Morphology and structure analysis
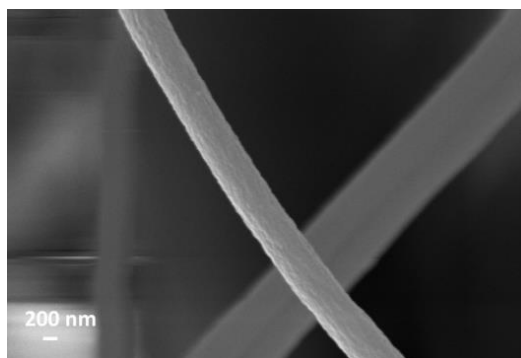
Figure 4. SEM image of PAN fibre
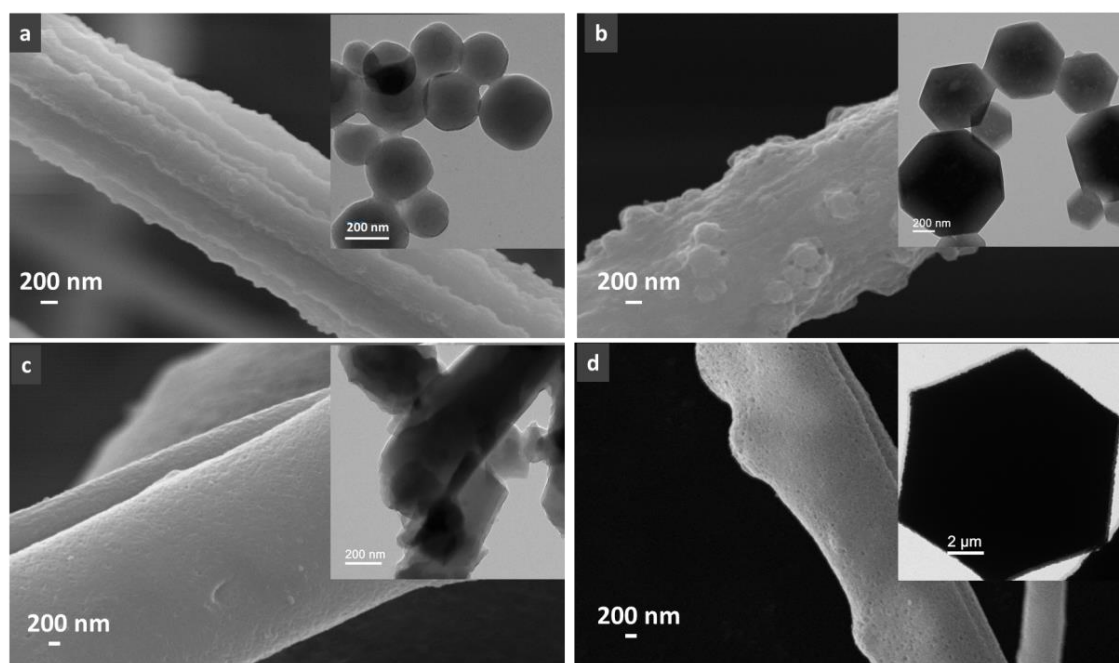
Figure 5. SEM images of MOF-incorporated PAN fibre a) ZIF-8 PAN, b) ZIF-67 PAN, c) MIL-100 PAN, and d) HKUST-1 PAN. The inset shows the TEM images of the corresponding MOF particles.

The morphological features of the MOFs and fibre composites were analyzed by Scanning electron microscopy (SEM) and Transmission electron microscopy (TEM). The TEM images evidence the morphology of the MOF particles. ZIF-8 and ZIF-67 were observed as nanometer particles with hexagonal morphology. ZIF-8 particles were observed as =200 nm size hexagons while ZIF-67 was $\approx$ 500 nm in dimension. The MOFs formed by the coordination with trimesic acid were seen in micrometer size. MIL-

100 (Fe) was seen as particles of dimension ≈ 3 μm, and HKUST-1 was also seen as hexagonal particles with dimensions of 7 μm (**Figure 5(inset)**).

The fibrous morphology of the composites was visible from the scanning electron microscopy. PAN fibres were~ 300 nm in diameter (**Figure 4**). The ZIF-8 PAN and ZIF-67 PAN were observed as particles decorated on the fibres. However, no particles were seen on MIL-PAN and HKUST-PAN, probably due to the large size of these particles (**Figure 5 (a-d)**).

The SEM-EDS was used to elucidate the surface elemental compositions of the PAN fibre, and MOF-incorporated PAN fibre composites. The PAN fibre contains C, N, and O in the 66 %, 27 %, and 6 % atomic percent ratios, respectively. The presence of oxygen in the electrospun fibre might be attributed to the partial adsorption of oxygen gas on the surface of PAN, which may give rise to surface roughness.[48] The quantification of different elements in PAN fibres is listed in **Figure 6**.

Element	Weight%	Atomic%
C	62.70	66.80
N	29.61	27.05
O	7.69	6.15
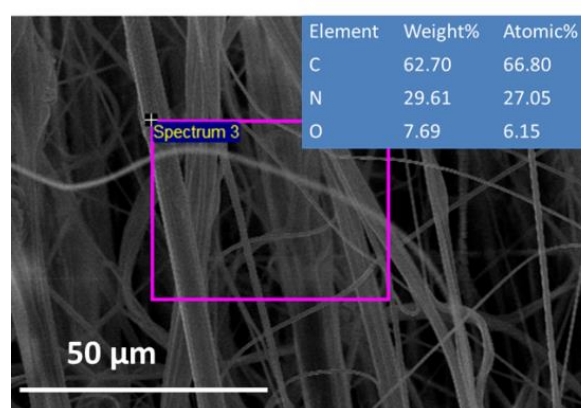
Figure 6. SEM-EDS analysis of PAN fibres along with elemental composition

Apart from the elements of PAN, MOF-PAN composites showed the presence of metal ions belonging to respective metal-organic frameworks, indicating the successful incorporation of MOF into the PAN fibre. The presence of Zn in ZIF-8, Co in ZIF-67, Fe in MIL-100 (Fe), and Cu in HKUST-1 were 1.68, 1.72, 0.34, and 0.55 at %, respectively. The surface elemental content in MIL-100 (Fe) and HKUST-1 was less than in ZIF frameworks due to the large size of the individual particles, which reduces the intensity of available MOF particles in a particular area (**Figure 7**).
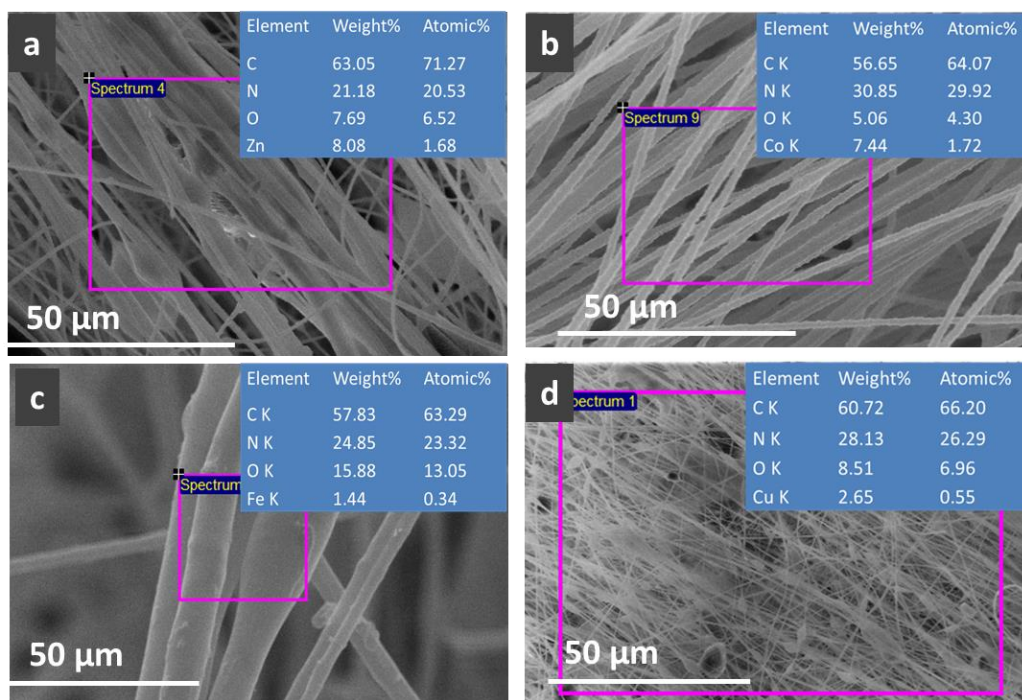
Figure 7. SEM-EDS analysis of MOF incorporated PAN fibres along with elemental composition; a) ZIF-8 PAN, b) ZIF-67 PAN , c) MIL-100 PAN, and d) HKUST-1 PAN**.**

The SEM-elemental mapping revealed the distribution patterns of elements of MOF and PAN in the electrospun fibres **(Figure 8)**. The elemental distribution of ZIF-8 PAN and ZIF-67 PAN showed a uniform pattern for all the elements. However, In the case of MIL-100 PAN and HKUST-1 PAN, some agglomerated distribution of Fe and Cu metals was observed, evidencing the reports that the electrospinning of large particles creates agglomerated droplets reducing its uniformity.[21, 49]
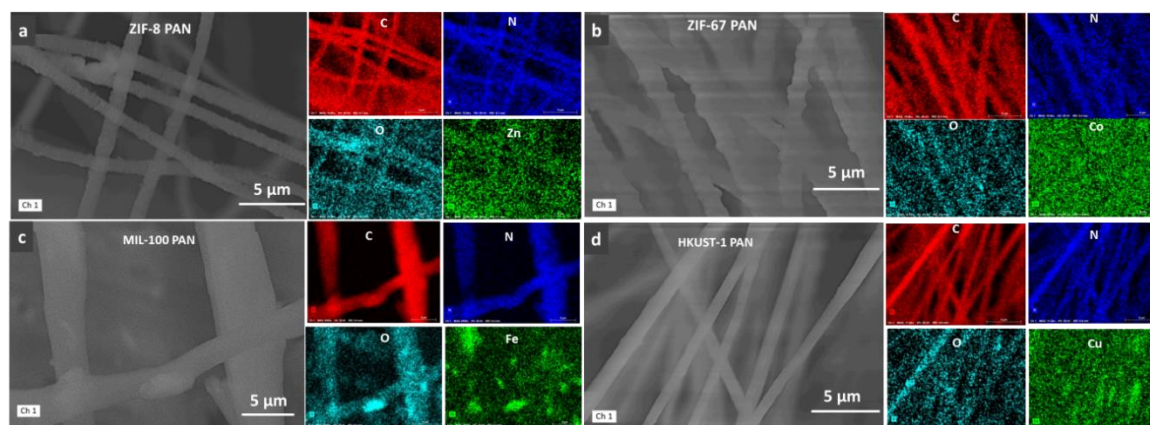
Figure 8. SEM- elemental distributions of; a) ZIF-8 PAN, b)ZIF-67 PAN, c) MIL-100 PAN and d) HKUST-1 PAN

4.3.4. Surface area analysis

In order to understand the porous features of the samples, BET N_2 adsorption-desorption isotherm was measured. All the MOFs exhibited a high surface area value, and the isotherms were predominately of microporous features (**Figure 9a**). The surface area values of ZIF-8, ZIF-67, MIL-100, and HKUST-1 were 1385, 782, 1124, and 1090 m^2/g, respectively(**Table 2**). The electrospun PAN fibre exhibited a surface area value of $\approx$ 8 m^2/g. It is to be noted that the incorporation of MOFs could improve the surface area of PAN fibres drastically. The BET isotherm of the MOF-PAN fibre composite showed isotherm patterns of both MOF and PAN fibre (**Figure 9b**). Among these, the sample ZIF-8 PAN fibre exhibited a higher surface area value of 331 m^2/g with predominately micropores. The fibre sample MIL-100 PAN exhibited the least surface area among all, which might be attributed to the fact that, as observed from the TEM, due to the stick-like morphology of MIL-100, the particle might be get aligned to the PAN fibres, thereby reducing the surface roughness that, intern reduces the surface area. These high surface areas and porosity are beneficial for higher output in TENG devices owing to the ability of the pores to hold charges. [23]
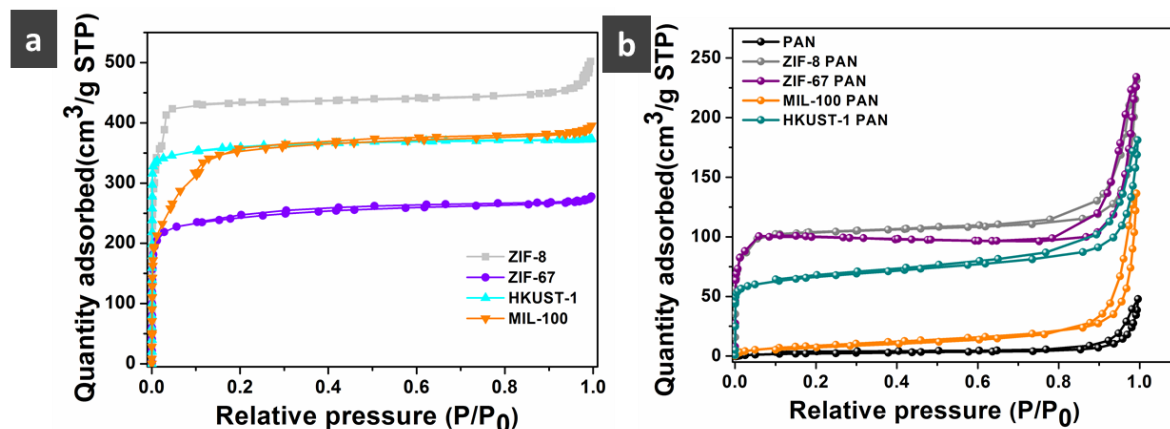
Figure 9. N_2 adsorption-desorption isotherms of a) Synthesized MOF samples and b) PAN fibre and MOF-incorporated PAN fibres

Table 2. Surface area and porosity of MOFs and electrospun fibres

Sample	Surface area (m²/g)	Pore volume (cm³/g)	Sample	Surface area (m²/g)	Pore volume (cm³/g)
ZIF-8	1385	0.12	ZIF-8 PAN	331	0.21
ZIF-67	782	0.08	ZIF-67 PAN	303	0.24
HKUST-1	1090	0.04	MIL-100 PAN	33	0.21
MIL-100	1124	0.10	HKUST-1 PAN	218	0.20

4.3.5. Output Characteristics of MOF-based TENGs

For sustainable development, future implantable devices based on TENGs and biodegradable sensors may employ porous, non-toxic MOFs. In the present study, the distinctive structural tunability offered by MOFs on Polyacrylonitrile (PAN) was used to optimize the energy conversion. Initially, a contact separation (CS) mode flexible TENG structure [50] was chosen to characterize the performance of these MOF-incorporated PAN fibres. The working of a CS-TENG can be summarised as depicted schematically in **Figure 10a**. At first, the layers are free of charges, but when the TENG is subjected to an external force, they come into contact with one another, and triboelectric charges are produced on them. According to the contact electrification behaviour, each contact layer becomes positive and negative. The charge disparity is the outcome when the layers separate after the withdrawal of the external force, and the shared charges get trapped due to the barrier potential. To combat this, charges are produced on the electrodes, and if an external circuit links them together, a unidirectional current will flow through the same. The current flow ceases when maximum separation is reached, and this point corresponds to the maximum potential difference between the electrodes for a TENG. When the layers come together again under an applied force, the current will flow again in the opposite direction. This cycle continues till the cyclic mechanical force subsides, resulting in continuous alternating electrical energy generation from this cyclic mechanical input.
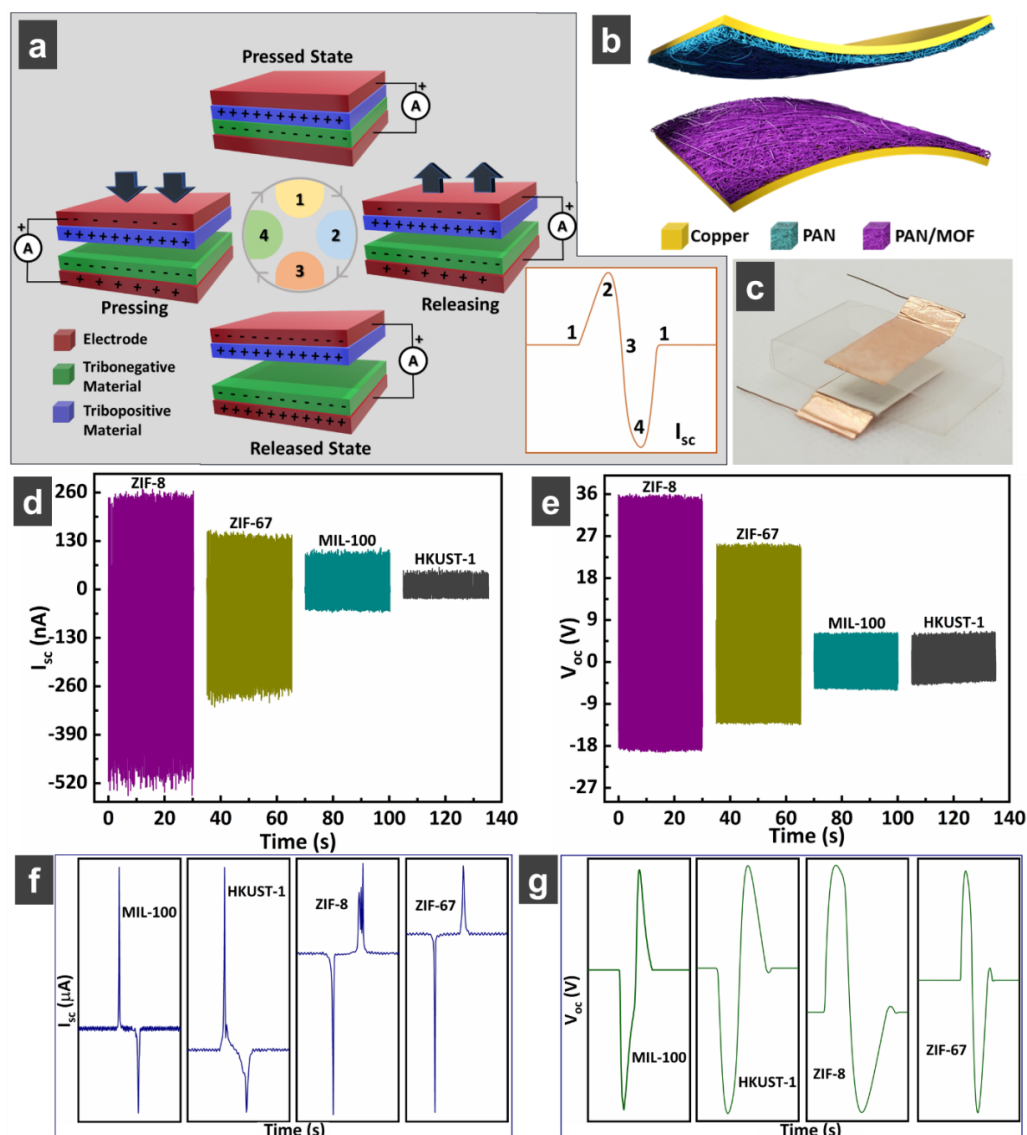
Figure 10. a)Schematic depiction of working of a contact separation mode TENG. b) Schematic and c) photograph of the fabricated MOF/PAN TENG. d) Short-circuit current and e) open-circuit voltage of different MOF-incorporated composite fibres against PAN. The individual signal symmetry in f) short-circuit current as well as (g) open-circuit voltage of each TENG.

The structure of the proposed device is shown in **Figure 10b**, where the photograph represents the original device fabricated with a 2 cm^2 contact area (**Figure 10c**). Initially, to understand the triboelectric nature of the composite fibres, they were paired against pure PAN fibres, and the corresponding outputs were evaluated. The short-circuit current and the open-circuit voltage obtained are depicted in **Figure 10d** and **Figure 10e**, respectively. The higher output is obtained for ZIF-8 incorporated nanofibre, followed by ZIF-67, then MIL-100, and finally HKUST-1. The maximum output of ZIF-8 is 35 V

and 540 nA, respectively, for output voltage and current. Adding MOF particles (25 wt %) into nanofibre enhances the output performance. The relative triboelectric nature of the films involved can be identified by analyzing the obtained output current for a lower frequency and input force (mild finger tapping),. In the case of ZIF-8 incorporated nanofibre, the positive terminal of the measurement system is connected to the electrode on the PAN side. It is clear from the output signal that (**Figure 10f**) the initial current pulse is towards the negative side, indicating that, during the pressing stage of a CS-TENG, the current flows from the ZIF-8 incorporated side towards the PAN side. The schematic representation(**Figure 10a**) shows that pure PAN is relatively positive compared to ZIF-8 PAN fibre. Thus, the incorporation of ZIF-8 tuned the triboelectric nature of the PAN fibre. A similar trend is observed for ZIF-67 incorporated fibre, where the current signal indicates the tribopositivity of pure PAN compared to the ZIF-67 incorporated one. However, the behaviour was completely opposite in the case of MIL-100, and HKUST-1 incorporated PAN fibres. A similar trend is shown by these materials in voltage signal also (**Figure 10g**). This evidences that the surface triboelectric polarity of the PAN nanofibres can be tailored by incorporating the MOF particle such as ZIF-8, ZIF-67, MIL-100, and HKUST-1.
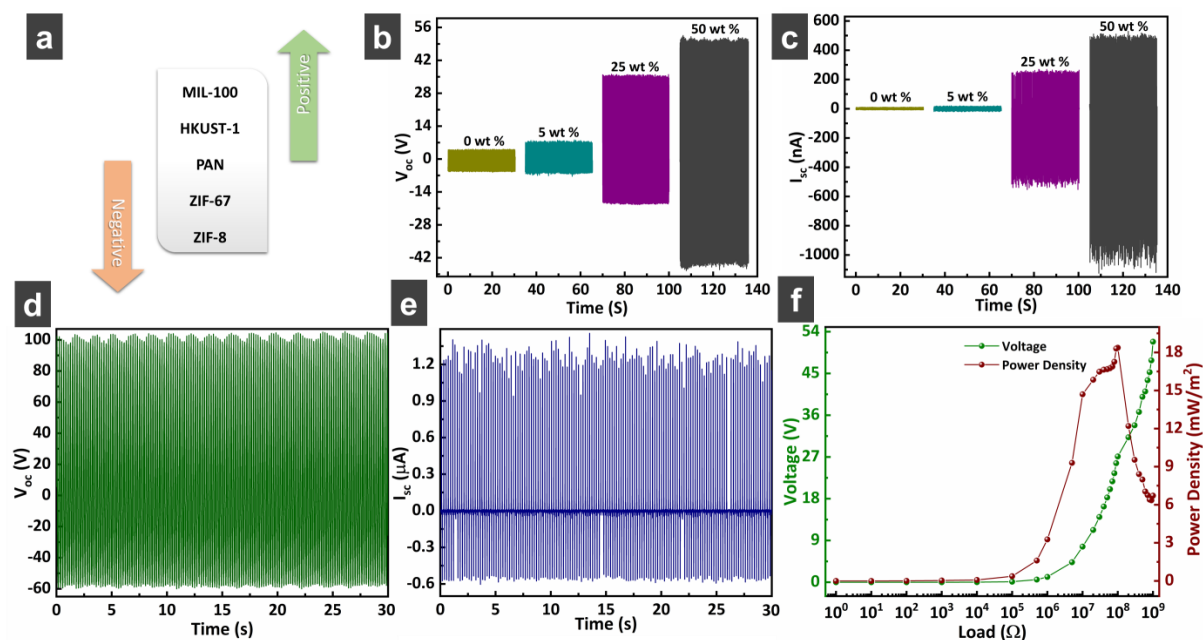
Figure 11. (a) Qualitative triboelectric series of MOF incorporated PAN. (b) open circuit voltage and (c) short-circuit current of ZIF-8 incorporated composite film at different concentrations against pure PAN nanofibre, (d) Open-circuit voltage, (e) short-circuit current, and (f) power density of MIL-100/PAN fibre against ZIF-8/PAN fibre.

Based on these findings, the MOF materials can be arranged as a qualitative triboelectric series with respect to PAN, as shown in **Figure 11a**, where MIL-100 is the most tribopositive, and ZIF-8 showed the least. Since the central metal in all MOFs belongs to the same group, it could be inferred that the triboelectric behaviour changed upon changing the coordinating ligands. A plausible reason could be attributed to the electron-donating and withdrawing power of the ligands attached to the metal in the composite fibres. The polyacrylonitrile contains nitrile functional groups with electron-deficient C and electron-rich N atoms.[8, 51] In the case of ZIF-8 and ZIF-67, the ligand molecule 2-methylimidazole is an electron-rich whereas, the C=O in carboxylate functional groups of the trimesic acid in MIL-100 and HKUST-1 is electron deficient. These MOFs can interact with the PAN in the composite through the ligands via different modes. Depending upon the types of interaction, the charge on the surface of the MOF-PAN composite fibre can be varied; hence the triboelectric nature is in opposite trends. [52-54] To further cement the fact that the addition of MOF material has an influence in tuning the triboelectric nature of the PAN fibres, different weight percentages (5, 25, and 50 wt %) of ZIF-8 incorporated PAN fibres are made. It is clear from the output performance of these devices (**Figure 11b&c**) that the open circuit voltage and short-circuit current increase linearly with the concentration of MOF particles. The maximum outputs of 50 V and 1 μA were obtained for the 50 wt % incorporation, which is the maximum weight % of MOF. This shows that the triboelectric nature of PAN can be precisely tuned via varying the MOF incorporation. Thus, incorporating MOFs is a very facile and effective method for enhancing triboelectric performance.

It is worth noting that when contact pairs are identical, a similar affinity for electrons is experienced, leading to a weaker charge transfer compared to the pairs of different materials. However, despite lower output performance, employing identical contact pairings can streamline production and guarantee uniform material qualities across the device. This will be an asset in some practical applications where concerns like cost, reliability, or scalability are prioritized. In these scenarios, the doping of MOF material is very valuable. To substantiate this point, a TENG with PAN on both sides is developed as a sustainable energy harvesting solution. Here MIL-100 and ZIF-8 are chosen as the two fillers. The choice of these two materials is apparent from their positions in the triboelectric series. Here, device fabrication is done as before, and output performance is characterized. The electrical output obtained from this pair and similar conditions is

100 V (**Figure 11d**) and 1.3 (**Figure 11e**), respectively. Similarly, the power density of this device is also measured, and the peak power density of 18.37 mW/m^2 at 100 MΩ is obtained(**Figure 11f**). This depicts the ability of the developed TENG to be a sustainable, green energy source that scavenges mechanical energy from the surroundings.
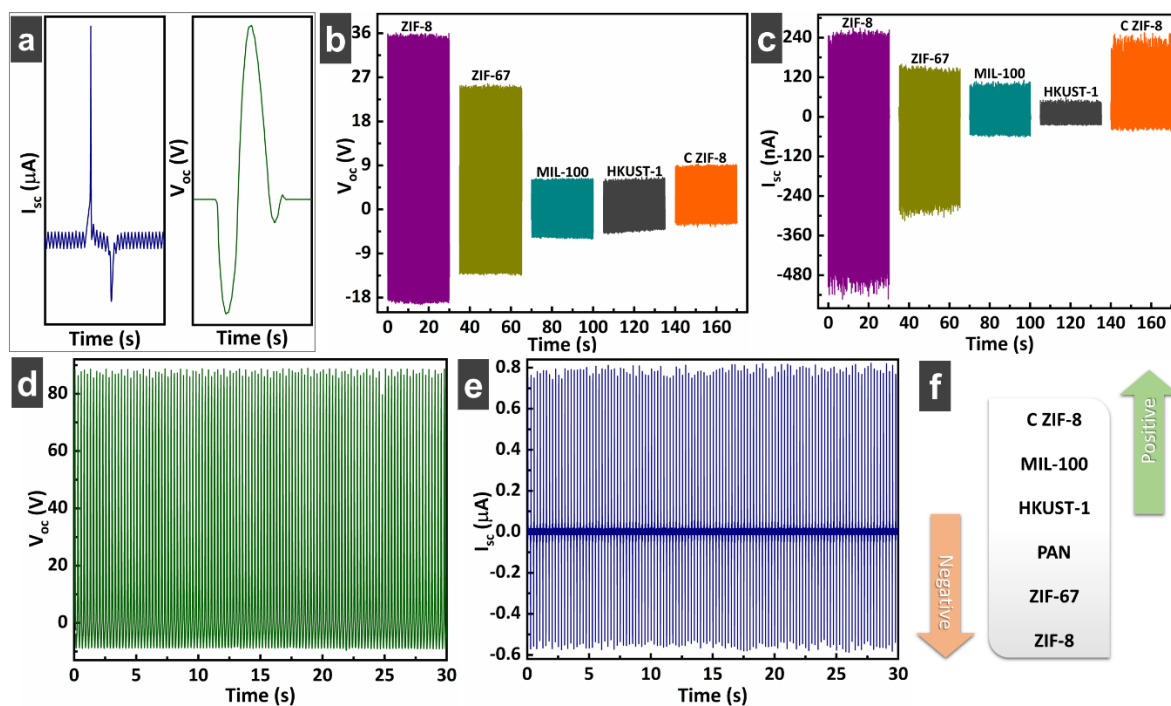
Figure 12. (a) Short-circuit current as well as open-circuit voltage of C-ZIF-8 with ZIF-8 TENG. (a) Open-circuit voltage and (c) short-circuit current of different MOF-incorporated composite fibres against PAN, including C-ZIF-8. Similarly, (d) open-circuit voltage and (e) short-circuit current of TENG having ZIF-8 against C-ZIF-8. (f) The modified triboelectric series of MOFs with C ZIF-8.

On the other hand, the carbonization of MOF will lead to heteroatom-doped porous carbon. Here, the effect of carbonization of MOF material on their ability to tune the triboelectric property of PAN polymer is studied. For this, ZIF-8 was chosen due to its greater influence on the triboelectric nature of PAN fibre among the MOF materials evaluated. ZIF-8 convertes to N-doped carbon on carbonization, as discussed in **Chapter 2**. The effect of the C-ZIF 8 on PAN was analyzed, as described in the case of MOF-incorporated PAN. Initially, the triboelectric nature of C ZIF-8 was analyzed with respect to pure PAN. As shown in **Figure 12a**, the short circuit current profile, similar to that of MIL-100, was obtained, which means that the C-ZIF 8 incorporated PAN is

triboelectrically positive compared to its pure form. It is evident that the N-doped carbon (C ZIF-8) is electron rich due to the presence of N atoms on the carbon, hence donating electrons when these two materials come together. This establishes that the carbonization of ZIF-8 can totally change the polarity of the triboelectric nature of PAN nanofibres compared to the pristine ZIF-8. Additionally, the output for C ZIF-8 compared with other earlier MOFs is represented in **Figure 12 b&c**. The difference in the triboelectric behaviour of ZIF-8 and C ZIF-8 was further analyzed by measuring the output performance of a TENG fabricated with these two materials as opposite triboelectric layers. An open circuit voltage of 85 V and short-circuit current of 800 nA was generated. Moreover, it showed that there are many possible ways to tailor the triboelectric nature of PAN via the incorporation of MOFs and MOF derivatives.

4.4. Conclusions

This study introduces a rational strategy to tailor the triboelectric nature of PAN polymer by incorporating stable MOF particles into the PAN matrix. The flexibility of PAN to incorporate various MOFs during electrospinning was utilized to fabricate flexible TENG with tuneable output performance. Moreover, the incorporation of various MOFs enabled the triboelectric nature of the PAN fibres to be tribopositive as well as tribonegative. The incorporation of ZIF-8, ZIF-67, HKUST-1, and MIL-100 has tuned the triboelectric behaviour of PAN fibres from tribonegative to the positive end. In addition, the effect of carbonization of ZIF-8 frameworks on the triboelectric nature of PAN is also evaluated. While the ZIF-8 incorporated PAN is positioned on the negative side of the pure PAN in the triboelectric series, the C ZIF-8 incorporation steered it towards the positive side. A triboelectric device was fabricated with ZIF-8, and the carbonized C ZIF-8 incorporated PAN fibres as opposite triboelectric layers. The device generated an output of 85 V and 0.8 μA. The present study thus establishes a novel method for tuning the triboelectric property of polymer materials by incorporating porous MOFs as fillers. The study can also be extended to other polymers for tuning their triboelectric nature. This method can be beneficial for advancing the fabrication of TENGs based on porous materials and polymers.

4.5. References

[1] Z. Wang, L. Lin, S. Niu, Y. Zi, Triboelectric Nanogenerators, 2016. https://doi.org/10.1007/978-3-319-40039-6.

[2] W.-G. Kim, D.-W. Kim, I.-W. Tcho, J.-K. Kim, M.-S. Kim, Y.-K. Choi, Triboelectric Nanogenerator: Structure, Mechanism, and Applications, ACS Nano 15(1) (2021) 258-287. https://doi.org/10.1021/acsnano.0c09803.

[3] W. Li, Y. Pei, C. Zhang, A.G.P. Kottapalli, Bioinspired designs and biomimetic applications of triboelectric nanogenerators, Nano Energy 84 (2021) 105865. https://doi.org/https://doi.org/10.1016/j.nanoen.2021.105865.

[4] W. Zhang, L. You, X. Meng, B. Wang, D. Lin, Recent Advances on Conducting Polymers Based Nanogenerators for Energy Harvesting, 12(11) (2021) 1308.

[5] Y. Wang, Y. Yang, Z.L. Wang, Triboelectric nanogenerators as flexible power sources, npj Flexible Electronics 1(1) (2017) 10. https://doi.org/10.1038/s41528-017-0007-8.

[6] M. Shanbedi, H. Ardebili, A. Karim, Polymer-based triboelectric nanogenerators: Materials, characterization, and applications, Progress in Polymer Science 144 (2023) 101723. https://doi.org/https://doi.org/10.1016/j.progpolymsci.2023.101723.

[7] J. Wang, J. Wang, Z. Kong, K. Lv, C. Teng, Y. Zhu, Conducting-Polymer-Based Materials for Electrochemical Energy Conversion and Storage, 29(45) (2017) 1703044. https://doi.org/https://doi.org/10.1002/adma.201703044.

[8] K. Sada, K. Kokado, Y. Furukawa, Polyacrylonitrile (PAN), in: S. Kobayashi, K. Müllen (Eds.), Encyclopedia of Polymeric Nanomaterials, Springer Berlin Heidelberg, Berlin, Heidelberg, 2015, pp. 1745-1750. https://doi.org/10.1007/978-3-642-29648-2_249.

[9] Y. Liu, J. Mo, Q. Fu, Y. Lu, N. Zhang, S. Wang, S. Nie, Enhancement of Triboelectric Charge Density by Chemical Functionalization, 30(50) (2020) 2004714. https://doi.org/https://doi.org/10.1002/adfm.202004714.

[10] Y.D. More, S. Saurabh, S. Mollick, S.K. Singh, S. Dutta, S. Fajal, A. Prathamshetti, M.M. Shirolkar, S. Panchal, M. Wable, S. Ogale, S.K. Ghosh, Highly Stable and End-group Tuneable Metal–Organic Framework/Polymer Composite for Superior Triboelectric Nanogenerator Application, 9(34) (2022) 2201713.doi.org/10.1002/admi.202201713.

[11] Z. Fang, K.H. Chan, X. Lu, C. Tan, G. Ho, Surface texturing and dielectric property tuning toward boosting of triboelectric nanogenerator performance, Journal of Materials Chemistry A 6 (2017). https://doi.org/10.1039/C7TA07696G.

[12] Z. Yang, X. Zhang, G. Xiang, 2D Boron Nitride Nanosheets in Polymer Nanofibers for Triboelectric Nanogenerators with Enhanced Performance and Flexibility, ACS Applied Nano Materials 5(11) (2022) 16906-16911. https://doi.org/10.1021/acsanm.2c03851.

[13] Y. Kim, X. Wu, J.H. Oh, Fabrication of triboelectric nanogenerators based on electrospun polyimide nanofibers membrane, Sci Rep 10(1) (2020) 2742. https://doi.org/10.1038/s41598-020-59546-7.

[14] M.S. Islam, B.C. Ang, A. Andriyana, A.M. Afifi, A review on fabrication of nanofibers via electrospinning and their applications, SN Applied Sciences 1(10) (2019) 1248. https://doi.org/10.1007/s42452-019-1288-4.

[15] M.R. Almafie, L. Marlina, R. Riyanto, J. Jauhari, Z. Nawawi, I. Sriyanti, Dielectric Properties and Flexibility of Polyacrylonitrile/Graphene Oxide Composite Nanofibers, ACS Omega 7(37) (2022) 33087-33096. https://doi.org/10.1021/acsomega.2c03144.

[16] H.-W. Chao, H.-C. Hsu, Y.-R. Chen, T.-H. Chang, Characterizing the dielectric properties of carbon fiber at different processing stages, Scientific Reports 11(1) (2021) 17475. https://doi.org/10.1038/s41598-021-96949-6.

[17] A. Haider, S. Haider, I.-K. Kang, A comprehensive review summarizing the effect of electrospinning parameters and potential applications of nanofibers in biomedical and biotechnology, Arabian Journal of Chemistry 11(8) (2018) 1165-1188. https://doi.org/https://doi.org/10.1016/j.arabjc.2015.11.015.

[18] A. Al-Abduljabbar, I. Farooq, Electrospun Polymer Nanofibers: Processing, Properties, and Applications, 15(1) (2023) 65.

[19] Z.a. Khan, F. Kafiah, Z. Hafiz, F. Shafi, Nufaiei, A. Sarfaraz, A. Furquan, A. Matin, Z. Hafiz, H. Shafi, Morphology, Mechanical Properties and Surface Characteristics of Electrospun Polyacrylonitrile (PAN) Nanofiber Mats, International Journal of Advanced Engineering and Nano Technology 3 (2015) 2347-6389.

[20] T.U. Rashid, R.E. Gorga, W.E. Krause, Mechanical Properties of Electrospun Fibers—A Critical Review, 23(9) (2021) 2100153.doi.org/10.1002/adem.202100153.

[21] Wahiduzzaman, K. Allmond, J. Stone, S. Harp, K. Mujibur, Synthesis and Electrospraying of Nanoscale MOF (Metal Organic Framework) for High-Performance CO_2 Adsorption Membrane, Nanoscale Research Letters 12(1) (2017) 6. https://doi.org/10.1186/s11671-016-1798-6.

[22] M.M. Rastegardoost, O.A. Tafreshi, Z. Saadatnia, S. Ghaffari-Mosanenzadeh, C.B. Park, H.E. Naguib, Recent advances on porous materials and structures for high-performance triboelectric nanogenerators, Nano Energy 111 (2023) 108365. https://doi.org/https://doi.org/10.1016/j.nanoen.2023.108365.

[23] Z. Shao, J. Chen, Q. Xie, L. Mi, Functional metal/covalent organic framework materials for triboelectric nanogenerator, Coordination Chemistry Reviews 486 (2023) 215118. https://doi.org/https://doi.org/10.1016/j.ccr.2023.215118.

[24] C. Wang, D. Liu, W. Lin, Metal–Organic Frameworks as A Tunable Platform for Designing Functional Molecular Materials, Journal of the American Chemical Society 135(36) (2013) 13222-13234. https://doi.org/10.1021/ja308229p.

[25] A.E. Baumann, D.A. Burns, B. Liu, V.S. Thoi, Metal-organic framework functionalization and design strategies for advanced electrochemical energy storage devices, Communications Chemistry 2(1) (2019) 86. doi.org/10.1038/s42004-019-0184-6.

[26] J.J. Calvo, S.M. Angel, M.C. So, Charge transport in metal–organic frameworks for electronics applications, APL Materials 8(5) (2020). https://doi.org/10.1063/1.5143590.

[27] G. Khandelwal, N.P. Maria Joseph Raj, S.-J. Kim, Materials Beyond Conventional Triboelectric Series for Fabrication and Applications of Triboelectric Nanogenerators, 11(33) (2021) 2101170. https://doi.org/https://doi.org/10.1002/aenm.202101170.

[28] G. Khandelwal, N.P. Maria Joseph Raj, S.-J. Kim, Zeolitic Imidazole Framework: Metal–Organic Framework Subfamily Members for Triboelectric Nanogenerators, 30(12) (2020) 1910162. https://doi.org/https://doi.org/10.1002/adfm.201910162.

[29] N. Jayababu, D. Kim, Co/Zn bimetal organic framework elliptical nanosheets on flexible conductive fabric for energy harvesting and environmental monitoring via triboelectricity, Nano Energy 89 (2021) 106355.doi.org/10.1016/j.nanoen.2021.106355.

[30] Y. Guo, Y. Cao, Z. Chen, R. Li, W. Gong, W. Yang, Q. Zhang, H. Wang, Fluorinated metal-organic framework as bifunctional filler toward highly improving output

performance of triboelectric nanogenerators, Nano Energy 70 (2020) 104517. https://doi.org/https://doi.org/10.1016/j.nanoen.2020.104517.

[31] G. Khandelwal, A. Chandrasekhar, N.P. Maria Joseph Raj, S.-J. Kim, Metal–Organic Framework: A Novel Material for Triboelectric Nanogenerator–Based Self-Powered Sensors and Systems, 9(14) (2019) 1803581.https://doi.org/10.1002/aenm.201803581.

[32] J. Ye, J.-C. Tan, High-performance triboelectric nanogenerators incorporating chlorinated zeolitic imidazolate frameworks with topologically tunable dielectric and surface adhesion properties, Nano Energy 114 (2023) 108687. https://doi.org/https://doi.org/10.1016/j.nanoen.2023.108687.

[33] K. Kida, M. Okita, K. Fujita, S. Tanaka, Y. Miyake, Formation of high crystalline ZIF-8 in an aqueous solution, CrystEngComm 15(9) (2013) 1794-1801. https://doi.org/10.1039/C2CE26847G.

[34] Z. Wei, W. Li, H. Yang, T. Li, S. He, Y. Wang, Y. Hu, Synthesis of 3D Co-based Zeolitic Imidazolate Framework and Application as Electrochemical Sensor for H2O2 Detection, International Journal of Electrochemical Science 17(11) (2022) 221132. https://doi.org/https://doi.org/10.20964/2022.11.27.

[35] L. Han, H. Qi, D. Zhang, G. Ye, W. Zhou, C. Hou, W. Xu, Y. Sun, A facile and green synthesis of MIL-100(Fe) with high-yield and its catalytic performance, New Journal of Chemistry 41(22) (2017) 13504-13509. https://doi.org/10.1039/C7NJ02975F.

[36] C. Chen, B. Li, L. Zhou, Z. Xia, N. Feng, J. Ding, L. Wang, H. Wan, G. Guan, Synthesis of Hierarchically Structured Hybrid Materials by Controlled Self-Assembly of Metal–Organic Framework with Mesoporous Silica for CO2 Adsorption, ACS Applied Materials & Interfaces 9(27) (2017) 23060-23071. https://doi.org/10.1021/acsami.7b08117.

[37] L. Zhang, Z. Su, F. Jiang, L. Yang, J. Qian, Y. Zhou, W. Li, M. Hong, Highly graphitized nitrogen-doped porous carbon nanopolyhedra derived from ZIF-8 nanocrystals as efficient electrocatalysts for oxygen reduction reactions, Nanoscale 6(12) (2014) 6590-6602. https://doi.org/10.1039/C4NR00348A.

[38] S. Narayanaru, G.M. Anilkumar, M. Ito, T. Tamaki, T. Yamaguchi, An enhanced electrochemical CO2 reduction reaction on the SnOx–PdO surface of SnPd nanoparticles

decorated on N-doped carbon fibers, Catalysis Science & Technology 11(1) (2021) 143-151. https://doi.org/10.1039/D0CY01437K.

[39] M. Qiao, H. Kong, X. Ding, Z. Hu, L. Zhang, Y. Cao, M. Yu, Study on the Changes of Structures and Properties of PAN Fibers during the Cyclic Reaction in Supercritical Carbon Dioxide, 11(3) (2019) 402.

[40] A.F. Gross, E. Sherman, J.J. Vajo, Aqueous room temperature synthesis of cobalt and zinc sodalite zeolitic imidizolate frameworks, Dalton Transactions 41(18) (2012) 5458-5460. https://doi.org/10.1039/C2DT30174A.

[41] N.T. Dung, T.T. Hue, V.D. Thao, N.N. Huy, Preparation of Mn2O3/MIL-100(Fe) composite and its mechanism for enhancing the photocatalytic removal of rhodamine B in water, RSC Advances 11(46) (2021) 28496-28507. https://doi.org/10.1039/D1RA03496K.

[42] D. Mohanadas, M.A.A. Mohd Abdah, N.H.N. Azman, T.B.S.A. Ravoof, Y. Sulaiman, Facile synthesis of PEDOT-rGO/HKUST-1 for high performance symmetrical supercapacitor device, Scientific Reports 11(1) (2021) 11747. https://doi.org/10.1038/s41598-021-91100-x.

[43] J. Begum, Z. Hussain, T. Noor, Adsorption and kinetic study of Cr(VI) on ZIF-8 based composites, Materials Research Express 7(1) (2020) 015083. https://doi.org/10.1088/2053-1591/ab6b66.

[44] Y. Hu, H. Kazemian, S. Rohani, Y. Huang, Y. Song, In situ high pressure study of ZIF-8 by FTIR spectroscopy, Chemical Communications 47(47) (2011) 12694-12696. https://doi.org/10.1039/C1CC15525C.

[45] M. Niknam Shahrak, M. Ghahramaninezhad, M. Eydifarash, Zeolitic imidazolate framework-8 for efficient adsorption and removal of Cr(VI) ions from aqueous solution, Environmental Science and Pollution Research 24(10) (2017) 9624-9634. https://doi.org/10.1007/s11356-017-8577-5.

[46] H. Lv, H. Zhao, T. Cao, L. Qian, Y. Wang, G. Zhao, Efficient degradation of high concentration azo-dye wastewater by heterogeneous Fenton process with iron-based metal-organic framework, Journal of Molecular Catalysis A: Chemical 400 (2015) 81-89. https://doi.org/https://doi.org/10.1016/j.molcata.2015.02.007.

[47] C.J. Wijaya, S. Ismadji, H.W. Aparamarta, S. Gunawan, Statistically Optimum HKUST-1 Synthesized by Room Temperature Coordination Modulation Method for the Adsorption of Crystal Violet Dye, 26(21) (2021) 6430.

[48] M. Peng, T. Kurokawa, J.P. Gong, Y. Osada, Q. Zheng, Effect of Surface Roughness of Hydrophobic Substrate on Heterogeneous Polymerization of Hydrogels, The Journal of Physical Chemistry B 106(12) (2002) 3073-3081. https://doi.org/10.1021/jp012521u.

[49] A. Centrone, Y. Yang, S. Speakman, L. Bromberg, G.C. Rutledge, T.A. Hatton, Growth of Metal−Organic Frameworks on Polymer Surfaces, Journal of the American Chemical Society 132(44) (2010) 15687-15691. https://doi.org/10.1021/ja106381x.

[50] H. Varghese, A. Chandran, Triboelectric Nanogenerator from Used Surgical Face Mask and Waste Mylar Materials Aiding the Circular Economy, ACS Applied Materials & Interfaces 13(43) (2021) 51132-51140. https://doi.org/10.1021/acsami.1c16557.

[51] J.C. Alipoyo, V.E.B. Magoncia, A.A.M. Perido, R.B. Gapusan, M.D.L. Balela, Optimization of hydrolysis of polyacrylonitrile-kapok fiber composite for the adsorption of lead ions in aqueous solution, Environmental Nanotechnology, Monitoring & Management 16 (2021) 100566. https://doi.org/https://doi.org/10.1016/j.enmm.2021.100566.

[52] G. Ndayambaje, K. Laatikainen, M. Laatikainen, E. Beukes, O. Fatoba, N. van der Walt, L. Petrik, T. Sainio, Adsorption of nickel(II) on polyacrylonitrile nanofiber modified with 2-(2′-pyridyl)imidazole, Chemical Engineering Journal 284 (2016) 1106-1116. https://doi.org/https://doi.org/10.1016/j.cej.2015.09.065.

[53] J. Xu, J. Liu, Z. Li, X. Wang, Y. Xu, S. Chen, Z. Wang, Optimized synthesis of Zr(iv) metal organic frameworks (MOFs-808) for efficient hydrogen storage, New Journal of Chemistry 43(10) (2019) 4092-4099. https://doi.org/10.1039/C8NJ06362A.

[54] L. Liu, Y. Duan, Y. Liang, A. Kan, L. Wang, Q. Luo, Y. Zhang, B. Zhang, Z. Li, J. Liu, D. Wang, Cyclized Polyacrylonitrile as a Promising Support for Single Atom Metal Catalyst with Synergistic Active Site, 18(8) (2022) 2104142. https://doi.org/https://doi.org/10.1002/smll.202104142.

Chapter 5

MIL-100 (Fe) framework derived Fe decorated carbon catalyst for Persulfate-activated degradation of organic contaminants from wastewater
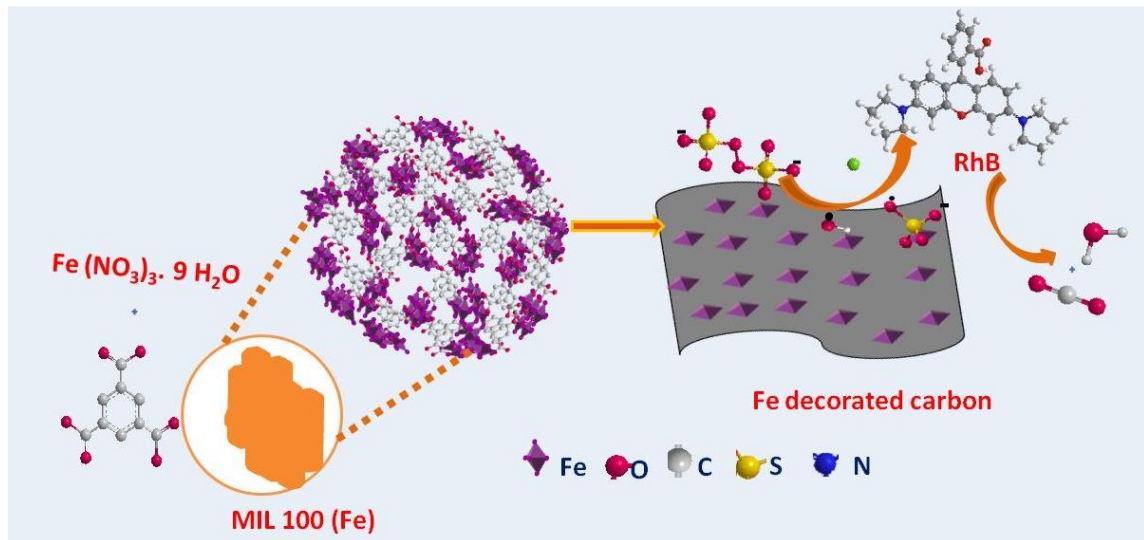
Abstract

Advanced oxidation processes (AOPs) employing persulfate activation are perceived as an effective approach for the removal of organic contaminants due to their non-selective degradation coupled with high efficiency. Recently, heteroatom-doped carbon derived from Metal-Organic Frameworks (MOFs) has been found to impart added advantages in the persulfate-based advance oxidation process. Compared to other preparation strategies, the exploitation of MOF as a sacrificial template provides a single synthetic route for high surface area carbon with defect-rich sites. Moreover, heteroatom doping leads to high efficiency in persulfate activation leading to appreciable organic pollutant degradation. Herein, we have synthesized Fe/Fe_3C decorated porous carbon by the high-temperature carbonization of the MIL-100 (Fe) metal-organic framework. The degradation activity of the obtained carbon was tested towards the degradation of the targeted contaminant Rhodamine (B). 100 % degradation was realized within 35 minutes with minimum catalyst loading of 100 mg/L in 30 mg/L contaminant solution. Also, the catalyst retained ~ 90 % of the removal rate even after 5 cycles of operation. The carbon exhibited high degradation activity towards various other organic compounds like Methylene blue, Benzoic acid, Nitro benzene, Phenol, 4-Chlorophenol, and antibiotics Tetracycline, Linezolid, Hydroxychloroquine, and Cefpodoxime proxetil. The homogeneous dispersion of Fe/Fe_3C species and the porous morphology features obtained on carbonization of MOF, has led to better adsorption of reactive species leading ultimately to efficient degradation.

5.1. Introduction

The increase in water pollution induced due to higher concentrations of organic contaminants from various resources has caused harmful effects on the environment. Untreated effluents discharged from different sectors contain diverse organic contaminants such as dyes, pharmaceutical waste, pesticides, etc., and have become a major threat to the water bodies. Advanced oxidation processes (AOPs) are considered effective in eliminating organic contaminants as harmless by products. [1-4] Among the advanced oxidation processes, degradation via the activation of persulfate over the catalyst surface has been considered a cost-effective strategy that involves the generation of reactive intermediates on the catalyst surface such as $SO_4^{-\bullet}$ or $OH^{\bullet}$ as well as $O_2^{\bullet-}$ which in turn can perform the non-selective degradation of organic pollutants from water bodies. Over the past few years, AOP based on persulfate (PS) or peroxymonosulfate (PMS) activation has been widely employed for the degradation of different organic pollutants. [5-9]

Transition metals, including Fe, Co, Ni, Mn, etc., are widely employed for AOPs as they can effectively break the O-O bond of persulfate and generate $SO_4^{-\bullet}$, which initiates the degradation process. However, prolonged use of these catalysts can lead to leaching of metals, resulting in secondary toxic effects. [10-13] Among transition metals, Fe^{2+}-based catalysts are widely explored due to their less toxicity and low cost. However, excess ferrous ions can consume reactive free radicals, which may hinder the degradation reaction. Furthermore, the low surface area and agglomeration of metal catalysts impede the performance for large-volume applications. [14, 15] Therefore, different approaches are employed to improve the activity of Fe-based catalysts. One of the proficient approaches is encapsulating Fe^{2+} in porous matrices, which in turn protect the metal sites, enhancing the overall performance. Encapsulation of transition metals in carbon can prevent the agglomeration of metal catalysts and helps in providing a better contact area. [12, 16-22] Over the past decade, metal-organic frameworks (MOFs) have been considered ideal candidates for the preparation of transition metal-doped carbon catalysts. The single carbonization route without any activation method can result in transition metal-doped carbon with tuned morphologies and porosity. MOF-derived heteroatom/metal-doped carbon catalyst exhibits improved activity, owing to their unique features such as uniformly dispersed active sites, excellent stability, and tunable structural composition to activate persulfate (PS), enabling rapid degradation rate towards dissolved organic contaminants in water. Recently Fe/ carbon hybrid catalysts containing

different Fe moieties, such as Fe_2O_3, Fe, Fe_3C, FeN_4, etc., were also prepared from different Fe-based MOFs and functionalized MOFs and were proven to be effective for persulfate activation. [23-29] These magnetic Fe-based catalysts exhibited excellent activity and recyclability, enabling long-term application. MIL-based MOFs have been widely explored as a catalyst for organic contaminant degradation via different AOPs, including Fenton and photocatalytic activation. Recently, different MIL frameworks containing Fe centers have been utilized to synthesize Fe/carbon hybrid catalysts with outstanding performances. Compared to pristine MOFs, these derived frameworks were found to exhibit outstanding performance. Qi et al. studied the enhancement in the activation of PMS on Fe@N-doped porous carbon prepared from functionalized NH_2-MIL-53(Fe) compared to Fe@porous carbon from pristine MIL-53(Fe) for acyclovir degradation. [30] Fe_2O_3/carbon nanorods prepared from MIL 88A were tested towards peroxide/persulfate activation by a Fenton-like reaction. [31] The Fe/Fe_3C@N-doped porous carbon hybrid was effectively synthesized from MIL-88B-NH_2 for 4-chlorophenol degradation by PMS activation leading to the generation of $SO_4^{\bullet-}$ and $OH^{\bullet}$. [23] The catalytic activity of these Fe / carbon hybrids primarily depends upon the parameters like the parent MOFs, their carbonization temperature, formed Fe phases, and the type of reactive species formed. However, most of the reported studies are limited only to particular contaminants limiting their practical application. Hence it demands further systematic studies exploring more environment-friendly Fe-based MOF frameworks towards the degradation of a broad range of organic contaminants.

Herein, we have synthesized Fe, Fe_3C dispersed porous carbon through a controlled single-step carbonization route from the well-known MIL-100 (Fe) metal-organic framework formed by a green hydrothermal synthesis route. The catalytic activity of the obtained carbon was tested towards the targeted contaminant Rhodamine (B) by a persulfate-activated advanced oxidation process. The Fe-containing carbon could achieve good degradation efficiency for RhB at room temperature with a minimum dosage of catalyst and persulfate. The degradation of various other organic compounds and antibiotics by the doped carbon was also explored. The uniform dispersion of the active sites, as well as the tuned porosity created due to the structural reorganization within the MOF's frameworks upon carbonization, enabled better mass transport of reactive species towards the catalytically active Fe, Fe_3C sites leading ultimately to the effective degradation of contaminants.

5.2. Experimental

5.2.1. Materials and methods

Iron nitrate nonahydrate ($Fe(NO_3)_3 \cdot 9H_2O$, $\geq$ 98%, Sigma-Aldrich), Trimesic acid (H_3BTC, Benzene-1,3,5- tricarboxylic acid, 95 %, Sigma-Aldrich), Rhodamine B ($C_{28}H_{31}ClN_2O_3$, $\approx$ 80 %,S.D. Fine-Chem limited),), Potassium persulfate($K_2S_2O_8$, , $\geq$ 98%, Merck), Methylene blue ($C_{16}H_{18}ClN_3S$, 82 %, Nice chemicals), ,Benzoic acid ($C_7H_6O_2$, > 99 %, spectrochem) , Nitro benzene ($C_6H_5NO_2$, 99 %, spectrochem) , Phenol (C_6H_6O,99 %, spectrochem), 4- Chlorophenol (C_6H_4ClOH , >98.%, TCI chemicals) are used as received . Antibiotics Tetracycline ($C_{22}H_{24}N_2O_8 \cdot HCl$, > 98%, TCI chemicals), Linezolid, Hydroxychloroquine (HCQ), and Cefpodoxime proxetil were purchased from Kerala State Drugs and Pharmaceuticals Ltd.(KSDPL, Alappuzha) and are used as received without further purification.

5.2.1. Preparation of MIL-100 (Fe)

MIL-100 (Fe) was synthesized by a solvent-free hydrothermal method reported elsewhere.[32] In this method, Iron nitrate nonahydrate and trimesic acid were mixed in the molar ratio of 1.5: 1 and blended properly at room temperature for 10 minutes. Then, the mixture was transferred into a Teflon-lined autoclave and kept in a hot air oven at 160 °C for 4 hours. After being cooled down to room temperature, an orange solid product was obtained. The obtained MIL-100 (Fe) was purified by washing it in distilled water and ethanol several times, dried at 150 °C in a vacuum oven overnight and collected.

5.2.2. Preparation of Fe, Fe₃C dispersed porous carbon from MIL-100 (Fe)

A known amount of prepared MIL-100 (Fe) was transferred into a quartz tube and carbonized in a tube furnace. The carbonization process was carried out at four different temperatures (700 °C, 800 ° C, 900 ° C & 1000 ° C) with a heating rate of 5 °C/min under a stream of N_2 gas after excluding air by flushing with N_2 for up to 3 times. The furnace was allowed to cool to room temperature, after which the products were collected as black powder. The resulting samples were named MIL-700C, MIL-800C, MIL-900C, and MIL-1000C, where 700C, 800C, 900C, and 1000C denote the carbonization temperature. The resulting Fe-decorated carbon was further washed with 1 M H_2SO_4 to remove the residual unreactive species present on the carbon surface.

5.2.3. Fabrication of MIL 800@MS sponge

The as-prepared MIL-800C was incorporated into a melamine sponge to test the energy-efficient RhB treatment. The fabrication of MIL-800C@MS was done by referring to a previously reported procedure. [33] Initially, the melamine sponge (MS) was shaped into cubes of dimensions 2x2x2 cm and was cleaned thoroughly in ethanol and dried. A dispersion of approximately 0.008 g of MIL-800C in acetone was sonicated for about 30 minutes, and the MS was added into it, ultrasonicated for 1h, and dried. The catalyst-incorporated MS was placed in a ceramic boat and treated under nitrogen flow at 300 °C for 1h to shrink the pore sizes of the melamine sponge, which can incorporate the MIL-800C carbon particles easily.

5.2.4. Structural characterization

The synthesized materials were analyzed using powder X-ray diffraction technique (PXRD, Malvern PANalytical B.V, EMPYREAN 3). The structural features of the synthesized MIL-100 (Fe) derived carbon were analyzed using FT-IR (Perkin Elmer, FT-IR, Spectrum Two). The surface area and porosity of the materials were analyzed by N_2 adsorption-desorption analysis from BET (Tristar II, Micromeritrics, USA). The total pore volume was calculated from the isotherm curve at a P/P_0 value of 0.99. The surface morphology and elemental distribution were recorded by scanning electron microscopy and SEM-EDS (JEOL, JSM-35). A deep understanding of the morphology was obtained from a high-resolution transmission electron microscope (HR-TEM, JEOL JEM F-200) operated at 120 kV. The surface electronic binding states of the carbon sample were analyzed from XPS spectra (ULVAC-PHI Inc., USA). Confocal Raman microscopy was used to analyze the structural features of carbon, which is operated at 633 nm (WI Tec, Germany)

5.2.5. Degradation experiments

The catalytic performance of an as-synthesized Fe, Fe_3C dispersed carbon catalyst for the persulfate activation and degradation of Rhodamine B (Rh B) was evaluated by batch experiments. All the experiments were conducted at room temperature. The catalyst powder was (100 mg/L) added into 80 mL of Rhodamine B solution (30mg/L) and stirred in the dark in a catalytic reactor for 1 hour until adsorption-desorption equilibrium was reached. All the experiments were conducted indoors to avoid the photocatalytic degradation of RhB in the presence of sunlight. After 1h, the catalytic degradation was initiated by adding 5mM

of potassium peroxodisulfate (PS) into the solution. The pH of the solution was adjusted by 0.1 M NaOH and 0.1 M HCl when required. 4 ml of the sample solution was taken out at regular intervals of 5 minutes, filtered, and the oxidation reaction was quenched immediately by adding 2 mL of methanol. The RhB degradation was characterized by measuring absorbance using a UV-Visible spectrophotometer at a wavelength of 543 nm. The rate of degradation of RhB is described as follows;

$$\text{Degradation rate of RhB} = C_t/C_0 \text{ ---------- [1]}$$

The rate constant of the degradation was calculated according to a pseudo-first-order kinetics equation;

$$\ln (C_t/C_0)= -kt \text{ ---------- [2]}$$

Where k is the rate constant of the reaction, and C0 and Ct denote the initial and final concentration of RhB at time t. The degradation activity of the catalyst was extended to various common organic contaminants by carrying out the reaction with optimized concentrations of catalyst, persulfate, and contaminants.

All the reaction intermediates involved in the degradation process were analyzed by conducting experiments with free radical scavengers like Terephthalic acid (TA) and Luminol (3-Aminophthalhydrazide). Terephthalic acid was used as the free radical quenching agent for $OH^{\bullet}$ as it can trap $OH^{\bullet}$ and form 2-Hydroxy Terephthalic acid. This can be confirmed by the emission spectrum at the wavelength of 425 nm when excited with the wavelength of 315 nm. On the other hand, Luminol can trap the $O_2^{\bullet-}$ to form 3-aminophthalate, which will give an emission peak at around 420 nm when excited at the wavelength of 350 nm. Initially, 5 mM of TA and Luminol were dissolved in 2×10^{-3} M NaOH and 0.1 M NaOH in different beakers, respectively. [34, 35] Degradation was initiated by adding 100 mg/L carbon catalyst and 5 mM persulfate into each. The samples were withdrawn and filtered at regular intervals of 5 m, and the photoluminescence spectrum was recorded immediately after collecting the samples.

5.3. Results and Discussion

5.3.1. Structural and morphological studies
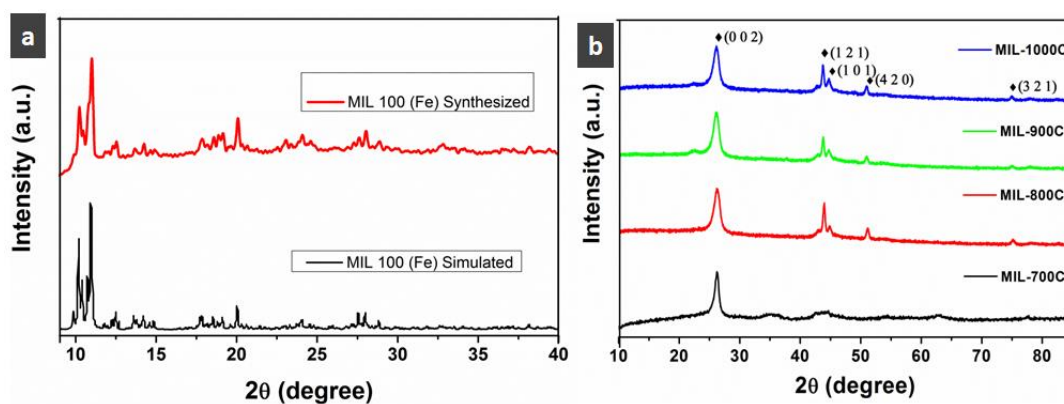
Figure 1. PXRD patterns of; a) synthesized MIL-100 (Fe) and b) MIL-100 (Fe) carbonized at different temperature

The PXRD pattern of MIL-100(Fe) is presented in **Figure 1a.** The peaks are in good agreement with the XRD patterns of simulated peaks of MIL 100 (Fe) as reported in the literature, indicating the formation of the MIL -100 (Fe) phase. [36-38] Thus, the one-pot hydrothermal synthesis has led to phase pure MIL 100 (Fe).

After carbonization, the samples MIL-800C, MIL-900C, and MIL-1000C exhibited sharp and well-resolved diffraction peaks corresponding to both graphitic carbon and Fe in its Fe_3C phases, as shown in **Figure 1b**. The diffraction peak at 25.9 ° and 44.6 ° is attributed to the (002) and (101) plane of graphitic carbon, respectively (JCPDS file no. 00-008-0415). The three distinct peaks at 43.4 °, 50.9 °, and 74.7 ° are associated with the (121), (420), and (321) planes of Iron carbide in Fe_3C and the carbon rich $Fe_{2.5}C$ phases (JCPDS file no. 01-085-0871 & 00-036-1248). Thus XRD analysis confirms the Fe_3C and $Fe_{2.5}C$ phases in the in-situ formed graphitic carbon. [39-41] In the case of MIL 700C, only the graphitic phase was observable without any distinct peaks of Fe on the carbon. Hence, it could be inferred that the carbonization process completes at 800 °C.

The decomposition profile of the MIL-100 (Fe) frameworks was traced using the thermogravimetric analysis (TGA) carried out at conditions akin to the carbonization process (up to 900 °C in N_2 atmosphere) **(Figure 2).** MIL-100(Fe) underwent decomposition in three stages with weight loss between 50 °C and 900 °C. The initial weight loss of 10 %, in the range of 50-150 °C, corresponds to the volatilization of the adsorbed

volatile components, including the water molecules trapped on the surface pores of MIL-100 (Fe) frameworks. The minimal weight loss at the first stage indicates that MIL-100 (Fe) is thermally stable at this temperature range. The second stage of thermal decomposition was found beyond 350 $^\circ$C with a considerable weight loss of about 40 %, corresponding to the continuous decomposition of the MIL-100 frameworks accompanied by the removal of the coordinated water molecule and the decomposition of the carboxylate linkage. The third stage of decomposition ends at 900 °C, indicating that MIL-100(Fe) framework is fully decomposed and reorganizes to Fe-incorporated carbon with a 24 % yield [42, 43]. However, the high boiling temperature of Fe (≈*2861°C)* leads to the persistence of Fe particles resulting in Fe incorporated carbon.
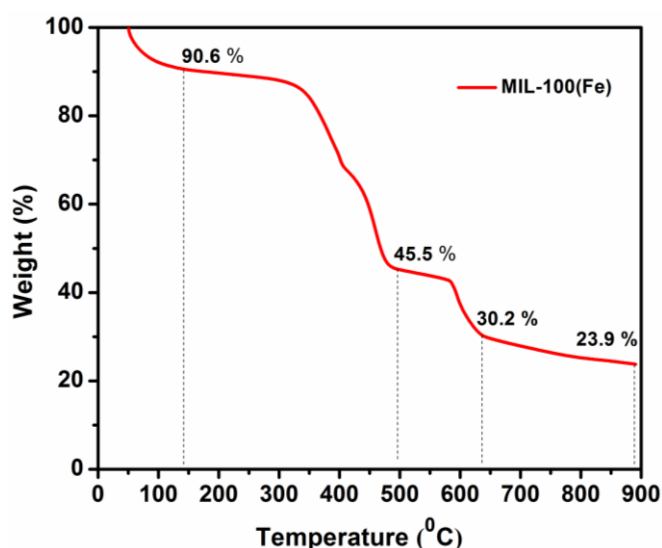
Figure 2. TGA profile of MIL-100 (Fe)

The morphological features of the samples were analyzed using Scanning Electron Microscope (SEM). The formed MIL-100 (Fe) particles are arranged as a group of stick-like morphology that extends to micrometer (µm) dimensions as reported **(Figure 3a)**. [32] The MIL-800C was seen as a particle with enormous numbers of pores on the surface. The decomposition of MIL-100 (Fe), accompanied by the structural reorganization and associated volatilization of elemental components from the MOF framework, has contributed to the formation of highly porous carbon **(Figure 3b)**.
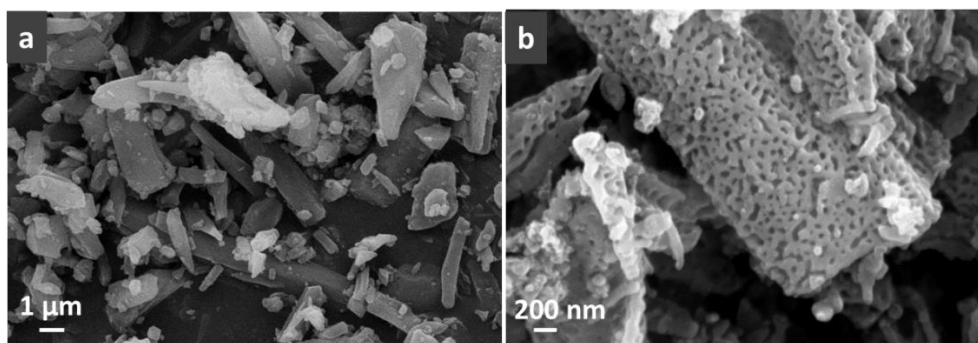
Figure 3. SEM images of a) MIL-100 (Fe), and b) MIL-800C

The quantified data obtained from SEM-EDS further provides the information that, around 0.68 at. % of Fe and 9.4 at. % of oxygen is dispersed on the carbon surface, contributing to heteroatom-carbon sites (**Figure 4b)**. The elemental mapping shows the uniform dispersion of heteroatoms on the carbon surface, thus ensuring the presence of dispersed active sites throughout the surface for better adsorption and degradation **(Figure 4 (c-e)).**

Element	Weight%	Atomic%
C K	85.14	89.91
O K	11.87	9.41
Fe K	3.00	0.68
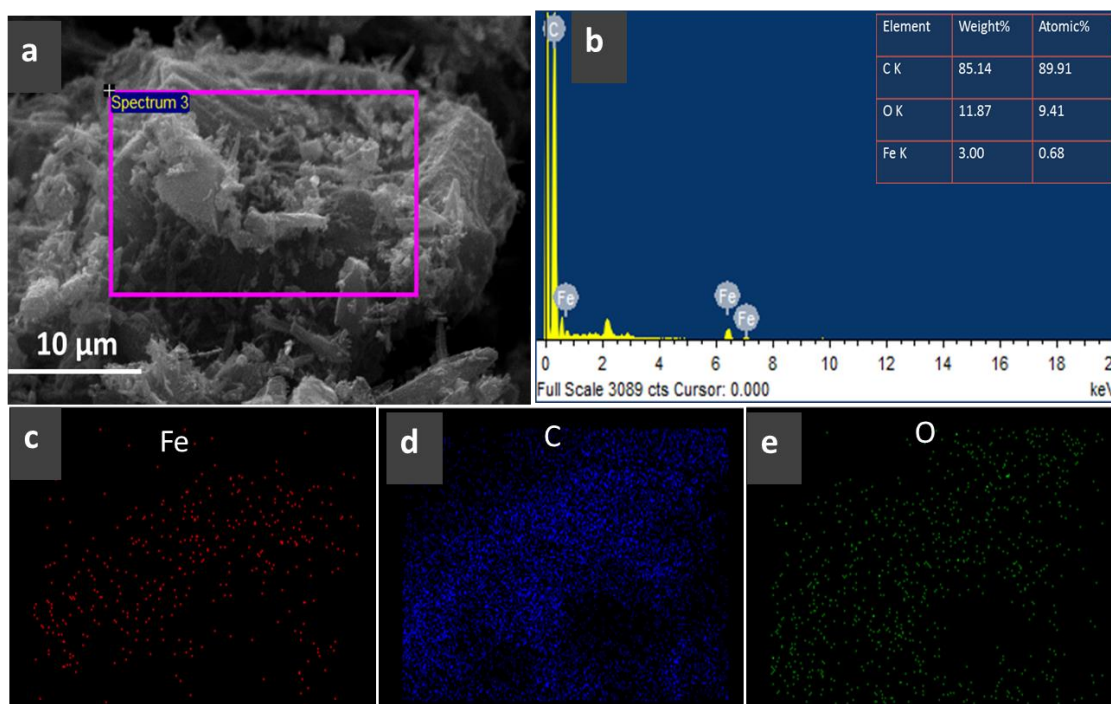
Figure 4. a) SEM image, b) SEM-EDS, and (c-e) Elemental distributions in MIL-800C.

The TEM image confirms the elongated stick-like morphology of hydrothermally formed MIL-100 (Fe) **(Figure 5a),** while MIL-800C indicates the presence of Fe nanoparticles encapsulated on the carbon sheets **(Figure 5b).** The HRTEM images evidence the formation of Fe_3C facets. Thus most of the Fe was incorporated as the Fe_3C phase, whereas the surrounding organic ligand contributed to the carbon matrix that encapsulates the Fe

particles. Here the surrounding carbon can protect and isolate the individual Fe_3C active sites that may provide resistance to the oxidation of Fe sites leading to higher stability for the long-term application of catalysts. The Fe-based active sites can generate the reactive species, while the carbon sheets with porous surfaces may create channels that lead to the effective degradation of the targeted contaminants. [44]
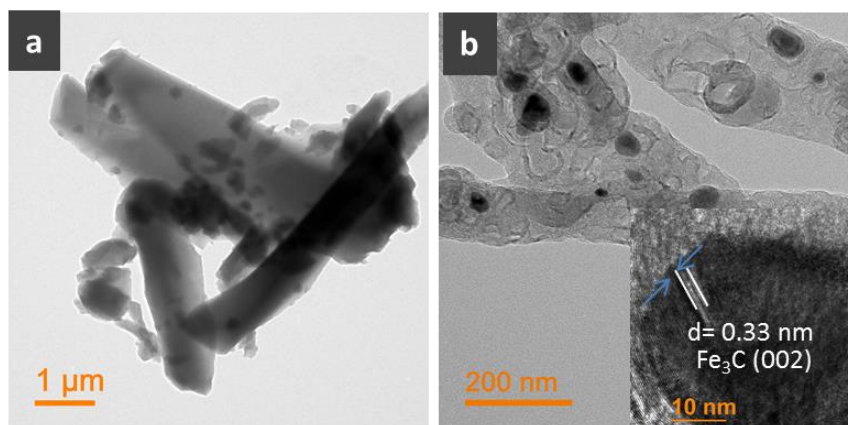
Figure 5. TEM images of; a) MIL 100 (Fe) and b) MIL-800C

The surface area and porous features are essential criteria for effective adsorption and subsequent generation of reactive species, ultimately leading to the degradation of the targeted contaminants. The surface area and porosity were calculated from the N_2 adsorption-desorption isotherms. MIL-100 (Fe) exhibited Type -1 isotherm with a high surface area of 1204 m^2/g and pore volume of 0.64 cm^3/g, respectively, implying a microporous structure **(Figure 6a & 6b).**[32]
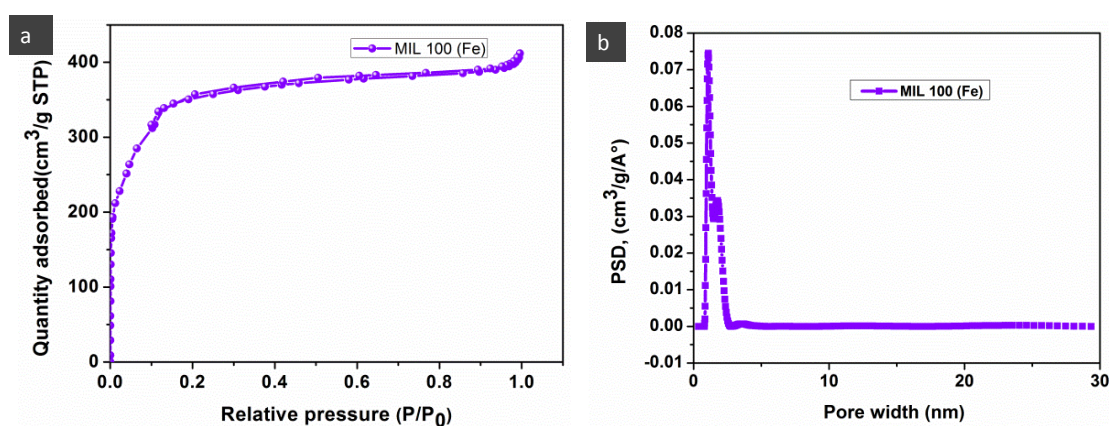
Figure 6. a) N_2 adsorption-desorption isotherm and b) Pore size distribution curve of MIL-100 (Fe).

After carbonization, the isotherm changed from type 1 to H4 hysteresis, indicating a transformation to micro-meso porous architecture with less microporosity compared to parent MOF (**Figure 7a**).[45-47] The drop in surface area value is expected as the microporosity decreases on heat treatment. Thus, micro-mesoporous channels were created on the surface, accompanied by the formation of Fe-incorporated carbon. The surface area and pore volume of the porous carbons thus formed are listed in **Table 1**. The surface area decreased from 431 m^2/g to 289 m^2/g upon increasing the carbonization temperature, probably due to the destruction of the MOF framework. The pore size analysis of MIL-700C obtained from NLDFT shows bimodal distribution with micropores and large inter-aggregate pore of about 20 nm whereas, MIL-800C, MIL-900C, and MIL-1000C showed tri-model distribution with a third peak about 10nm (**Figure 7b**). In the case of MIL-700C, the isotherm exhibited both the characteristics of parent MIL-100 (Fe) and the mesoporous carbon, as we can see a higher amount of microporosity along with some mesopores owing to the incomplete carbonization at 700 °C. However, with increasing carbonization temperature, the porosity changed predominantly to mesoporous type. This evidenced the role of central metal Fe in MIL-100(Fe) in creating mesoporosity upon carbonization.[48,49] Among the carbonized samples, MIL-800C exhibited high surface area and pore volume of 431 m^2/g and 1.08 cm^3/g, respectively, and was therefore used for further degradation studies.
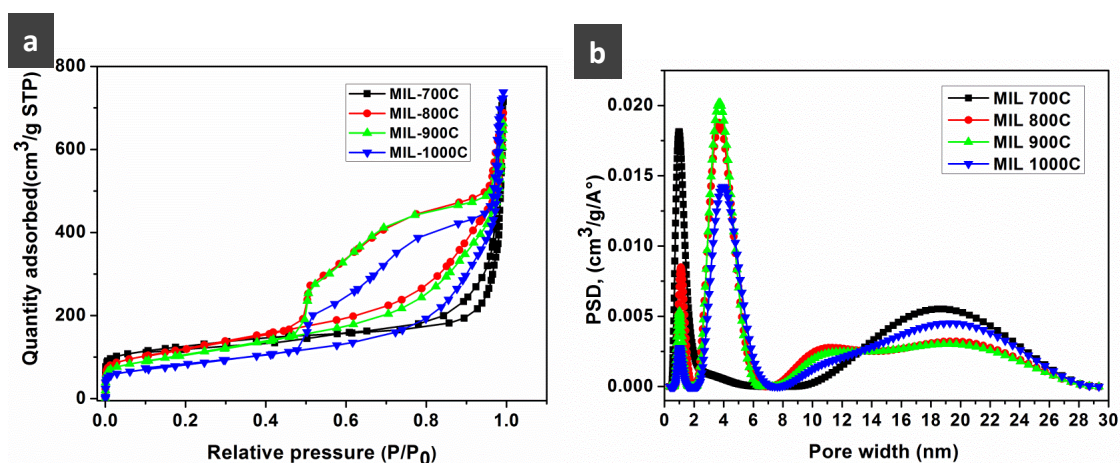
Figure 7. a) N_2 adsorption-desorption isotherms and b) pore size distribution of Fe-incorporated carbon samples.

Table 1. BET surface area and pore size distribution of MIL-100 (Fe) and derived carbon samples.

Sample	Surface area (m^2/g)	Total Pore volume (cm^3/g)	Micropore volume (cm^3/g)
MIL-100 (Fe)	1204	0.64	0.37
MIL-700 C	429	1.13	0.16
MIL-800 C	431	1.08	0.14
MIL -900 C	380	1.04	0.12
MIL- 1000 C	289	1.17	0.09

The XPS measurement was carried out to estimate the surface composition of the prepared MIL-100 (Fe) derived carbon catalysts. The XPS survey spectrum shows characteristic peaks at binding energies corresponding to C 1s and O 1s. The peak corresponding to Fe 2p was not observed in the survey scan, possibly due to the low response of the XPS, as the Fe is trapped inside the carbon sheets(**Figure 8**). The surface composition of the samples listed in **Table 2** also evidences the low Fe content on the surface. The deconvoluted spectra drawn for MIL-800C samples show the existence of different binding states of the elements Fe, C, and O. The deconvoluted C1s spectrum exhibits peaks corresponding to the binding energy of C=C (284.6 eV), C-O (285.2 eV), C=O (286.2 eV) as well as Fe-C bonding (283.7 eV). The O1s spectrum gives signals corresponding to C-O-H (532.5 eV) and C=O (531.1 eV). In the Fe 2p spectrum, the peaks at 711 eV and 724.4 eV correspond to the $Fe2p_{3/2}$ and $Fe2p_{1/2}$ peaks of Fe^{3+}, respectively, and the peaks at 715.2 eV and 729.9 eV correspond to the satellite peaks. Along with that, the Fe 2p spectrum shows two small signals at 706.9 eV and 720 eV corresponding to the Fe^0 state suggesting the presence of a small quantity of Fe^0 phase along with Fe_3C encapsulated within the carbon sheets. The formation of Fe_3C is usually accompanied by a small amount of Fe^0 on graphite-like carbon. This heteroatom doping on the carbon surface would thus enhance the creation of channels for adsorption and presumably aid the degradation process. [50, 51]
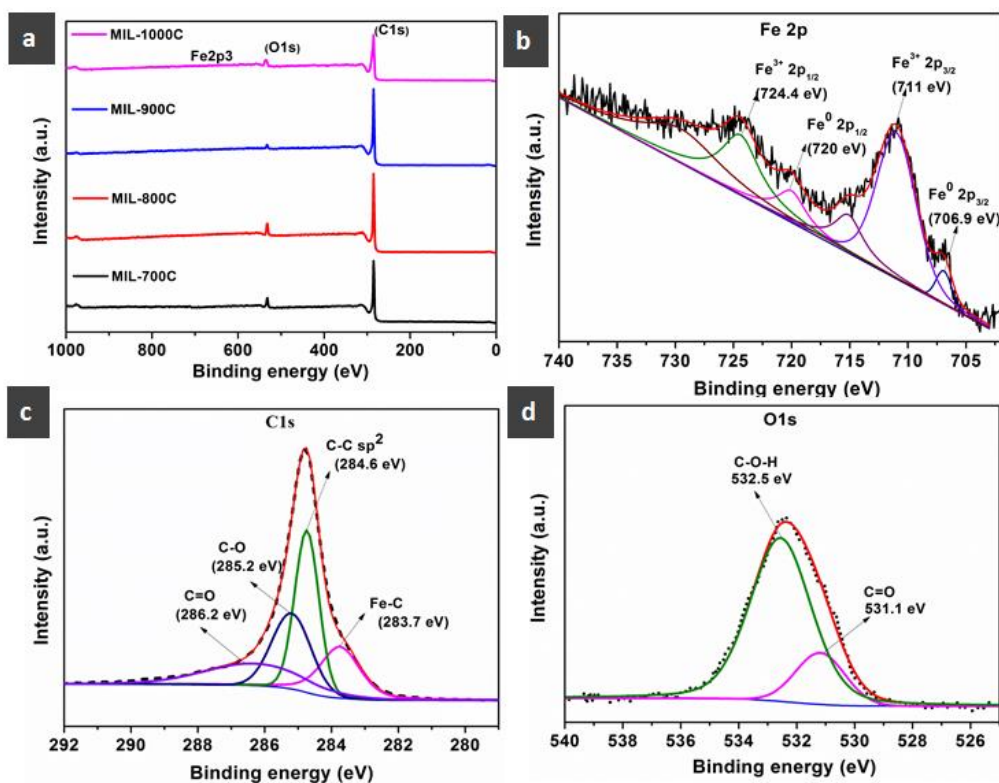
Figure 8. a) XPS survey spectra of MIL-800C and corresponding b) Fe, c) C1, and d) O1 high-resolution spectra.

Table 2. Distribution of various elements on the MIL-100 (Fe) derived Fe doped carbon samples in atomic % obtained from XPS.

Sample name	Elemental distribution (Atomic %)		
	C	O	Fe
MIL-700C	93.4	6.5	0.1
MIL-800C	93.2	6.3	0.5
MIL-900C	97.2	2.8	< 0.1
MIL-1000C	91.5	8.3	0.1

The Raman spectra were used to elucidate the structural properties of MIL-100 (Fe) derived carbon samples. Upon carbonization, the obtained samples exhibited two significant peaks at around 1350 cm^{-1} and 1560 cm^{-1}, which correspond to the D and G bands, respectively **(Figure 9).** The D band arises from the sp^3 carbon and corresponds to the extent of defects

in its structure, whereas the G band originates from the sp^2 bonded state corresponding to the graphitization of carbon. [52, 53] The intensity of D and G bands are used to estimate the extent of defect formation and graphitization. These structural defects can create more active sites in carbon that can adsorb and accommodate the RhB and persulfate molecules. The graphitization can contribute to electron delocalization, thereby initiating electron transfer mechanisms that generate reactive species. The ID/IG value calculated for carbon samples decreases from 2.1 to 0.99 for MIL-700C and MIL-800C, respectively. This indicates the formation of highly graphitized Fe-doped carbon upon the complete decomposition of the MOF framework in MIL-800C, as observed from the XRD and TGA profiles.
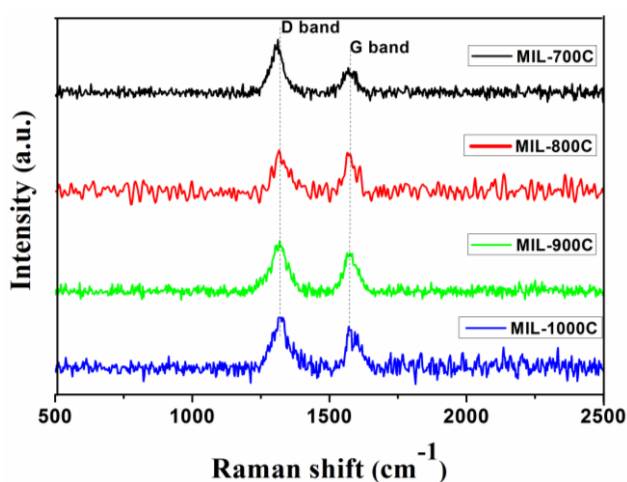
Figure 9. Raman spectra of MIL-100 (Fe) derived carbon samples

MIL-700C exhibited a higher ID/IG ratio among the carbonized samples, though the PXRD pattern shows a sharp graphitic carbon phase. The plausible reason for the improvement in graphitization is the presence of Fe_3C, Fe^0 phase on the carbon that occurred after 800 °C. Some recent reports evidence the tendency of the Fe phase to create graphitization after 715 °C. [54, 55] On further increasing the carbonization temperature from 800 °C to 1000 °C, the ID/IG ratio also increased, presumably due to excess structural decomposition that may destroy the graphitized carbon structure **(Table 3).** Hence, for MIL-800C, the higher graphitization and an equal extent of defects (ID/IG ≈ 1) may contribute to a higher degradation rate.

Table 3. ID/IG ratio of MIL-100 (Fe) derived carbon samples calculated from the Raman spectra

Sample	ID/IG ratio
MIL-700C	2.1
MIL-800C	0.99
MIL-900C	1.32
MIL-1000C	1.37

5.3.2. Dye Degradation studies

The persulfate-activated advanced oxidation process on the prepared carbon catalysts was studied by taking Rhodamine B (RhB) as a targeted organic pollutant. The degradation rate on Fe^0, Fe_3C incorporated carbon was systematically evaluated by analyzing the rate of degradation of RhB determined from its characteristic absorption peak at 543nm.

Initially, the activity of the prepared carbon catalysts was compared by adding 100 mg/L catalyst into Rhodamine B solution of 30 mg/L concentration. The degradation process was initiated by adding 5 mM of persulfate into the catalyst-dye system after reaching adsorption-desorption equilibrium. The adsorption capacity of the MIL-100(Fe) derived samples was calculated and compared with activated carbon(AC) **(Table 4)**. It is to be noted that the Fe-doped carbon samples exhibited higher adsorption capacity than AC even though the surface area was much higher. This is ascribed to the presence of mesopores and the affinity of Fe centres towards Rhodamine (B). [56,57].

Table 4. Adsorption capacity of different carbon samples after 1h ; [RhB] = 30 mg/L, catalyst loading = 100 mg/L

Sample	Adsorption capacity Qm (mg/g)
MIL-700C	183
MIL-800C	191
MIL-900C	143
MIL-1000C	164
AC	107

The degradation activity of the Fe-incorporated carbon catalysts MIL-700C, MIL-800C, MIL-900C, and MIL-1000C was evaluated and compared with commercially available activated carbon **(Figure 10a&10b)**. It could be observed that the degradation activity of the catalysts followed the order MIL-800C>MIL-900C>MIL-1000C> AC> MIL-700C. The catalyst MIL-700C exhibited the lowest degradation activity among all the catalysts due to incomplete carbonization, as evident from the PXRD, due to less availability of Fe-based active sites to initiate the degradation. However, after increasing the carbonization temperature from 800 °C to 1000 °C, the degradation activity was decreased. The rate constant also indicated the same trend suggesting an excess collapse of the carbon structure, thereby the decrease of available active regions at high temperatures. The decrease in the surface area and the adsorption capacity of the catalyst corroborated the degradation results. The RhB degradation efficiency was less for activated carbon, indicating the beneficiary contribution of Fe^0 and Fe_3C phases as active sites in the carbon matrix. In order to check the persistence of adsorbed dye on the carbon surface, a desorption study was conducted for MIL-800C, where the volume of isopropanol: water mixture was taken in a ratio of V(P: W)= 5:5. [58] However, the presence of RhB was not detected in the solution after 4h of the desorption experiment, implying that the adsorbed RhB was also degraded during the PS-activated reaction.
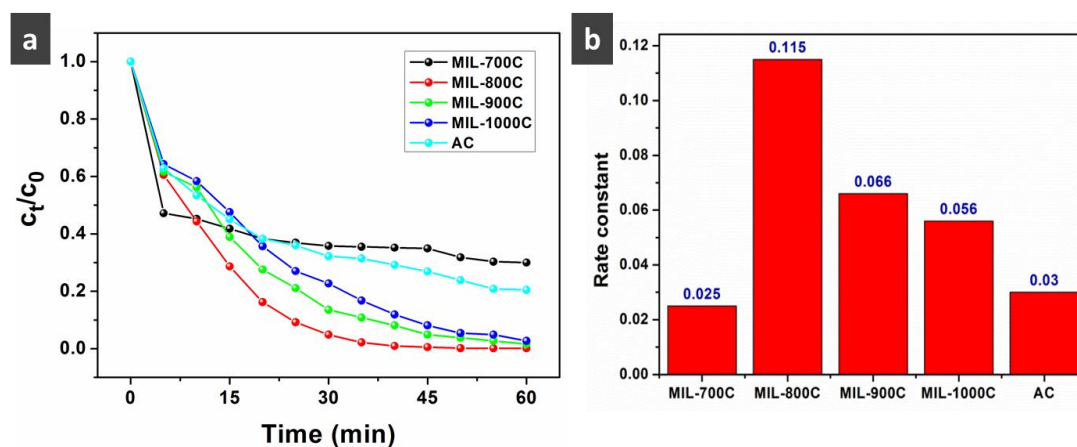
Figure 10. Degradation of RhB on different carbon samples

Figure 11. Persulfate activated degradation of RhB on MIL-800 C catalyst.

5.3.3. Optimization of persulfate dosage

Initially, the degradation activity was evaluated individually for the catalyst and persulfate alone in the Rhodamine solution. However, neither of them showed good performance in the degradation process. The catalyst MIL-800C alone removed only up to 39 % RhB by the adsorption on the porous carbon surface. The persulfate system could degrade only 31 % of RhB within 1h, indicating that the self-activation of persulfate is poor. The addition of 100 mg/L catalyst with varying persulfate (PS) concentrations (from 1 mM to 7 mM) improved the degradation process at a rapid rate. When the PS dosage was increased from 1 mM to 7 mM, faster kinetics could be achieved. At a PS dosage of 5 mM, the catalyst could degrade about 100 % RhB within 35 minutes and was optimized for further degradation studies **(Figure 11&12)**. The improvement in the degradation mechanism with the increase in the persulfate concentration was attributed presumably to the generation of more reactive species on the surface of the catalyst, accelerating further the degradation kinetics. The rate constant value increased from 0.068 to 0.119 min^{-1} on increasing the persulfate dosage from 1 mM to 7 mM.

Figure 12. Degradation of RhB with varying persulfate dosage

5.3.4. Optimization of catalyst dosage

The effect of catalyst dosage on the degradation of RhB was studied with an optimized 5 mM concentration of persulfate. The degradation rate with varying catalyst concentrations was studied by taking the MIL-800C carbon catalyst in the range of 50 mg/L,75 mg/L, 100 mg/L, and 125 mg/L in the solution. When the catalyst dosage was 50mg/L, about 80 % RhB was degraded in 60 minutes (**Figure 13a&13b**). The degrada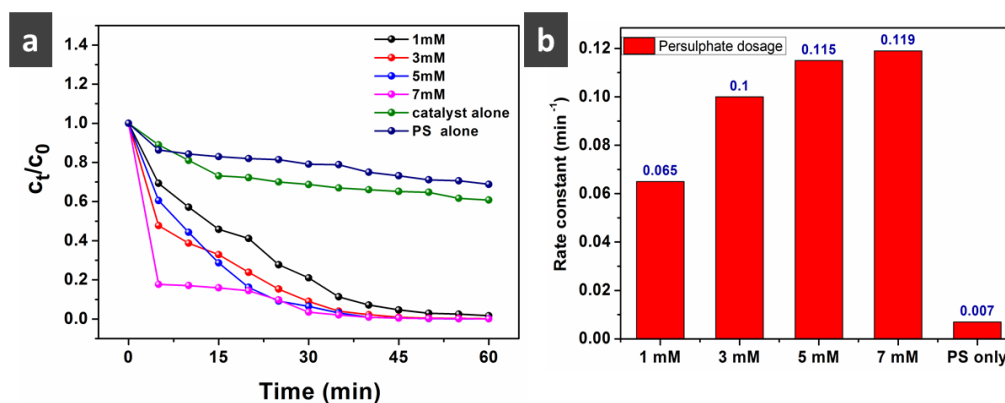tion rate increased with increasing catalyst amount from 50 mg/L to 125 mg/L with an increase in rate constant value from 0.038 to 0.118 min^{-1}. The degradation rate of RhB significantly increased to 100 % within 35 minutes as the catalyst dosage was 100mg/L. This gives evidence for the involvement of the MIL-800C catalyst in the degradation process. With the increase in catalyst dosage, the higher Fe^0 and Fe_3C active centres in the reaction medium accelerate the generation of reactive species from persulfate, hence the degradation rate. Further increase of catalyst dosage to 125 mg/L did not yield an appreciable increase in the degradation rate, probably due to the insufficient quantity of persulfate with respect to catalyst amount to generate $SO_4^{\bullet-}$. This proves the inevitable role of both the catalyst and persulfate in the degradation process. The optimized catalyst dosage of 100 mg/L and a persulfate dosage of 5 mM have been thus used for further optimization studies.
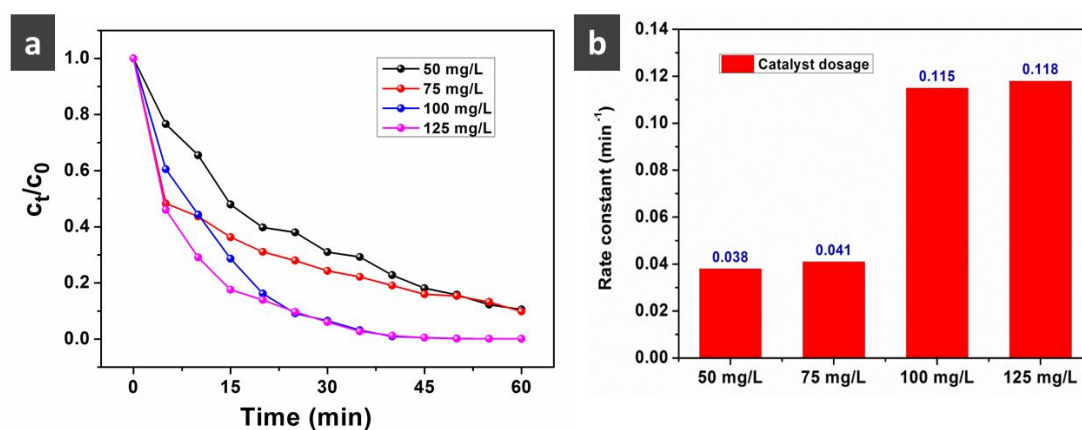
Figure 13. Degradation of RhB with varying MIL-800C catalyst dosage

Table 5 provides a comparison of the present work with the reported MOF-derived Fe/carbon hybrid catalysts for the degradation of various organic contaminants. It can be noted that the prepared carbon MIL-800C catalyst could achieve faster degradation performance for a higher concentration of RhB with a minimum catalyst dosage of 100 mg/L and a persulfate dosage of 5 mM.

5.3.5. Evaluation of degradation mechanism

To understand the degradation mechanism, quenching experiments were conducted by adding radical scavengers into the solution. The effect of free radical quenching agents methanol (MeOH) and tertiary butyl alcohol (TBA) was analyzed by conducting experiments with an excess amount of TBA and MeOH **(Figure 14)**. MeOH reacts with both OH $^\bullet$ and SO4$^{\bullet-}$, whereas TBA can only react with OH $^\bullet$. [59, 60] The free radical scavenging experiments were conducted by adding 500 mM and 1000 mM of MeOH and TBA in separate experiments. The degradation efficiency decreased by adding MeOH and TBA into the system, confirming the involvement of free radicals OH $^\bullet$ or SO$_4^{\bullet-}$ in the degradation mechanism. When the system was introduced with TBA, the degradation rate was lower than a similar MeOH concentration. This proves that the degradation mechanism is more OH $^\bullet$ oriented than SO$_4^{\bullet-}$ radical. Also, an even higher concentration of 1000 mM of MeOH was not efficient in slowing down the degradation rate compared to TBA, indirectly evidencing the generation of O$_2^{\bullet-}$.
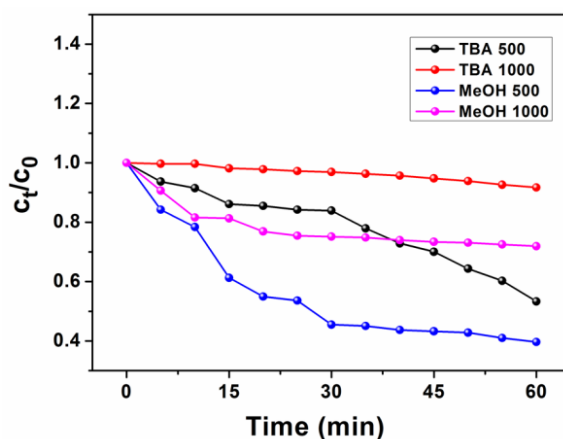
Figure 14. Influence of Scavengers TBA and MeOH on RhB degradation.

The effect of OH$^\bullet$ was further analyzed using free radical trapping experiments with Terephthalic acid (TA). The formed OH$^\bullet$ can be trapped by TA to form 2-Hydroxyterephthalic acid. The photoluminescence (PL) spectra of the samples give an emission peak of around 425 nm upon adding 100 mg/L of the catalyst MIL-800C and 5 mM persulfate into 5 mM TA solution. The intensity of the emission peak increased upon increasing the reaction time and reached $\approx 6.4 \times 10^5$ indicating the generation of a higher

amount of $OH^\bullet$ during the degradation process. The generation of $O_2^{\bullet-}$ in the system was analyzed by adding Luminol as the trapping agent. The characteristic PL peak of 3-aminophthalate, formed by the reaction of $O_2^{\bullet-}$ with Luminol (3-Aminophthalhydrazide), was observed with high intensity at around 420 nm upon excitation with 350 nm.[61] However, the intensity of $OH^\bullet$ is much higher compared to $O_2^{\bullet-}$ (3x 10^5), proving that $OH^\bullet$ is the prominent reaction intermediate in the degradation experiment. Also, the intensity of $O_2^{\bullet-}$ was found to increase up to an initial 30 min, after which the intensity decreased (**Figure 15a&15b**). This might be attributed to the interconversion of the formed $O_2^{\bullet-}$ to $OH^\bullet$ in the aqueous medium according to (**mechanisms 6&7**).[62] Thus, the Fe^{3+}, as evident from the XPS, could be reduced by $S_2O_8^{2-}$ in the aqueous medium, thereby forming Fe^{2+}, which will further react with $S_2O_8^{2-}$ to form $SO_4^{\bullet-}$ (**mechanisms [1]&[2]**). Also, the additional Fe^0 present in the system can form Fe^{2+}, further enhancing the formation of $SO_4^{\bullet-}$ (**mechanism 3**). Therefore, these Fe_3C and Fe^0 phases effectively contribute to the overall degradation mechanism.[15, 16, 62]

$$Fe^{2+} + S_2O_8^{2-} \rightarrow Fe^{3+} + SO_4^{\bullet-} + SO_4^{2-} \quad \text{---------- [1]}$$

$$Fe^{3+} + S_2O_8^{2-} \rightarrow Fe^{2+} + S_2O_8^{\bullet-} \quad \text{---------- [2]}$$

$$Fe (0) + 2S_2O_8^{2-} \rightarrow Fe^{2+} + 2SO_4^{2-} + 2SO_4^{\bullet-} \quad \text{---------- [3]}$$

$$Fe^{3+} + S_2O_8^{\bullet-} + 2H_2O \rightarrow Fe^{2+} + 2HSO_5^- + 2H^+ SO_4^{\bullet-} + H_2O \rightarrow SO_4^{2-} + OH^\bullet + H^+ \text{ -[4]}$$

$$Fe^{2+} + O_2 \rightarrow O_2^{\bullet-} + Fe^{3+} \quad \text{--------- [5]}$$

$$O_2^{\bullet-} + S_2O_8^{2-} \rightarrow {}^1O_2 + SO_4^{\bullet-} + SO_4^{2-} \text{ ----- [6]}$$

$$1/2\ O_2^{\bullet-} + H_2O \rightarrow 2\ OH^\bullet \quad \text{---------------- [7]}$$
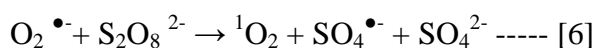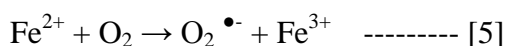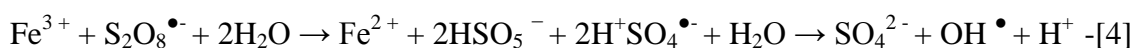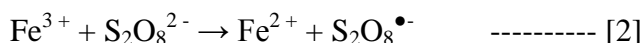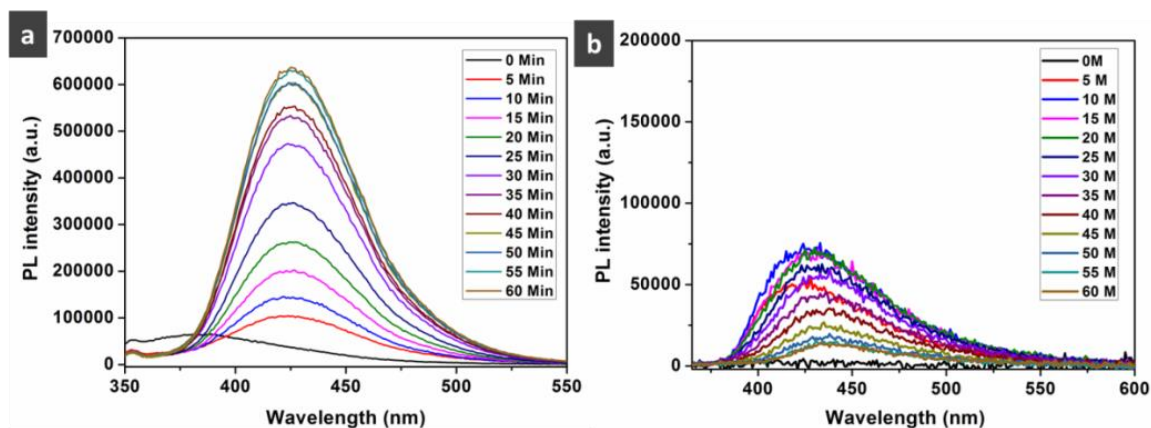
Figure 15 Variation in the PL intensity as a function of time by adding a) 5mM of Terephthalic acid and b) 5mM of Luminol into the catalyst-PS system, respectively. [catalyst]= 100 mg/L, [PS]= 5 mM, [RhB]= 30 mg/L, [TA]=[Luminol]= 5 mM .

To further understand the degradation mechanism, the HR-MS of the solution was analyzed before and after the addition of catalysts (**Figure 16**). Based on the intermediate degradation products obtained, a possible degradation mechanism is proposed (**Figure 17**). The peak at the m/z value of 443 corresponds to unreacted Rhodamine B (**Figure 16a**). After the addition of the catalysts, the HR-MS spectrum was recorded at time intervals of 10 minutes and 30 minutes. The peaks at m/z values of 415 and 386 correspond to the N-deethylated products. Peaks at m/z 370,308, 290, and 212 can be assigned to the oxidized products. The peaks at 206, 173, and 122 correspond to the products after fragmentation of the chromophore, which may be further converted to CO_2, H_2O, etc. Hence, the degradation proceeds mainly through N-deethylation and chromophore cleavage by the $OH^{\bullet}$ and $O_2^{\bullet-}$ generated in the medium. With the increase in reaction time, the intensity of the peak at m/z 212 dominated, indicating that it is the main intermediate product formed during the degradation. [63-66]
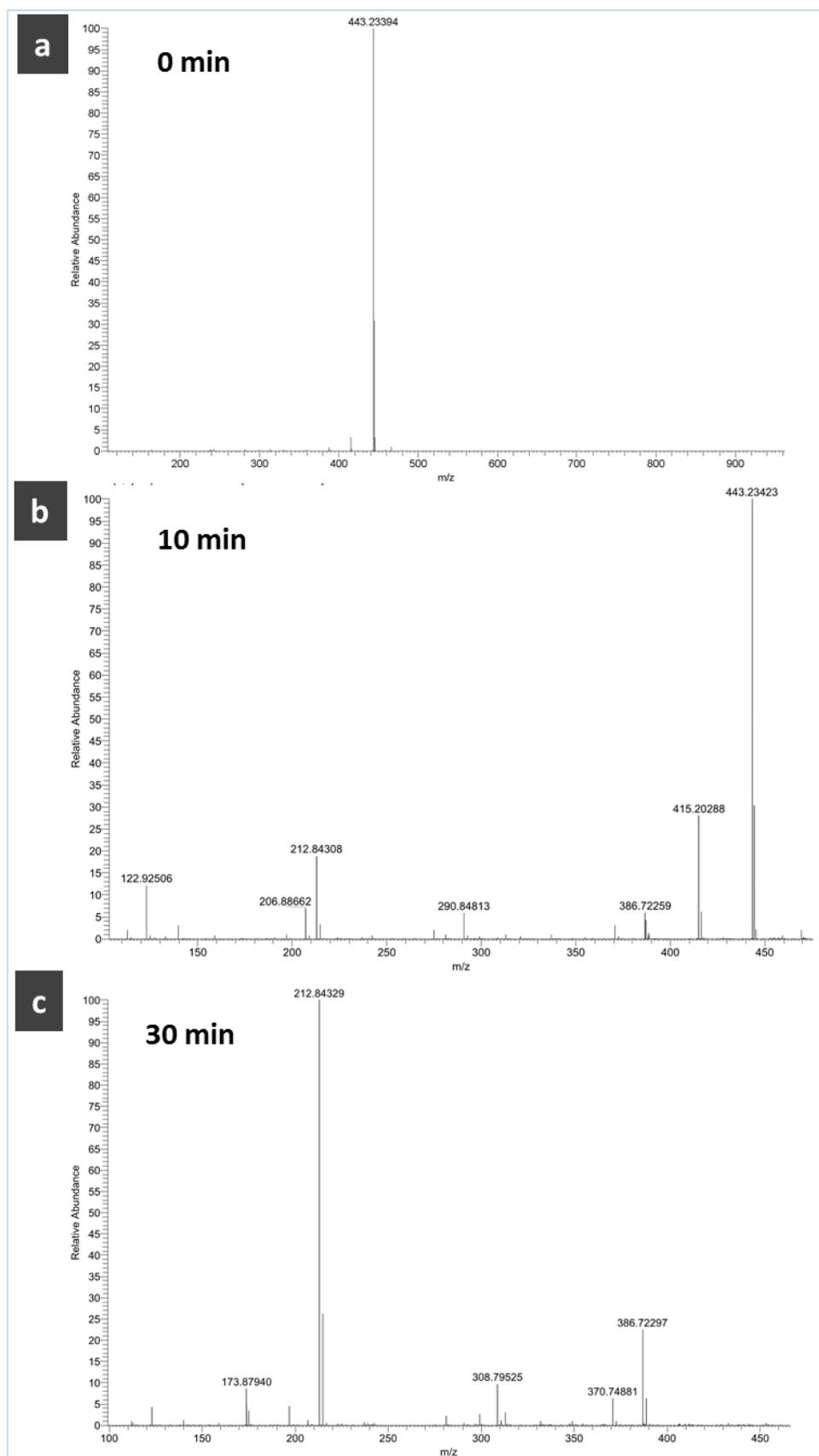
Figure 16. Mass spectra of the RhB solution extracted at a) 0 min, b) 10 min, and c) 30 min during the degradation experiment
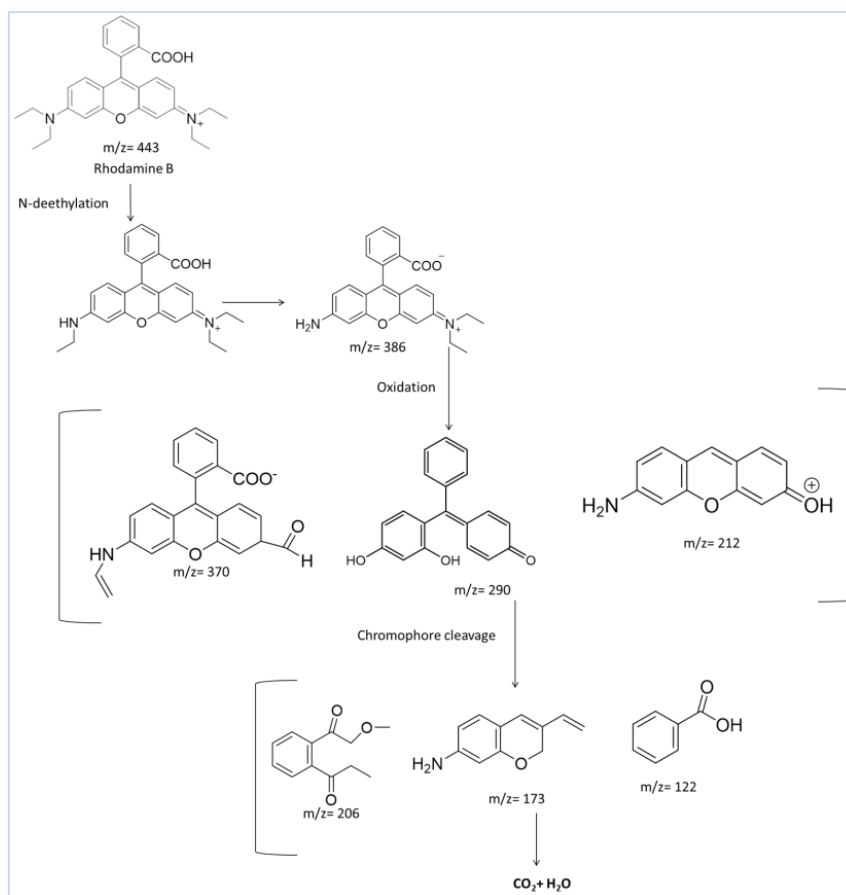
Figure 17. The possible degradation pathway of Rhodamine B

5.3.6. Study on the influence of reaction conditions

The effect of initial pH on the degradation rate was examined to understand the adaptability of the catalyst toward various pH ranges. Initially, the pH of the solution was varied in the desired range by adding appropriate amounts of 1 M NaOH and 1 M H_2SO_4 into the dye solution. The degradation of RhB was then studied at the pH values of $\approx$ 3, 4, 7, and 10. The catalyst-persulfate system showed higher degradation activity at neutral and acidic pH ranges. When the initial pH was changed to an alkaline pH of $\approx$10, the degradation efficiency declined to 35 % in 30 minutes (**Figure 18a&18b)**. The plausible reason for the decline of the RhB degradation at alkaline pH is the presence of excess OH⁻ ions which may hydroxylate the active metal centres hindering the PS molecule from being adsorbed on the surface of the catalyst due to the electrostatic repulsion. [24]

The initial temperature on the reaction medium has effects on the reaction rate due to the collision factors and the increase in the movement of the molecules upon the rise in kinetic energy. The RhB degradation was studied at varying temperatures, 35 °C, 45 °C, and 55 °C

with optimized catalyst-persulfate dosage and dye concentration. It is found that the initial reaction temperature has a positive effect on the RhB degradation mechanism as the rate constant showed an increase from 0.116 min^{-1} to 0.143 min^{-1}. The rise in reaction temperature from 35 °C to 55 °C shifted the reaction kinetics faster and achieved the complete degradation within 25 minutes **(Figure 18c & 18d).** This might be due to the vigorous interaction of the persulfate with the catalyst and the associated generation of reactive species with the increase in temperature. The attack of reactive radicals on the RhB target was accelerated, leading to faster degradation kinetics.
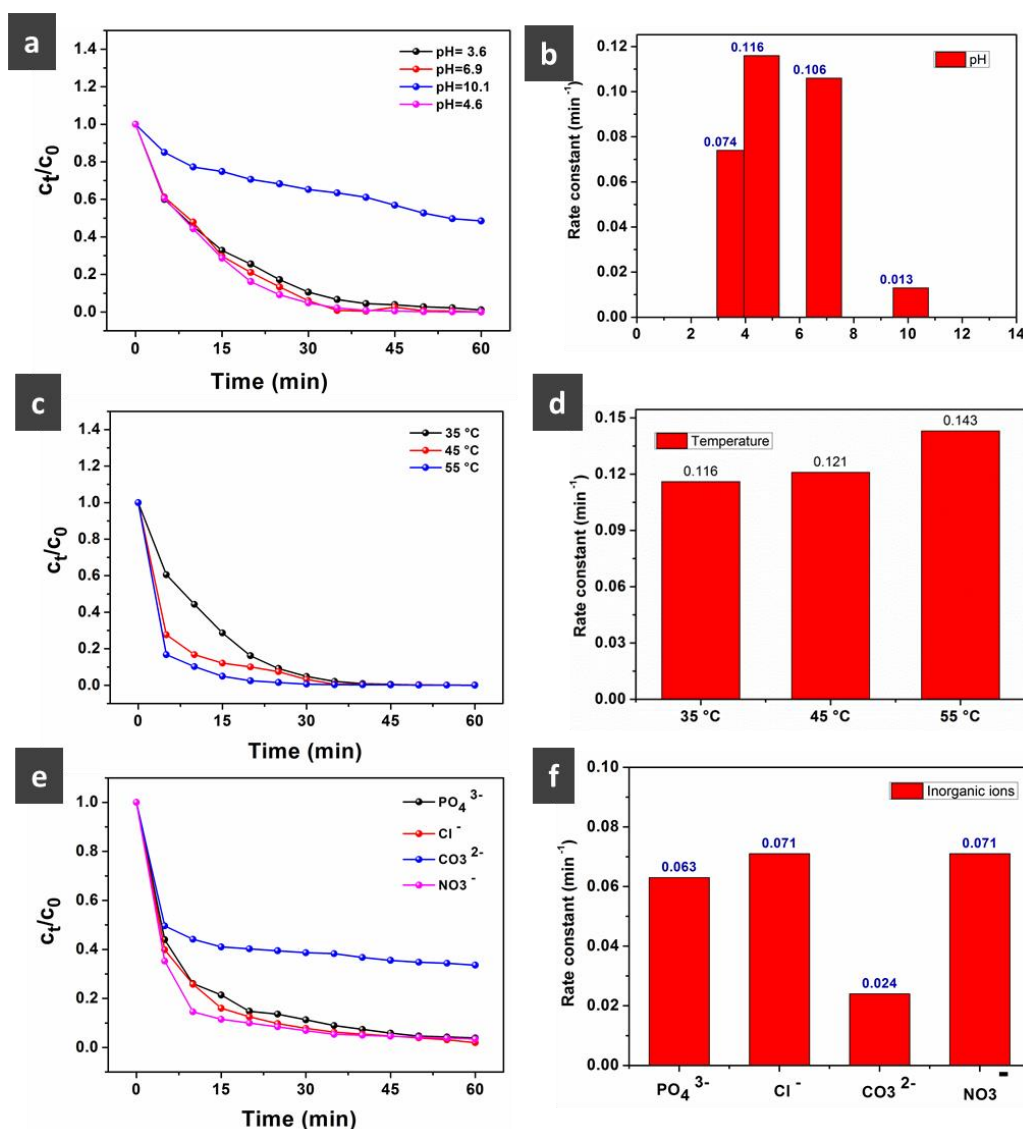
Figure 18. Influence of different parameters on the degradation of RhB a) Initial pH, c) reaction temperature, e) presence of different inorganic ions in the solution, and (b,d&f) corresponding degradation rate constant values. Optimized reaction conditions: [RhB] = 30 mg/L, catalyst loading = 100 mg/L, [PS] = 5 mM and temperature = 25 °

Generally, contaminated water contains multiple inorganic species that can poison the catalyst and interfere with the PS activation affecting the degradation process. The effect of different inorganic species in the water on the degradation efficiency of the catalyst-persulfate system is studied by incorporating 5 mM NO_3^-, CO_3^{2-}, PO_4^{3-}, and Cl^- in the RhB solution. It can be noted that the catalyst-PS system showed tolerance to almost all inorganic ions except a slight decrease in the presence of CO_3^{2-} ions **(Figure 18e& 18f)**. This is attributed to the fact that the CO_3^{2-} species in the reaction medium can act as a scavenger for the reaction intermediate $OH^\bullet$ and $O_2^{\bullet-}$ radicals, adversely influencing the RhB degradation process. [24]

5.3.7. Degradation study of other organic pollutants

The capability of the MIL-800C catalyst to degrade other organic pollutants was also analyzed by extending the degradation experiments with various chemical and pharmaceutical contaminants. The Fe^0, Fe_3C encapsulated carbon-persulfate system could degrade Methylene blue dye (100 %), 4-chlorophenol (53 %), Phenol (52 %), Nitrobenzene (45 %), and benzoic acid (30 %) as well as the pharmaceutical waste Linezolid (88 %), HCQ (79 %) and Cefpodoxime proxetil (55 %) within 60 min suggesting that MIL-800 C has a broad spectrum activity towards the persulfate based degradation of organic contaminants **(Figure 19a& 19b)**.
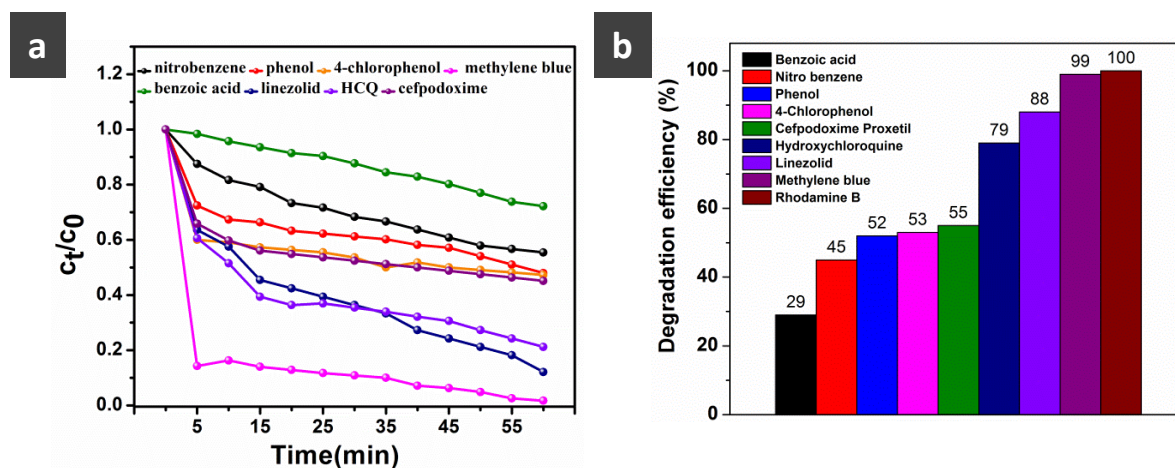
Figure 19. Degradation of other organic contaminants over MIL-800C catalyst and b) degradation rate constants. Reaction conditions: [PS] = 5 mM, [Organic contaminants] = 30 mg/L, catalyst loading = 100 mg/L and temperature = 25 °C

The poor degradation efficiency of the catalyst towards compounds such as benzoic acid, Nitrobenzene, phenol, 4-Chlorophenol, and cefpodoxime proxetil correlates with the electron-withdrawing groups present in these compounds evidencing the selective oxidation of organic groups containing electron-donating groups, in the presence of singlet oxygen generated from the catalyst as has been reported recently. [67, 68, 69]

The effect of a catalyst in treating real-time textile effluent was also evaluated. The change in the COD values was measured before and after 1h of treatment of the prepared Rhodamine B solution and effluent collected from the nearby textile industry (**Figure 20**). It could be observed that the COD was reduced by 65 % after 1h of treatment in the industrial effluent, whereas an 83 % reduction was observed for the optimized RhB solution, highlighting the practical application of the prepared catalyst.
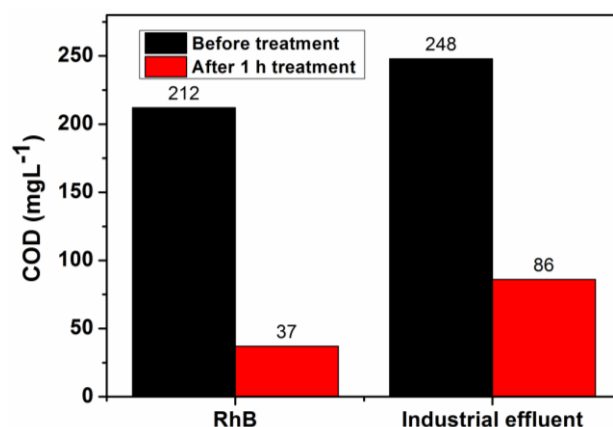
Figure 20. Variation in the COD values of RhB solution and the collected Industrial effluent before and after 1h treatment. Reaction conditions: [PS] = 5 mM, [RhB]= 30 mg/L, catalyst loading = 100 mg/L and temperature = 25 °C

5.3.8. Analysis of cyclic stability of the catalyst

The stability and recyclability of a catalyst were examined by running 5 consecutive cyclic tests to ascertain the utility of the catalyst for practical applications **(Figure 21a)**. The catalyst was separated after each consecutive cycle by magnetic separation and used after drying in an oven at 100 °C. The presence of Fe species aided the easy recovery of the catalyst due to its high magnetization. Even after 5 consecutive cycles, the activity of the catalyst remained high with > 90 % degradation efficiency. TEM images taken after 5 cycles of operation confirmed that the morphology of the catalyst remained unchanged, indicating appreciable stability of the catalyst **(Figure 21b)**. PXRD of the catalyst MIL-

800C was recorded after 5 cycles of operation, indicating that all the peaks remain the same. However, an extra peak at 22.1 corresponding to the (220) plane of Fe_2O_3 indicated partial oxidation of Fe particles in the presence of solvents. The reduced concentration of the Fe phases, as indicated by the decrease in the intensity of the Fe phases, caused a slight decline in the degradation activity owing to the fewer Fe-based catalytic active sites **(Figure 21c)**. Here, the encapsulation of Fe phases within the carbon sheets upon the carbonization of MIL-100 (Fe) frameworks could shield the active sites to an extent, as evidenced by its high cyclic stability.
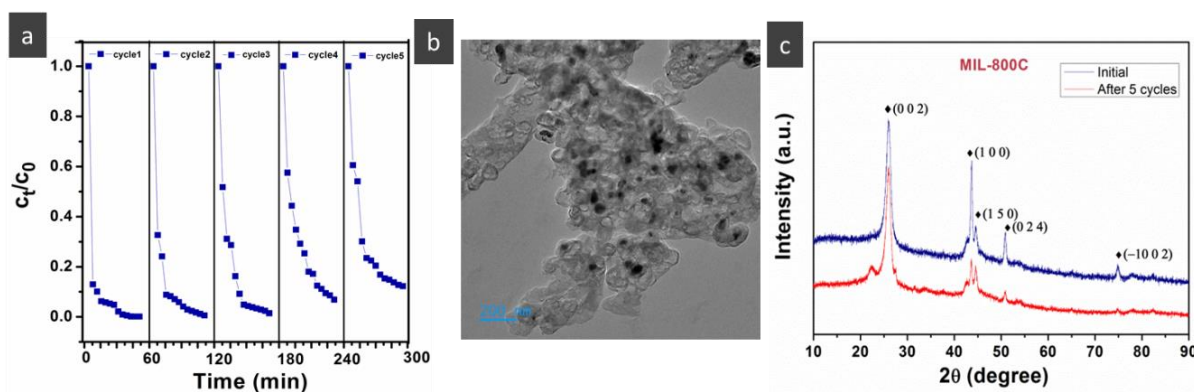
Figure 21. a) Evaluation of the recyclability of MIL-800C catalyst for RhB degradation, b) HRTEM image, and c) PXRD patterns of MIL-800C before and after 5 consecutive cycles, respectively

5.3.9. Fabrication of MIL-800@MST sponge for practical application

The carbon catalyst in the powder form has inherent advantages like high surface area and easy miscibility. Nevertheless, the employment and recovery of the catalyst are difficult, thus raising the limitation of MIL-800C carbon powder for practical applications. Hence, we incorporated the MIL-800C powders into a melamine sponge (MS) of size 2 cmx2 cm x2 cm via ultrasonication followed by heat treatment at 300 °C. The heat treatment enables the shrinking of pore sizes of the sponge, making it capable of holding the carbon catalyst. [70] The dye degradation studies were tested by submerging the carbon sponge into the solution containing 30 mg/L of dye solution and 5 mM persulfate. The system was kept under observation, and the degradation rate was analyzed every 12 h. The catalytic degradation of the MIL-800@MS was compared with a melamine sponge carbonized without the catalyst (MST) and a bare Melamine sponge. Even though the carbonized sponge itself showed some extent of degradation performance, the rate was much accelerated by the incorporation

of MIL-800C. It could be observed that the system showed complete degradation within 24 h, even without any stirring, indicating the possibility for large-scale application of the catalyst MIL-800C for water purification applications **(Figure 22)**. To further calculate the mineralization efficiency of the Rhodamine B solution, the TOC removal rate was calculated. The removal rate reached 61.6 % within 24 h, indicating good degradation efficiency of the catalyst even under static conditions.

Figure 22. a) The fabrication of MIL-800@MS sponge and b) degradation of RhB at 24 h with and without MIL-800@MST sponge catalyst with [RhB]= 30 mg/L and [PS] = 5 mM

Table 5. Comparison of degradation performance of different MOF-derived Fe containing carbon catalysts

Catalyst	Parent MOF	Reaction conditions	Contaminants	Time (min)	Degradation efficiency	Ref
N-doped $Fe^0/Fe_3C@C$	polydopamine-coated PB micro cubes	BPA (50 mg L-1) Catalyst (~0.2 g L^{-1}),[PS] = 0.5 g L^{-1} pH 7, 298 K	BPA	150 min	85 %	[1]
Fe@C	Fe(Hbidc)	[SMX] = 10 mg L^- 1, [PS] = 0.2 mM, catalyst = 0.4 g L^{-1} 1, T=30 ∘C, ambient pH.	SMX	90 min	98.3 %	[2]
MICN	MIL-88A	Oxidant 300 mg $L^{-1,}$ MICN 300 mg L^{-1}, RB 10 mg L^{-1}, T 25 ∘C, PSF persulfate.	Rhodamine B	100 min	90 %	[3]
Fe/Fe$_3$C@NC	MIL-88B-NH2	catalyst (0.2 g L-1) PMS (2 g L-1) 4-CP aqueous solution (20 mg L-1)	4-chlorophenol	60	93%	[4]

FexC FexCN	MIL-53(Fe) NH2-MIL-53(Fe)	[catalyst]=100 mg/L, [PMS]=0.65 mM, [ACV]=10 mg/L, room temperature	ACV	4 min 30 min	100 % 100 %	[5]
XFeNC	Fe-ZIF-8	catalyst (0.15 g/L) phenol 100 mL (20 mg/L),20 mg of PMS	Phenol	30 min	100 %	[6]
N-G	MIL-100 with dicyandiamide	catalysts (0.1 g/L) PMS 3.25 mM phenol (50 ppm), SCP (20 ppm), TCP (50 ppm), and PHBA(20 ppm))	phenol (50 SCP (20 ppm), TCP (50 ppm), and PHBA (20 ppm)	30 min	100 %	[7]
rGOF	Fe-BTC MOF with rGO	[PDS] = 1.0 mM, [rGOF] = 50 mg L^{-1}, [PCs] = 0.1 mM, T = 298.15 K, pH0 = 7	BPA	30 min	100 %	[8]
Ni-Fe-C-600-acid/GO	Ni-Fe-MOF with GO	[catalysts] = 15 mg/L, [PCA] = 0.15 mM, [PDS] = 0.25 mM, pH = 5.0, T = 25 ∘C	PCA	60 min	95.4 %	[9]
SAFe-x-N-C	Iron phthalocyanine @ZIF-8	[CAP] = 0.1 mM, [Catalyst] = 100 mg/L, [PDS] = 1.0 mM, initial pH = 7.	CAP	8 h	95.5 %	[10]
MIL-800C	MIL-100 (Fe)	Catalyst (0.1 g/L) PMS (5 mM) RhB (30 mg/L)	Rhodamine B	35 min	100 %	Present work

5.4. Conclusions

In summary, we have synthesized highly porous Fe, Fe_3C encapsulated carbon from the metal-organic framework MIL-100 (Fe) via a simple carbonization route. The carbon MIL-800C, derived at 800 °C, exhibited a high surface area value of 431 m^2/g with a micro-meso porous architecture and well-dispersed Fe^0 and Fe_3C phases incorporated on carbon sheets. The obtained carbon was utilized for the persulfate-activated degradation of Rhodamine (B) dye. The catalyst showed a 100 % degradation rate for RhB within 35 minutes at room temperature, with a catalyst loading of 100 mg/L and a 5 mM concentration of persulfate in a 30 mg/L dye solution. The catalyst also exhibited a higher degradation rate within the pH range of (3-7). The degradation process occurred via the free radical-mediated ($OH^\bullet$ and $O_2^{\bullet-}$) advanced oxidation processes. The catalyst showed higher stability and retained 90 % of the removal rate even after 5 cycles of operation. It also showed an appreciable degradation rate towards other organic and pharmaceutical contaminants, indicating a broad range of degradation activity. The prepared Fe-incorporated carbon catalyst can be an efficient candidate for the degradation of organic pollutants and, thereby, can be utilized for the remediation of water contamination caused by organic pollutants.

4.5. References

1. J. Lukač Reberski, J. Terzić, L.D. Maurice, D.J. Lapworth, Emerging organic contaminants in karst groundwater: A global level assessment, Journal of Hydrology 604 (2022) 127242. https://doi.org/https://doi.org/10.1016/j.jhydrol.2021.127242.

2. G. Crini, E. Lichtfouse, Advantages and disadvantages of techniques used for wastewater treatment, Environmental Chemistry Letters 17 (2019) 145-155. https://doi.org/10.1007/s10311-018-0785-9.

3. P. Kokkinos, D. Mantzavinos, D. Venieri, Current Trends in the Application of Nanomaterials for the Removal of Emerging Micropollutants and Pathogens from Water, Molecules, 2020.

4.   U. Ushani, X. Lu, J. Wang, Z. Zhang, J. Dai, Y. Tan, S. Wang, W. Li, C. Niu, T. Cai, N. Wang, G. Zhen, Sulfate radicals-based advanced oxidation technology in various environmental remediation: A state–of–the–art review, Chem Eng J 402 (2020) 126232. https://doi.org/https://doi.org/10.1016/j.cej.2020.126232.

5.   J. Wang, S. Wang, Activation of persulfate (PS) and peroxymonosulfate (PMS) and application for the degradation of emerging contaminants, Chem Eng J 334 (2018) 1502-1517. https://doi.org/https://doi.org/10.1016/j.cej.2017.11.059.

6.   J. Lee, U. von Gunten, J.-H. Kim, Persulfate-Based Advanced Oxidation: Critical Assessment of Opportunities and Roadblocks, Environmental Science & Technology 54(6) (2020) 3064-3081. https://doi.org/10.1021/acs.est.9b07082.

7.   R. Xiao, Z. Luo, Z. Wei, S. Luo, R. Spinney, W. Yang, DD. Dionysiou, activation of peroxymonosulfate/persulfate by nanomaterials for sulfate radical-based advanced oxidation technologies, Current Opinion in Chemical Engineering 19 (2018) 51-58. https://doi.org/https://doi.org/10.1016/j.coche.2017.12.005.

8.   J. Scaria, P.V. Nidheesh, Comparison of hydroxyl-radical-based advanced oxidation processes with sulfate radical-based advanced oxidation processes, Current Opinion in Chemical Engineering 36 (2022) 100830. https://doi.org/https://doi.org/10.1016/j.coche.2022.100830.

9.   P.V. Nidheesh, G. Divyapriya, F. Ezzahra Titchou, M. Hamdani, Treatment of textile wastewater by sulfate radical based advanced oxidation processes, Separation and Purification Technology 293 (2022) 121115. https://doi.org/https://doi.org/10.1016/j.seppur.2022.121115.

10. [10] L. Ge, B. Shao, Q. Liang, D. Huang, Z. Liu, Q. He, T. Wu, S. Luo, Y. Pan, C. Zhao, J. Huang, Y. Hu, Layered double hydroxide-based materials applied in persulfate-based advanced oxidation processes: Property, mechanism, application and perspectives, J Hazard Mater 424 (2022) 127612. https://doi.org/https://doi.org/10.1016/j.jhazmat.2021.127612.

11. D. Kiejza, U. Kotowska, W. Polińska, J. Karpińska, Peracids - New oxidants in advanced oxidation processes: The use of peracetic acid, peroxymonosulfate, and

persulfate salts in the removal of organic micropollutants of emerging concern − A review, Science of The Total Environment 790 (2021) 148195. https://doi.org/https://doi.org/10.1016/j.scitotenv.2021.148195.

12. Q. Shi, S. Deng, Y. Zheng, Y. Du, L. Li, S. Yang, G. Zhang, L. Du, G. Wang, M. Cheng, Y. Liu, The application of transition metal-modified biochar in sulfate radical based advanced oxidation processes, Environmental Research 212 (2022) 113340. https://doi.org/https://doi.org/10.1016/j.envres.2022.113340.

13. C. Amor, J.R. Fernandes, M.S. Lucas, J.A. Peres, Hydroxyl and sulfate radical advanced oxidation processes: Application to an agro-industrial wastewater, Environmental Technology & Innovation 21 (2021) 101183. https://doi.org/https://doi.org/10.1016/j.eti.2020.101183.

14. J. Liu, C. Peng, X. Shi, Preparation, characterization, and applications of Fe-based catalysts in advanced oxidation processes for organics removal: A review, Environmental Pollution 293 (2022) 118565.https://doi.org/10.1016/j.envpol.2021.118565.

15. Y. Wu, X. Chen, Y. Han, D. Yue, X. Cao, Y. Zhao, X. Qian, Highly Efficient Utilization of Nano-Fe(0) Embedded in Mesoporous Carbon for Activation of Peroxydisulfate, Environmental Science & Technology 53(15) (2019) 9081-9090. https://doi.org/10.1021/acs.est.9b02170.

16. H. Luo, Y. Zeng, D. He, X. Pan, Application of iron-based materials in heterogeneous advanced oxidation processes for wastewater treatment: A review, Chemical Engineering Journal 407 (2021) 127191. https://doi.org/https://doi.org/10.1016/j.cej.2020.127191.

17. A.A. Babaei, M. Golshan, B. Kakavandi, A heterogeneous photocatalytic sulfate radical-based oxidation process for efficient degradation of 4-chlorophenol using TiO2 anchored on Fe oxides@carbon, Process Safety and Environmental Protection 149 (2021) 35-47. https://doi.org/https://doi.org/10.1016/j.psep.2020.10.028.

18. M. Brienza, I.A. Katsoyiannis, Sulfate Radical Technologies as Tertiary Treatment for the Removal of Emerging Contaminants from Wastewater, Sustainability, 2017.

19. W. Wang, Y. Liu, Y. Yue, H. Wang, G. Cheng, C. Gao, C. Chen, Y. Ai, Z. Chen, X. Wang, The Confined Interlayer Growth of Ultrathin Two-Dimensional Fe3O4 Nanosheets with Enriched Oxygen Vacancies for Peroxymonosulfate Activation, ACS Catal 11(17) (2021) 11256-11265. https://doi.org/10.1021/acscatal.1c03331.

20. J. Yu, L. Tang, Y. Pang, G. Zeng, J. Wang, Y. Deng, Y. Liu, H. Feng, S. Chen, X. Ren, Magnetic nitrogen-doped sludge-derived biochar catalysts for persulfate activation: Internal electron transfer mechanism, Chemical Engineering Journal 364 (2019) 146-159. https://doi.org/https://doi.org/10.1016/j.cej.2019.01.163.

21. C.-D. Dong, Y.-C. Lu, J.-H. Chang, T.-H. Wang, C.-W. Chen, C.-M. Hung, Enhanced persulfate degradation of PAH-contaminated sediments using magnetic carbon microspheres as the catalyst substrate, Process Safety and Environmental Protection 125 (2019) 219-227. https://doi.org/https://doi.org/10.1016/j.psep.2019.03.011.

22. D. Ma, Y. Yang, B. Liu, G. Xie, C. Chen, N. Ren, D. Xing, Zero-valent iron and biochar composite with high specific surface area via K2FeO4 fabrication enhances sulfadiazine removal by persulfate activation, Chemical Engineering Journal 408 (2021) 127992. https://doi.org/https://doi.org/10.1016/j.cej.2020.127992.

23. T. Zeng, M. Yu, H. Zhang, Z. He, J. Chen, S. Song, Fe/Fe3C@N-doped porous carbon hybrids derived from nano-scale MOFs: robust and enhanced heterogeneous catalyst for peroxymonosulfate activation, Catalysis Science & Technology 7(2) (2017) 396-404. https://doi.org/10.1039/C6CY02130A.

24. J. He, Y. Wan, W. Zhou, ZIF-8 derived Fe–N coordination moieties anchored carbon nanocubes for efficient peroxymonosulfate activation via non-radical pathways: Role of FeNx sites, Journal of Hazardous Materials 405 (2021) 124199. https://doi.org/https://doi.org/10.1016/j.jhazmat.2020.124199.

25. Z. Huang, H. Yu, L. Wang, M. Wang, X. Liu, D. Shen, S. Shen, S. Ren, T. Lin, S. Lei, Ferrocene doped ZIF-8 derived Fe-N-C single atom catalyst to active peroxymonosulfate for removal of bisphenol A, Separation and Purification Technology 305 (2023) 122402. https://doi.org/10.1016/j.seppur.2022.122402.

26. C. Liu, L. Liu, X. Tian, Y. Wang, R. Li, Y. Zhang, Z. Song, B. Xu, W. Chu, F. Qi, A. Ikhlaq, Coupling metal–organic frameworks and g-C3N4 to derive Fe@N-doped graphene-like carbon for peroxymonosulfate activation: Upgrading framework stability and performance, Applied Catalysis B: Environmental 255 (2019) 117763. https://doi.org/https://doi.org/10.1016/j.apcatb.2019.117763.

27. J. Joseph, S. Iftekhar, V. Srivastava, Z. Fallah, EN Zare, M. Sillanpää, Iron-based metal-organic framework: Synthesis, structure and current technologies for water reclamation with deep insight into framework integrity, Chemosphere 284 (2021) 131171. https://doi.org/https://doi.org/10.1016/j.chemosphere.2021.131171.

28. J. Zan, H. Song, S. Zuo, X. Chen, D. Xia, D. Li, MIL-53(Fe)-derived Fe2O3 with oxygen vacancy as Fenton-like photocatalysts for the elimination of toxic organics in wastewater, Journal of Cleaner Production 246 (2020) 118971. https://doi.org/https://doi.org/10.1016/j.jclepro.2019.118971.

29. T.A. Wezendonk, V.P. Santos, M.A. Nasalevich, Q.S.E. Warringa, A.I. Dugulan, A. Chojecki, A.C.J. Koeken, M. Ruitenbeek, G. Meima, H.-U. Islam, G. Sankar, M. Makkee, F. Kapteijn, J. Gascon, Elucidating the Nature of Fe Species during Pyrolysis of the Fe-BTC MOF into Highly Active and Stable Fischer–Tropsch Catalysts, ACS Catalysis 6(5) (2016) 3236-3247. https://doi.org/10.1021/acscatal.6b00426.

30. C. Liu, Y. Wang, Y. Zhang, R. Li, W. Meng, Z. Song, F. Qi, B. Xu, W. Chu, D. Yuan, B. Yu, Enhancement of Fe@porous carbon to be an efficient mediator for peroxymonosulfate activation for oxidation of organic contaminants: Incorporation NH2-group into structure of its MOF precursor, Chemical Engineering Journal 354 (2018) 835-848. https://doi.org/https://doi.org/10.1016/j.cej.2018.08.060.

31. X. Li, F. Liao, L. Ye, L. Yeh, Controlled pyrolysis of MIL-88A to prepare iron/carbon composites for synergistic persulfate oxidation of phenol: Catalytic performance and mechanism, Journal of hazardous materials 398 (2020) 122938. https://doi.org/10.1016/j.jhazmat.2020.122938.

32. L. Han, H. Qi, D. Zhang, G. Ye, W. Zhou, C. Hou, W. Xu, Y. Sun, A facile and green synthesis of MIL-100(Fe) with high-yield and its catalytic performance, New Journal of Chemistry 41(22) (2017) 13504-13509. https://doi.org/10.1039/C7NJ02975F.

33. L. Zhu, J. Ji, J. Liu, S. Mine, M. Matsuoka, J. Zhang, M. Xing, Designing 3D-MoS2 Sponge as Excellent Cocatalysts in Advanced Oxidation Processes for Pollutant Control, 59(33) (2020) 13968-13976. https://doi.org/https://doi.org/10.1002/anie.202006059.

34. X. Zhang, L. Li, Y. Zeng, F. Liu, J. Yuan, X. Li, Y. Yu, X. Zhu, Z. Xiong, H. Yu, Y. Xie, TiO2/Graphitic Carbon Nitride Nanosheets for the Photocatalytic Degradation of Rhodamine B under Simulated Sunlight, ACS Applied Nano Materials 2(11) (2019) 7255-7265. https://doi.org/10.1021/acsanm.9b01739.

35. Z. Li, X. Chen, X. Teng, C. Lu, Chemiluminescence as a New Indicator for Monitoring Hydroxylated Intermediates in Persulfate-Based Advanced Oxidation Processes, The Journal of Physical Chemistry C 123(35) (2019) 21704-21712. https://doi.org/10.1021/acs.jpcc.9b07058.

36. R. Nivetha, K. Gothandapani, V. Raghavan, G. Jacob, R. Sellappan, P. Bhardwaj, S. Pitchaimuthu, A.N.M. Kannan, S.K. Jeong, A.N. Grace, Highly Porous MIL-100(Fe) for the Hydrogen Evolution Reaction (HER) in Acidic and Basic Media, ACS Omega 5(30) (2020) 18941-18949. https://doi.org/10.1021/acsomega.0c02171.

37. M.A. Simon, E. Anggraeni, F.E. Soetaredjo, S.P. Santoso, W. Irawaty, T.C. Thanh, SB Hartono, M. Yuliana, S. Ismadji, Hydrothermal Synthesize of HF-Free MIL-100(Fe) for Isoniazid-Drug Delivery, Scientific Reports 9(1) (2019) 16907. https://doi.org/10.1038/s41598-019-53436-3.

38. P. Horcajada, S. Surblé, C. Serre, D.-Y. Hong, Y.-K. Seo, J.-S. Chang, J.-M. Grenèche, I. Margiolaki, G. Férey, Synthesis and catalytic properties of MIL-100(Fe), an iron(iii) carboxylate with large pores, Chemical Communications (27) (2007) 2820-2822. https://doi.org/10.1039/B704325B.

39. M. He, H. Jin, L. Zhang, H. Jiang, T. Yang, H. Cui, F. Fossard, J.B. Wagner, M. Karppinen, E.I. Kauppinen, A. Loiseau, Environmental transmission electron microscopy investigations of Pt-Fe2O3 nanoparticles for nucleating carbon nanotubes, Carbon 110 (2016) 243-248. https://doi.org/https://doi.org/10.1016/j.carbon.2016.09.026.

40. Z. Wang, Y. Jiang, Y. Li, H. Huo, T. Zhao, D. Li, K. Lin, X. Xu, Synthesis of Porous Fe3C-Based Composite Beads as Heterogeneous Oxidation Catalysts, 25(16) (2019) 4175-4183. https://doi.org/https://doi.org/10.1002/chem.201805936.

41. M. Liu, Z. Zhao, C. He, F. Wang, X. Liu, X. Chen, J. Liu, D. Wang, Application of Functional Modification of Iron-Based Materials in Advanced Oxidation Processes (AOPs), 14(9) (2022) 1498.https://doi.org/10.3390/w14091498

42. Y. Shi, C. Li, X. Liu, H. Zhang, Q. Zhao, X. Li, MIL-100(Fe) as a new catalyst for selective catalysis reduction of NOx with ammonia, Integrated Ferroelectrics 181(1) (2017) 14-25. https://doi.org/10.1080/10584587.2017.1352302.

43. T.K. Le, Q.V. Ca, L.C. Nguyen, T.S. Cu, H.T. Nguyen, Q.-T. Nguyen, T.T.T. Nguyen, Heterogeneous Catalytic Ozonation of Aqueous p-nitrophenol over MIL-100(Fe) Metal–Organic Framework, Ozone: Science & Engineering 44(5) (2022) 414-425. https://doi.org/10.1080/01919512.2021.1935210.

44. M. Thommes, K. Kaneko, A.V. Neimark, J.P. Olivier, F. Rodriguez-Reinoso, J. Rouquerol, K.S.W. Sing, Physisorption of gases, with special reference to the evaluation of surface area and pore size distribution (IUPAC Technical Report), 87(9-10) (2015) 1051-1069. https://doi.org/doi:10.1515/pac-2014-1117.

45. H. Wang, F.-X. Yin, N. Liu, R.-H. Kou, X.-B. He, C.-J. Sun, B.-H. Chen, D.-J. Liu, H.-Q. Yin, Engineering Fe–Fe3C@Fe–N–C Active Sites and Hybrid Structures from Dual Metal–Organic Frameworks for Oxygen Reduction Reaction in H2–O2 Fuel Cell and Li–O2 Battery, 29(23) (2019) 1901531. https://doi.org/https://doi.org/10.1002/adfm.201901531.

46. V. Priya K, M. Thomas, R. Illathvalappil, S. K, S. Kurungot, B.N. Nair, A.P. Mohamed, G.M. Anilkumar, T. Yamaguchi, U.S. Hareesh, Template assisted synthesis of Ni,N co-doped porous carbon from Ni incorporated ZIF-8 frameworks for electrocatalytic oxygen reduction reaction, New Journal of Chemistry 44(28) (2020) 12343-12354. https://doi.org/10.1039/D0NJ01373K.

47. C. Bläker, J. Muthmann, C. Pasel, D. Bathen, Characterization of Activated Carbon Adsorbents – State of the Art and Novel Approaches, 6(4) (2019) 119-138. https://doi.org/https://doi.org/10.1002/cben.201900008.

48. H. Li, L. Liu, J. Cui, J. Cui, F. Wang, F. Zhang, High-efficiency adsorption and regeneration of Methylene blue and aniline onto activated carbon from waste edible fungus residue and its possible mechanism, RSC Advances 10(24) (2020) 14262-14273. https://doi.org/10.1039/D0RA01245A.

49. D. Guo, S. Han, J. Wang, Y. Zhu, MIL-100-Fe derived N-doped Fe/Fe3C@C electrocatalysts for efficient oxygen reduction reaction, Applied Surface Science 434 (2018) 1266-1273. https://doi.org/https://doi.org/10.1016/j.apsusc.2017.11.230.

50. Z. Tian, C. Wang, J. Yue, X. Zhang, L. Ma, Effect of a potassium promoter on the Fischer–Tropsch synthesis of light olefins over iron carbide catalysts encapsulated in graphene-like carbon, Catalysis Science & Technology 9(11) (2019) 2728-2741. https://doi.org/10.1039/C9CY00403C.

51. T. Jawhari, A. Roid, J. Casado, Raman spectroscopic characterization of some commercially available carbon black materials, Carbon 33(11) (1995) 1561-1565. https://doi.org/https://doi.org/10.1016/0008-6223(95)00117-V.

52. A.C. Ferrari, Raman spectroscopy of graphene and graphite: Disorder, electron–phonon coupling, doping, and nonadiabatic effects, Solid State Communications 143(1) (2007) 47-57. https://doi.org/https://doi.org/10.1016/j.ssc.2007.03.052.

53. S.J. Goldie, K.S. Coleman, Graphitization by Metal Particles, ACS Omega 8(3) (2023) 3278-3285. https://doi.org/10.1021/acsomega.2c06848.

54. A. Gomez-Martin, Z. Schnepp, J. Ramirez-Rico, Structural Evolution in Iron-Catalyzed Graphitization of Hard Carbons, Chemistry of Materials 33(9) (2021) 3087-3097. https://doi.org/10.1021/acs.chemmater.0c04385.

55. Y. Zhang, Z. Lou, C. Wang, W. Wang, J. Cai, Synthesis of Porous Fe/C Bio-Char Adsorbent for Rhodamine B from Waste Wood: Characterization, Kinetics and Thermodynamics, Processes 7(3) (2019) 150.https://doi.org/10.3390/pr7030150

56. L. Yao, J. Yang, P. Zhang, L. Deng, In situ surface decoration of Fe3C/Fe3O4/C nanosheets: Towards bi-functional activated carbons with supercapacitance and efficient dye adsorption, Bioresource Technology 256 (2018) 208-215. https://doi.org/https://doi.org/10.1016/j.biortech.2018.02.027.

57. X. Xing, H. Qu, R. Shao, Q. Wang, H. Xie, Mechanism and kinetics of dye desorption from dye-loaded carbon (XC-72) with alcohol-water system as desorbent, Water Science and Technology 76(5) (2017) 1243-1250. https://doi.org/10.2166/wst.2017.268.

58. J. Huang, H. Zhang, Mn-based catalysts for sulfate radical-based advanced oxidation processes: A review, environment International 133 (2019) 105141. https://doi.org/https://doi.org/10.1016/j.envint.2019.105141.

59. R. Li, J. Kong, H. Liu, P. Chen, G. Liu, F. Li, W. Lv, A sulfate radical based ferrous–peroxydisulfate oxidative system for indomethacin degradation in aqueous solutions, RSC Advances 7(37) (2017) 22802-22809. https://doi.org/10.1039/C7RA03364H.

60. J. Shajeelammal, S. Mohammed, K.P. Prathish, A. Jeeva, A. Asok, S. Shukla, Treatment of real-time textile effluent containing azo reactive dyes via ozonation, modified pulsed low-frequency ultrasound cavitation, and integrated reactor, Journal of Hazardous Materials Advances 7 (2022) 100098. https://doi.org/https://doi.org/10.1016/j.hazadv.2022.100098.

61. K. Pavel, Advanced Oxidation Processes (AOPs) – Utilization of Hydroxyl Radical and Singlet Oxygen, in A. Rizwan (Ed.), Reactive Oxygen Species, IntechOpen, Rijeka, 2021, p. Ch. 15. https://doi.org/10.5772/intechopen.98189.

62. M. Pu, J. Wan, F. Zhang, M.L. Brusseau, D. Ye, J. Niu, Insight into degradation mechanism of sulfamethoxazole by metal-organic framework derived novel magnetic Fe@C composite activated persulfate, Journal of Hazardous Materials 414 (2021) 125598. https://doi.org/https://doi.org/10.1016/j.jhazmat.2021.125598.

63. X. Shi, P. Hong, H. Huang, D. Yang, K. Zhang, J. He, Y. Li, Z. Wu, C. Xie, J. Liu, L. Kong, Enhanced peroxymonosulfate activation by hierarchical porous Fe3O4/Co3S4 nanosheets for efficient elimination of rhodamine B: Mechanisms, degradation pathways and toxicological analysis, Journal of Colloid and Interface Science 610 (2022) 751-765. https://doi.org/https://doi.org/10.1016/j.jcis.2021.11.118.

64. X. Ma, H. Yuan, Q. Qiao, S. Zhang, H. Tao, Enhanced catalysis for degradation of rhodamine B by amino-functionalized Fe-MOFs with high adsorption capacity, Colloids

and Surfaces A: Physicochemical and Engineering Aspects 664 (2023) 131099. https://doi.org/https://doi.org/10.1016/j.colsurfa.2023.131099.

65. X. Liu, Y. Li, D. Deng, N. Chen, X. Xing, Y. Wang, A one-step nonaqueous sol–gel route to mixed-phase TiO2 with enhanced photocatalytic degradation of Rhodamine B under visible light, CrystEngComm 18(11) (2016) 1964-1975. https://doi.org/10.1039/C5CE02322J.

66. Y. Liu, H. Guo, Y. Zhang, X. Cheng, P. Zhou, G. Zhang, J. Wang, P. Tang, T. Ke, W. Li, Heterogeneous activation of persulfate for Rhodamine B degradation with 3D flower sphere-like BiOI/Fe3O4 microspheres under visible light irradiation, Separation and Purification Technology 192 (2018) 88-98. doi.org/10.1016/j.seppur.2017.09.045.

67. N. Du, Y. Liu, Q. Li, W. Miao, D. Wang, S. Mao, Peroxydisulfate activation by atomically-dispersed Fe-Nx on N-doped carbon: Mechanism of singlet oxygen evolution for nonradical degradation of aqueous contaminants, Chemical Engineering Journal 413 (2021) 127545. https://doi.org/10.1016/j.cej.2020.127545.

68. P. Sun, H. Liu, M. Feng, L. Guo, Z. Zhai, Y. Fang, X. Zhang, V.K.Sharma, Nitrogen-sulfur co-doped industrial graphene as an efficient peroxymonosulfate activator: Singlet oxygen-dominated catalytic degradation of organic contaminants,Applied Catalysis B: Environmental 251(2019) 335-345 doi.org/10.1016/j.apcatb.2019.03.085.

69. X. Duan, H. Sun, S. Wang, Metal-Free Carbocatalysis in Advanced Oxidation Reactions, Accounts of Chemical Research 51(3) (2018) 678-687. https://doi.org/10.1021/acs.accounts.7b00535.

70. A. Stolz, S. Le Floch, L. Reinert, S.M.M. Ramos, J. Tuaillon-Combes, Y. Soneda, P. Chaudet, D. Baillis, N. Blanchard, L. Duclaux, A. San-Miguel, Melamine-derived carbon sponges for oil-water separation, Carbon 107 (2016) 198-208. https://doi.org/https://doi.org/10.1016/j.carbon.2016.05.05

Chapter 6

Summary and Scope of Future Work
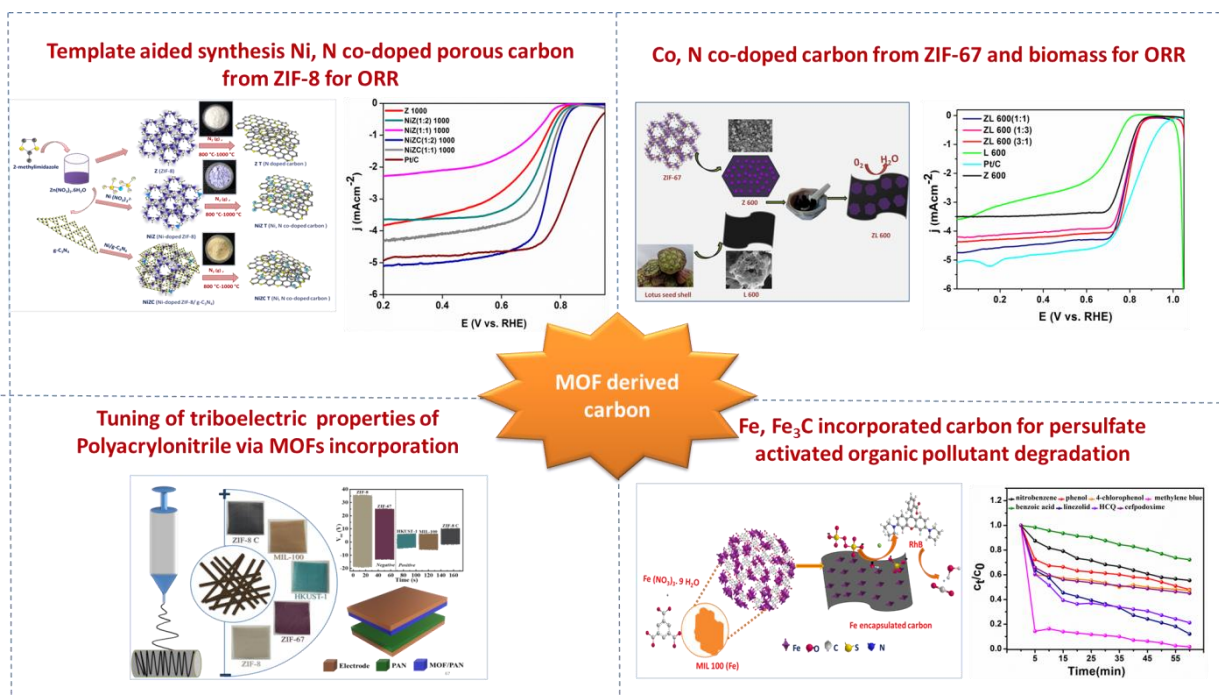
Developing cost-effective and sustainable materials are crucial for energy storage-conversion devices and treating environmental pollutants. Heteroatom-doped porous carbon is demonstrated to be a potential candidate by virtue of its tuned morphology, conductivity, surface area, etc. Metal-organic frameworks(MOFs) are established to be suitable templates for preparing transition metal, heteroatom-doped carbon, as the MOFs contain heteroatoms in the frameworks. The present thesis focuses on the preparation of various facile methods for the preparation of MOFs and MOFs derived heteroatom-doped carbon for applications in different energy and environment-related sectors.

ZIF-8 framework is formed by the coordination of Zn^{2+} ions with 2-methylimidazole ligands and possesses high surface area and porosity, due to which it is widely employed for adsorption and separation applications. ZIF-8 is also demonstrated to be an ideal precursor for preparing N-doped carbon and is found to possess good electrocatalytic activity for Oxygen reduction reaction(ORR) due to the higher electronic conductivity caused by the N-doping on the carbon. However, the ORR activity of the ZIF-8 derived carbon is limited due to its less effective adsorption-diffusion pathway around the micropores. Transition metal

incorporation into the ZIF-8 framework is found to be an effective method for obtaining transition metal-doped carbon with tuned porosity and morphology. These transition metals can act as active centres, enhancing their ORR activity. Template-assisted carbonization is also considered an efficient method to modulate the pore characteristics and improve the catalytic activity. Initially, we demonstrated the successful synthesis of Ni, N co-doped porous carbon by the high-temperature carbonization of the Ni-doped ZIF-8 precursors incorporated with g-C_3N_4 as a template. The guest metal atom Ni and the sacrificial g-C_3N_4 template have contributed to the evolution of carbon surfaces of varying morphology and with an increase in electrocatalytic ORR activity in the alkaline medium. The optimized composition of NiZC(1:2) 1000 exhibited higher ORR activity than other samples with a limiting current density of 5.2 mA cm^{-2} and a half-wave potential of 0.76 V vs. RHE. The sample also exhibited higher durability and methanol tolerance in the alkaline medium compared to commercial Pt/C electrocatalysts.

The MOF, ZIF-67, is also widely used to prepare Co, N co-doped carbon for application as ORR electrocatalyst. However, pristine ZIF-67 derived carbon possesses limited activity due to the agglomeration of excess metal particles and the reduced surface area upon carbonization. Therefore, a biomass (lotus seed shell) derived high surface area porous carbon was used as a support matrix for ZIF-67 derived Co, N co-doped carbon by preparing composites of the two carbons. The surface area was tuned with varying compositions of the mixtures in the composites. The optimized catalyst ZL 600(3:1) exhibited a half-wave potential of 0.79 V vs. RHE and a current density of -4.38 mA cm^{-2} when applied as an electrocatalyst in alkaline medium. The high surface area, pyridinic–pyrrolic nitrogen contents, and enriched Co active centres sheathed by carbon sheets favourably contributed to the efficient ORR mechanism.

Triboelectric devices are also considered ideal energy conversion devices due to their simple operation mode and cost-effectiveness. Polymer-based materials are widely employed in triboelectric devices due to their flexibility in fabrication. However, tuning their triboelectric behavior is still a challenge, and the applications thus demonstrated utilize only a particular set of materials in triboelectric devices. The addition of inorganic materials like metals and carbon materials is found to be an efficient strategy to improve the triboelectric output of the parent polymer. Porous material, by virtue of the ability of its pores to hold the charges for long time, is demonstrated to be good candidates in triboelectric applications. We made an attempt to tune the triboelectric behavior of the Polyacrylonitrile(PAN) fibre using different

metal-organic frameworks(MOFs), such as ZIF-8, ZIF-67, MIL-100, and HKUST-1, by incorporating them during the electrospinning process. While the ZIF-8 and ZIF-67 incorporated PAN fibre showed tribonegative nature, the trimesic acid coordinated MOFs, MIL-100 and HKUST-1, shifted the triboelectric behavior towards the positive side. This tuning of triboelectric behavior depended upon the nature of the ligand, the amount of MOF, and the particle size of the MOFs. The effect of carbonized ZIF-8 frameworks on the triboelectric nature of PAN is also evaluated. While the ZIF-8 incorporated PAN was toward the negative side of the pure PAN in the triboelectric series, the N-doped carbon obtained from ZIF-8(C ZIF-8) steered it towards the positive side. A triboelectric device was fabricated with ZIF-8, and the carbonized C ZIF-8 incorporated PAN fibers as opposite triboelectric layers. The device generated an output of 80 V and 0.8 μA. This method can be beneficial for advancing the fabrication of TENG based on porous materials and polymers, which can lead to devices with higher output when used against a suitable triboelectric layer.

Water pollution arising from the increased amount of organic pollutants is another challenge to society that demands advanced treatment methods. Advanced oxidation processes based on reactive free radicals from persulfate, mediated by a catalyst, are considered as an efficient method to remove harmful organic pollutants. Fe-based catalysts are demonstrated to be effective catalysts in AOPs. We synthesized Fe/Fe_3C encapsulated porous carbon by the single-step carbonization of the MIL-100 (Fe) metal-organic frameworks. The activity of the prepared carbon was optimized towards the degradation of the targeted contaminant Rhodamine (B). 100 % degradation was realized within 35 minutes with a minimum catalyst loading of 100 mg/L in 30 mg/L contaminant solution. The catalyst derived at 800 °C also exhibited high degradation activity towards various other organic compounds like Methylene blue, Benzoic acid, Nitro benzene, Phenol, 4-Chlorophenol, and antibiotics like Tetracycline, linezolid, Hydroxychloroquine, and Cefpodoxime proxetil. Moreover, the catalyst also effectively reduced the COD value of effluent collected from a nearby textile industry. The catalyst showed high stability and retained 90 % of its activity after five cycles of operation, owing to the protected Fe-based active sites within the carbon matrix.

The present study thus demonstrates that MOFs and MOF derivatives can serve as potent materials for different energy and environment-related applications.

Suggestions for Future Work:

➢ Exploring new sustainable and low-cost metal-organic frameworks

➢ Tailoring the morphology, porosity, and heteroatom content of MOF-derived carbon to reach the desired performance by employing various methods like template incorporation, transition metal introduction, etc.

➢ Efficient utilization of MOF derivatives as catalysts for fuel cells, advanced oxidation process and in triboelectric nanogenerators for powering devices.

ABSTRACT

Name of the Student: **Vaishna Priya K**	Registration No.: **10CC17A39009**
Faculty of Study: **Chemical Sciences**	Year of Submission: **2023**
AcSIR academic centre/CSIR Lab: **CSIR-National Institute for Interdisciplinary Science and Technology (CSIR-NIIST)**	
Name of the Supervisor**: Dr. U. S. Hareesh**	
Title of the thesis**: Metal-organic frameworks (MOFs) derived heteroatom-doped carbon for energy and environmental applications**	

This thesis mainly explores the effective application of various MOFs and MOF-derived heteroatom-doped porous carbon in diverse areas such as energy conversion devices and wastewater treatment. Chapter 1 gives an introduction to heteroatom-doped carbon and its preparation from various MOFs using different approaches. A comprehensive literature review on the applications of MOFs derived carbon towards fuel cell oxygen reduction reaction (ORR), triboelectric nanogenerators, and advanced oxidation-based water treatment is also summarized. Chapter 2 deals with the application of Ni, N co-doped porous carbon obtained from ZIF-8 via Ni incorporation and a template-aided strategy for enhanced ORR performance. The compositional and morphological tuning ultimately boosted the ORR activity, and the composition NiZC(1:2) 1000 showed a higher current density of 5.2 mA cm^{-2} and higher stability in alkaline medium. Chapter 3 reports the beneficial role of an external biomass-derived high surface area carbon in enhancing the ORR activity of ZIF-67 framework-derived Co, N co-doped carbon by tuning the surface area and providing support channels for ORR. Chapter 4 deals with the role of different sustainable MOFs and MOF-derived N-doped carbon in modulating the triboelectric behavior of electrospun polyacrylonitrile(PAN) fiber. Based on the nature of the ligand, the amount of the MOF loading, and the particle size, the triboelectric behavior of the PAN changed, and a reversal of the polarity was also achieved. Chapter 5 deals with the beneficial role of Fe and Fe_3C sites in porous carbon sheets on the persulfate-activated degradation of organic pollutants. The catalyst showed degradation towards a broad range of pollutants, including dyes, antibiotics, etc. The encapsulation of the active sites within the carbon could protect and impart better stability to the catalyst.

List of publications emanating from thesis work

1. Vaishna Priya K, M. Thomas, R. Illathvalappil, S. K, S. Kurungot, B. N. Nair, A. P. Mohamed, G. M. Anilkumar, T. Yamaguchi and U.S. Hareesh, Template assisted synthesis of Ni, N co-doped porous carbon from Ni incorporated ZIF-8 frameworks for electrocatalytic oxygen reduction reaction, **New Journal of Chemistry, 2020**, 44, 12343-12354.

2. Vaishna Priya K, Anupriya A, A. Peer Mohamed, U.S. Hareesh, MIL-100 (Fe) framework derived Fe encapsulated carbon catalyst for persulfate-activated degradation of organic contaminants from wastewater (Under review)

3. Vaishna Priya K., Geeta Pandurang Kharabe, Sidharth Barik, Sreekumar Kurungot, and U. S. Hareesh, ZIF-67 derived Co, N decorated carbon catalyst modified with biomass-derived high surface area porous carbon for enhanced oxygen reduction reaction (Manuscript communicated)

4. Vaishna Priya K., Harris Varghese, Achu Chandran, and U.S. Hareesh, Tuning of triboelectric properties of electrospun Polyacrylonitrile fiber via Metal-organic frameworks incorporation (Manuscript under preparation)

List of Publications out of thesis

1. B.S. Athira, A. George, **K. Vaishna Priya**, U.S. Hareesh, E.B. Gowd, K.P. Surendran, A. Chandran, High-Performance Flexible Piezoelectric Nanogenerator Based on Electrospun PVDF-BaTiO3 Nanofibers for Self-Powered Vibration Sensing Applications, **ACS Applied Materials & Interfaces**, 2022, 14,(39) 44239-44250.

2. Harris Varghese, **Vaishna Priya K**., U.S. Hareesh, and Achu Chandran, A High-performance Flexible Mechanical Energy Harvester based on PAN-PDMS Triboelectric Nanogenerator for Self-Powered Navigation (communicated)

List of conference presentations

1. Vaishna Priya K, Minju Thomas, Balagopal N. Nair, A. Peer Mohamed, U. S. Hareesh, Synthesis and Tuning of Ni Incorporated Nitrogen-Doped Porous Carbon from Ni/Zn ZIF-8 based Structures for Enhanced Electrocatalytic applications, *International Conference on Recent Trends in Materials Science and Technology (ICMST-2018)*

2. Vaishna Priya K, Minju Thomas, Balagopal N. Nair, A. Peer Mohamed, U. S. Hareesh, Morphological Tuning Ni, Nitrogen co-doped Porous Carbon Structure Derived from Ni Incorporated Zeolitic Imidazolate Framework-8, *National Conference on Emerging Trends in Science, Technology & Application of Electron Microscope (STAEM- 2018)*

3. **Vaishna Priya K,** Anupriya A, A. Peer Mohamed, and U.S Hareesh, MIL-100 Derived Fe Decorated Carbon for Persulphate Based Rhodamine B Degradation, *International Conference on Chemistry and Applications of Soft Materials (CASM 2022)*

4. Vaishna Priya K, Minju Thomas, Balagopal N. Nair, A. Peer Mohamed, U. S. Hareesh*, Template assisted synthesis of Ni, N co-doped porous carbon from Ni incorporated ZIF-8 framework for electrocatalytic oxygen reduction reaction, *Annual Technical Meeting -2020, Materials Research Society of India, Trivandrum chapter (Oral presentation)*

NJC

PAPER

Check for updates

Template assisted synthesis of Ni,N co-doped porous carbon from Ni incorporated ZIF-8 frameworks for electrocatalytic oxygen reduction reaction†

Vaishna Priya K., [ab] Minju Thomas, [ab] Rajith Illathvalappil,[bc] Shijina K., [ab] Sreekumar Kurungot, [bc] Balagopal N. Nair,[de] A. Peer Mohamed,[a] Gopinathan M. Anilkumar, [df] Takeo Yamaguchi[f] and U. S. Hareesh [*ab]

A heteroatom doped porous carbon electrocatalyst with enhanced oxygen reduction reaction (ORR) performance in alkaline medium was obtained by high temperature treatment of Ni incorporated ZIF-8 frameworks and its composite with g-C$_3$N$_4$ as a supporting matrix template. The morphology and porosity of this heteroatom containing carbon were tuned by varying the Ni:Zn molar ratio in Ni/Zn ZIF-8 and Ni/Zn ZIF-8@g-C$_3$N$_4$ composites. The template aided synthetic strategy using g-C$_3$N$_4$ helped in the controlled decomposition of composites leading to a heteroporous sheet like architecture with increased nitrogen content. The Ni/Zn ZIF-8 sample on heat treatment in the 800–1000 °C temperature range led to the formation of Ni,N co-doped porous carbon (Ni-NPC) with Ni–C active sites. The defective sites induced by nickel carbide along with the distributed N atoms on the carbon surface enabled active O$_2$ adsorption sites. The high surface area, high degree of graphitisation as well as the defects created by well dispersed N and Ni on porous carbon matrices favoured charge separation leading to higher electrochemical ORR activity. The Ni,N co-doped carbon catalyst in alkaline medium exhibited a limiting current density of 5.2 mA cm^{-2} with a half-wave potential of 0.76 V *vs.* RHE in 0.1 M KOH. The catalyst also showed improved methanol tolerance and better stability compared to the standard Pt/C catalyst.

1. Introduction

The undesirable climatic variations induced by global warming could be ascribed primarily to the uncontrolled emission of greenhouse gases as the fossil fuel consumption has increased manifold. This has prompted a genuine demand for greener energy storage/conversion technologies. The fuel cell is

^{a} Materials Science and Technology Division (MSTD), National Institute for Interdisciplinary Science and Technology, Council of Scientific and Industrial Research (CSIR-NIIST), Pappanamcode, Thiruvananthapuram, Kerala 695019, India. E-mail: hareesh@niist.res.in

^{b} Academy of Scientific and Innovative Research (AcSIR), Ghaziabad-201002, India

^{c} Physical and Materials Chemistry Division, CSIR-National Chemical Laboratory, Pune, Maharashtra, 411008, India

^{d} R&D Centre, Noritake Company Ltd, 300 Higashiyama, Miyoshi, Aichi 470-0293, Japan

^{e} School of Molecular and Life Sciences (MLS), Faculty of Science and Engineering, Curtin University, GPO Box U1987, Perth, Western Australia 6845, Australia

^{f} Laboratory for Chemistry and Life Science, Institute of Innovative Research, Tokyo Institute of Technology, Nagatsuta 4259, Midori-ku, Yokohama 226-8503, Japan

† Electronic supplementary information (ESI) available: HRTEM, electrochemical analysis, TGA and additional figures. See DOI: 10.1039/d0nj01373k

perceived to be an electrochemical energy conversion device that promises reliability and environmentally benign operating conditions.[1–3] The efficiency of fuel cells is rooted in the kinetics of the electrochemical redox reaction occurring at the membrane electrode assembly (MEA). The sluggish kinetics of oxygen reduction reaction (ORR) occurring at the cathode of the electrochemical cell necessitates the use of a catalyst for appreciable performance of fuel cells.[4–6] However, the use of platinum based metal catalysts increases the fuel cell cost and hinders its widespread commercial applications.[7,8] Among low temperature fuel cell technologies, alkaline fuel cells (AFCs) are preferred to proton exchange membrane fuel cells (PEMFCs) owing to the advantages of relatively faster ORR kinetics in alkaline medium and the less corrosive environment. AFCs thus offer higher efficiency and the possibility of employing non-noble metal catalysts.[9–11] This could in effect lead to a viable strategy of making the fuel cell cost effective by replacing the precious noble metal based catalysts with high surface area porous carbon catalysts.[12–14] However, the application of porous carbon requires further improvements in order to combat the poor conductivity and catalytic properties. It is well

accepted that, the doping of heteroatoms into porous carbon is an effective method to impart better catalytic activity by altering the spin density and charge separation of the carbon matrix.[15,16] Consequently, carbon based catalysts incorporating heteroatoms like B, N, S, and P as well as transition metals are currently being explored as ORR electrocatalysts.[17–23] Studies show that co-doping transition metals with N can boost the electrocatalytic performance of carbon owing to the better conductivity as well as high active surface area imparted by synergistic effects.[24,25] Over the past few years, nickel, being a metal occupying the same group as that of platinum, has got considerable attention due to its higher electrical conductivity, corrosion resistance properties and larger abundance, enabling it to be a promising electrocatalyst for Oxygen Reduction Reaction (ORR), Oxygen Evolution Reaction (OER) and Hydrogen Evolution Reaction (HER).[26] Nickel dispersed on the carbon matrix has been recently investigated for electrochemical applications. B. Devi et al. have made a notable contribution in this area by synthesising N doped graphitized carbon encapsulated Ni nanoparticles from a Ni(II)-dimeric complex with pyridine derivatives for trifunctional (ORR, OER, and HER) applications.[27] Tyagi et al. have reported ORR studies on atomically dispersed nickel (Ni)/nickel sulfide (Ni_xS_y) on heteroatom doped hierarchical porous carbonaceous sheets from nickel nitrate and guanidine thiocyanate.[28]

Metal Organic Frameworks (MOFs), by virtue of their high surface area and designed morphology, are widely used as precursor materials to synthesise heteroatom doped porous carbons. Moreover, the precursor chemistry could be easily tuned to incorporate the dopant elements of choice, and its direct conversion by pyrolysis could yield heteroatom doped carbons with high surface area and favourable pore characteristics.[29–31] Among MOFs, Zeolitic Imidazolate Frameworks (ZIFs) are considered as promising materials with a multitude of applications due to their exceptional chemical and temperature stability. ZIFs are basically transition metal coordinated imidazolate frameworks with 3-D sodalite topology. The structural resemblance to zeolites enables them to be good materials for adsorption and separation applications.[32–35] One of the featured applications of ZIFs is to utilise them as precursors for the synthesis of high surface area porous carbon. These materials have potential electrochemical applications as electrode materials for fuel cell systems and other energy storage devices.[36–38]

An efficient method to synthesise transition metal, N co-doped carbon with tuned morphology is by the incorporation of less volatile transition metals into the parent ZIF frameworks. The incorporated metal centres of cobalt, iron and nickel could contribute as catalytically active centres for the growth of various morphologies of carbon.[39–43] Recently, notable contributions have emerged in the development of highly graphitised porous carbon surfaces doped with nickel from bimetallic Ni/Zn ZIF-8 frameworks, prepared by chemical vapour deposition (CVD) and hydrothermal techniques[44,45] The resultant porous carbons displayed improved electrocatalytic activity for HER, OER and ORR in alkaline medium. Nevertheless, the ZIF derived carbon has limitations in its application due to the less efficient

adsorption–diffusion pathways around the microporous sites during electrocatalysis. Template assisted carbonisation was thus employed as an efficient method to modulate the pore characteristics and to improve the catalytic activity. Consequently, studies are reported with the incorporation of templates like rGO,[46,47] melamine sponge,[48] carbohydrates,[49] etc., which can effectively improve the porosity distribution and can also perform as self-sacrificing templates. Recently, Wang et al. obtained a highly efficient ORR catalyst of Co,N co-doped porous bamboo like carbon nanotubes by using $g-C_3N_4$ as the sacrificial template with bimetallic Co/Zn ZIF frameworks. $g-C_3N_4$ served as a medium for the growth of ZIF particles by attracting the metal precursors of ZIF to its electron rich sites, and the catalyst exhibited remarkable ORR activity and stability.[50]

Herein, we have made an attempt to synthesise Ni,N co-doped porous carbon with nickel carbide active centres by high temperature treatment of $g-C_3N_4$ incorporated Ni containing ZIF-8 frameworks. The added $g-C_3N_4$ aided easy decomposition of the ZIF frameworks that led to sheet like hetero-porous carbon, and compensated the severe nitrogen loss upon high temperature carbonisation. Since the self-sacrificing $g-C_3N_4$ template was finally converted to N doped porous carbon upon carbonisation, no complex etching procedure was required for the removal of the external template on the final catalyst, highlighting the advantage of $g-C_3N_4$ as the template in N doped carbon systems. As the rate of co-ordination of Ni^{2+} is slower compared to that of Zn^{2+}, attempts were made to study the effect of nickel concentration as well as carbonisation temperature on the formed frameworks. The surface area, porosity, morphological features and the electrochemical oxygen reduction activity of the resulting carbon catalysts were influenced by the Ni/Zn molar ratio of the precursor of ZIF-8 and the carbonisation temperature. The catalyst exhibited good ORR activity, stability and methanol tolerance in alkaline medium by virtue of its high surface area and nitrogen content.

2. Experimental

i. Materials and methods

Analytical grade zinc nitrate hexahydrate ($Zn(NO_3)_2 \cdot 6H_2O$, Merck, India), nickel nitrate hexahydrate ($Ni(NO_3)_2 \cdot 6H_2O$, Merck, India), 2-methylimidazole (2-MeIm, $C_4H_6N_2$, 98%, Sigma Aldrich), methanol (CH_3OH, ≥99.8%, Merck, India) and urea (NH_2CONH_2, Merck, India) were used 'as-received' without any further purification.

ii. Preparation of catalysts

Preparation of Z (ZIF-8). Preparation of ZIF-8 in methanol was analogous to a previously reported procedure.[36] In a typical synthesis, 1.466 g of $Zn(NO_3)_2 \cdot 6H_2O$ dissolved in 200 mL of methanol was added to a solution containing 3.325 g of 2-MeIm in 200 mL of methanol (the molar ratio of Zn : 2-MeIm : methanol was 1 : 8 : 700). The precursor solution was then kept under stirring for 15 h at room temperature and the white precipitate formed was collected after washing with methanol

by centrifugation. The sample was further dried overnight at 60 °C in an air oven.

Preparation of NiZ. The synthesis of NiZ was similar to the synthesis of ZIF-8 with some modifications. Initially, a mixture of $Ni(NO_3)_2 \cdot 6H_2O$ and $Zn(NO_3)_2 \cdot 6H_2O$ with a specific molar ratio of Ni^{2+}/Zn^{2+} was prepared in methanol as follows:

The desired concentration of Ni^{2+}/Zn^{2+} was prepared by adding $Ni(NO_3)_2 \cdot 6H_2O$ salt into a solution of 1.466 g of $Zn(NO_3)_2 \cdot 6H_2O$ in 200 mL of methanol. This mixture was then added to a solution containing 3.325 g of 2-MeIm in 200 mL of methanol and stirred for 15 h. The procedure was repeated by changing the concentration of $Ni(NO_3)_2 \cdot 6H_2O$ to get the molar concentration of $Ni^{2+} : Zn^{2+}$ as 1 : 2 and 1 : 1 while keeping the molar ratio of Zn : 2-MeIm : methanol constant (1 : 8 : 700). The pale blue precipitate formed was collected by centrifugation after washing with methanol and then dried at 60 °C. The obtained samples were named as NiZ(X : Y), where X and Y stand for the molar ratios of Ni and Zn, respectively.

Preparation of NiZC. $g-C_3N_4$ was prepared by heat treatment of urea at 550 °C for 4 h in a muffle furnace.[51] A dilute suspension of $g-C_3N_4$ was made by dispersing 1 g of $g-C_3N_4$ in 150 mL of methanol by ultrasonication for 1 h. Similar to the synthesis of NiZ, a mixture of $Zn(NO_3)_2 \cdot 6H_2O$ and $Ni(NO_3)_2 \cdot 6H_2O$ with a specific molar ratio of Ni^{2+}/Zn^{2+} (the molar ratio of $Ni^{2+} : Zn^{2+}$ was 1 : 2 and 1 : 1) was prepared in 50 mL of methanol. The above solution was added to the $g-C_3N_4$ dispersion and ultrasonicated for 2 h. This mixture was then added to 3.325 g of 2-MeIm in 200 mL of methanol followed by stirring for 15 h. The precipitate formed was collected by centrifugation after washing with excess methanol and dried at 60 °C. The amount of $g-C_3N_4$ added to the reaction mixture was constant for all the samples. The samples prepared with varying molar ratio of Ni^{2+}/Zn^{2+} were named as NiZC(X : Y), where the additional letter C indicates the presence of $g-C_3N_4$.

Preparation of N doped carbon from ZIF-8. The ZIF-8 powder was carbonised in the temperature range of 800–1000 °C for 2 h under a nitrogen atmosphere at a heating rate of 3 °C min^{-1} in a quartz tube, and cooled to obtain N-doped porous carbon. The resulting carbon was then acid leached by overnight soaking in 3 M H_2SO_4 at room temperature followed by washing with deionised water multiple times to remove unreactive species from the surface of porous carbon, which may otherwise decrease the activity of the catalyst by clogging the pores.[52] The samples were named as "Z T", where Z represents ZIF-8 and T denotes the temperature at which the samples were carbonised (Z 800, Z 900 and Z 1000).

Preparation of Ni,N co-doped porous carbon from NiZ and NiZC. The prepared NiZ and NiZC samples were subjected to high temperature carbonisation in the temperature range of 800–1000 °C followed by acid washing as described above. The resulting samples were denoted as NiZ(X : Y) T and NiZC(X : Y) T, where X : Y represents the $Ni^{2+} : Zn^{2+}$ ratio of the precursor and T the carbonisation temperature.

iii. Characterisation

The phase purity and crystalline phase of the samples were analysed by powder X-ray diffraction (PXRD) analysis

(PW1710 Philips, The Netherlands) using Cu Kα radiation. The infrared spectrum of the samples was analysed using Fourier Transform-Infrared spectroscopy (PerkinElmer, FT-IR, Spectrum Two). The morphological features of the samples were observed using a Scanning Electron Microscope (JEOL, JSM-35) operating at 15 kV and a High Resolution Transmission Electron Microscope (HRTEM, TecnaiG2, FEI, The Netherlands) operating at 300 kV. The elemental mapping and quantification of the samples were carried out by Energy Dispersive Spectroscopy (EDS). Raman spectra were recorded utilizing an alpha 300 R confocal Raman microscope (WI Tec, Germany) using a laser beam of excitation wavelength 633 nm. The surface chemistry and elemental composition of the samples were analysed using an X-ray Photoelectron Spectrometer (ULVAC-PHI Inc., USA) equipped with a monochromatic Al-Kα X-ray source ($h\nu$ = 1486.6 eV) having a micro focused beam (200 μm, 15 kV). Survey scans were recorded using an X-ray source power of 50 W and a pass energy of 187.85 eV. A pass energy of 46.95 eV was used to record high-resolution spectra of the elements. The surface area and porous characteristics of the samples were analysed using the N_2 adsorption–desorption measurement technique (Tristar II, Micrometrics, USA). The total pore volume and micropore volume were calculated from the isotherm at a P/P_0 value of 0.990 and 0.035 respectively for easier comparison of the values and the porous structures, although micropore volume values may have been influenced by monolayer adsorption in some cases. Thermogravimetric Analysis (TGA) was conducted (PerkinElmer STA6000 TGA) at a heating rate of 3 °C min^{-1} in a N_2 atmosphere.

All the electrochemical measurements were performed in a Bio-Logic electrochemical work station. A three-electrode rotating disk setup was used to analyse the activity of the catalyst for electrochemical oxygen reduction reaction in which Hg/HgO was used as the reference electrode and a graphitic rod was used as the counter electrode. The working electrode was prepared according to the following procedure: the catalyst slurry was prepared by adding a mixture of 1 mL of isopropyl alcohol–water (1 : 3) and 40 μL of Nafion solution into 5 mg of catalyst followed by sonication for 1 h. The electrode was prepared by coating 10 μL of the prepared catalyst slurry on a glassy carbon electrode (surface area 0.196 cm^2) followed by drying at room temperature. All the ORR measurements were conducted in 0.1 M KOH solution and the analysis was carried out by saturating with N_2 and O_2 gases. For comparison of the electrocatalytic activity of the samples, the state-of-the-art electrocatalyst with 40 wt% Pt/C (Johnson Matthey) was used following the same procedure. The rotating ring disk electrode (RRDE) experiments were performed under the same conditions with the catalyst coated on a glassy carbon (surface area 0.2826 cm^2) electrode having a platinum ring around the surface as the working electrode. The stability of the catalyst was analysed by the accelerated durability test (ADT) and by performing linear sweep voltammetry (LSV) before and after 5000 cycles of CV performed in the potential range of 0.57 V to 0.97 V at a scan rate of 100 mV s^{-1} in 0.1 M KOH.

3. Results and discussion

Fig. 1 depicts the schematic diagram of the synthesis of ZIF-8, NiZ as well as NiZC samples in methanol medium by a chemical precipitation method at room temperature. ZIF-8 was synthesised according to the reported procedure in methanol medium and the high temperature carbonisation resulted in N doped carbon (Scheme 1). In the second stage, ZIF-8 was modified by incorporating Ni in the matrix with varying Ni^{2+}/Zn^{2+} in the precursor medium (Scheme 2). As a next stage, the influence of the supporting template on the formation of porous carbon was studied by preparing Ni incorporated ZIF-8 (NiZ) samples on the surfaces of g-C_3N_4 sheets by introducing a dispersion of g-C_3N_4 in methanol in the reaction medium containing Zn^{2+}, Ni^{2+} and 2-MeIm (Scheme 3). The carbonisation of NiZ($X:Y$) and NiZC($X:Y$) samples in a N_2 atmosphere in the temperature range of 800–1000 °C resulted in Ni,N co-doped porous carbon matrices.

The powder X-ray diffraction (PXRD) patterns recorded for all the samples indicated the formation of pure ZIF-8 (JCPDS 00-062-1030) (Fig. 2a),[53] with sodalite topology. The XRD pattern of the NiZ sample confirmed the absence of any other phase than ZIF-8. The XRD patterns of the reaction product obtained after the reaction of Ni salt (with no Zn addition) with 2-MeIm were also recorded and the results indicated the absence of any zeolitic imidazolate type of framework (Fig. S1, ESI†). The XRD peaks of the reaction product between Ni and 2-MeIm could be attributed to the square planar or distorted octahedral Ni complexes with imidazolate in the reaction medium which is the preferred geometry of Ni complexes or Ni MOFs.[54] It is clear that, Ni imidazolate frameworks, analogous to ZIF-8, were not formed in the absence of Zn^{2+} in the medium. It can be thus inferred that while employing the Ni/Zn mixture, some of the Ni^{2+} ions present in the
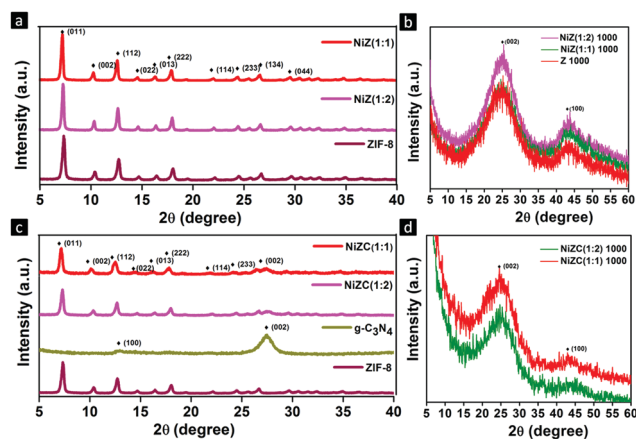

Fig. 2 PXRD patterns of (a) ZIF-8 and NiZ samples, (b) carbon samples obtained by carbonisation of ZIF-8 and NiZ samples at 1000 °C, (c) NiZC composites and (d) carbon samples obtained after carbonisation of NiZC samples at 1000 °C.

medium are presumably incorporated into the 3D ZIF framework mimicking the tetrahedral geometrical alignment of Zn^{2+} with imidazolate ions. The XRD pattern of g-C_3N_4 contained the characteristic peaks at around 13.1° of the (100) plane and 27.4° of the (002) plane (JCPDS 87-1526) corresponding to the packing of the in-plane structural motif of the graphite like structure and hexagonal tri-s-triazine units of graphitic carbon nitride respectively.[55]

The XRD patterns of composites exhibited all the peaks of ZIF-8 as well as g-C_3N_4 indicating the growth of the ZIF-8 phase on g-C_3N_4 matrices. The peaks corresponding to nickel phases were not observed, probably due to the very small amount incorporated. However, a modification in the (011) plane of the ZIF phase was observed in the nickel incorporated samples as evidenced by the shift of the 2θ value from 7.3° to 7.2° in
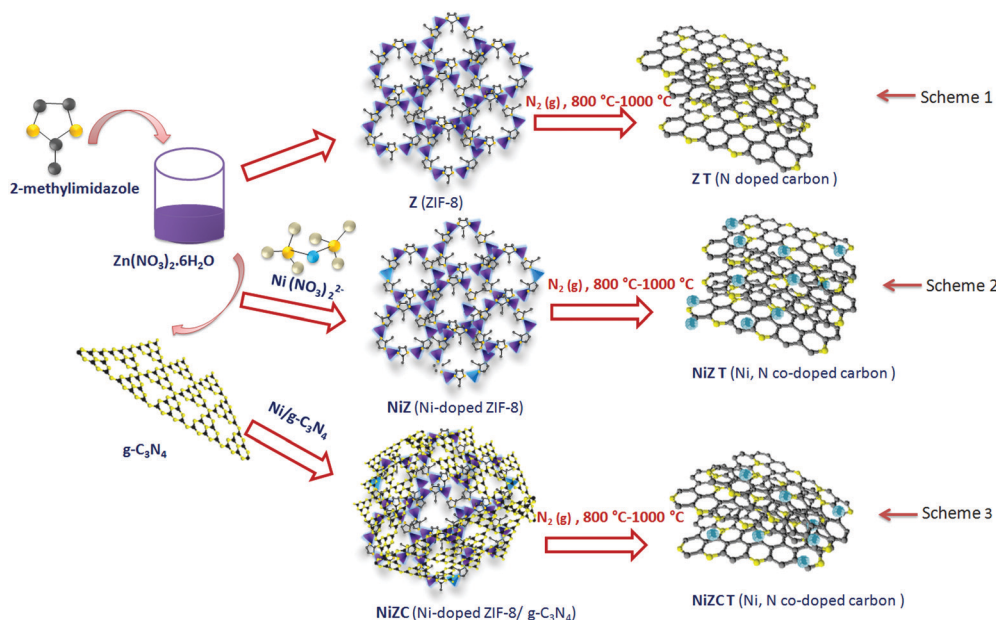

Fig. 1 Scheme showing the formation of N-doped carbon and Ni,N co-doped carbon.

NiZ(1 : 2) and NiZC(1 : 2) samples and 7.1° in NiZ(1 : 1) and NiZC(1 : 1) samples (Fig. 2a and c). The shift was more visible with increasing nickel content, and could be an indication of nickel species present in the frameworks. In the high temperature carbonisation process, the Zn ion in the coordination sphere volatilised, due to which the network structure collapsed around the metal atom, leading to the formation of N-doped porous carbon matrices. The peaks at 2θ values of 26° and 44°, corresponding respectively to the (002) plane and (100) plane, were due to the diffraction from the polyarene planes and confirmed the formation of graphitised N-doped carbon (Fig. 2b and d).[56]

The FT-IR analysis clearly evidenced C–N, C=C and metal–C bonds in "as-synthesised" metal organic frameworks as well as in the carbonised samples (Fig. S2a and b, ESI†). The IR pattern of the NiZ sample was similar to that of ZIF-8 confirming the similarity in the bonding type of NiZ with ZIF-8 and its variation from Ni–MOF. For carbonised samples, the IR pattern showed characteristic peaks of unsaturated heteroatomic bonding of the C–N bonded carbon as well as the M–C functional group, indicating the creation of heteroatomic bonding in the carbon matrix. Compared to Z 1000, the NiZ 1000 and NiZC 1000 samples exhibited a shift in the transmittance peak of C–N stretching frequency to a lower wave number. This could probably be attributed to the weakening of C–N bond strength upon electron donation by the incorporated nickel atom.[36]

In order to elucidate the carbonisation pathways of the samples, thermogravimetric analysis (TGA) of the composite sample was performed in a flowing N_2 atmosphere. As can be interpreted from the TG curves (Fig. S3, ESI†), the presence of less volatile nickel reduced the weight loss in the ZIF-8 framework during carbonisation. While Zn^{2+} ions easily volatilised during the high temperature carbonisation, nickel persisted in the matrix due to its high boiling temperature of $\sim$2732 °C. In addition, the g-C_3N_4 containing NiZC(1 : 2) sample exhibited higher weight loss compared to pure ZIF-8. The decomposition profiles of the composites were shifted to lower temperature because of the presence of the easily decomposing g-C_3N_4 template.[57]

The specific surface area and pore characteristics of the samples were evaluated using N_2 adsorption–desorption analysis (Fig. 3). The ZIF-8 and NiZ samples showed a Type I adsorption isotherm, indicative of the microporous nature of the framework material (Fig. 3a). At the same time, the rise in adsorption at large P/P_0 values > 0.9 indicated condensation of adsorbates in the interparticle void of the samples constituted by secondary pores from the aggregation of the particles.[58,59] The surface area values were 1246, 1260 and 1275 $m^2\ g^{-1}$ for ZIF-8, NiZ(1 : 2) and NiZ(1 : 1) respectively. The g-C_3N_4 supported NiZC samples exhibited a predominantly microporous nature though some larger pores were also observed, presumably originating from folded g-C_3N_4 sheets (Fig. 3b). The surface area values of the g-C_3N_4 supported samples were 663 and 692 $m^2\ g^{-1}$ for NiZC(1 : 2) and NiZC(1 : 1) respectively, much lower compared to that of pure ZIF-8 (Table 1); g-C_3N_4 has a relatively less surface area (108 $m^2\ g^{-1}$) and its
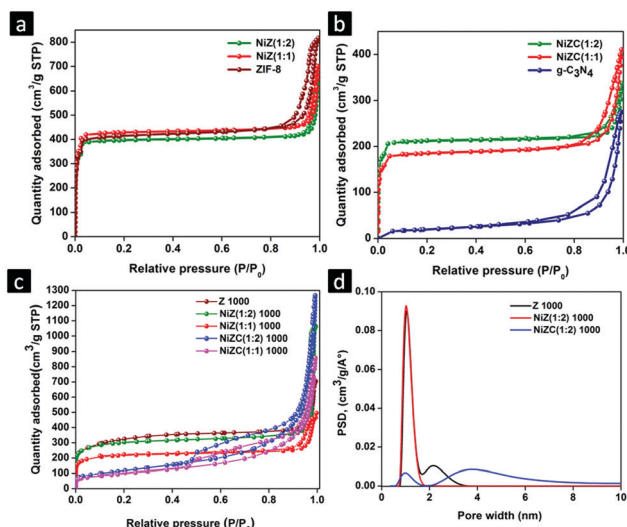

Fig. 3 N_2 adsorption–desorption isotherms of (a) ZIF-8 and NiZ samples, (b) g-C_3N_4 and NiZC samples, (c) ZIF-8, NiZ and NiZC samples carbonised at 1000 °C and (d) NLDFT pore size distribution curves of the samples carbonised at 1000 °C.

Table 1 Pore volumes and surface areas of the samples before and after carbonisation at 1000 °C

Sample	Before carbonisation			After carbonisation at 1000 °C		
	S_{BET} ($m^2\ g^{-1}$)	V_{total} ($cm^3\ g^{-1}$)	V_{micro} ($cm^3\ g^{-1}$)	S_{BET} ($m^2\ g^{-1}$)	V_{total} ($cm^3\ g^{-1}$)	V_{micro} ($cm^3\ g^{-1}$)
g-C_3N_4	108	0.42	0.01	—	—	—
Z (ZIF-8)	1246	1.26	0.61	1050	1.08	0.39
NiZ(1 : 2)	1260	0.98	0.59	933	1.63	0.39
NiZ(1 : 1)	1275	1.09	0.63	672	0.73	0.28
NiZC(1 : 2)	663	0.51	0.30	426	1.93	0.13
NiZC(1 : 1)	692	0.63	0.26	349	1.31	0.10

incorporation inherently reduced the surface area of the composite samples. The high temperature carbonisation resulted in porous carbon with surface area values in the range of 349–1050 $m^2\ g^{-1}$ (Table 1). The formation of a porous structure was also aided by the vaporisation of the Zn metal from the co-ordination spheres. The decomposition of framework structures upon high temperature carbonisation led to a decrease in surface area. After carbonisation, the ZIF-8 and NiZ derived carbons retained their Type I adsorption behaviour, but the surface area varied with varying Ni/Zn ratio and the carbonisation temperature. The surface area of the carbon derived from ZIF-8 was found to increase with increasing temperature above 800 °C and the sample after carbonisation at 1000 °C exhibited the highest surface area of 1050 $m^2\ g^{-1}$, owing to the formation of fully extended porous textures upon evaporation of zinc. ZIF and NiZ samples showed a decrease in micro-porosity and surface area on heat treatment at 800 °C obviously owing to incomplete carbonisation at this temperature. NiZ(1 : 2) and ZIF-8 samples showed a systematic increase in micro-porosity and surface area on heat treatment from 800 to 1000 °C, although the evolution of micro-porosity was slightly delayed in the NiZ(1 : 2) sample (lower micro-porosity at 800 °C but

similar at 900 and 1000 °C). This delay should be due to the increased thermal stability of the materials owing to the presence of Ni along with Zn. The lower volatility of Ni should be the reason; the more Ni containing sample NiZ(1 : 1) in fact has shown an even further delay in the evolution of microporous carbon structure (very low micro-porosity at 800 and 900 °C but high micro-porosity at 1000 °C). Hence, the metal content seems to have a great influence on pore structure formation (Fig. S4 and Table S1, ESI†).

In the case of NiZC samples, an increase in heat treatment temperature from 800 °C to 1000 °C only slightly increased their surface area and the micro-porosity remained more or less the same. It could be expected that carbonisation was more or less complete by 800 °C in these samples due to the easier decomposition of g-C$_3$N$_4$ present. While the porous carbon derived from ZIF frameworks retained its microporous structure, the template assisted synthesis of porous carbon using g-C$_3$N$_4$ facilitated the formation of hetero-porous architecture of the derived carbon, as clearly indicated by Type II isotherms with H3 hysteresis (Fig. 3c). At higher temperatures, the pore volume of NiZC(X : Y) T samples was found to be higher, aided by the hybrid structure formed by the micro–meso porous architecture of NiZ–C$_3$N$_4$ combination. This extended micro–meso porosity of the catalysts, upon using g-C$_3$N$_4$ as the supporting matrix, might be beneficial for the easier diffusion of the O$_2$ molecules towards the catalytic sites. All the samples had macro porosity, due to the presence of secondary aggregates. The NLDFT curves were drawn for the carbons derived from ZIF-8, NiZ(1 : 2) and NiZC(1 : 2) samples at 1000 °C for a better understanding of the pore sizes (Fig. 3d). It is clear that the cavity created by the tetrahedral coordination of Zn^{2+} ions to 2-MeIm led to 3-D frameworks with many channels and open pores in the microporous size range of <2 nm. As can be seen from the NLDFT curves, the NiZ derived carbon at 1000 °C exhibited the same amount of microporosity as the ZIF-8 derived ones. However, the carbon derived from NiZC samples exhibited a well-defined micro–mesoporous architecture evidencing the ability of g-C$_3$N$_4$ in tuning the pore characteristics of the matrix. Thus, the templating strategy with g-C$_3$N$_4$ resulted in a hetero-porous architecture for the carbonised

catalyst, which can facilitate better transport of O$_2$ molecules across the porous channels in the catalytically active surface thus enhancing ORR efficiency.

Electrochemical analysis

The electrocatalytic ORR activity of the samples was investigated by analysing the cathodic cyclic voltammetry (CV) profiles obtained in N$_2$/O$_2$ saturated 0.1 M KOH solution. The CV profiles were initially analysed in N$_2$ saturated solution followed by O$_2$ saturated solution. The CV curves showed a characteristic shift in current at a potential of around 0.80 V compared to that in N$_2$ saturated solution indicating the reductive nature of the catalysts in the presence of O$_2$ (Fig. 4a).

The ORR activity of the carbon samples was further confirmed by evaluating the linear sweep voltammetry (LSV) curves in 0.1 M KOH solution saturated with O$_2$ gas, at 1600 rpm. In order to study the influence of the carbonisation temperature on the electrocatalytic activity, a comparison of the LSV curves was done for the ZIF-8 derived Z 800, Z 900 and Z 1000 samples. The activity was found to increase from 800 to 1000 °C, and the carbon derived at 1000 °C exhibited the maximum catalytic activity (Fig. S5a, ESI†). The activity was then evaluated further on all the samples prepared at the optimised temperature of 1000 °C, and a variation in the order ZT < NiZ(X : Y) T < NiZC(X : Y) T was observed (Fig. S5b, ESI†). The sample NiZC(1 : 2) 1000 exhibited maximum ORR activity, with a limiting current density of 5.2 mA cm^{-2} and a half-wave potential of ~0.76 V vs RHE (Fig. 4b). The current density exceeded over 40% of that of Pt/C and is also higher compared to that of other reported nickel containing carbon materials in the literature (Table S5, ESI†).[7,28,71–74] The activity was found to be better for NiZC(1 : 2) 1000 compared to NiZC(1 : 1) 1000. The high metal content in NiZC(1 : 1) 1000 may have created the aggregation of particles on the surface, leading to the reduction in the surface area and thereby active catalytic surface, as evident from Fig. 3. This subsequently led to reduction in the electrocatalytic ORR activity.

Structure and morphological analysis

In order to get further insights into the correlation between the electrocatalytic activity of the samples and their microstructural
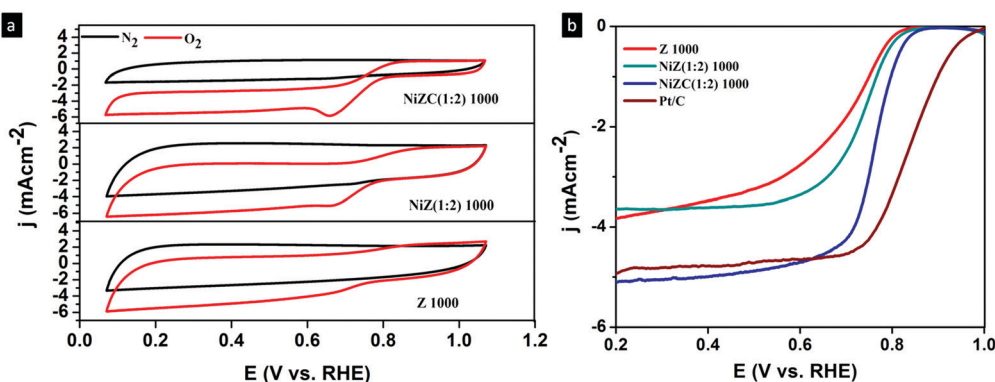

Fig. 4 (a) Cyclic voltammograms recorded in N$_2$ and O$_2$ saturated 0.1 M KOH solution of Z 1000, NiZ(1 : 2) 1000, and NiZC(1 : 2) 1000 and (b) comparison of the LSV curves of Z 1000, NiZ(1 : 2) 1000, NiZC(1 : 2) 1000 and commercial 40% Pt/C in O$_2$ saturated 0.1 M KOH solution recorded at 1600 rpm.
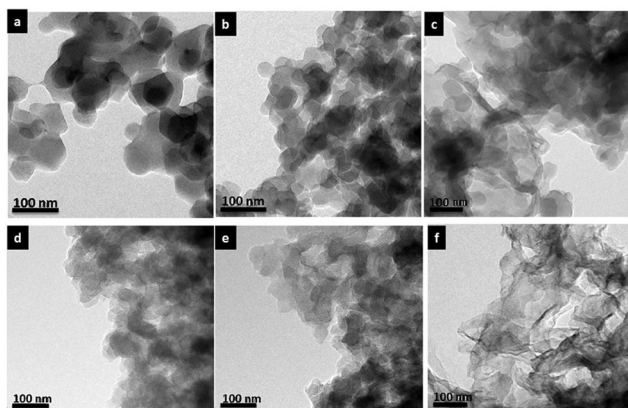
Fig. 5 TEM images of (a) ZIF-8, (b) NiZ(1 : 2), and (c) NiZC(1 : 2) and (d–f) the corresponding carbon samples obtained after carbonisation at 1000 °C.

features, the morphological analysis of the samples was carried out. The microstructure evaluations of the ZIF-8, NiZ(1 : 2) and NiZC(1 : 2) samples were carried out by TEM analysis. Fig. 5a shows ZIF-8 as dodecahedral particles with an average diameter of around 80 nm. Fig. 5b shows the NiZ(1 : 2) particles with a similar morphology to that of ZIF-8. Even though the addition of Ni has no influence on the particle shape, the size of the particles was found to be reduced ($\approx$50 nm) compared to pure ZIF-8 particles. This may be primarily due to the presence of a higher number of cationic sites due to the presence of extra Ni^{2+} ions together with the Zn^{2+} ions in the synthesis medium. After the addition of g-C_3N_4, the composites appeared with mixed morphology as shown in Fig. 5c, where the dodecahedral particles of Ni incorporated ZIF-8 of 50 nm size were found to be grown on the sheet like structures of g-C_3N_4. Upon high temperature treatment, the 3-D frameworks composed of C–N, C–C as well as Zn–N linkages were ruptured leading to the

formation of Ni,N co-doped porous carbon. The microporosity mainly arose from the volatilization of Zn from the framework as discussed previously. As can be interpreted from the TEM pictures, the substitution of nickel in the Zn-imidazolate frameworks and the presence of g-C_3N_4 helped in tuning the morphology of the resulting carbon. Distorted hexagonal structures, tubes and sheets were formed, influenced by the carbonisation temperature, the supporting template and the molar ratio of nickel ions (Fig. S7, ESI†). The samples Z 1000 and NiZ(1 : 2) 1000 exhibited distorted hexagonal morphology of parent ZIF structures. The decomposition aided by g-C_3N_4 helped in the formation of sheet like morphology in NiZC(1 : 2) 1000 as shown in Fig. 5(d–f).

The incorporation of nickel helped in catalysing the growth of tube like morphology while g-C_3N_4 as a template influenced the formation of sheet like structures in the derived carbon. The SEM image of the NiZC(1 : 2) composite confirmed the growth of spherical NiZ particles on the sheet like g-C_3N_4 template (Fig. 6a and b). The SEM-EDS analysis of the sample detected the presence of C, N and Ni elements. The distribution ratio of the various elements is summarised in Table S2 (ESI†). The presence of nickel, identified in trace amounts (0.01–0.3 at%), indicated that the incorporation of nickel was only minimal. It is to be noted that, the competing effect of Ni^{2+} to form a zeolitic type framework during the room temperature synthesis condition is very limited as Ni^{2+} favours yellowish brown square planar complexes (Fig. S12, ESI†). Since the rate of reaction of Zn^{2+} ions with the imidazolate ligand is higher, the ZIF-8 structure is formed having only a few of the metal centres occupied by Ni^{2+} ions. The remaining unreacted Ni^{2+} ions along with Zn get leached away during the washing of the precipitate with excess methanol and water. The surface atomic percentage of nitrogen content was identified as 32.85% for the NiZ(1 : 2) and 58.11% for the NiZC(1 : 2) composites. The excess nitrogen is contributed by g-C_3N_4 in the composite. g-C_3N_4 is a polymer
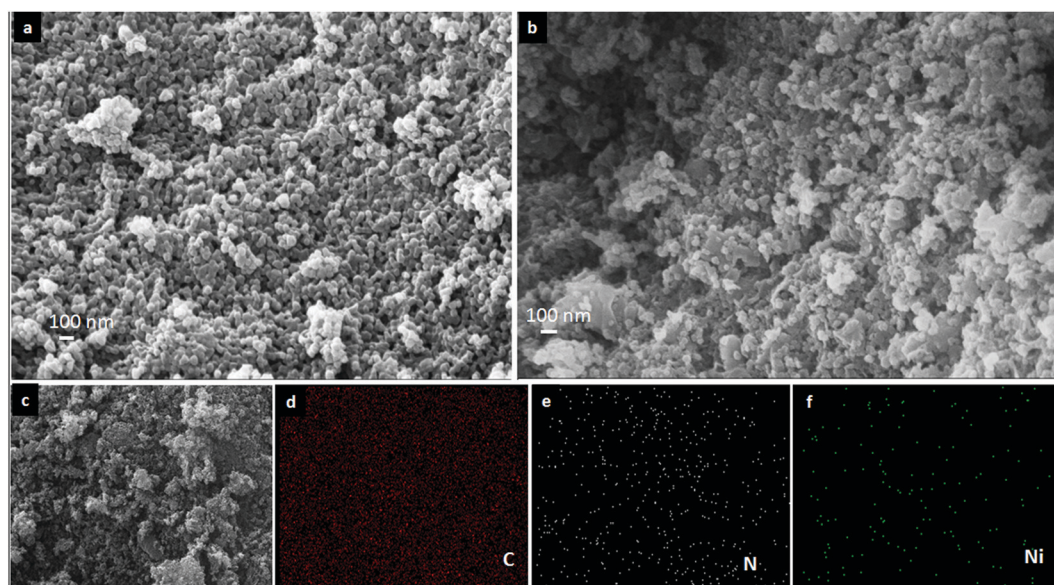

Fig. 6 (a and b) SEM images of NiZ(1 : 2) and NiZC(1 : 2) and (c–f) SEM images of NiZC(1 : 2) 1000 and the corresponding map of elemental distribution.
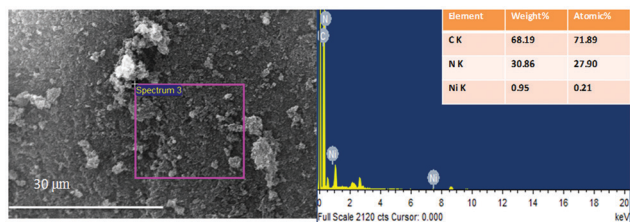
Fig. 7 SEM-EDS analysis of NiZC(1:2) 1000 along with elemental composition.

Fig. 8 (a) Survey spectra of the samples and (b–d) XPS deconvoluted spectra of (b) Ni2p, (c) C1s, and (d) N1s of the NiZC(1:2) 1000 sample.

formed by tri-*s*-triazine units of carbon and nitrogen, and contains a remarkably higher amount of nitrogen. As a result, the composite of ZIF frameworks with g-C$_3$N$_4$ improved the total nitrogen content because of the contribution from both ZIF and g-C$_3$N$_4$ components. The atomic percentage of nitrogen reduced from 20.26% to 19.71% for the Z 1000 and NiZ(1:2) 1000 samples. The loss of nitrogen was more evident for NiZ samples, probably due to distortion in the size and topology of ZIF-8 upon incorporation of Ni atoms. The existence of double metallic centres with different atomic radii and the associated electronic characteristics might have caused some distortion in the ZIF frameworks, facilitating easy volatilisation of the nitrogen atoms at high temperatures. The atomic percentage of nitrogen was found to be increased to 27.9% due to the presence of g-C$_3$N$_4$ (Fig. 7). As we increased the carbonisation temperature from 800 to 1000 °C, the presence of nitrogen was reduced from 48.24% to 27.9% (Table S3, ESI†), indicating severe loss of nitrogen at higher temperatures as volatile N$_2$ gas. The elemental mapping of the sample NiZC(1:2) 1000 further revealed the distribution pattern of C, N and Ni elements on the porous carbon surfaces. The well dispersed dopants might create active regions for O$_2$ adsorption and the subsequent reduction reaction.

The presence of elements in the carbonised samples was further confirmed and quantified by XPS analysis. The XPS survey spectrum showed the presence of carbon, nitrogen, and oxygen in Z 1000, NiZ(1:2) 1000 and NiZC(1:2) 1000 samples (Fig. 8a). The binding energy peaks corresponding to the nickel species were absent in the survey spectrum due to the insignificant quantity in the carbon matrix. The atomic percentages of C, N, O and Ni in samples Z 1000, NiZ(1:2) 1000, and NiZC(1:2) 1000 are presented in Table 2. The amount of nitrogen content in ZIF-8 derived carbon (Z 1000) was 8 at% and upon Ni incorporation, the atomic percentage of nitrogen was decreased to 5.9% in the NiZ(1:2) 1000 sample. This nitrogen loss was primarily due to the decomposition of the frameworks induced by defect formation upon nickel incorporation in the ZIF-8 frameworks.[60] The template mediated synthesis of porous carbon with g-C$_3$N$_4$ medium resulted in an overall increase of total N content (9.2 at%) highlighting the contribution of g-C$_3$N$_4$ in the composites. At high temperatures, g-C$_3$N$_4$ transformed completely into N-doped carbon along with the ZIF-8 frameworks and compensated for the N loss by providing its own N atoms to the carbon matrix.[61]

The high resolution spectrum of N1s detected the presence of pyridinic (398.7 eV), pyrrolic (399.9 eV), graphitic (401.2 eV)
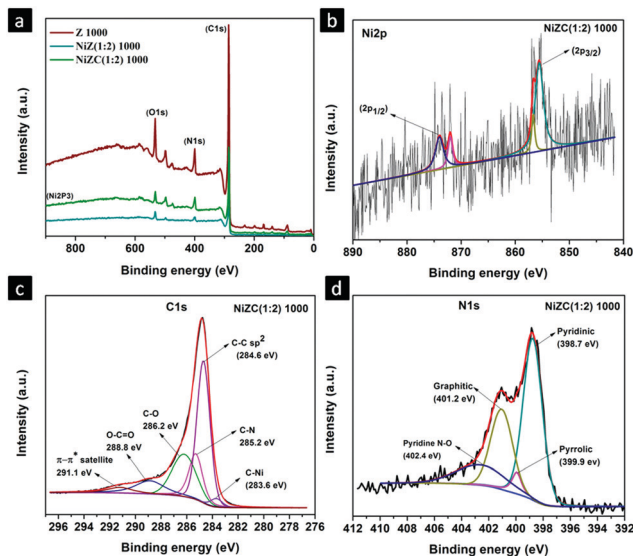
and surface pyridinic N–O species (402.4 eV) in NiZC(1:2) 1000 (Fig. 8d). The presence of pyridinic and graphitic nitrogen can generate an accumulated polarity on the carbon surface, and can easily attract other electronegative elements like oxygen contributing towards a better catalytic effect during oxygen reduction reaction. The atomic percentage of the different types of N present in the samples is compared (Fig. 9 and Table S4, ESI†). The atomic percentages of pyridinic N and pyridinic N–O were 4.74% and 1.45% respectively for NiZC(1:2) 1000 sample.

Table 2 Distribution of various elements on the carbon samples in atomic% obtained from XPS

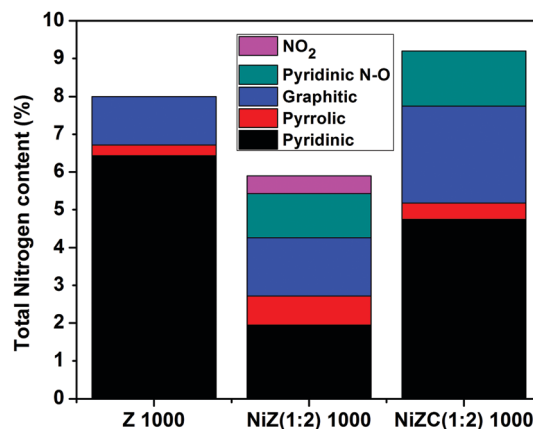| Sample name	Elemental distribution (atomic%)			
	C	N	O	Ni
Z 1000	85	8	7	—
NiZ(1:2) 1000	87.3	5.9	6.1	0.7
NiZC(1:2) 1000	85.8	9.2	4.7	0.3

Fig. 9 Distribution of various types of nitrogen in the Z 1000, NiZ(1:2) 1000 and NiZC(1:2) 1000 samples.

The presence of these pyridinic active sites presumably offers a better ORR kinetic pathway during electrocatalysis.[62]

The deconvoluted C1s spectrum was particularly resolved into five types of carbon binding and included a high intense sp^2 graphitic C–C bond of carbon (284.6 eV), C–N (285.2 eV), C–O ($\approx$286.0 eV) and O–C$=$O (288 eV) bonds. A satellite peak corresponding to π–π^* transition in the aromatic carbon rings contributed by the graphitic type of carbon (291.0 eV) indicated the conducting nature of carbon surfaces. In addition to this, the resolved spectra of NiZ(1:2) 1000 and NiZC(1:2) 1000 contained an additional peak at around 283.6 eV arising from the C–Ni bonding and confirmed the incorporation of nickel as nickel carbide in the carbon matrix[63–66] (Fig. 8c and Fig. S8, S9, ESI†). The modification of density of states (DOS) of the valence band of the parent nickel atom, caused by the electronic interaction between the nickel and the carbon atom in the nickel carbide,[67] can provide suitable binding energy for the O_2 molecule in the medium. Moreover, the higher synergistic effect contributed by transition metal carbide along with the sufficient amount of nitrogen distributed in the porous carbon surface could have led to higher affinity for oxygen adsorption, conduction and reduction in alkaline solution.

The resolved Ni2p spectra of NiZC(1:2) 1000 could be mainly divided into two regions (Fig. 8b). The peaks in the low binding energy region (852–860 eV) indicated the $2p_{3/2}$ states of Ni^{2+} and the region corresponding to high binding energy (860–875 eV) indicated the $2p_{1/2}$ states of Ni^{2+}[68] confirming the Ni–C binding states. Even though the XPS analysis detected the Ni–C bonded phase in the carbonised materials, the corresponding XRD peaks were absent for the carbonised samples. This is possibly due to the overlapping of the high intense (113) peak of Ni_3C which is present in a low amount with the broad (100) plane of graphitic carbon.

Raman spectroscopy was performed to analyse the extent of graphitisation as well as the defect formation on the carbonised samples. The two distinct peaks observed around 1350 cm^{-1} and 1580 cm^{-1} corresponded to the defective or diamond like band (D band) and graphitic band (G band) respectively (Fig. 10). The D band was generated from the sp^3 bonded states on the graphitic carbon lattice caused by imperfections or defects. The G band in the higher frequency region was due to the
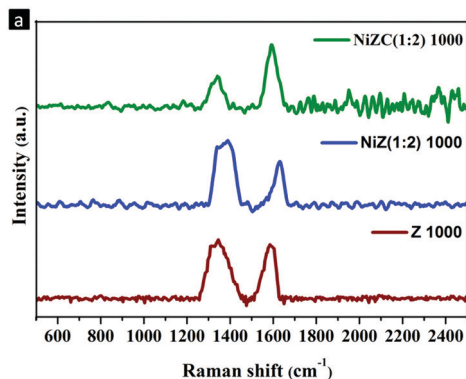
vibrations of the sp^2 bonded states of the perfect graphitic plane.[69,70] The calculated I_D/I_G ratios were 1.08, 1.43 and 0.51 for the samples Z 1000, NiZ(1:2) 1000 and NiZC(1:2) 1000 respectively. It is inferred that the carbonisation of Ni incorporated ZIF-8 presumably created more defects due to the presence of nickel atoms along with nitrogen in the matrix leading to imperfect bonding or aggregation even after the treatment at 1000 °C. On the other hand, in the case of NiZC(1:2) 1000, the extent of graphitisation was increased along with the concurrent defective nature of the heteroatom doped surfaces. The extra carbon and nitrogen atoms contributed by g-C_3N_4 sheets might have helped in the formation of the hybridised surface of the graphitic structure with a certain amount of defects. While the defects created adsorption sites for O_2, the graphitic structure helped to create an efficient conductive pathway for the electrons during electrochemical oxygen reduction reaction.

In order to further look into the electron transfer mechanism during ORR, RRDE experiments at different rotation rates were conducted (Fig. 11a and Fig. S10, ESI†). As evident from the figures, with the increase in the rotation rate, the number of electrons transferred also increased which contributed to the increase in high current density. The kinetic parameters were investigated by calculations according to the Koutecky–Levich plot (K–L plot) equation:

$$\frac{1}{J} = \frac{1}{J_K} + \frac{1}{B\omega^{0.5}}$$

where J is the obtained current density, J_K is the kinetic current density and ω is the angular rotation rate. The constant B can be calculated from the equation

$$B = 0.62nF\left(D_{O_2}\right)^{\frac{2}{3}}\nu^{-\frac{1}{6}}C_{O_2}$$

where n is the number of electrons transferred during oxygen reduction reaction, F is Faraday's constant indicating the

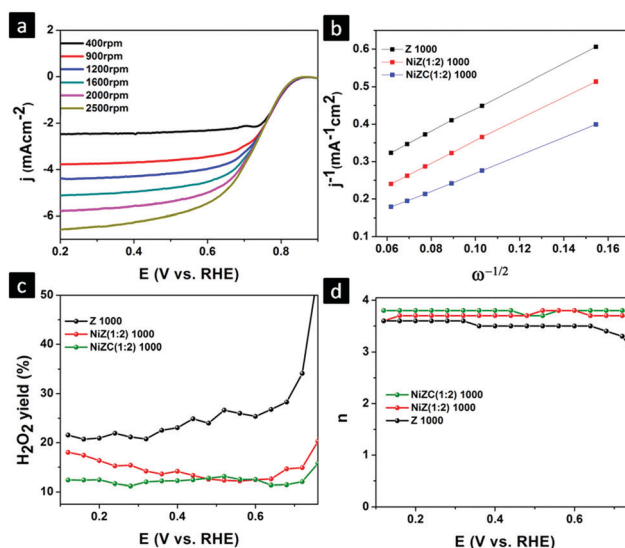Fig. 10 Raman spectra of the samples carbonised at 1000 °C.

Fig. 11 (a) LSV curves of NiZC(1:2) 1000, (b) K–L plots of samples at 0.6 V, (c) % H_2O_2 yield and (d) number of f electrons transferred measured by RRDE of Z 1000, NiZ(1:2) and NiZC(1:2) 1000.

charge associated with the electron transfer, D_{O_2} is the diffusion coefficient of O_2 gas molecules in 0.1 M KOH solution $(1.9 \times 10^{-5} \text{ cm}^2 \text{ s}^{-1})$, ν is the kinematic viscosity of the electrolyte used $(0.01 \text{ cm}^2 \text{ s}^{-1})$ and C_{O_2} is the concentration of O_2 $(1.2 \times 10^{-3} \text{ mol L}^{-1})$.

The K–L plots obtained by plotting $1/J$ against $\omega^{-1/2}$ drawn for Z 1000, NiZ(1:2) 1000 and NiZC(1:2) 1000 at 0.6 V (Fig. 11b) showed an increase in the number of electron transferred in the order NiZC(1:2) 1000 > NiZ(1:2) 1000 > Z 1000. The RRDE experiments were conducted to find out the intermediate product H_2O_2 produced due to the partial $2e^-$ mechanism. The average amount of H_2O_2 produced during the electrochemical oxygen reduction was around 26%, 16% and 13% for the Z 1000, NiZ(1:2) 1000 and NiZC(1:2) 1000 samples respectively. The corresponding number of electrons transferred was found to be around 3.5–3.6 for Z 1000, 3.6–3.7 for NiZ(1:2) 1000 and increased to 3.8 for NiZC(1:2) 1000, which confirmed that the incorporation of nickel ions as well as g-C_3N_4 into the supporting matrix has favourably contributed to the easy transport of the O_2 molecule as well as the electron transport mechanism on the porous carbons derived at high temperature, thereby increasing the overall ORR activity (Fig. 11c and d).

In addition to the high ORR activity, the stability and methanol tolerance of the catalysts are also important parameters that decide the applicability of the catalysts. In order to understand the sensitivity of the electrocatalyst in the presence of methanol, the chronoamperometry test was carried out for the best performing electrocatalyst and was compared with the commercial Pt/C catalyst. The chronoamperometry test was carried out in O_2 saturated 0.1 M KOH solution under a rotation rate of 1600 rpm for 1800 s under an applied potential of 0.60 V. 3 M MeOH solution was added into the above O_2 saturated KOH solution at the time period of 300 s and the variation in current was measured. As can be seen from Fig. S11 (ESI†), the NiZC(1:2) 1000 sample was almost insensitive to the addition of methanol. On the other hand, the current density of Pt/C showed a sharp decline as a response to methanol addition revealing its sensitivity to methanol. This ensures better methanol tolerance of the prepared catalyst material in alkaline medium.

The stability of the best catalyst was investigated further by the accelerated durability test (ADT) in 0.1 M KOH electrolyte solution by performing CV at a scan rate of 100 mV s^{-1}. The measurement was done under a rotation rate of 1600 rpm and the recorded LSV was compared before and after 5000 cycles of the ADT test. After 5000 cycles, the catalyst exhibited 96% retention in limiting current. The half-wave potential of the NiZC(1:2) 1000 samples underwent a negative shift of 14 mV while the Pt/C catalyst showed negative shift of 30 mV, further confirming the better stability of the prepared catalyst materials relative to that of Pt/C (Fig. 12a and b).

Thus, it has been observed that, the template assisted synthesis of heteroatom doped porous carbon from Ni incorporated ZIF-8 frameworks has resulted in Ni,N co-doped hetero-porous carbon with Ni–C active centres with appreciable ORR
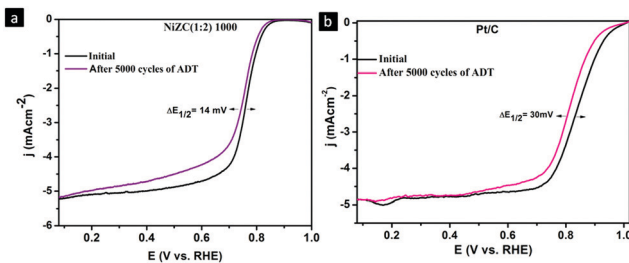

Fig. 12 Durability curves of (a) NiZC(1:2) and (b) commercial Pt/C.

performance in alkaline medium. The defective sites created by the incorporated heteroatoms were found to be beneficial for creating adsorption sites for the O_2 molecule, thus initiating the ORR mechanism. The modulation in the surface electronic properties facilitated by the combined synergistic effect of Ni–C along with N atoms on the porous carbon surface could have contributed to the high ORR activity. The catalysts exhibited maximum ORR at the optimum nickel concentration of the sample NiZC(1:2) and at the higher carbonisation temperature of 1000 °C. Furthermore, the template aided synthetic strategy using g-C_3N_4 aided in the decomposition of the ZIF-8 framework and the formation of a hetero-porous sheet like architecture with well dispersed nitrogen content. The fugitive template also helped in compensating the severe nitrogen loss upon high temperature carbonisation of ZIF-8, by completely transforming into N doped carbon together with the parent ZIF framework. The chemical, morphological and structural changes induced in the newly designed catalyst derived at 1000 °C enabled easier diffusion and conduction of O_2 molecules through the catalyst surfaces, thus providing excellent ORR performance with higher current density.

4. Conclusions

In summary, we have demonstrated the successful synthesis of Ni,N co-doped porous carbon by high temperature decomposition of g-C_3N_4 templated Ni doped ZIF-8 precursors. By varying the Ni/Zn molar ratio and the carbonisation temperature, we were able to get heteroatom doped porous carbon with various architectures as well as pore characteristics. The nickel ion contributed towards the creation of defective sites through the formation of nickel carbide and the presence of g-C_3N_4 in the composite enabled the formation of a micro–meso porous architecture with high nitrogen content and surface area. The incorporation of the guest metal atom Ni as well as the sacrificial template of g-C_3N_4 has contributed to the evolution of carbon surfaces of varying morphology with an increase in electrocatalytic activity for ORR in alkaline medium. The sample NiZC(1:2) 1000 exhibited higher electrocatalytic activity compared to other samples with a limiting current density of 5.2 mA cm^{-2} and a half-wave potential of 0.76 V vs. RHE. The sample also exhibited higher durability and methanol tolerance in alkaline medium compared to the commercial Pt/C electrocatalyst. The hetero-porous carbon electrocatalysts

thus developed can contribute towards the development of economically viable fuel cells.

Conflicts of interest

There are no conflicts to declare.

Acknowledgements

Notes and references

1 P. P. Edwards, V. L. Kuznetsov, W. I. F. David and N. P. Brandon, *Energy Policy*, 2008, **36**, 4356–4362.

2 M. Momirlan and T. N. Veziroglu, *Int. J. Hydrogen Energy*, 2005, **30**, 795–802.

3 M. S. Dresselhaus and I. L. Thomas, *Nature*, 2001, **414**, 332–337.

4 S. M. Haile, *Acta Mater.*, 2003, **51**, 5981–6000.

5 A. A. Gewirth and M. S. Thorum, *Inorg. Chem.*, 2010, **49**, 3557–3566.

6 M. Debe, *Nature*, 2012, **486**, 43–51.

7 Y. Sun, M. Delucchi and J. Ogden, *Int. J. Hydrogen Energy*, 2011, **36**, 11116–11127.

8 C. Sealy, *Mater. Today*, 2008, **11**, 65–68.

9 P. Gouérec, L. Poletto, J. Denizot, E. Sanchez-Cortezon and J. H. Miners, *J. Power Sources*, 2004, **129**, 193–204.

10 J. R. Varcoe and R. C. T. Slade, *Fuel Cells*, 2005, **5**, 187–200.

11 S. Mekhilef, R. Saidur and A. Safari, *Renewable Sustainable Energy Rev.*, 2012, **16**, 981–989.

12 M. Zhang and L. Dai, *Nano Energy*, 2012, **1**, 514–517.

13 M. lefèvre and J.-P. Dodelet, *ECS Trans.*, 2012, **45**, 35–44.

14 A. Morozan, B. Jousselme and S. Palacin, *Energy Environ. Sci.*, 2011, **4**, 1238–1254.

15 H. Wang, T. Maiyalagan and X. Wang, *ACS Catal.*, 2012, **2**, 781–794.

16 S. M. Unni, S. N. Bhange, R. Illathvalappil, N. Mutneja, K. R. Patil and S. Kurungot, *Small*, 2015, **11**, 352–360.

17 Y. J. Sa, C. Park, H. Y. Jeong, S. H. Park, Z. Lee, K. T. Kim, G. G. Park and S. H. Joo, *Angew. Chem., Int. Ed.*, 2014, **126**, 4186–4190.

18 J. Zhang and L. Dai, *ACS Catal.*, 2015, **5**, 7244–7253.

19 Z. Zhao, M. Li, L. Zhang, L. Dai and Z. Xia, *Adv. Mater.*, 2015, **27**, 6834–6840.

20 S. Kottarathil, R. Illathvalappil, S. Nisa, G. S. Sailaja, A. P. Mohamed, B. N. Nair, M. A. Gopinathan, S. Kurungot, T. Yamaguchi and U. S. Hareesh, *Mater. Lett.*, 2020, **264**, 127365.

21 R. Gokhale, S. M. Unni, D. Puthusseri, S. Kurungot and S. Ogale, *Phys. Chem. Chem. Phys.*, 2014, **16**, 4251–4259.

22 X. Peng, V. Kashyap, B. Ng, S. Kurungot, L. Wang, J. R. Varcoe and W. E. Mustain, *Catalysts*, 2019, **9**, 264.

23 J. P. Paraknowitsch and A. Thomas, *Energy Environ. Sci.*, 2013, **6**, 2839–2855.

24 S. Kim, S. Kato, T. Ishizaki, O. L. Li and J. Kang, *Nanomaterials*, 2019, **9**, 742.

25 A. Sarapuu, E. Kibena-Põldsepp, M. Borghei and K. Tammeveski, *J. Mater. Chem. A*, 2018, **6**, 776–804.

26 V. Vij, S. Sultan, A. M. Harzandi, A. Meena, J. N. Tiwari, W.-G. Lee, T. Yoon and K. S. Kim, *ACS Catal.*, 2017, **7**, 7196–7225.

27 B. Devi, R. R. Koner and A. Halder, *ACS Sustainable Chem. Eng.*, 2019, **7**, 2187–2199.

28 A. Tyagi, K. K. Kar and H. Yokoi, *J. Colloid Interface Sci.*, 2020, **571**, 285–296.

29 S. Pandiaraj, H. B. Aiyappa, R. Banerjee and S. Kurungot, *Chem. Commun.*, 2014, **50**, 3363–3366.

30 L. Yang, X. Zeng, W. Wang and D. Cao, *Adv. Funct. Mater.*, 2018, **28**, 1704537.

31 J. Song, C. Zhu, B. Z. Xu, S. Fu, M. H. Engelhard, R. Ye, D. Du, S. P. Beckman and Y. Lin, *Adv. Energy Mater.*, 2017, **7**, 1601555.

32 H. Hayashi, A. P. Côté, H. Furukawa, M. O'Keeffe and O. M. Yaghi, *Nat. Mater.*, 2007, **6**, 501–506.

33 R. Banerjee, A. Phan, B. Wang, C. Knobler, H. Furukawa, M. O'Keeffe and O. M. Yaghi, *Science*, 2008, **319**, 939–943.

34 K. Li, D. H. Olson, J. Seidel, T. J. Emge, H. Gong, H. Zeng and J. Li, *J. Am. Chem. Soc.*, 2009, **131**, 10368–10369.

35 X. C. Huang, Y. Y. Lin, J. P. Zhang and X. M. Chen, *Angew. Chem., Int. Ed.*, 2006, **45**, 1557–1559.

36 L. Zhang, Z. Su, F. Jiang, L. Yang, J. Qian, Y. Zhou, W. Li and M. Hong, *Nanoscale*, 2014, **6**, 6590–6602.

37 S. Ma, G. A. Goenaga, A. V. Call and D.-J. Liu, *Chem. – Eur. J.*, 2011, **17**, 2063–2067.

38 T. Palaniselvam, B. P. Biswal, R. Banerjee and S. Kurungot, *Chem. – Eur. J.*, 2013, **19**, 9335–9342.

39 J. Wang, G. Han, L. Wang, L. Du, G. Chen, Y. Gao, Y. Ma, C. Du, X. Cheng, P. Zuo and G. Yin, *Small*, 2018, **14**, 1704282.

40 W. Zhang, X. Yao, S. Zhou, X. Li, L. Li, Z. Yu and L. Gu, *Small*, 2018, **14**, 1800423.

41 M. Thomas, R. Illathvalappil, S. Kurungot, B. N. Nair, A. P. Mohamed, G. M. Anilkumar, T. Yamaguchi and U. S. Hareesh, *ChemistrySelect*, 2018, **3**, 8688–8697.

42 K. Shijina, R. Illathvalappil, N. S. Sumitha, G. S. Sailaja, S. Kurungot, B. N. Nair, A. Peer Mohamed, G. M. Anilkumar, T. Yamaguchi and U. S. Hareesh, *New J. Chem.*, 2018, **42**, 18690–18701.

43 S. M. Unni, G. M. Anilkumar, M. Matsumoto, T. Tamaki, H. Imai and T. Yamaguchi, *Sustainable Energy Fuels*, 2017, **1**, 1524–1532.

44 S. Gadipelli, Z. Li, T. Zhao, Y. Yang, T. Yildirim and Z. Guo, *J. Mater. Chem. A*, 2017, **5**, 24686–24694.

45 J. Mao, P. Liu, J. Li, D. Liang, J. Yan and W. Song, *Adv. Mater. Interfaces*, 2019, **6**, 1901186.

46 H. x. Zhong, J. Wang, Y. w. Zhang, W. l. Xu, W. Xing, D. Xu, Y. f. Zhang and X. b. Zhang, *Angew. Chem., Int. Ed.*, 2014, **53**, 14235–14239.

47 M. Thomas, R. Illathvalappil, S. Kurungot, B. N. Nair, A. P. Mohamed, G. M. Anilkumar, T. Yamaguchi and U. S. Hareesh, *ACS Appl. Mater. Interfaces*, 2016, **8**, 29373–29382.

48 G. Jia, W. Zhang, G. Fan, Z. Li, D. Fu, W. Hao, C. Yuan and Z. Zou, *Angew. Chem., Int. Ed.*, 2017, **56**, 13781–13785.

49 P. Zhang, F. Sun, Z. Xiang, Z. Shen, J. Yun and D. Cao, *Energy Environ. Sci.*, 2014, **7**, 442–450.

50 R. Wang, T. Yan, L. Han, G. Chen, H. Li, J. Zhang, L. Shi and D. Zhang, *J. Mater. Chem. A*, 2018, **6**, 5752–5761.

51 J. Liu, T. Zhang, Z. Wang, G. Dawson and W. Chen, *J. Mater. Chem.*, 2011, **21**, 14398–14401.

52 X. X. Wang, D. A. Cullen, Y.-T. Pan, S. Hwang, M. Wang, Z. Feng, J. Wang, M. H. Engelhard, H. Zhang, Y. He, Y. Shao, D. Su, K. L. More, J. S. Spendelow and G. Wu, *Adv. Mater.*, 2018, **30**, 1706758.

53 A. F. Gross, E. Sherman and J. J. Vajo, *Dalton Trans.*, 2012, **41**, 5458–5460.

54 W. J. Eilbeck, F. Holmes, C. E. Taylor and A. E. Underhill, *J. Chem. Soc. A*, 1968, 128–132.

55 C. Hu, Y.-C. Chu, Y.-R. Lin, H.-C. Yang and K.-H. Wang, *Polymers*, 2019, **11**, 182.

56 A. Chakrabarti, J. Lu, J. Skrabutenas, Z. Xiao, J. Maguire and N. Hosmane, *J. Mater. Chem.*, 2011, **21**, 9491–9493.

57 N. Bao, X. Hu, Q. Zhang, X. Miao, X. Jie and S. Zhou, *Appl. Surf. Sci.*, 2017, **403**, 682–690.

58 J. L. C. Rowsell, E. C. Spencer, J. Eckert, J. A. K. Howard and O. M. Yaghi, *Science*, 2005, **309**, 1350–1354.

59 S. K. Nune, P. K. Thallapally, A. Dohnalkova, C. Wang, J. Liu and G. J. Exarhos, *Chem. Commun.*, 2010, **46**, 4878–4880.

60 S. Gadipelli, W. Travis, W. Zhou and Z. Guo, *Energy Environ. Sci.*, 2014, **7**, 2232–2238.

61 J. Liu, Y. Zhang, L. Zhang, F. Xie, A. Vasileff and S.-Z. Qiao, *Adv. Mater.*, 2019, **31**, 1901261.

62 D. Guo, R. Shibuya, C. Akiba, S. Saji, T. Kondo and J. Nakamura, *Science*, 2016, **351**, 361.

63 L. Qin, D. Huang, P. Xu, G. Zeng, C. Lai, Y. Fu, H. Yi, B. Li, C. Zhang, M. Cheng, C. Zhou and X. Wen, *J. Colloid Interface Sci.*, 2019, **534**, 357–369.

64 Y. Fu, P. Xu, D. Huang, G. Zeng, C. Lai, L. Qin, B. Li, J. He, H. Yi, M. Cheng and C. Zhang, *Appl. Surf. Sci.*, 2019, **473**, 578–588.

65 Y.-C. Chiang, W.-H. Lin and Y.-C. Chang, *Appl. Surf. Sci.*, 2011, **257**, 2401–2410.

66 F. A. Permatasari, A. H. Aimon, F. Iskandar, T. Ogi and K. Okuyama, *Sci. Rep.*, 2016, **6**, 21042.

67 Y. Liu, T. G. Kelly, J. G. Chen and W. E. Mustain, *ACS Catal.*, 2013, **3**, 1184–1194.

68 H. Wang, C. M. B. Holt, Z. Li, X. Tan, B. S. Amirkhiz, Z. Xu, B. C. Olsen, T. Stephenson and D. Mitlin, *Nano Res.*, 2012, **5**, 605–617.

69 T. Jawhari, A. Roid and J. Casado, *Carbon*, 1995, **33**, 1561–1565.

70 A. C. Ferrari and J. Robertson, *Phys. Rev. B: Condens. Matter Mater. Phys.*, 2000, **61**, 14095–14107.

71 B. Li, H. Nam, J. Zhao, J. Chang, N. Lingappan, F. Yao, T. H. Lee and Y. H. Lee, *Adv. Mater.*, 2017, **29**, 1605083.

72 E. M. Miner, T. Fukushima, D. Sheberla, L. Sun, Y. Surendranath and M. Dincă, *Nat. Commun.*, 2016, **7**, 10942.

73 J. Huai, K. Ma, Y. Lu, T. Chen and Z. Zhao, *ChemCatChem*, 2019, **11**, 4818–4821.

74 G. Fu, X. Yan, Y. Chen, L. Xu, D. Sun, J.-M. Lee and Y. Tang, *Adv. Mater.*, 2018, **30**, 1704609.

This journal is © The Royal Society of Chemistry and the Centre National de la Recherche Scientifique 2020